Towards a complete census of active galactic nuclei in the nearby Universe

GOULDING, ANDREW

Towards a complete census of Active Galactic Nuclei in the nearby Universe

Andrew David Goulding

A thesis presented in accordance with the regulations for admittance to the degree of Doctor of Philosophy.

Extragalactic Astronomy
Department of Physics
University of Durham
United Kingdom

September 2010

To my family.

Towards a complete census of
active galactic nuclei in the nearby Universe

Andrew D. Goulding

Abstract

As it is well established that almost all galaxies host a central supermassive black hole (SMBH), it is natural to ask, how many of these SMBHs are actively accreting? Studies aimed at answering this question can better define the fraction of nearby galaxies that harbour active galactic nuclei (AGNs), provide constraints on the growth of local SMBHs, and further our understanding towards the connection between AGN activity and galaxy evolution.

In the first part of this thesis, we use high-quality mid-infrared (IR) spectroscopy to investigate the ubiquity of AGN activity in a complete volume-limited sample of nearby galaxies to $D < 15$ Mpc. We present analyses based on the detection of high-excitation emission lines to unambiguously identify AGNs in even the most heavily dust-obscured and gas-rich galaxies. We find that almost half of the AGN population are not identified in large-scale optical surveys, most likely due to strong circumnuclear star-formation activity and/or extinction through the host galaxy. In the second part of this thesis, we use sensitive hard X-ray (2–10 keV) and mid-IR constraints to calculate bolometric luminosities of these $D < 15$ Mpc AGNs and combine these luminosities with well-constrained SMBH masses to estimate relative mass accretion rates. We use these data to calculate the volume-average SMBH growth rate of galaxies in the local Universe and find that AGNs hosting SMBHs with $\mathrm{M_{BH}} \approx 10^{6}$–$10^{7}\,\mathrm{M_{\odot}}$ are dominated by optically unidentified AGNs. These relatively small SMBHs are acquiring a significant proportion of their mass in the present-day and are amongst the most rapidly growing in the local Universe.

In the third part of this thesis, we using [NeV]λ3427Å as an unambiguous indicator of AGN activity to assess the incidence of AGNs in a statistically significant galaxy sample derived from the Sloan Digital Sky Survey (SDSS). On the basis of [NeV], we find strong empirical evidence that the theoretical maximum starburst limit provides a good identification threshold for AGNs. However, we find that only ≈ 27 percent of Seyfert galaxies have strong detections of [NeV]λ3427Å in their optical spectroscopy.

Using spectral stacking analyses we determine that the lack of high-ionisation emission line signatures are due to poor spectral sensitivity and/or high levels of dust extinction.

In the final part of this thesis, we use a suite of mid-IR, optical and X-ray luminosity indicators to search for Compton-thick AGNs at $z \sim 0.03$–0.2, a region of parameter space which is currently poorly constrained by deep narrow-field X-ray surveys. We use the *XMM-Newton* serendipity survey and the SDSS to select a sample of 14 candidate Compton-thick AGNs. On the basis of the optical [OIII], mid-IR [OIV] $\lambda 25.89\,\mu\mathrm{m}$ and $6\,\mu\mathrm{m}$ AGN continuum luminosities we conservatively find that the X-ray emission in almost half of our sample appear to be attenuated by a factor $\gtrsim 15$, i.e., they are likely to be obscured by Compton-thick material with $N_H > 1.5 \times 10^{24}\,\mathrm{cm}^{-2}$. Under the reasonable assumption that our 14 AGNs are representative of the overall X-ray undetected AGN population in the SDSS–XMM parent sample, we estimate that $\gtrsim 20$ percent of the optical Type-2 AGN population are likely to be obscured by Compton-thick material. These Compton-thick AGNs identified in our sample harbour some of the most rapidly growing SMBHs in the nearby Universe. Overall, the techniques and results presented in this thesis have arguably provided the most complete and unambiguous census of AGN activity in nearby galaxies to date.

Declaration

The work described in this thesis was undertaken between October 2007 and August 2010 while the author was a research student under the supervision of Dr. David M. Alexander in the Department of Physics at the University of Durham. This work has not been submitted for any other degree at the University of Durham or any other University.

Chapter 2 of this thesis is partially a compilation of data analysis sections from the published papers presented in Chapters 3, 4 and 6.
Chapter 3 of this thesis has been published in the form of a paper:

- **Goulding, A. D. & Alexander, D. M.**, 2009, *Towards a complete census of AGNs in nearby galaxies: a large population of optically unidentified AGNs*, *Monthly Notices of the Royal Astronomical Society*, Volume 398, Issue 3, pp. 1165-1193.

The work presented in Chapter 4 has been published in the form of a paper:

- **Goulding, A. D.; Alexander, D. M.; Lehmer, B. D.; Mullaney, J. R.**, 2010, *Towards a complete census of AGNs in nearby galaxies: the incidence of growing black holes*, *Monthly Notices of the Royal Astronomical Society*, Volume 406, Issue 1, pp. 597-611.

Chapter 5 will form a paper that is to be submitted to *Monthly Notices of the Royal Astronomical Society* as Goulding, Alexander, Hickox & Mullaney.

The work presented in Chapter 6 has been submitted in the form of a paper:

- **Goulding, A. D.; Alexander, D. M.; Mullaney, J. R.; Gelbord, J.; Hickox, R.C., Ward, M., Watson, M.**, 2010, *Searching for Compton-thick active galactic nuclei at* $z \sim 0.1$, *Monthly Notices of the Royal Astronomical Society*, submitted

The work described in Chapters 2, 3, 4, 5 and 6 was performed in collaboration with others. All text was written by myself. Chapters 3, 4 and 6 are based on the results of successful observing proposals led by my supervisor, Dr. D.M. Alexander, with all data reduction and measurements performed by myself.

Acknowledgments

With any work of this size there are always a few people to thank. First of all, I owe a profound debt of gratitude to my supervisor, Dave Alexander, for (1) giving me the opportunity to do this Ph.D. and guiding me through fantastically over these past three years; (2) showing me that numbered lists are extremely important when making a strong point; and (3) making me realise that absolute clarity in any paper is almost an impossibility! It is truly difficult to place into words how great a pleasure it has been to be taught by Dave and how grateful I am for the experience he has instilled into me; so I simply say, thank-you. I would also especially like to thank Martin Ward, Chris Done, Tim Roberts for their extremely insightful and stimulating discussions, and not least Alastair Edge – one summer, as an undergraduate student, Alastair kindly gave me the opportunity to experience 'research life' in Durham, and I can honestly say that I've never looked back.

It has been my experience that no student can ever leave a Ph.D. without thanking the post-docs closest to them – these hallowed people who have tirelessly put up with the student traipsing into their office, week-after-week, with question-after-question. In light of this, I would like to thank Bret Lehmer, James Mullaney, Ryan Hickox, Matthew Middleton, Mark Swinbank and James Geach. Without them, I'm almost certain that I would not have made it this far.

I have also been lucky enough to meet some great friends whilst at Durham, who have certainly made this time worth while. Singling out certain people is no easy task, but without a doubt I must thank my office mate Julie, who has somehow put up with me in 311 over the past three years. She has been fantastic. I'd also like to say a quick thank-you to Adam Ingram, Sarah Hutton, Kristen Geach, Mike Hill, Tim Rawle, Jeanette Gladstone and others!

My family have provided me with unwavering support over the past ≈ 25 years, and I owe them a great deal. When I first announced at the age of 5 that I wanted to be a scientist (how naive I was), my parents did not question, but simply smiled and nodded. Despite this somewhat strange career path which I have undertaken, they have stood by me ever since, and I hope I've shown it was worth it.

Finally, I save my last, and by no means least, thank-you to my beautiful wife, Hannah. She has quite honestly been my rock. Thank-you for being there for me when I needed you the most – for constantly distracting me and for reminding me that astrophysics is only the second most important thing in my life!

Contents

List of Figures

List of Tables

'Well the thing about a black hole – its main distinguishing feature – is its black. And the thing about space, the colour of space, your basic space colour, is black.
So how are you supposed to see them?'

Holly, *Marooned*, *Red Dwarf*

Chapter 1

Introduction

It is now well established that all massive galaxies ($M_* \approx 10^{10}$–$10^{12}\,\mathrm{M}_\odot$) in the local Universe harbour central super-massive black holes (SMBHs; $\mathrm{M_{BH}} \approx 10^5$–$10^9\,\mathrm{M}_\odot$; e.g., Kormendy and Richstone 1995). These SMBHs have grown through mass accretion events, so called active galactic nucleus (AGN) phases. The seminal discovery that the masses of SMBHs are proportional to those of their stellar spheroids (e.g., Magorrian et al. 1998; Gebhardt et al. 2000) implies a strong physical association between AGN activity and galaxy evolution. To fully interpret the role played by AGN in this symbiosis therefore requires a complete census of growing SMBHs across cosmic time. In this chapter, I will give a brief introduction to the history of AGNs, the spectrum of emission we expect to observe from such objects, the role that we believe the accreting SMBH population plays in galaxy evolution, and finally, a discussion on the observational techniques which are necessary in order to build towards a complete census of AGN activity across cosmic time.

1.1 History

The first AGN was discovered in 1908 by Edward A. Fath whilst analysing the nuclear spectrum of the "spiral nebula", NGC 1068. Of course, external galaxies beyond the Milky Way were not known at this time, let alone the existence of AGNs. Retrospectively, this was the first documented case of a galaxy showing strong *emission lines* in addition to the continuum and absorption-lines which were typically observed in other "nebulae" (see Fath 1908). By 1943, twelve "emission-line nebulae" had been discovered, leading to the publication of the historic paper of Carl K. Seyfert (Seyfert, 1943). In his paper, Seyfert describes the main features of the six brightest known emission-line

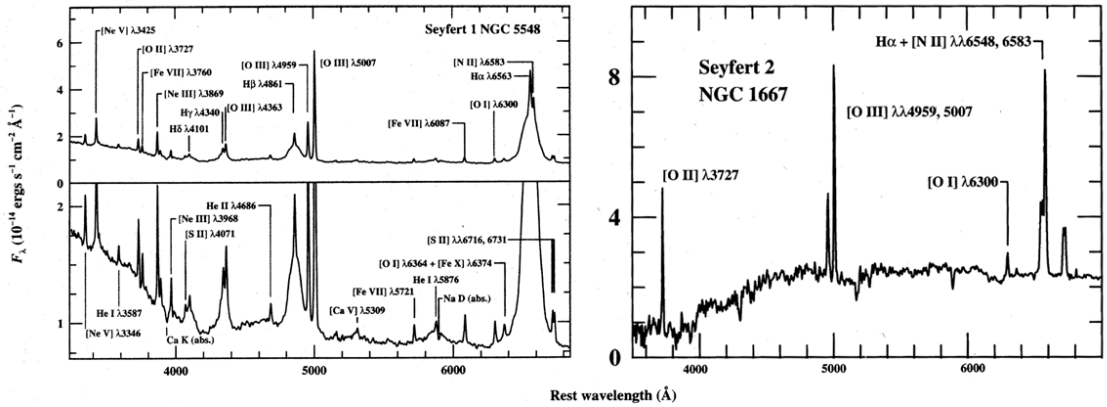

Figure 1.1: **Left panel:** Optical spectrum of NGC 5548, a typical nearby Seyfert 1 galaxy. Narrow lines appear super-imposed onto broadened bases for the Hα, Hβ and Hγ permitted emission lines. These broad permitted lines are an indicative signature of Type-1 AGNs. **Right panel:** Optical spectrum of NGC 1667, a nearby Seyfert 2 galaxy. By contrast to NGC 5548, the balmer lines, in this particular AGN, are weak and have similar widths ($< 1000\,\mathrm{km\,s^{-1}}$) to the forbidden emission lines (e.g., [OIII] λ5007Å). The spectra shown were first presented in Ho et al. (1995).

galaxies (NGC 1068, NGC 1275, NGC 3516, NGC 4051, NGC 4151 and NGC 7469). He found that the emission-lines were roughly correlated with increasing absolute magnitude, as well as the majority of the luminosity being concentrated at the galactic nuclei. Furthermore, Seyfert became the first to note that in all six of these galaxies, the emission-line profiles themselves were significantly broader (full-width zero intensity up to $\approx 8500\,\mathrm{km\,s^{-1}}$) than any lines previously measured in even the brightest known "normal" nebulae. Arising from his seminal work, this class of AGNs became known as *Seyfert galaxies*.

Seyfert galaxies are essentially spiral galaxies that produce strong nuclear emission which is comparable in bolometric luminosity to that of the host galaxy. The generally accepted criteria for a Seyfert galaxy are those with $M_B > -21.51 + 5\log h_0$ (Schmidt and Green, 1983). Depending on optical selection criteria, between 5 and 10 percent of local galaxies are believed to be Seyfert galaxies (e.g., Maiolino and Rieke 1995; Ho et al. 1997b). Khachikian and Weedman (1974) further sub-divided the Seyfert galaxies into two new classifications based on Balmer ("permitted") emission line width. Type-1 Seyfert galaxies (Sy1) are those with Doppler broadened Balmer lines at full-width half-

maximum (FWHM) in excess of $\approx 1000\,\mathrm{km\,s^{-1}}$, whilst in Type-2 Seyfert galaxies (Sy2) only the narrow-component of the Balmer emission lines is present.[1] See Fig. 1.1. The Sy1:Sy2 classification scheme was to form the basis of the "unified model" for AGNs.

Spectropolarimetry observations of some Sy2s were found to contain weak broad permitted emission lines which are thought to be scattered by free electrons in the corona of the AGN (e.g., Antonucci and Miller 1985; Miller and Goodrich 1990). In light of these observations, Antonucci (1993) presents a unified model of AGNs (see also the review of Urry and Padovani 1995) by which the different Seyfert classifications can be understood as one single entity. See Fig. 1.2. In this simplified model, a torus of gas and dust surrounds the central nucleus which obscures a direct line-of-sight to the broad-line emitting region (BLR; $r \sim 0.1$–1 pc) of the AGN when viewed from opposing orientations. Specifically, a Sy1 is viewed along the axis of the torus so that the BLR is unobscured; whilst, in Sy2 galaxies the central SMBH and the BLR are hidden behind the optically thick material, leaving visible only the more extended narrow-line region (NLR; $r \sim 10$–100 pc).

It is clear that the classification of an AGN from broadened emission lines is relatively straight forward when there is a direct line-of-sight to the BLR. However, a problem arises when considering galaxies which appear to only produce narrow-lines (i.e., Sy2). To this end, a landmark emission-line flux ratio classification scheme was introduced by Baldwin et al. (1981; hereafter, BPT diagnostics). They suggested that AGNs should generically have greater [OIII] $\lambda 5007$Å $/H\beta$ ratios than galaxies where the emission lines are due only to stellar processes. The creation of [OIII] $\lambda 5007$Å by photoionization requires ≈ 35 eV, and is only produced by AGNs or the most massive stars, hence its production is relatively low in typical star-forming galaxies. Furthermore, for similar reasons, AGNs are believed to produce greater [NII] $\lambda 6583/H\alpha$ ratios than normal galaxies. A standard definition for Sy2s are those galaxies with [OIII] $\lambda 5007$Å $/H\beta \gtrsim 3$ and [NII] $\lambda 6583/H\alpha \gtrsim 0.5$ (see Fig.1.3).

A class of low-luminosity narrow-line Seyfert galaxies was further introduced by Heckman (1980). Low ionisation nuclear emission regions (or LINERs) are extremely common in the local Universe, and are generally found in large spiral (Hubble-type S0) or early-type elliptical galaxies. LINERs are detected in ≈ 40 percent of optically selected nearby galaxies (e.g., Ho et al. 1997b), and are identified by the presence of less ionised

[1] An alternate, yet similar classification scheme, compares the width of the permitted to the narrow forbidden (e.g., [OIII] $\lambda 5007$Å) emission lines (e.g., Robson 1996).

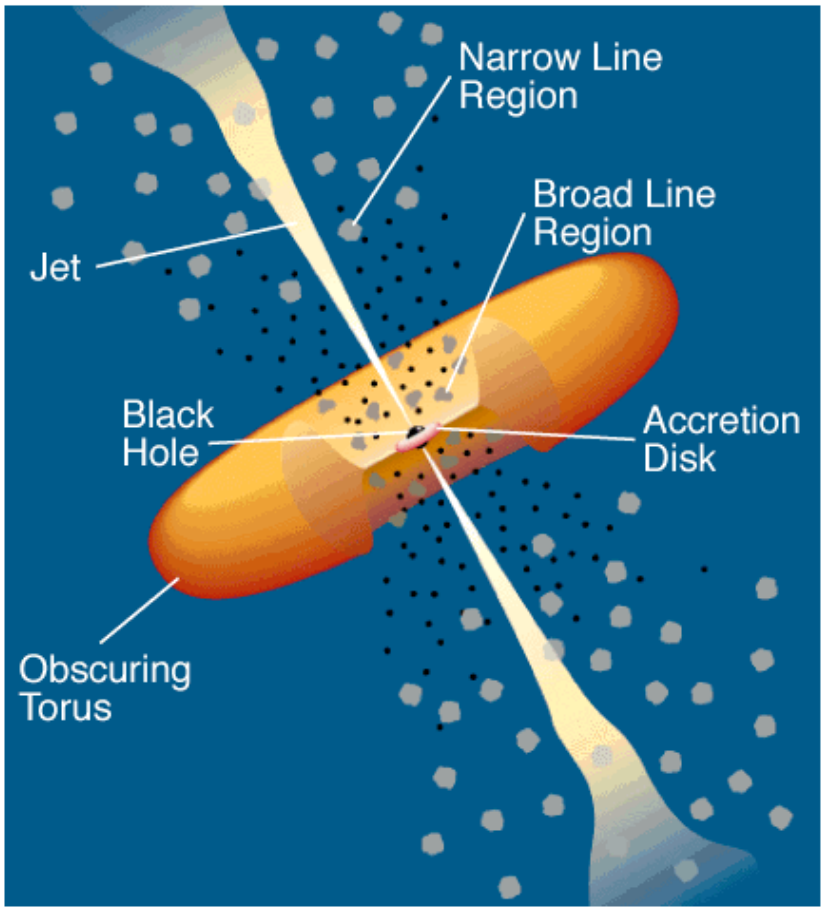

Figure 1.2: Schematic of the AGN unification model (adapted from Urry & Padovani 1995). The main components consist of a central SMBH and an accretion disc, surrounded, on larger scales, by a smooth optically thick torus of gas and dust aligned with the disc. The torus dictates the observed spectral energy distribution for a given line-of-sight orientation. This particular model is applicable to both radio-loud and radio-quiet AGNs (which would not have the depicted jets).

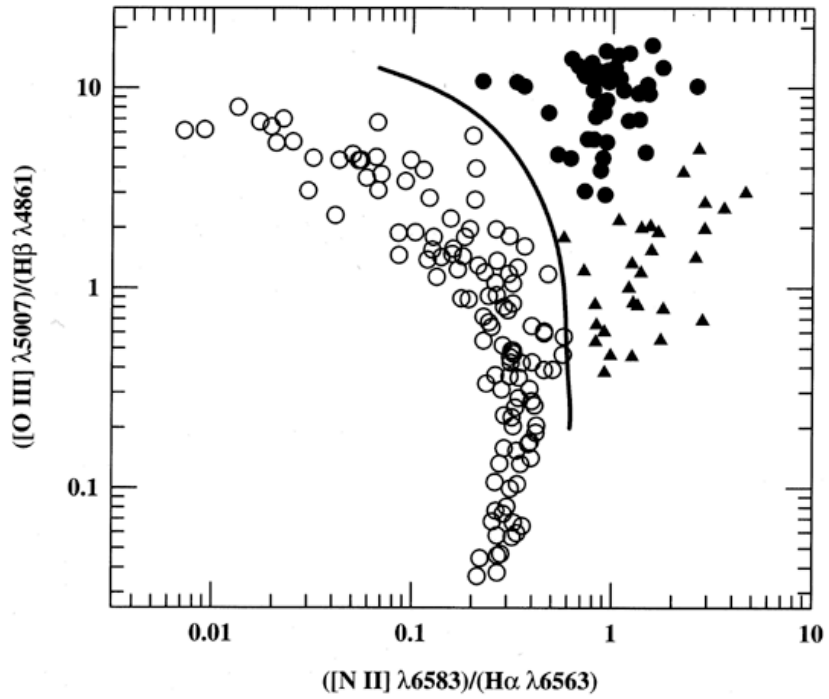

Figure 1.3: Emission-line ratio diagnostic diagram proposed by Baldwin et al. (1981) to separate galaxies based on their nuclear emission properties. Open circles represent star-forming galaxies, filled triangles are LINERs and filled circles are narrow-line AGNs (i.e., Sy2s). Figure adapted from Peterson (1997).

emission lines than typical Seyfert galaxies (e.g., [OI]λ6300; [SII]λ6716,6731; [NII]λ6583). However, it must be noted that there may now be evidence that many LINERs are actually powered by post-AGB stars and not a central accreting SMBH (e.g., Sarzi et al. 2010), though this is still a matter of on-going research and beyond the scope of this brief history.

Typically, emission from an AGN covers the majority of the electromagnetic spectrum, ranging from the highest energy photons emitted at γ-ray and X-ray energies to low-energy radio emission. Approximately 20 percent of Seyfert galaxies are known to produce strong emission at radio frequencies which is substantially in excess of that expected from star-formation, these are often referred to as radio-loud AGNs (e.g., Kellermann et al. 1989).[2] The most powerful radio-loud AGNs are quasi-stellar radio objects (or quasars).[3] These extremely luminous, star-like sources were first discovered by radio-

[2]The accepted definition of a radio-loud AGN is one with a ratio of radio emission at 5 GHz to optical B-band flux of $f_{5GHz}/f_B \gtrsim 10$.

[3]A radio-loud Quasi-stellar object (or quasar) is defined as a radio-loud AGN with $M_B < -23$. Hereafter, we refer to radio-quiet Quasi-stellar objects as QSOs.

surveys in the 1950s, but the connection between these and AGNs was not made until 1963. By identifying the strange emission lines in the spectrum of the archetypal radio galaxy, 3C 273 as being redshifted ($z \sim 0.158$) broadened Balmer lines, Schmidt (1963) deduced that quasars were, in fact, extremely luminous and very distant AGNs. This however, remained a fiercely contested issue for at least another decade (see Weedman 1976 for a review). It is now generally accepted that quasars (and QSOs) are similar to nearby Seyfert galaxies, although, the intrinsic luminosity of the central source is greater in quasars, and their prevalence is likely to have peaked at a much earlier epoch in the Universe ($z \sim 2$; e.g., Hewett et al. 1993; Richards et al. 2006).

1.2 The physical picture of AGNs

In the previous section, we provided a brief history into the discovery of the first Seyfert galaxies, their physical reconciliation with previously observed radio galaxies, and the introduction of basic AGN sub-classes based on emission line width and luminosity. Despite the obvious differences in observed properties for each of the AGN categories, it is almost universally agreed that these objects are powered by the same physical process, the accretion of matter onto a SMBH (e.g., Salpeter 1964; Lynden-Bell 1969). In this section, we outline basic AGN accretion physics and the subsequent production of the AGN spectral energy distribution (SED).

1.2.1 The central engine

Comparisons between the SMBH mass density in the local Universe and the total energy produced by AGNs across cosmic time have shown that SMBHs have primarily grown through mass-accretion events (e.g., Soltan 1982; Rees 1984; Marconi et al. 2004). Through the process of accretion, matter is predicted to lose angular momentum and spiral into a black hole in the form of a Shakura-Sunyaev disc (Shakura and Sunyaev 1973). The luminosity associated with the accretion can be parameterised as

$$L_{\rm acc} = \epsilon \dot{M} c^2 \tag{1.1}$$

where $\dot{M} = dM/dt$ is the mass accretion rate, and ϵ the efficiency parameter. The accretion efficiency is strongly dependent on the compactness of the accreting object, and is directly related to the inner-most stable orbit (r_{in}) of the black hole, where $\epsilon \sim 1/2r_{in}$.

The accretion efficiency parameter has typical values of 0.06 to 0.31 for a stationary and maximally spinning SMBH, respectively (for a recent review see Done 2010).

In a steady spherically symmetric system the luminosity due to accretion of fully ionized hydrogen onto a black hole will exert a radiation pressure on the electrons in the surrounding material due to Compton scattering.

$$F_{\rm rad} = L\frac{\sigma_T}{4\pi r^2 c} \tag{1.2}$$

At the same time, gravity exerts an inward force on the protons,

$$F_{\rm Grav} = \frac{GM_{BH}(m_p + m_e)}{r^2} \approx \frac{GM_{BH}m_p}{r^2} \tag{1.3}$$

we may negate the force of gravity on the electrons as their mass (m_e) is inconsequential compared to that of the proton (m_p). The luminosity at which the two opposing forces become equal, i.e., the maximum achievable luminosity due to accretion is therefore

$$L_{\rm Edd} = \frac{4\pi GM_{BH}m_p c}{\sigma_T} \approx 1.3\times10^{38}\left(\frac{M_{BH}}{\rm M_\odot}\right)\,{\rm erg\,s^{-1}} \tag{1.4}$$

and is known as the Eddington luminosity. The equation, of course, makes a gross over-simplification of the actual geometry of a black hole system during accretion. For example, before falling into the black hole the matter is expected to form an accretion disc. The specific geometry of this disc, is likely to shift the Eddington limit to higher luminosities for a black hole with a radiatively efficient thin disc. However, the assumption of a spherically symmetric geometry appears to provides a good first-order approximation for $L_{\rm Edd}$ and is used throughout the current literature (e.g., McLure and Dunlop 2004; Marconi et al. 2004; Kollmeier et al. 2006).

The ratio of the observed accretion luminosity and the Eddington luminosity (the so-called, Eddington ratio; η) presents a standard measure for which to compare SMBH accretion over a wide mass parameter space.

$$\eta = L_{acc}/L_{Edd} \tag{1.5}$$

For typical SMBH masses of nearby AGNs ($\rm M_{BH} \approx 10^6$–$10^8\,M_\odot$), Eddington ratios are estimated to be in the range $\eta \sim 0.001$–0.1. A small fraction of sources have been observed with seemingly 'Super-Eddington' SMBHs (i.e., $\eta > 1$), suggesting that these AGNs are either under going significant mass accretion events which are outputting energy at a rate capable of expelling the surrounding material or that they have unusual geometries (e.g., beamed emission; slim discs).

Equating (1.1) and (1.4), we may also derive the characteristic time scale (t_{Edd}) of an accreting black hole,

$$t_{\rm Edd} = \epsilon \frac{c\,\sigma_T}{4\pi G m_p} \approx 4\epsilon \times 10^8 \text{ years} \tag{1.6}$$

and is the time taken for a black hole to radiate its entire rest mass at the Eddington rate (i.e., the mass doubling-time).

Throughout this work, frequent reference is made to the equations outlined in this section. The observed accretion luminosity is hereafter referred to as the bolometric AGN luminosity ($L_{\rm bol,AGN}$), and in Chapter 4, we use equations (1.5) and (1.6) to derive the average characteristic mass doubling times of SMBHs in the nearby Universe.

1.2.2 The spectral energy distribution of AGNs

Towards the latter half of the 20th century, observatories and instruments had been developed which were capable of observing the Universe throughout almost the entire electromagnetic spectrum. Luminous quasars were amongst the first objects to have their spectral energy distributions (SEDs) mapped from the radio to γ-ray energies. See Fig. 1.4. Despite quasars being luminous radio sources, it quickly became apparent that the radio emission does not dominate the total energy output of the object. If we assume that the AGN accretion disc is optically thick, the emitted continuum spectrum would be thermally dominated and defined by a black-body with temperature,

$$T_{\rm bb} = \left(\frac{L_{\rm acc}}{4\pi R_*^2 \sigma} \right)^{1/4} \tag{1.7}$$

where $R_* \sim 2GM_{BH}/c^2$ is the radius of the black hole and σ is the Stefan-Boltzmann constant. Hence, we may define the maximum temperature of an accreting black hole as,

$$T_{\rm max} \approx 2.4 \times 10^5 \left(\frac{\dot{M}}{0.1\dot{M}_{Edd}} \right)^{1/4} \left(\frac{\eta}{0.1} \right)^{-1/4} \left(\frac{M_{BH}}{10^8\,{\rm M}_\odot} \right)^{-1/4} K \tag{1.8}$$

For a typical AGN with $M_{BH} \approx 10^8\,{\rm M}_\odot$ and $\eta \approx 0.1$, $kT_{\rm max} \approx 30eV$, implying the peak emission for an accretion disc to be at Ultra-violet (UV) wavelengths. Indeed, the peak emission for most AGNs is believed to occur in the UV, and is often referred to as the 'big blue bump' (e.g., Shields 1978).

Thermal processes dominate the continuum spectra for the majority of AGNs, though not necessarily at UV wavelengths alone. AGNs are also powerful X-ray ($E \sim 0.2$–100 keV), optical ($\lambda \sim 4000$–9000Å) and infrared (IR; $\lambda \sim 1$–1000 μm) emitters, whilst

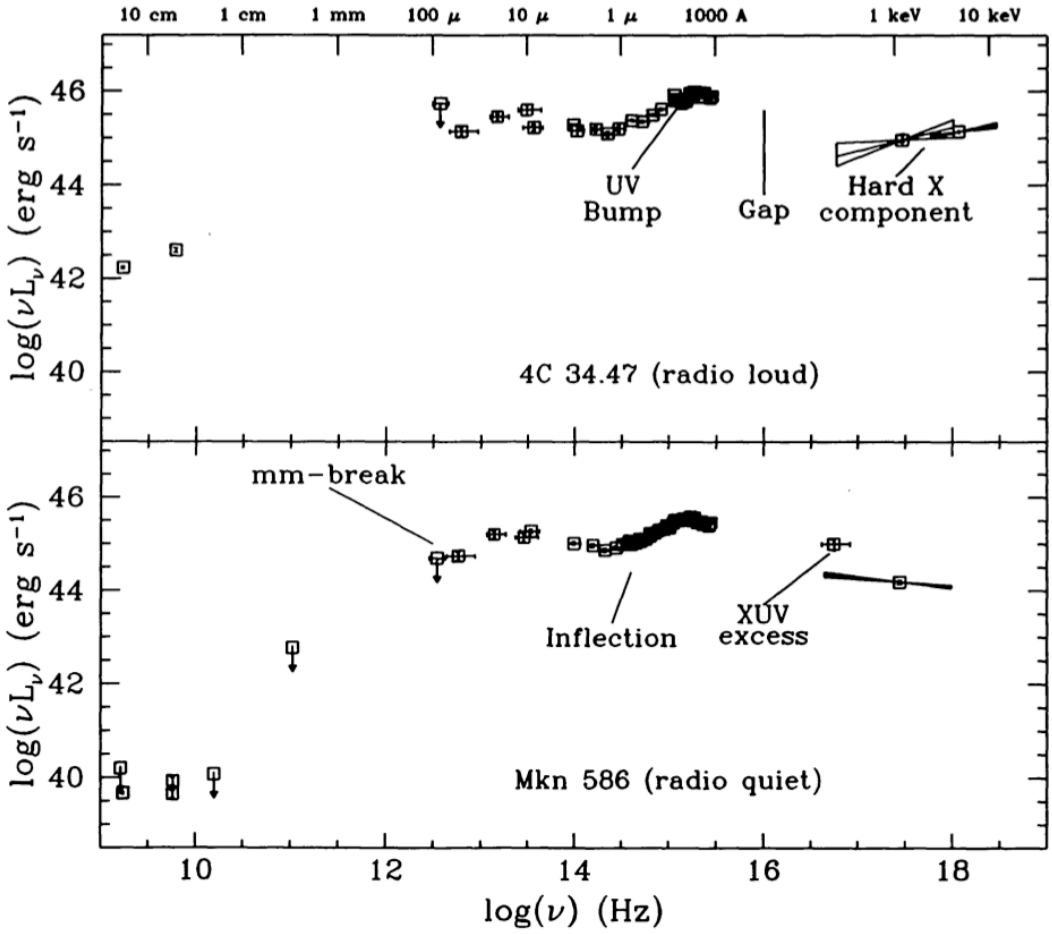

Figure 1.4: Spectral energy distributions of two quasars, 4C34.47 (upper panel) and Mkn 586 (lower panel) from the study of Elvis et al. (1994). The figure is shown in νL_ν representation as this better depicts the power output of the photons as function of the frequency. The SED of a typical quasar is believed to peak in the UV ($kT \approx 30$ eV), at a wavelength that unfortunately cannot be observed. The peak of the emission is often erroneously named the 'Big Blue Bump'.

$\approx$ 10–20 percent are also luminous at radio wavelengths. The intrinsic X-ray emission takes the form of a powerlaw at $E > 0.2$ keV and is believed to be produced by inverse Compton scattering where-by the thermally produced photons are up-scattered by the relativistic electrons in the corona (believed to effectively be the accretion-disc 'atmosphere') surrounding the central SMBH. The X-ray emission peaks at $E \sim 3kT_e$ and falls off sharply towards higher E. The optical continuum arises from the Wien tail of the thermal accretion disc emission. Finally, the IR emission is due to the isotropic thermal dust-reprocessing of the disc photons by the torus. It is due to AGNs producing luminous emission throughout the whole electromagnetic spectrum that we are capable of tracing their growth/evolution throughout cosmic time.

1.3 AGN activity across cosmic time

1.3.1 The AGN–host-galaxy connection

Whilst AGNs were originally considered to be interesting objects to study in isolation, there is now compelling evidence that despite their vastly differing size scales, the growth of the SMBH and the evolution of its host galaxy may be inextricably connected. The current evidence for this connected growth/evolution is: (1) the relationship between the mass of the SMBH and that of the stellar spheroid (e.g., Magorrian et al. 1998); (2) the tight correlation between $\mathrm{M_{BH}}$ and the stellar velocity dispersion (e.g., the so-called M–σ relation; Gebhardt et al. 2000; Tremaine et al. 2002; see Fig. 1.5), and (3) the histories of cosmic star-formation and luminous AGN activity appear to closely trace one another, peaking at $z \sim 2$ and declining rapidly towards the present-day (e.g., Madau et al. 1996; Franceschini et al. 1999; Zheng et al. 2009; Serjeant et al. 2010). Hence, it is predicted that these processes may be understood in the form of a fundamental framework where-by the formation of the SMBH and the galaxy was coeval (e.g., Hopkins et al. 2008).

Sensitive blank-field X-ray surveys have traced the evolution of luminous AGN activity out to $z \approx$ 5–6, providing a window on the growth of SMBHs across $\approx 95\%$ of cosmic time (e.g., Ueda et al. 2003; Croom et al. 2004; Fan et al. 2004; Hasinger et al. 2005; Richards et al. 2006). Using these surveys it has been established that the space density of high-luminosity AGNs appears to have peaked at higher redshifts than lower-luminosity AGNs, suggesting that the most massive SMBHs ($\mathrm{M_{BH}} \approx 10^8$–$10^9\,\mathrm{M_\odot}$) grew first, a result commonly referred to as 'AGN cosmic downsizing' (e.g., Cowie et al. 2003; McLure and Dunlop 2004; Hasinger et al. 2005; Alonso-Herrero et al. 2008). Extrapola-

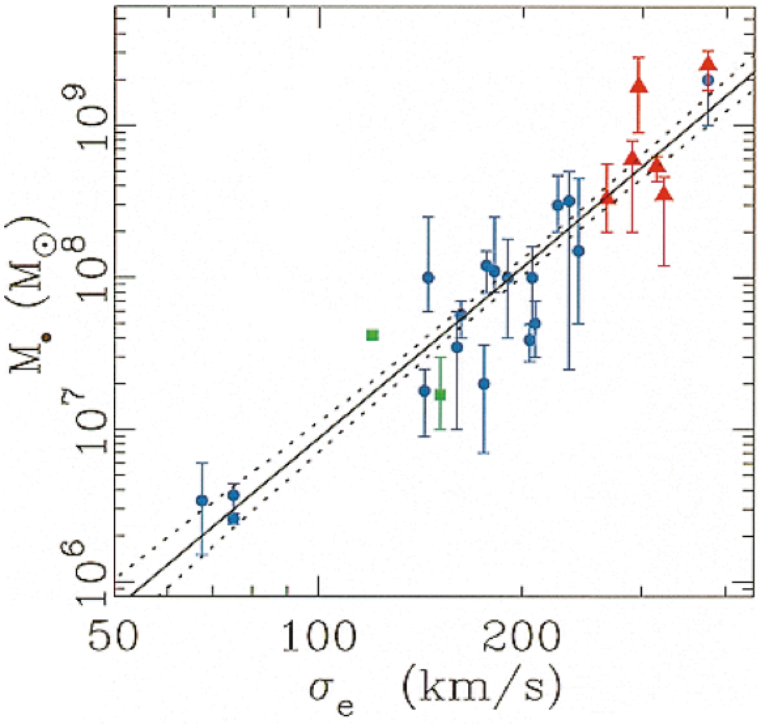

Figure 1.5: The distribution of SMBH mass ($\mathrm{M_{BH}}$) versus stellar velocity dispersion (σ_e) for a sample of local galaxies (adapted from Gebhardt et al. 2000).

tion of these results imply that the most rapidly growing SMBHs in the nearby Universe should be of comparatively low mass ($\mathrm{M_{BH}} \ll 10^8\,\mathrm{M_\odot}$). To determine the characteristic masses of these growing SMBHs requires a complete census of AGN activity and SMBH masses in the local Universe.

1.3.2 AGN activity in the local Universe

Over the past two decades, large scale optical studies (e.g., the Palomar spectral survey of nearby galaxies [Ho et al 1997]; the Sloan Digital Sky Survey [Kauffmann et al. 2003; Heckman et al. 2004]) have been highly influential in the classification and understanding of the properties of AGNs in the local Universe ($z < 0.03$). Arguably, the most complete optical census of AGN activity in the local Universe is the spectroscopic survey of Ho et al. (1997a,b, hereafter Ho97). Ho97 classified nearly all galaxies with $B_T \leq 12.5$ mag in the Northern hemisphere and identified AGNs on the basis of emission-line ratio diagnostics (e.g., Baldwin et al. 1981; Veilleux and Osterbrock 1987; Kewley et al. 2001a; see section 1.1 and Fig. 1.3); objects with a broad permitted line component were also classified as AGNs. Using this classification scheme, Ho97 found that $\approx 10\%$ of galaxies

unambiguously host AGN activity (i.e., optically classified as Seyfert galaxies), predominantly residing in moderately massive bulge-dominated galaxies (Hubble type E–Sbc). However, more recently it has emerged that, even in the nearby Universe, optical spectroscopy alone cannot accurately identify all AGNs.

1.4 The challenges in constructing a complete census of AGN activity in the local Universe: the obscuration issue

As suggested by the Unified model, the central regions of many AGNs appear to contain obscuring dust which prevents UV/optical wavelengths from directly penetrating. Whilst the torus may obscure a direct line of sight to the BLR, the NLR is expected to be extended beyond the torus, and hence an object should be detected as a Sy2 at optical wavelengths. However, optically obscuring material is not confined only to the central region of an AGN. Indeed the host galaxy contains high concentrations of dust and gas which may obscure the AGN, as well as significant emission from the host galaxy possibly diluting the AGN signatures. For example, some galaxies which are optically classified as "starbursts" are revealed to host heavily-obscured, but intrinsically luminous AGNs (e.g., NGC 4945; NGC 6240; Iwasawa et al. 1993; Armus et al. 2006) when observed at wavelengths which are relatively unaffected by dust/gas obscuration (e.g., hard X-rays; mid-IR). The construction of a complete census of AGN activity is a multi-tiered, multi-wavelength problem.

1.4.1 Dust and gas obscuration in the inner ≈ 10 parsecs

The specific geometry and composition of the optically (BLR) obscuring torus is currently not well known. Recent observations and theory favour a geometry where-by the dust may not be in the form of a smooth torus but instead may be distributed as dust clumps (though not necessarily in a fixed volume), the so-called clumpy torus model (Nenkova et al. 2008b). See Fig. 1.6. The inner radius of the torus is defined by the dust sublimation temperature, $T_{\rm sub}$,

$$R_d \approx 0.4 \left(\frac{L}{10^{45}\,{\rm erg\,s^{-1}}} \right)^{0.5} \left(\frac{1500{\rm K}}{T_{\rm sub}} \right)^{2.6} {\rm pc} \tag{1.9}$$

and varies as a function of intrinsic AGN luminosity. $T_{\rm sub}$ is typically in the range 1000–1500 K. In more luminous AGNs, R_d increases, and hence the opening angle of the torus

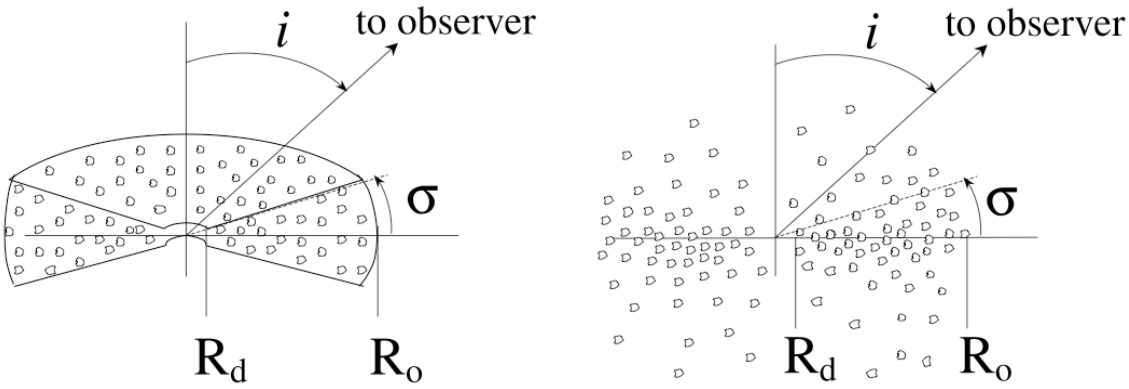

Figure 1.6: **Left:** The clumpy model for dust clouds with individual optical depth, τ, in a fixed toroidal volume. The inner radius (R_d) is determined by the dust-sublimation temperature. **Right:** The clumpy model where the dust clouds are not bound in a fixed volume. For this particular geometry, there is a small, non-zero probability that a dust cloud may obscure the BLR when the incident angle of the observer is $i = 0$. Figure adapted from Nenkova et al. (2008b).

must also increase. This leads to a luminosity dependence on the observed Sy1:Sy2 ratio; this is often referred to as the receding torus (e.g., Lawrence 1991; Simpson 2005).

There is now overwhelming evidence that the optically obscuring dust may also be co-spatial with the absorbing gas which can affect X-ray emission. In general, Type-2 AGNs appear to be obscured at 2–10 keV X-ray energies, but Type-1 AGNs appear relatively unobscured (see Maiolino et al. 2007, and references there-in).[4] Unlike emission produced at optical wavelengths, X-ray emission remains relatively unaffected by absorption in the host galaxy. For AGNs without significantly high columns of gas ($N_H \lesssim 10^{24}\,\mathrm{cm}^{-2}$) in the central region, the detection of hard X-ray emission provides an unambiguous indicator for AGN activity as well as a direct measurement of the intrinsic luminosity of the central source. Indeed, in the local Universe, X-ray observations have revealed potential AGNs in many galaxies in the Ho97 sample lacking optical AGN signatures (e.g., Ho et al. 2001; Desroches and Ho 2009).

However, the direct identification of AGNs at X-ray energies becomes complicated, and not without its pit-falls, when considering those AGNs with column densities exceeding the inverse Thomson cross-section ($N_H \sim 1.5 \times 10^{24}\,\mathrm{cm}^{-2}$; i.e., Compton-thick

[4]We note here that the situation is likely to be far more complicated than this due to the presence of highly ionised gas (a so-called warm-absorber) originating close to the torus which may also partially absorb UV and X-ray emission (see Blustin et al. 2005)

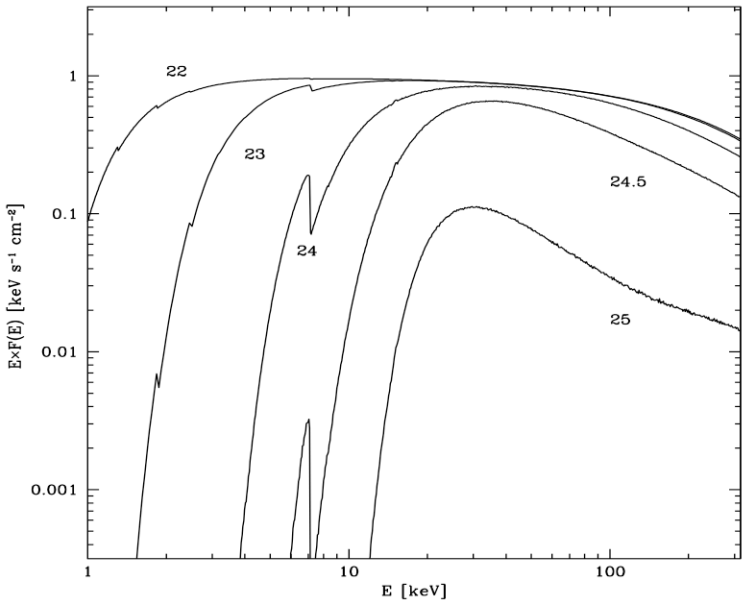

Figure 1.7: The effects of photoelectric absorption on a typical X-ray spectrum produced by an AGN. Spectrum depicted is a simple power law with $\Gamma = 2$ and an exponential cut-off at 300 keV. The labels indicate the logarithm of the column density (Comastri 2004)

absorption). The presence of high levels of absorbing gaseous material results in a strongly depressed nuclear X-ray emission observed at $E \sim 0.5$–10 keV, in-fact very few photons are detected at $E < 10$ keV due to significant absorption and scattering. Moreover, for sources with $N_H > 10^{25}\,\mathrm{cm}^{-2}$, the entire high energy spectrum is down-scattered and, eventually, absorbed by the heavily Compton-thick material. See Fig. 1.7. Consequently, the observed X-ray flux in Compton-thick AGNs is often rendered so weak that it becomes comparable to the X-ray emission arising from the host-galaxy (e.g., there can be significant contamination from X-ray binaries), making their unambiguous detection extremely difficult. The direct identification of mildly Compton-thick AGNs ($N_H \sim (1.5\text{–}10) \times 10^{24}\,\mathrm{cm}^{-2}$) is possible through X-ray observations at $E > 10$ keV (e.g., using *Beppo*-SAX, *Swift*, *Suzaku*) where the relatively unabsorbed high-energy emission can be detected. However, the sensitivities of current $E > 10$ keV observatories are substantially limited by high backgrounds, poor effective areas and poor spatial resolution. Indeed, to date, only 18 Compton-thick AGNs have been unambiguously identified in the Universe at $E > 10$ keV, mainly at $z \lesssim 0.01$ (for a recent review, see Della Ceca et al. 2008).

In the absence of higher-energy $E > 10$ keV data, the presence of a Compton-thick AGN may still be inferred using indirect methods: (1) from the detection of a high equivalent width (> 1 keV) Fe K_α fluorescence line at $E \sim 6.4$ keV (e.g., Awaki et al. 1991), and/or (2) nuclear emission which has been reflected into the line-of-sight by the highly ionised optically-thick material (a so-called, Compton-reflection component; e.g., Ghisellini et al. 1994; Matt et al. 1996). However, the detection of either of these Compton-thick AGN signatures is still difficult given the required high sensitivity of the X-ray data (spectra containing $\gtrsim 200$ counts). For example, even at low redshifts ($z \sim 0.05$) the observed X-ray flux required to detect FeK_α at a high significance often requires long exposure times even with the most sensitive X-ray observatories (of the order 100s of kiloseconds with *Chandra* and *XMM-Newton*). Indeed, only a further ≈ 30 local ($z < 0.01$) AGNs have been robustly determined to be Compton-thick AGNs in the absence of $E > 10$ keV data. Hence, although Compton-thick AGNs are predicted to comprise a large proportion of the overall AGN population ($\gtrsim 40$ percent; Risaliti et al. 1999; Matt et al. 2000), to date, only a handful have been detected at high redshift (e.g., Norman et al. 2002; Tozzi et al. 2006; Georgantopoulos et al. 2009); conversely, only ≈ 50 Compton-thick AGNs have been robustly identified in the nearby Universe at $z \lesssim 0.05$ (Comastri, 2004; Della Ceca et al., 2008). Clearly, whilst X-ray spectroscopy can identify a large proportion of the obscured AGN population and is relatively unaffected by the host-galaxy, large columns of gas in the central region can significantly reduce the ability to detect the most Compton-thick systems.

Whilst the torus readily extinguishes AGN emission at UV/optical wavelengths and X-ray energies, it isotropically re-emits the AGN emission at IR wavelengths. Local mid-IR ($\lambda \sim 5$–$40\ \mu$m) surveys (e.g., Sturm et al. 2002; the *Spitzer* Infrared Nearby Galaxy Survey [SINGS] Legacy Project [Dale et al. 2006; hereafter D06]; Gandhi et al. 2009) have shown that IR-detected AGN continuum emission provides a fantastic resource for the identification of AGN activity. Even the AGN continuum emission from heavily Compton-thick central sources that are weak at X-ray energies can be identified using mid-IR spectroscopy (e.g., the well-studied NGC 1068 with $N_{\rm H} > 10^{25}\,{\rm cm}^{-2}$). However, the detection of the AGN continuum at IR wavelengths (as with the optical and X-rays) has its own pit-falls. Stellar processes from the circumnuclear region of the host galaxy also strongly emit at IR wavelengths and are often found to dominate the continuum emission in IR spectroscopy. This complication can be overcome with significantly high signal-to-noise mid-IR observations (see Chapter 6) or with high-spatial resolution

ground-based mid-IR imaging (e.g., Gandhi et al. 2009).

1.4.2 Host galaxy dilution/extinction

Almost all AGNs are found to have a NLR which extends beyond the inner region of the central source (possibly on scales up to ≈ 1 kiloparsec). The NLR is not affected by the obscuration due to the torus and hence forbidden emission produced in this region is readily identified in even heavily Compton-thick AGNs. However, the NLR is still embedded within the host galaxy, which in itself contains large quantities of obscuring dust/gas. Throughout the current literature, the Balmer decrement (the $H\alpha/H\beta$ ratio) is used as a measure for the extinction occurring towards the NLR, and hence is used to correct the observed optical NLR emission for dust obscuration. This however makes the assumption that the line-of-sight to the Balmer emitting region and the NLR are one and the same. As AGNs are identified using X-ray observations which appear to produce little or no optical NLR emission (even after correcting for dust extinction as inferred from the Balmer decrement), it is logical to conclude that the NLR emission may be additionally obscured or over-whelmed by the host galaxy. However, (as in the previous section) ≈ 40 percent of AGNs are predicted to be Compton-thick, and hence are unlikely to be detected at X-ray wavelengths. In order to detect the remaining population of X-ray weak and host-galaxy obscured AGNs we can use infrared observations to detect the NLR emission which is being obscured by the host-galaxy.

Due to the extreme conditions required to produce the high ionisation emission line [NeV] $\lambda 14.32$, $24.32\ \mu$m (97.1 eV), mid-IR spectroscopy provides an unambiguous indicator of AGN activity in nearby galaxies (e.g., Weedman et al. 2005; Armus et al. 2006).[5] The relative optical depth at mid-IR wavelengths is considerably lower than at optical wavelengths ($A_{\lambda 14.3\ \mu\mathrm{m}}/A_{\mathrm{V}} \approx 50$; Li and Draine 2001) and hence, [NeV] emission will be relatively unaffected by the host-galaxy. Thus, the identification of high-ionisation [NeV] $\lambda 14.32$, $24.32\ \mu$m provides a relatively optically thin means by which to probe the central engine of nearby AGNs. On the basis of the identification of [NeV] emission in a heterogeneous sample of late-type spiral galaxies within the local Universe, Satyapal et al. (2008; hereafter, S08) have suggested that, contrary to the optical study of Ho97, a large number of Sc–Sm galaxies host AGN activity at mid-IR wavelengths. However, despite the obvious advantages to the use of mid-IR wavelengths to identify AGNs, no

[5] We note that [OIV] λ 25.9 μm (54.9 eV) is also often used for AGN identification, although energetic starbursts may also produce luminous [OIV] emission; see § 3.2.4

previous studies have used this to provide a complete unambiguous census of AGN activity within the local Universe.

1.5 Outline of this thesis

In this thesis I aim to provide an obscuration independent, and hence the most complete, census of AGN activity in the local Universe to date by combining new mid-infrared data with optical and X-ray observations. Such a census is required to (1) provide definitive constraints on the growth of SMBHs in the local Universe (e.g., the growth rates of SMBHs; the relative amount of obscured and unobscured SMBH growth; the galaxies and environments where SMBHs are growing); and (2) provide a baseline with which to interpret the results obtained for distant AGNs from blank-field surveys.

1.5.1 Chapter 2 – the reduction of *Spitzer*-IRS spectroscopic data

The main analyses presented in Chapters 3, 4 and 6 are based on the use of mid-infrared *Spitzer*-IRS spectroscopy. In this chapter we present a detailed description of the reduction techniques employed to produce science-quality low and high-resolution *Spitzer*-IRS spectroscopy. For a given observation, 2-dimensional Basic Calibrated Data (BCD) images may be retrieved from the *Spitzer* Space Center (SSC) archive. We outline the optimal set of data (pre-)processing steps used by our custom reduction pipeline in order to clean and combine these BCD images before spectral extraction is carried out using the SSC software program, SPICE. Final flux-calibrated science-quality 1-dimensional spectra are then produced by the pipeline following post-extraction processing.

1.5.2 Chapter 3 – A large population of optically unidentified AGNs at $D < 15$ Mpc

In this chapter we use *Spitzer*-IRS spectroscopy to investigate the ubiquity of AGN in a complete (≈ 94 percent), volume-limited sample of the most bolometrically-luminous galaxies ($L_{IR,\,8-1000\,\mu m} \gtrsim$ (0.3–20) $\times 10^{10}\,L_{\odot}$) to $D < 15$ Mpc. Our analyses are based on the detection of the high-excitation emission line [NeV] $\lambda 14.32\,\mu$m (97.1 eV) to unambiguously identify AGN activity. We find that 17 of the 64 IR-bright galaxies in our sample host AGN activity ($\approx 27^{+8}_{-6}$ percent), $\gtrsim 50$ percent of which are not identified as AGNs using optical spectroscopy alone. The optically unidentified AGNs span a wide range of galaxy type (S0–Ir) and are typically starburst-dominated systems hosting

modest-luminosity AGN activity ($\mathrm{L_{[NeV]}} \approx 10^{37}$–$10^{39}\,\mathrm{erg\,s^{-1}}$). The non-identification of optical AGN signatures in the majority of these galaxies appears to be due to extinction towards the AGN, rather than intrinsically low-luminosity AGN activity. Examination of optical images shows that the optically unidentified AGNs with evidence for extinction are hosted in either highly inclined galaxies or galaxies with dust lanes, indicating that obscuration of the AGN is not necessarily due to an obscuring torus. We therefore conclude that optical spectroscopic surveys miss approximately half of the AGN population simply due to extinction through the host galaxy.

1.5.3 Chapter 4 – The incidence of growing black holes to $D < 15$ Mpc

In this chapter, we investigate the local SMBH density function and relative mass accretion rates of all AGNs identified in the volume-limited sample of infrared (IR) bright galaxies ($\mathrm{L_{IR}} > 3 \times 10^9\,\mathrm{L_\odot}$) to $D < 15$ Mpc from Goulding and Alexander (2009). A database of accurate SMBH mass ($\mathrm{M_{BH}}$) estimates is compiled from literature sources using physically motivated AGN modeling techniques (reverberation mapping, maser mapping and gas kinematics) and well-established indirect $\mathrm{M_{BH}}$ estimation methods (the M-σ_* and $\mathrm{M_{BH}}$–$L_{\mathrm{K,bul}}$ relations). For the three sources without previously published $\mathrm{M_{BH}}$ estimates, we use 2MASS K-band imaging and GALFIT to constrain the bulge luminosities, and hence SMBH masses. In general, we find that the AGNs in the sample host SMBHs which are spread over a wide mass range ($\mathrm{M_{BH}} \approx (0.1\text{–}30) \times 10^7\,\mathrm{M_\odot}$), but with the majority in the poorly studied $\mathrm{M_{BH}} \approx 10^6$–$10^7\,\mathrm{M_\odot}$ region. Using sensitive hard X-ray (2–10 keV) and mid-IR constraints we calculate the bolometric luminosities of the AGNs ($L_{\mathrm{Bol,AGN}}$) and use them to estimate relative mass accretion rates. We use these data to calculate the volume-average SMBH growth rate of galaxies in the local Universe and find that the AGNs hosting SMBHs in the mass range $\mathrm{M_{BH}} \approx 10^6$–$10^7\,\mathrm{M_\odot}$ are dominated by optically unidentified AGNs. These relatively small SMBHs are acquiring a significant proportion of their mass in the present-day, and are amongst the most rapidly growing in the local Universe (SMBH mass doubling times of ≈ 6 Gyrs). Overall, we conclude that significant mass accretion onto small SMBHs may be missed in even the most sensitive optical surveys due to absent or weak optical AGN signatures.

1.5.4 Chapter 5 – The unambiguous identification of AGNs in the SDSS-DR7

In this chapter we explore the incidence of high-ionisation detected AGNs in the seventh data release of the Sloan Digital Sky Survey (SDSS-DR7). We define a well-selected sample of 18,059 emission-line galaxies at $0.14 < z < 0.31$ with $S/N_{(H\alpha,H\beta,[\mathrm{OIII}],[\mathrm{NII}])} \gtrsim 5$ and classify these on the basis of traditional optical emission-line ratio diagnostics. We then independently classify the sources in terms of AGN activity based on the detection of the [NeV] $\lambda3427$ emission-line. From our parent sample, we find that 1226 galaxies ($\approx 6.8 \pm 0.2$ percent) have detected [NeV] emission (i.e., are unambiguously identified as AGNs), with the majority lying in the Seyfert region of a BPT diagram. We suggest that this provides good empirical evidence for the use of the theoretical starburst limit of Kewley et al. (2001) as an AGN discriminator. However, we find that only $\approx 27 \pm 4$ percent of Seyfert galaxies in the SDSS-DR7 have detected [NeV] emission. Using spectral stacking analyses, we show that the lack of [NeV] signatures in the majority of Seyfert galaxies is due to: (1) sensitivity of the SDSS spectra to the detection of [NeV] ; and (2) higher levels of dust-extinction in [NeV] undetected AGNs, which obscure the high ionisation emission line. We compare the population of SDSS [NeV] $\lambda3427$ detected AGNs to the sample of [NeV] $\lambda14.32$ μm detected optically unidentified AGNs presented by Goulding & Alexander (2009). We find that optically unidentified AGNs occupy a significantly different region of colour-magnitude parameter space to those galaxies identified in the SDSS. Optically unidentified AGNs are predominantly hosted in blue ($u-r < 1.5$), low-luminosity galaxies ($M_{r,AB} \gtrsim -20$), and hence are not generally identified in wide-field optical surveys.

1.5.5 Chapter 6 – Searching for Compton-thick AGNs at $z \sim 0.1$

In this chapter we use a suite of X-ray, mid-IR and optical AGN luminosity indicators to search for Compton-thick AGNs at $z \sim 0.03$–0.2, a region of parameter space which is currently poorly constrained by deep narrow-field X-ray surveys. We have used the widest *XMM-Newton* survey (the serendipitous source catalogue) to select a representative sub-sample (14; ≈ 10 percent) of the 147 X-ray undetected candidate Compton-thick AGNs in the SDSS with $f_X/f_{[\mathrm{OIII}]} < 1$; the 147 sources account for ≈ 50 percent of the overall Type-2 AGN population in the SDSS–XMM overlap region. We use mid-IR spectral decomposition analyses and emission-line diagnostics, determined from pointed *Spitzer*-IRS spectroscopic observations of these candidate Compton-thick AGNs, to es-

timate the intrinsic AGN emission (predicted 2–10 keV X-ray luminosities, $L_X \approx (0.2\text{–}30) \times 10^{42}\,\mathrm{erg\,s^{-1}}$). On the basis of the optical [OIII], mid-IR [OIV] $\lambda 25.89\ \mu\mathrm{m}$ and $6\ \mu\mathrm{m}$ AGN continuum luminosities we conservatively find that the X-ray emission in at least 6/14 ($\gtrsim 50$ percent) of our sample appear to be attenuated by a factor $\gtrsim 15$, i.e., they are likely to be obscured by Compton-thick material with $N_H > 1.5 \times 10^{24}\,\mathrm{cm^{-2}}$. Under the reasonable assumption that our 14 AGNs are representative of the overall X-ray undetected AGN population in the SDSS–XMM parent sample, we find that $\gtrsim 20$ percent of the optical Type-2 AGN population are likely to be obscured by Compton-thick material. Furthermore, using the [OIV] $\lambda 25.89\ \mu\mathrm{m}$ luminosity to infer the intrinsic AGN luminosity and the stellar velocity dispersion to estimate $\mathrm{M_{BH}}$, we find that the Compton-thick AGNs identified in this sample harbour some of the most rapidly growing black holes (median $\mathrm{M_{BH}} \approx 3 \times 10^7\,\mathrm{M_\odot}$) in the nearby Universe, with a median Eddington ratio of $\eta \approx 0.2$.

1.5.6 Chapter 7 – Conclusions, summary and future work

In this final chapter I summarise the major conclusions which arise from this work, and discuss future research which will be conducted to further these results.

Chapter 2

The reduction of *Spitzer*-IRS spectroscopic data

In the proceeding chapters, a large proportion of the analyses will be based on the identification of AGNs using mid-IR spectroscopic data obtained by the NASA *Spitzer* Space Telescope (hereafter, *Spitzer*.) The *Spitzer* observatory was launched on 23rd August 2003 and is a 950 kg, cryogenically cooled 4×2 m spacecraft with a 0.85 m diameter mirror placed in a receding Earth-trailing heliocentric orbit.[1] The observatory consists of three primary science instruments: the infrared spectrograph (IRS), the multi-band imaging photometer (MIPS) and the infrared array camera (IRAC). In this chapter, I outline the properties of the spectrograph instrument and the data-reduction processes used throughout this thesis.

2.1 The *Spitzer* infrared spectrograph

The cold assembly of the *Spitzer* infrared spectrograph primarily consists of four mid-IR spectrograph modules, providing low and moderate resolution spectroscopy at $\lambda \sim 5.2$–38.0 μm, with each operating at tightly controlled temperatures of $T \sim 1.4$–1.6 K. Specifically, the two long-slit modules provide low-resolution $R \sim 60$–120 spectroscopy at $\lambda \sim 5.2$–38.0 μm (short-low and long-low), whilst the two cross-dispersed echelle modules provide higher resolution ($R \sim 600$) spectroscopy at $\lambda \sim 9.9$–37.2 μm (short-high and long-high). Each detector is a 128×128 pixel array CCD with varying plate

[1] *Spitzer* is now in its 'warm-phase' after its cryogen fluid expired on 15th May 2009 (towards the end of the G05 proposed program presented in Chapter 6).

scales (1.8–5.1″ pixel^{-1}). The main properties of each module and associated dispersal sub-slits are summarised in Table 2.1.

Observations are available for each module in two modes: (1) a spectral mapping mode which consists of a custom grid of slits around a central target position (see Fig. 2.1) and (2) a standard "point and shoot" nod-staring mode (see Fig. 2.2).

All *Spitzer*-IRS observations are pre-processed for all '*Spitzer* specific' effects by the *Spitzer* Science Center (SSC) prior to being made available to the observer. Specifically, the raw IRS data consists of individual data collection events (DCEs) which are produced on a per exposure basis. During the SSC pre-processing, these DCEs are flagged for obvious cosmic rays, and then gain, droop, dark and ramp corrected. The corrected frames are then collapsed to 2-D images and flat-fielded to produce final Basic Calibrated Data (BCD) images which may then be additionally processed by the observer (see Fig. 2.3). For further information on the high- and low-resolution *Spitzer*-IRS pre-processing pipelines, see Chapter 7 of the *Spitzer* Observers Manual.[2] Retrieval of all BCDs for a specific *Spitzer*-IRS observation is carried-out through the SSC Legacy program, LEOPARD.

The majority of currently published *Spitzer*-IRS spectroscopy is produced using the contributed software package, the Spectroscopic Modeling Analysis and Reduction Tool (SMART; Higdon et al. 2004). It has been our experience that whilst the SMART package is sufficient for quick-look spectra of bright sources, in-general it does not produce optimal science-quality spectroscopy of most sources. In the following sections, we outline the custom pipeline processes which we have designed in-conjunction with available SSC packages, in order to produce science-quality *Spitzer*-IRS spectroscopy for low– and high-resolution IRS-staring observations (§§ 2.2 and 2.3.1) and high-resolution IRS mapping observations (§ 2.3.2). The final resulting spectroscopy is then analysed in Chapters 3, 4 and 6 using the spectral-line fitting routines built into SMART.

[2]The *Spitzer*-IRS Data Handbook and observer's manual are available at http://ssc.spitzer.caltech.edu/irs/dh/

Table 2.1: IRS module and slit descriptions

Module Name and Order	Wavelength Range (μm)	Abbreviation	Detector Compound	Plate Scale ($''$ pixel^{-1})	R
(1)	(2)	(3)	(4)	(5)	(6)
Short-low 2$^{\rm nd}$ order	5.2–8.7	SL2	Si:As	1.8	60–127
Short-low 1$^{\rm st}$ order	7.4–14.5	SL1	Si:As	1.8	61–120
Long-low 2$^{\rm nd}$ order	14.0–21.3	LL2	Si:Sb	5.1	57–126
Long-low 1$^{\rm st}$ order	19.5–38.0	LL1	Si:Sb	5.1	58–112
Short-high	9.9–19.6	SH	Si:As	2.3	~ 600
Long-high	18.7–37.2	LH	Si:Sb	4.5	~ 600

NOTES: (1) Formal module and sub-slit name. (2) Operating wavelength range including bonus-segment for 2nd order low-resolution modules. (3) Module abbreviation. (4) Chemical compound of module detector. (5) Detector plate scale. (6) Resolving power.

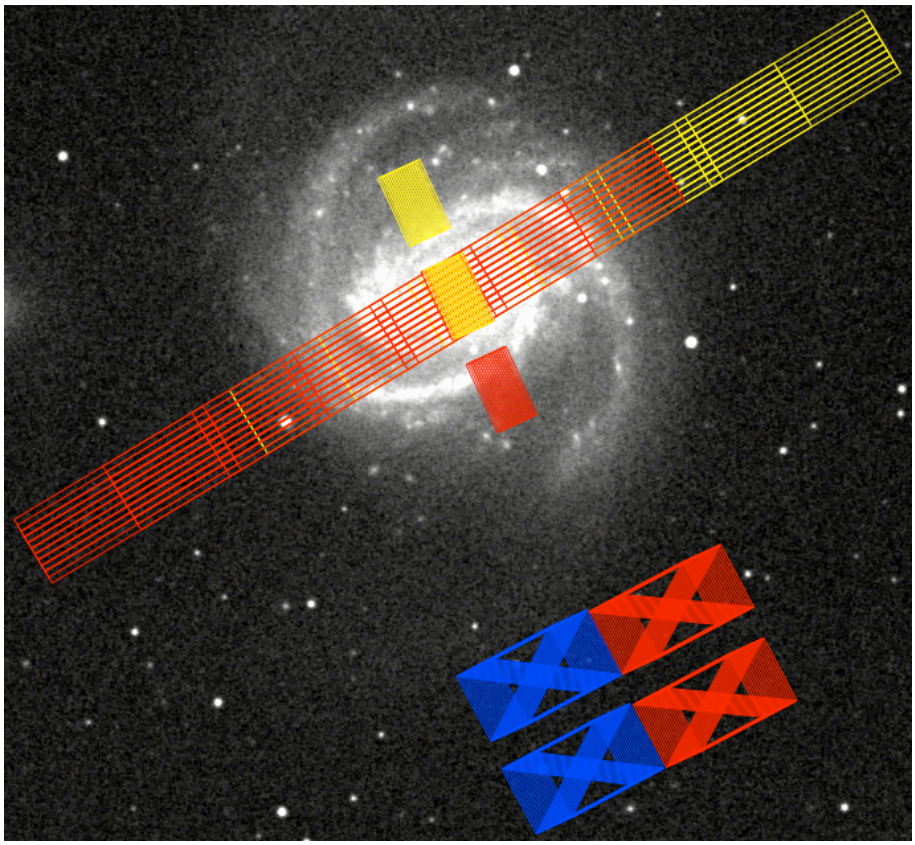

Figure 2.1: ESO Digital Sky Server image ($11' \times 12'$) of a typical nearby spiral galaxy with *Spitzer*-IRS SL ($3.6'' \times 136.0''$) and LL ($10.5'' \times 360.0''$) apertures overlaid in a 2×10 (SL) and 6×10 (LL) mapping-mode observation. Essentially, a mapping mode observation consists of a grid-style configuration of IRS slit positions arranged around a central target position. Slits are nodded as in a standard IRS-staring observation; $1^{\rm st}$ and $2^{\rm nd}$ order modules are shown in yellow and orange, respectively. The object shown is the Sbc galaxy, NGC 4321 at $D \approx 15.2$ Mpc with $\rm L_{IR} \approx 2.5 \times 10^{10}\,L_{\odot}$. Additionally, we show peak-up imaging apertures (red and blue overlays) used for photometric and positional calibration of the SL modules during SSC pre-processing.

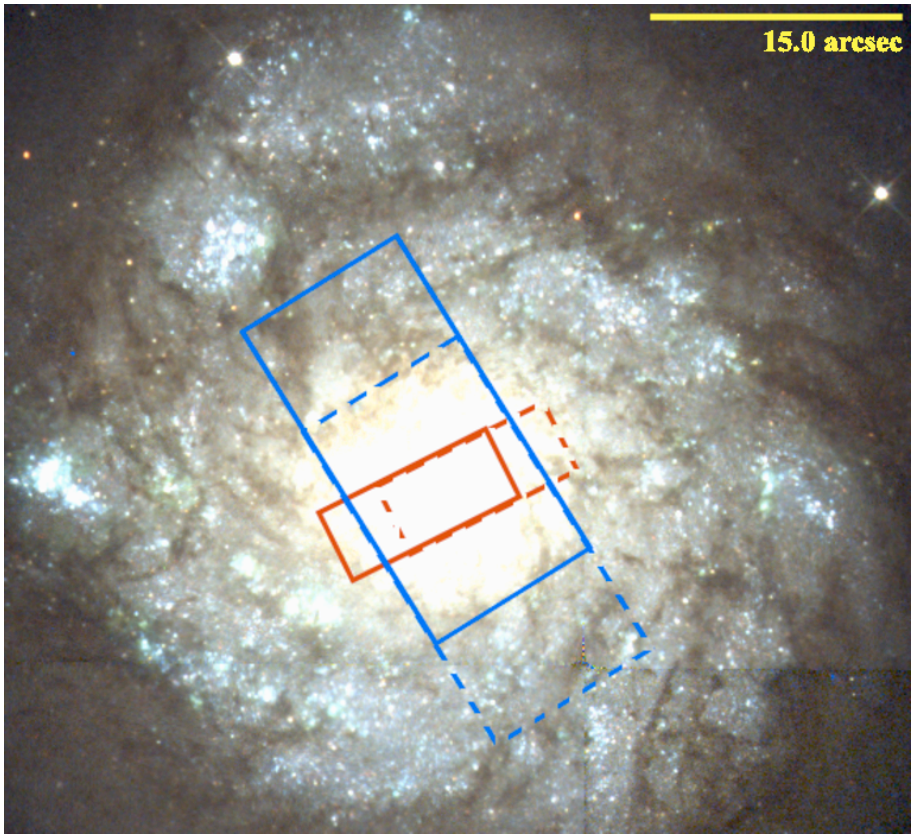

Figure 2.2: *Hubble Space Telescope* (*HST*) WFPC2 (3-colour) optical image of the circumnuclear region of a typical galaxy in the $D < 15$ Mpc sample (studied in Chapters 3 and 4), with *Spitzer*-IRS SH ($4.7'' \times 11.3''$, $\lambda \sim 9.9$–$19.6\ \mu$m) and LH ($11.1'' \times 22.3''$, $\lambda \sim 18.7$–$37.2\ \mu$m) apertures overlaid in the two nod positions (staring-mode observations). The object shown is the Sbc galaxy, NGC 0278 at $D \approx 11.4$ Mpc with $\mathrm{L_{IR}} \approx 1.1 \times 10^{10}\,\mathrm{L_{\odot}}$. Linear size-scales of apertures are $\approx 0.26 \times 0.63$ kpc (SH) and $\approx 0.61 \times 1.23$ kpc (LH). In highly resolved sources such as NGC 0278 the two nod positions will produce slightly differing spectra but the inner central region will be bright and thus will dominate.

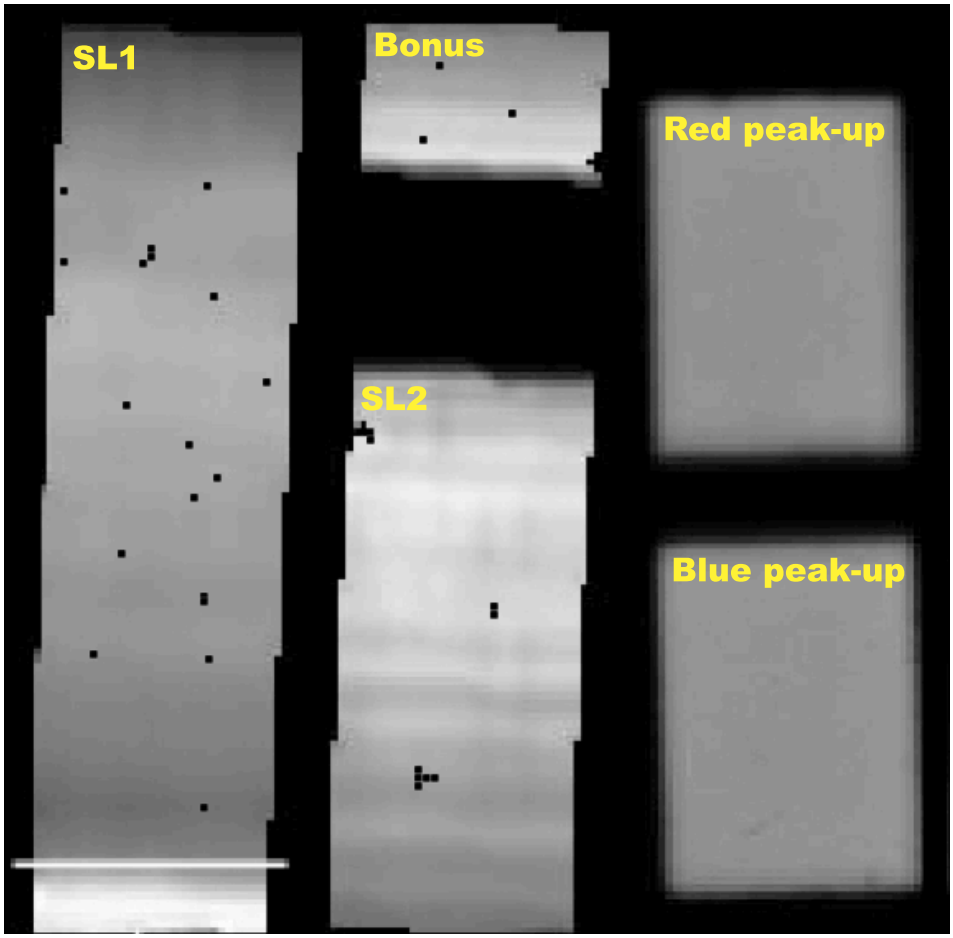

Figure 2.3: An example of a mock Basic Calibrated Data (BCD) image for the SL *Spitzer*-IRS module (Left panel of Fig. 5.2 of *Spitzer*-IRS observer's manual). Columns from left to right: SL1 (7.4–14.5 μm), SL2 and bonus segment (5.2–8.7 μm), and red (top) and blue (bottom) peak-up images. Dark areas around the dispersion regions are masked during the processing steps described in § 2.2. Additionally, single and group rogue 'hot' pixels are clearly evident in both SL1 and SL2 modules, respectively which must be identified and masked.

2.2 Low-resolution IRS data-reduction

In this section and § 2.3, we outline the data processing steps which are carried out by our custom IDL-based routine for the data reduction of low and high-resolution *Spitzer*-IRS spectroscopy. Both sections are intended to be a recipe-style data-process which may be followed in-order to produce science-standard *Spitzer*-IRS spectroscopy.

1. Combine similar pointings: BCD 128×128 pixel images for DCEs at identical pointing co-ordinates are stored into 3-dimensional image data cubes; i.e., an individual data cube is constructed for each order (i.e., 1st and 2nd) IRS module (i.e., short and long) in each of the two nod positions.

2. Hot pixel masking I: During the building of the cubes, those pixels which have been previously flagged by the SSC calibration files as damaged or unreliable (hereafter, 'hot' pixels) are assigned NAN values. We note here that hot pixel identification and masking is an extremely important process which greatly affects the quality of the final spectroscopy produced for *Spitzer*-IRS data and the ability to significantly detect weak spectral features.

3. Mask non-dispersion region: those pixels which lie outside of the standard dispersion zones of the CCD are now masked and are removed from further analyses (see Fig. 2.3).

4. Source detection: Module regions are collapsed in the dispersion direction to construct a profile of mean wavelength pixel value (i.e., the mean row profile) versus column number. Significant peaks within these row profiles are flagged as possible spectroscopic sources within the image.[3] The peak of the profile is normalised and a weighting image is constructed based on the normalised mean row value. The weighting image is used when analysing the image for further 'hot' pixels in the proceeding steps.

5. Hot pixel masking II: A pixel-by-pixel closest neighbour analysis is used to identify variable hot pixels (rogues) in each frame of the data cubes (i.e., those pixels which may be usable in some frames but not in others). Each image within the cube is artificially convolved with the weighting image constructed in the previous step. If a pixel is then found to be $> 10\sigma$ that of each of its closest neighbours, it is

[3]For those sources in isolated fields, the row profile is approximately Gaussian.

deemed to be hot and assigned a NAN value.[4] Weighting each of the pixels based on their proximity to the target has the advantage that where a target is detected in the dispersion plane, it is more likely that a pixel has neighbours which have pixel values significantly less than itself, especially for faint sources which are spatially extended over only 1–2 columns. The weighted image correctly accounts for this source emission and hence, does not remove flux from the source. The frames are then deconvolved from the weighting image to restore the original pixel values with these newly detected rogue pixels flagged as 'hot'.

6. Latent charge removal: As described in §8.3 of the *Spitzer*-IRS Data Handbook, after each integration, a small fraction of latent charge ($\sim$ 1–2%) still exists on the detector which decays slowly over time (see footnote 2) Over the course of a long observing request, this latent charge can build to significant levels (30–50% of the true background signal) and must be removed, especially in the cases of faint sources. The latent charge is a function of both wavelength (i.e., row number) and time (i.e., DCE number), and hence may be assessed by fitting the slope of the perceived background in an individual row and the frame number in the data cube with either a first or second-order polynomial (see Fig. 2.4). The latent charge is then removed by subtracting the slope of the sky value row-by-row from each DCE.

7. Hot pixel masking III: Pixels are compared with their values in other DCE frames of the data cube. If a pixel value is $> 10\sigma$ than that of its counterparts in the other DCEs in the cube it is assigned a NAN value.[5]

8. Collapse the data cubes: At this point in the reduction process, the data cubes have been rigorously cleaned of all obvious defects. The images are now averaged using a resistant mean in the direction of the stacked images for each nod-position, in effect, collapsing the 3-D cube into a 2-D image, one per module per nod-position. The variance as a function of time for each pixel is used to create a 128×128 pixel uncertainty image. All pixels with NAN values are ignored in both of these processes as 'missing' data.

[4] Variances and means are calculated using resistant (outlier invariant) statistics.

[5] This step should not be implemented for timing analyses or for sources which are known to be variable.

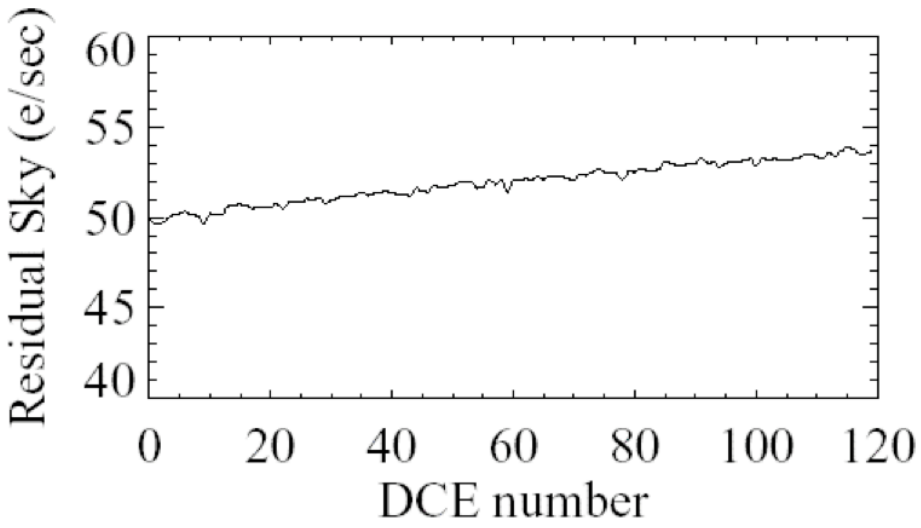

Figure 2.4: An example of the latent charge build up on the LL1 module as a function of DCE number (Fig. 8.1 of the IRS Data Handbook). This residual charge is well fit by a first or second order polynomial and removed row-by-row as a function of DCE number.

9. Flag likely emission lines: Regions of the images which contain emission/absorption lines (i.e., spectral features) are often strongly positive/negative when compared to background or source continuum image regions. Simple smoothing interpolation algorithms are likely to remove these important spectral features, especially if strongly peaked. Each image is scanned therefore for regions ($\geqq 3$ pixels wide) which are well-fit by 2-d Gaussian profiles. These pixels are flagged as regions which are likely to contain emission lines, and they are partially shielded from smoothing in Step 10. The failure rate of this process (i.e., bad detection of emission features) is $\approx 1\ \%$, and hence a shielding factor of $1/100$ is assigned.

10. Image smoothing: IRSCLEAN is an interactive tool created by the SSC to further remove/mask rogue pixels within BCD images. IRSCLEAN is invoked in an automated iterative method to remove any remaining strongly positive/negative pixels in the image. Within the sub-routine IRSCLEAN_MASK, the aggressive parameter is set to 1.5, this has the advantage that IRSCLEAN will search the image for noise that is within 3σ of the background level (n.b., emission-features are partially shielded from this process in the previous step), analyse clusters of pixels and will not flag

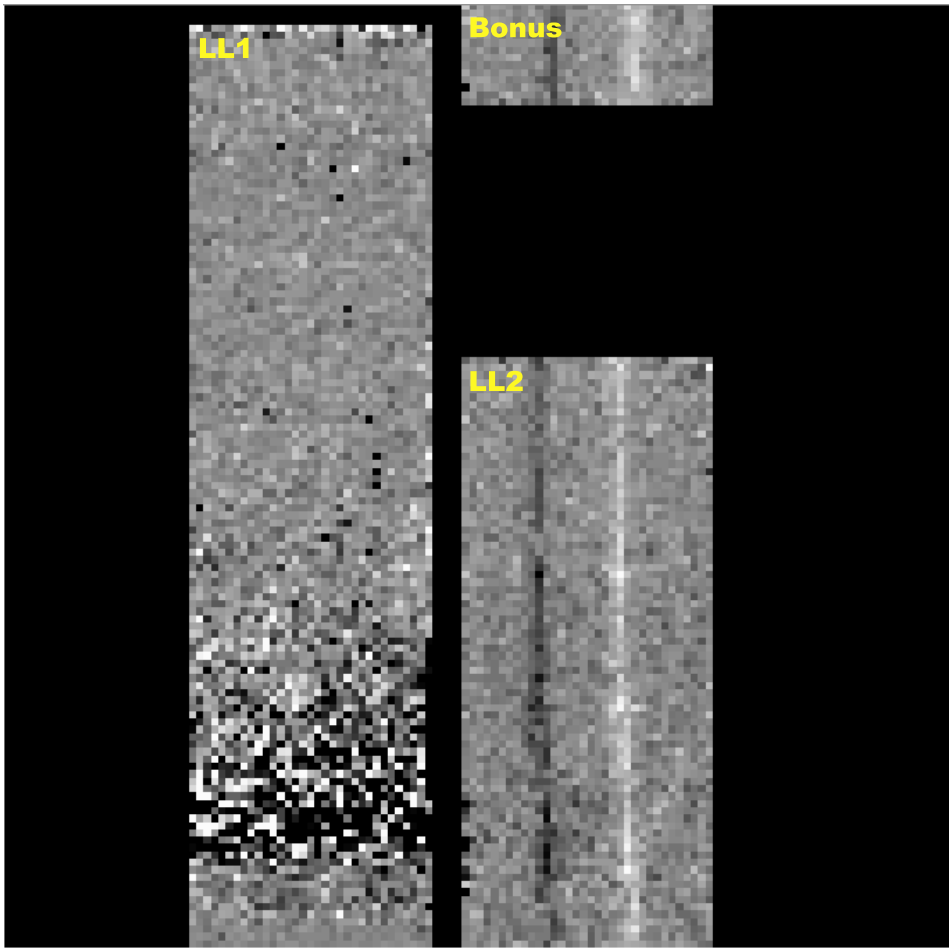

Figure 2.5: An example of a LL2 module *Spitzer*-IRS BCD image which has been rigorously cleaned of rogue pixels, co-added and alternately background subtracted in the two nod positions. This has produced a background-subtracted source and a negative image of the source in the other nod-position.

more than 20 rogue pixels within the image. The image is analysed by IRSCLEAN in three stages: (1) only the pixels with values > 0.0; (2) only the pixels with values < 0.0; and (3) all of the pixels. Pixels which are flagged as 'bad' in (1) and (3), or (2) and (3), are assigned the mean value of their immediate neighbours. This process is repeated until < 0.1 % of the pixels are identified as 'bad'.

11. Hot pixel masking IV: Co-added BCDs in each nod-position are visually inspected for any remaining rogue pixels. Any rogue pixels identified at this stage are rejected and assigned NAN values. This stage is conveniently completed using IRSCLEAN. Indeed, IRSCLEAN will automatically modify/create the bad-pixel mask FITS file

and the uncertainty image which are both required during spectral extraction.

12. Background subtraction: The residual charge on the detector after dark subtraction (i.e., the background) is now removed from the cleaned co-added BCDs by alternately subtracting the BCDs at differing nod-positions for each module. This produces an image with a background-subtracted source and a negative image of the source in the other nod-position (see Fig. 2.5)

13. Spectral extraction: The final rigorously-cleaned, co-added and background-subtracted BCD images are ready to have the spectra extracted. See § 2.4.

2.3 High-resolution IRS data-reduction

2.3.1 IRS-staring mode

In staring mode, the reduction of high-resolution *Spitzer*-IRS proceeds similarly to that of low-resolution data. However, we note that while the SL and LL modules produce one DCE image per order per nod-position, the high resolution Echelle SH and LH modules produce a DCE image containing all 10 spectral orders in a single pointing.

BCD image cubes are constructed in the same manner as in the previous section, and the steps are followed similarly up to and including step 8. As can be seen in Fig. 2.6, a lack of spatial extent in each of the orders, caused by the small apertures of the SH and LH modules, does not allow for a clean smoothing of the image nor a background subtraction. Hence, steps 9, 10 and 12 (outlined in § 2.2) are skipped in the reduction of high-resolution data.[6] The co-added BCDs are visually inspected using IRSCLEAN before the spectroscopy is extracted.

2.3.2 IRS-mapping mode

For the reduction of IRS-spectral mapping data, the SSC and the SINGS group have developed The CUbe Builder for IRS Spectral Maps (CUBISM; Smith et al. 2007). CUBISM is a tool for constructing spectral cubes and performing subsequent spectral extractions from *Spitzer*-IRS mapping mode observations. Specifically, CUBISM was designed to produce

[6]Sources observed with high-resolution IRS are generally bright, and dominate over any background emission. Hence, dedicated off-source observations used to produce background spectroscopy are found to have little or no correcting effect on the source spectroscopy.

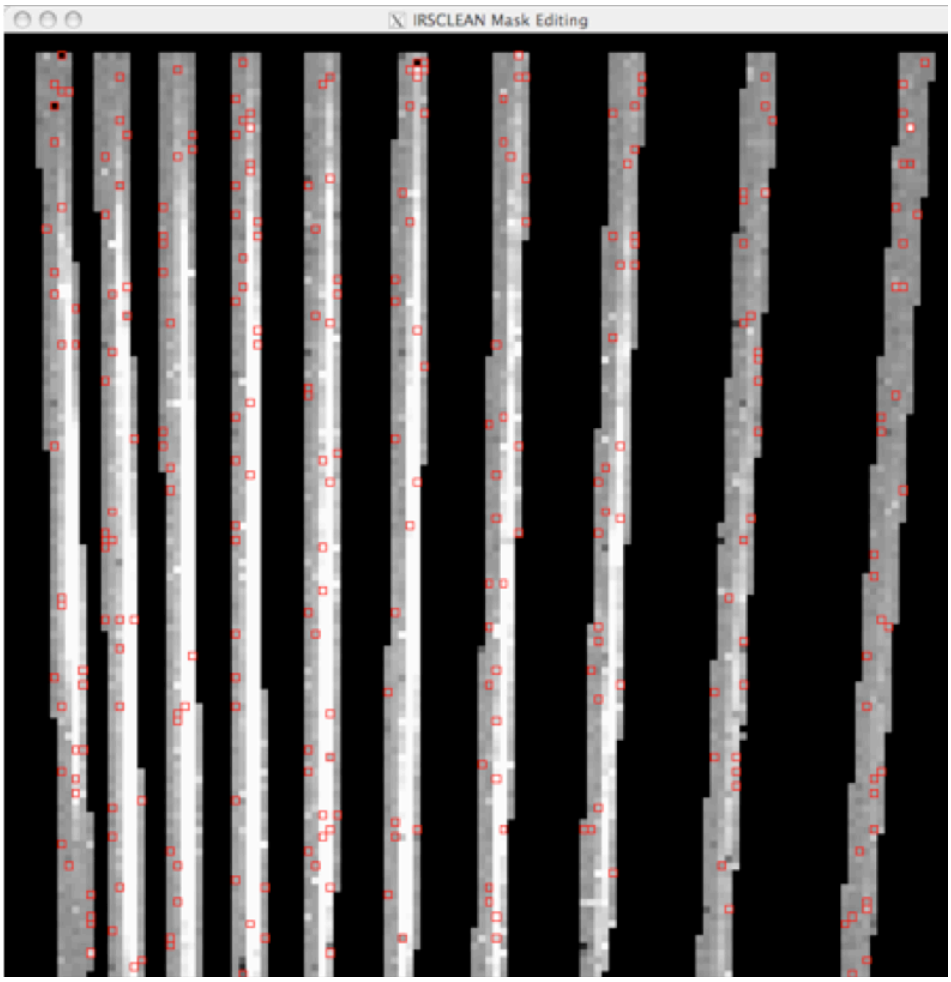

Figure 2.6: An example of a LH module *Spitzer*-IRS BCD image during the visual inspection process using IRSCLEAN. The 10 narrow Echelle dispersion regions are clearly seen. Pixels defined as damaged by the SSC or rogue during our custom reduction routine are highlighted with open red squares.

1D spectroscopy of the nearby SINGS galaxy sample, and is extremely well-matched to the sample of $D < 15$ Mpc galaxies studied in Chapters 3 and 4.

The data reduction of the 18 galaxies in the $D < 15$ Mpc sample with high-resolution *Spitzer*-IRS mapping-mode spectroscopic observations was conducted using CUBISM and is described and discussed extensively in Recipe 7 of the *Spitzer* Data Analysis Cookbook. CUBISM is in-built with its own version of IRSCLEAN, which was used to rigorously construct the custom bad-pixel masks to be applied to the BCD images. CUBISM was then used in conjunction with the latest SSC flux calibration files to construct final data cubes and extract spectra of the central regions matched to the sizes of projected standard SH and LH apertures (see Table 2.1).

2.4 Spectral Extraction of IRS-Staring data

For all IRS-staring mode data presented in this thesis, spectral extraction is performed using the *Spitzer*-IRS Custom Extraction (SPICE) software provided by the SSC. SPICE allows the user to visualise the source BCDs, customise the spectral extraction processes and examine the features in the resulting spectroscopy. A detailed description of the full features and the use of SPICE can be found in the SPICE User's Guide.[7]

To extract a spectrum for a given nod-position and module, SPICE requires three FITS files: the main BCD, the bad-pixel mask and the uncertainty files. The creation of these files is outlined in the previous sections of this Chapter. Similar to Step 4 outlined in § 2.2, SPICE creates a wavelength-collapsed average profile in order to identify the location of the peak of the source emission in the slit.[8] SPICE then allows one of two spectral extraction algorithms: 'regular' and 'optimal'. The 'regular', unweighted spectral extraction method is sufficient for sources with high S/N. Testing between these two approaches has shown little improvement in the S/N of the final spectroscopy for sources with S/N > 30. The 'optimal' extraction mode is used for low S/N faint sources with the aim of minimising the noise in the extracted spectra. This is achieved by weighting the extraction of the object by a point-source point spread function (PSF) and the S/N of each individual pixel. For sources with S/N~ 3, the 'optimal' extraction can improve the S/N in the final spectra by a factor ~ 2 (e.g., Teplitz et al. 2007; Pope et al. 2008). For sources presented in this thesis, we use the 'regular' extraction option for all

[7]The SPICE User's Guide is available at

http://ssc.spitzer.caltech.edu/dataanalysistools/tools/spice/spiceusersguide/

[8]This may also be user specified if, for example, the investigated source was not the brightest in the slit.

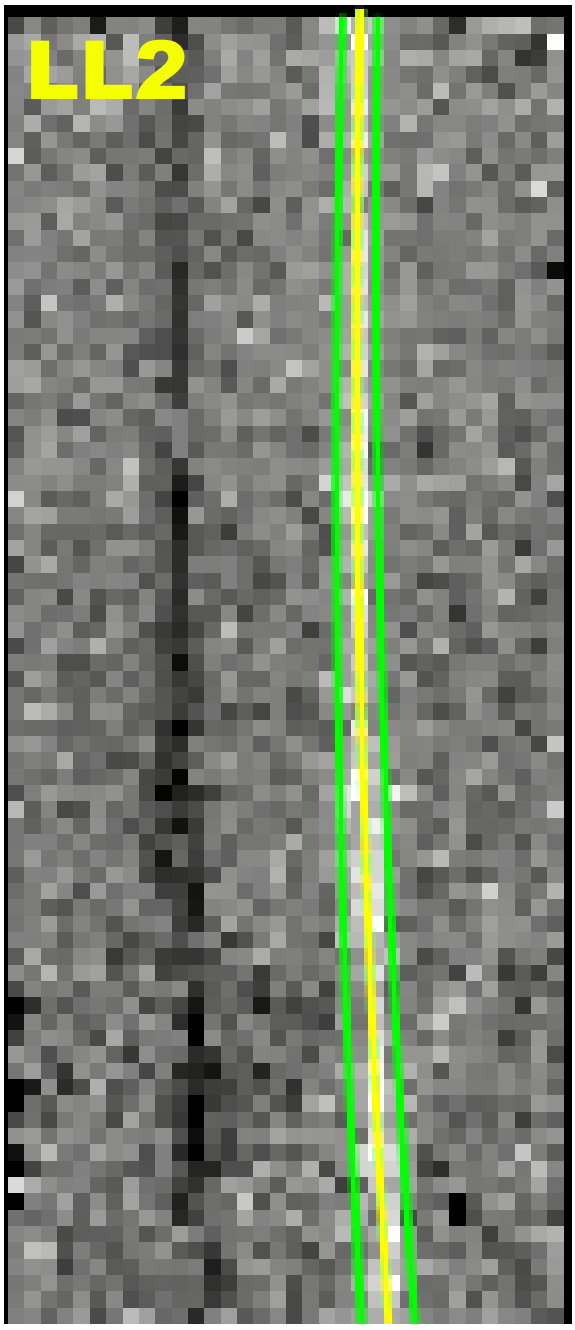

Figure 2.7: An example of the LL2 module from a BCD image which has been inputted into SPICE. The BCD/object shown is the same as in Fig. 2.5 with a correctly aligned wavelength expanding spectral extraction window (width $\sim$ 2 pixels at the blue end) overlaid onto the source (yellow and green solid lines).

high-resolution data as this is comparably faster and 'optimal' for low-resolution data. Specifically, for the low-resolution spectroscopy presented in Chapter 6, the data were extracted using an optimally calibrated 2-pixel wide spectral window (at the blue end of the spectrum) which expands linearly with wavelength.[9]

In Fig. 2.7, we show an example of a correctly profile-centered source which is ready for source extraction. It must be noted that IRS spectroscopy is not rectilinear on the CCD in either the dispersal or spatial direction. As such, during the spectral extraction process, the EXTRACT module in SPICE does not extract whole pixel values but rather it subdivides the pixel values into very small polygons which trace the source spectrum. The final flux is the sum of the fractional incident signal which falls within the non-flagged pixels in these polygons.

After spectral extraction, the calculated flux (f) is converted from units of e^{-} s^{-1} at a given wavelength (λ) to Jy using Equation (2.1) combined with the continuously updated Flux Calibration Tables provided by the SSC,

$$f(\mathrm{Jy}) = f(e^{-}s^{-1})/(y_0 \times (a_0 + a_1 \times [\lambda - \lambda_0] + a_2 \times [\lambda - \lambda_0]^2 + a_3 \times [\lambda - \lambda_0]^3)) \quad (2.1)$$

where λ_0 is the key order wavelength, y_0 is the order specific flux conversion parameter and $\{a_0, a_1, a_2, a_3\}$ are the associated conversion coefficients.

On spectral extraction, SPICE automatically propagates all errors from the initial uncertainty input file to produce a flux uncertainty as a function of wavelength. In general, this is sufficient for spectra extracted with the 'regular' algorithm (i.e., high-resolution data). However, for low-resolution IRS of faint sources and following Pope et al. (2008), errors should be estimated for spectra extracted with the 'optimal' algorithm using a second spectral window offset from the source in the spatial direction.[10] In effect, this provides a measure of the uncertainty in the background which may dominate the perceived source flux, and hence the error in the source.

After extraction of the raw spectra, the ends of each long-slit or echelle order are trimmed to remove the additional spectral noise caused by the poor response of the grating.[11] For low-resolution IRS, the extracted spectra for each of the modules are then

[9] We note that the use of the 'optimal' calibration also produces flux calibration irregularities. Hence, the final spectroscopy in Chapter 6 has been flux calibrated using IR photometric data.

[10] This extraction window should not be placed over or immediately in the vicinity of any serendipitous sources which are within the slit. We also note, that due to the small aperture sizes, this process would not be possible for high-resolution data.

[11] Wavelength trim ranges are given in Table 5.1 of the *Spitzer*-IRS Observers Manual.

corrected for their differing apertures and normalized to the flux level of the 1st LL module. To produce single continuous spectroscopy for a source, a first or second order polynomial is fit to each individual order and then matched to the adjoining spectral continuum. The ensure good flux calibration of the final spectrum, the spectra should be compared to photometric data points (e.g., MIPS 12, $24\mu m$) before scientific analyses are conducted.

A similar process may be adopted for high-resolution *Spitzer*-IRS spectroscopy by fitting each spectral continuum from a given echelle order with either a first or second order polynomial. Each echelle order continuum should then be combined by matching and calibrating to the 1st echelle order of the relevant slit to construct the final SH and LH continua. However, it should be noted that due to the different aperture shapes and sizes, the SH and LH spectra should not be combined to be produce one continuous spectrum. Furthermore, given the small wavelength ranges of the individual echelle orders, the stitching of orders can produce artificially steep spectra for poorly calibrated observations. An example of the raw spectral output from SPICE, and resulting processed mid-IR spectrum for the SH module of a well-studied local AGN (NGC 1068) is shown in Fig. 2.8.

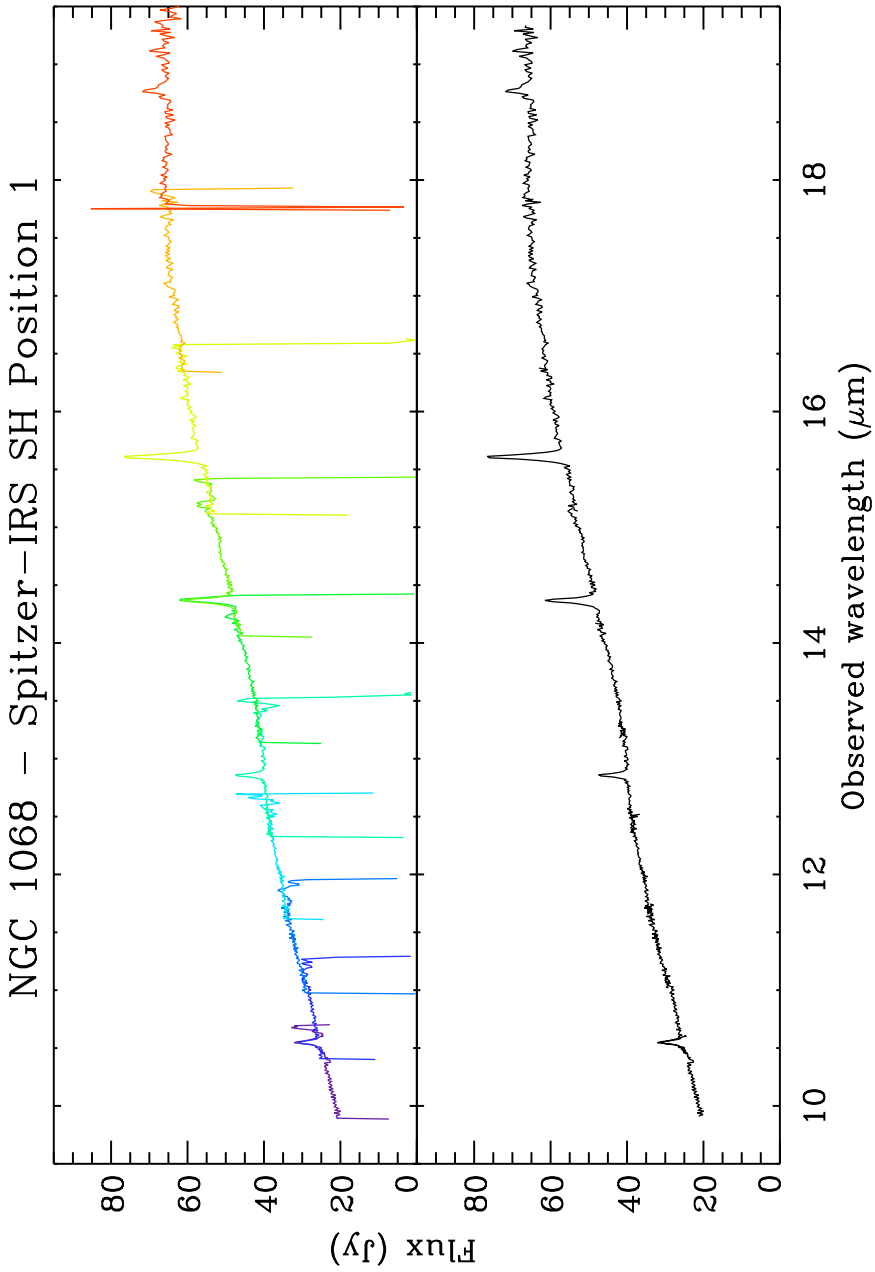

Figure 2.8: **Upper panel:** Raw IRS spectrum as produced by SPICE after following the procedures outlined in section 2.3.1. Spectra shown is the 1st position of the Short-High echelle module of NGC 1068, a local Seyfert 1.9 galaxy. This source is included in the $D < 15$ Mpc sample and its mid-IR properties are analyzed in detail in Chapters 3 and 4. Differing echelle orders are shown in rainbow colours. **Lower panel:** Wavelength trimmed and continuum matched spectroscopy of the data shown in the upper panel.

Chapter 3

A large population of optically unidentified AGNs at $D < 15$ Mpc

This chapter is based on the work published in Goulding & Alexander (2009).

3.1 Introduction

Local mid-IR surveys (e.g., Sturm et al. 2002; SINGS; S08) have shown the advantages of using mid-IR spectroscopy as an AGN diagnostic. However, these samples are heterogenous and not complete to a given flux, luminosity or distance. In this chapter, we use sensitive high-resolution *Spitzer*-IRS spectroscopy to identify AGNs within a complete volume-limited IR-sample of galaxies in the local Universe.[1] By selecting galaxies at IR wavelengths, our sample will comprise the most active galaxies in the local Universe and will also include the most dust-obscured systems. We use these data to unambiguously identify AGNs using the high-ionization [NeV] $\lambda 14.32$ μm emission line to produce the most sensitive census of AGN activity in the local Universe to date.

3.2 The Sample and Data Reduction

3.2.1 Sample Selection

Using *IRAS*, the Revised Bright Galaxy Survey (Sanders et al. 2003; hereafter, RBGS) has provided an accurate census of all IR-bright galaxies ($|b| > 5^{\circ}$, $f_{60\mu m} > 5.24$ Jy) in the local Universe. The aim of our study is to identify AGN activity in the most

[1] L_{IR} corresponds to the 8–1000 μm luminosity, as defined by Sanders and Mirabel (1996).

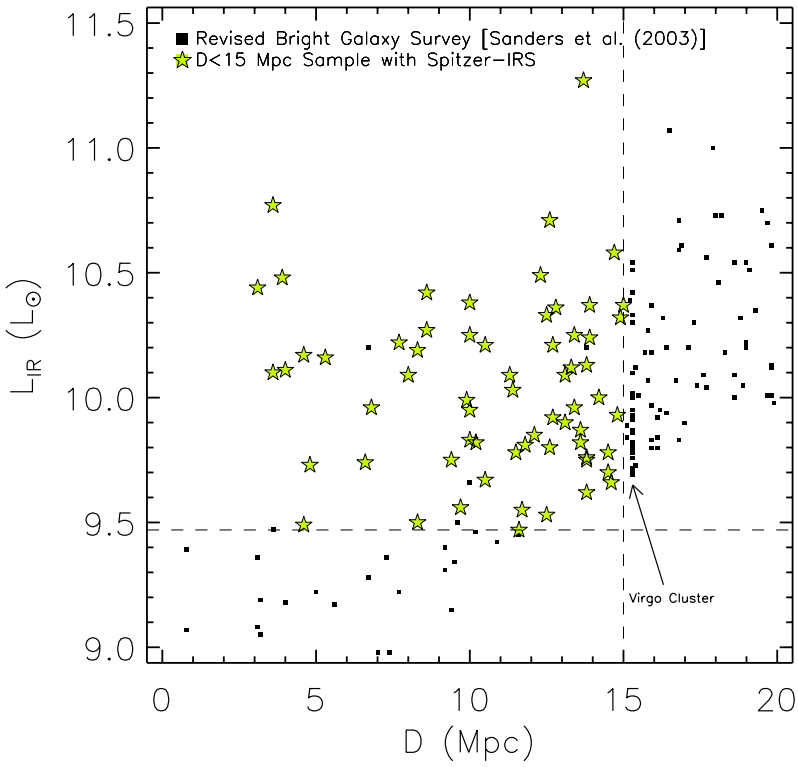

Figure 3.1: Logarithm of IR luminosity versus luminosity distance for all objects in the RBGS (Sanders et al. 2003; squares). The 64 IR-bright galaxies ($L_{IR} \approx 3 \times 10^9\, L_\odot$) to $D < 15$ Mpc with high-resolution *Spitzer*-IRS spectroscopy are explored here (stars).

bolometrically luminous galaxies ($L_{IR} > 3 \times 10^9 L_\odot$) in the RBGS out to $D < 15$ Mpc.[2] The distance constraint of 15 Mpc was placed so as to not include the Virgo cluster at 16 Mpc (i.e., our sample is representative of a local field-galaxy population; see Section 4.5.4.1). The IR luminosity threshold was chosen to be well matched to the flux limit of the RBGS (see Fig. 3.1) and ensures that we do not include low-luminosity dwarf galaxies and relatively inactive galaxies. Based on the principle of reprocessed emission in the Unified AGN model, selection on the basis of IR-luminosity will select all bolometrically luminous AGNs with $L_X \gtrsim 10^{41}\,\mathrm{erg\,s^{-1}}$. However, we note that it will also select dust-rich star-forming systems which may dominate the bolometric luminosity of the galaxy. In the RBGS there are 68 *IRAS* detected galaxies to a distance of $D < 15$ Mpc with $L_{IR} > 3 \times 10^9 L_\odot$, 64 of which have *Spitzer*-IRS high-resolution spectroscopy publicly available (i.e., ≈ 94 percent complete in the volume-limit): P3124 (28 objects; PI: D.M. Alexander), P159 (18 objects; PI: R. Kennicutt [SINGS]), P14 (11 objects; PI: J.R. Houck), P59 (4 objects; PI: G. Rieke) and P86 (3 objects; PI: M. Werner).

In Fig. 3.1 we plot IR luminosity versus luminosity distance for the RBGS and highlight the 64 galaxies with *Spitzer*-IRS observations in our volume-limited $D < 15$ Mpc sample. The basic properties from the RBGS for the sources in our sample are combined with published optical data and listed in Table 3.1. The objects are all late-type galaxies (Hubble classification of S0 or later), which is unsurprising since early-type galaxies are typically IR faint and undetected by *IRAS* (e.g., Knapp et al. 1989).

The four galaxies that match our selection criteria but lack sufficient high-resolution *Spitzer*-IRS observations of the central regions are shown in Table 3.2. Specifically, NGC 3486 has Short-High (SH) and Long-High (LH) observations but the data are noisy and no statistically useful information can be extracted; NGC 4565 and NGC 5457 have only high-resolution observations of extranuclear regions; NGC 5248 has no high-resolution observations. NGC 5248 and NGC 5457 are optically classified as star-forming HII galaxies while NGC 3486 and NGC 4565 are optically classified as Seyfert galaxies (Ho97). Both NGC 3486 and NGC 4565 have published [OIV] $\lambda 25.89\,\mu$m fluxes from low-resolution ($R \sim 100$) *Spitzer*-IRS spectroscopy in Diamond-Stanic et al. (2009); the derived [OIV] $\lambda 25.89\,\mu$m luminosities suggest that the AGNs are contributing < 5 percent to the total bolometric luminosity of the galaxy.

[2]Distances have been calculated using the cosmic attractor model of Mould et al. (2000), which adjusts heliocentric redshifts to the centroid of the local group, taking into account the gravitational attraction towards the Virgo cluster, the Great Attractor, and the Shapley supercluster.

3.2.2 Data Reduction

Each of the galaxies in our $D < 15$ Mpc sample were observed using both the SH ($4.7" \times 11.3"$, $\lambda \sim 9.9$–19.6 μm) and LH ($11.1" \times 22.3"$, $\lambda \sim 18.7$–37.2 μm) resolution spectrographs onboard the NASA *Spitzer* Space Telescope (Houck et al. 2004; Werner et al. 2004). The spectral resolution is $R \sim 600$ for both SH and LH modules. The raw data are compiled from multiple observing programs (see § 3.2.1) and they consist of both spectral mapping and staring observations, with differing exposure times. As an example, in Fig. 2.2 we projected the SH and LH apertures onto a galaxy in our sample (NGC 0278), showing the two differing nod positions.

Many of the objects in our sample do not have dedicated off-source observations. However, as we only require emission-line flux measurements no background subtraction was necessary for the observations (see §7.2.5.2 of the *Spitzer*-IRS Observers Manual).[3] Furthermore, the targets are bright compared to the background and therefore any background corrections would be small.

The reduction of the IRS data proceeds as described at length in section 2.3.1 and 2.3.2. Briefly, for the IRS-staring data, Basic Calibrated Data (BCD) images were co-added and mean averaged at each nod position. Few of the observations were pre-processed with the same *Spitzer* pipeline version. Therefore, to ensure consistency, we extracted the spectra of each galaxy using a custom pipeline based on the *Spitzer* data reduction packages IRSCLEAN (to apply individual custom bad-pixel masks for each of the BCDs) and SPICE (to extract full slit spectra using the latest flux calibration files: version 17.2). For the reduction of the IRS-spectral mapping data, custom bad-pixel masks were again applied to the BCD images. CUBISM (Smith et al., 2007) was then used in conjunction with the latest flux calibration files to construct final data cubes and extract spectra of the central regions matched to the sizes of projected SH and LH apertures.

[3]The *Spitzer*-IRS Observers Manual is available at http://ssc.spitzer.caltech.edu/irs/dh/

Table 3.1: Catalogue of sources and derived quantities for all galaxies to $D < 15$ Mpc in the RBGS with high-resolution *Spitzer*-IRS spectroscopy.

Common Name	RA	DEC	Dist (Mpc)	SH (kpc)	LH (kpc)	Morph Class	L_{IR} ($L_\odot$)	Spectral Class	$\frac{H_\alpha}{H_\beta}$	$\frac{[OIII]}{H_\beta}$	$\frac{[SII]}{H_\alpha}$	$\frac{[NII]}{H_\alpha}$	$10^{15} f_{[OIII]}$ ($\mathrm{erg\,cm^{-2}\,s^{-1}}$)	Ref.
(1)	(2)	(3)	(4)	(5)	(6)	(7)	(8)	(9)	(10)	(11)	(12)	(13)	(14)	(15)
ESO 121-G006	06h07m29.5s	–61d48m28s	14.5	0.33×0.79	0.78×1.57	Sc	9.70	-	-	-	-	-	-	-
ESO 209-G009	07h58m14.9s	–49d51m09s	11.8	0.27×0.65	0.64×1.28	Scd	9.81	-	-	-	-	-	-	-
ESO 265-G007	11h07m48.8s	–46d31m38s	11.7	0.27×0.64	0.63×1.26	Scd	9.55	-	-	-	-	-	-	-
IC 2056	04h16m24.2s	–60d12m26s	13.8	0.31×0.76	0.74×1.49	Sbc	9.62	-	-	-	-	-	-	-
IC 342	03h46m49.4s	+68d05m49s	4.6	0.10×0.25	0.25×0.50	Scd	10.17	HII	3.27	0.10	0.22	0.45	0.90	1
IIZW40	05h55m42.0s	+03d23m30s	11.6	0.26×0.64	0.62×1.25	Sbc	9.47	HII	2.89	6.31	0.05	0.04	22574.40	6
M 82	09h55m53.1s	+69d40m41s	3.6	0.08×0.20	0.19×0.40	Ir	10.77	HII	21.93	0.36	0.18	0.56	66.15	1
NGC 0253	00h47m33.1s	–25d17m15s	3.1	0.07×0.17	0.17×0.34	Sc	10.44	HII	0.47	0.36	0.34	0.72	27.06	2
NGC 0278	00h52m04.3s	+47d33m01s	11.4	0.26×0.62	0.61×1.23	Sab	10.03	HII	3.84	0.24	0.28	0.50	1.89	1
NGC 0613	01h34m17.8s	–29d25m10s	15.0	0.34×0.82	0.81×1.62	Sbc	10.37	HII	6.80	0.48	0.35	0.59	17.22	4
NGC 0628	01h36m41.2s	+15d47m29s	10.0	0.23×0.55	0.54×1.08	Sc	9.95	HII	-	0.61	0.13	0.41	7.62	8
NGC 0660	01h43m02.1s	+13d38m45s	12.3	0.28×0.67	0.66×1.33	Sa	10.49	L	13.65	2.19	0.43	0.85	7.72	1
NGC 0891	02h22m33.5s	+42d21m18s	8.6	0.20×0.47	0.46×0.93	Sab	10.27	HII	12.37	1.00	0.30	0.29	0.18	1
NGC 1055	02h41m44.3s	+00d26m36s	11.3	0.26×0.62	0.61×1.22	Sb	10.09	L	-	-	0.41	0.66	-	1
NGC 1068	02h42m41.4s	+00d00m45s	13.7	0.31×0.75	0.74×1.48	Sb	11.27	S2 (1.8)	5.29	12.82	0.24	0.76	38235.10	1
NGC 1448	03h44m32.1s	–44d38m41s	11.5	0.26×0.63	0.62×1.24	Scd	9.78	HII	> 1.67	-	1.60	0.60	< 0.60	4

Continued on Next Page...

NGC 1559	04h17m37.4s	–62d46m59s	12.7	0.29×0.70	0.68×1.37	Scd	10.21	HII	> 3.14	> 1.00	0.82	-	0.70	4
NGC 1569	04h30m49.5s	+64d51m01s	4.6	0.10×0.25	0.25×0.50	Ir	9.49	HII	3.74	5.48	0.03	0.04	10.14	1
NGC 1792	05h05m13.7s	–37d58m46s	12.5	0.28×0.68	0.67×1.35	Sbc	10.33	HII	-	0.16	0.21	0.54	0.30	4
NGC 1808	05h07m42.3s	–37d30m48s	12.6	0.29×0.69	0.68×1.36	Sa	10.71	HII	2.95	0.16	0.21	0.54	16.31	2
NGC 2681	08h53m33.6s	+51d18m46s	12.5	0.28×0.68	0.67×1.35	Sa	9.53	L	4.77	1.74	0.76	2.34	12.66	1
NGC 2903	09h32m10.5s	+21d30m05s	8.3	0.19×0.45	0.45×0.90	Sbc	10.19	HII	4.42	0.03	0.19	0.34	2.66	1
NGC 3059	09h50m08.1s	–73d55m24s	14.2	0.32×0.78	0.76×1.54	Sbc	10.00	-	-	-	-	-	-	-
NGC 3175	10h14m42.9s	–28d52m25s	13.4	0.31×0.73	0.72×1.45	Sb	9.96	HII	-	-	-	-	-	-
NGC 3184	10h18m12.1s	+41d25m53s	12.6	0.29×0.69	0.68×1.36	Scd	9.80	HII	4.42	0.13	0.20	0.33	1.07	1
NGC 3198	10h19m55.6s	+45d32m54s	13.8	0.31×0.76	0.74×1.49	Sc	9.75	HII	6.44	0.23	0.32	0.42	0.41	1
NGC 3351	10h43m58.1s	+11d42m10s	10.0	0.23×0.55	0.54×1.08	Sb	9.83	HII	4.38	0.27	0.24	0.46	2.19	1
NGC 3368	10h46m45.6s	+11d49m13s	10.5	0.24×0.58	0.57×1.14	Sab	9.67	L	7.46	1.82	0.98	1.12	3.24	1
NGC 3511	11h03m24.2s	–23d05m15s	13.6	0.31×0.75	0.73×1.47	Sc	9.82	HII	12.30	0.28	0.27	0.44	-	7
NGC 3521	11h05m49.2s	+00d02m15s	6.8	0.15×0.37	0.37×0.74	Sbc	9.96	L	3.71	1.00	0.87	0.65	7.39	1
NGC 3556	11h11m31.5s	+55d40m23s	13.9	0.32×0.76	0.75×1.50	Scd	10.37	HII	7.29	0.26	0.29	0.32	1.81	1
NGC 3621	11h18m16.7s	–32d48m47s	6.6	0.15×0.36	0.36×0.71	Sd	9.74	S2	3.42	8.61	0.21	1.46	2.24	9
NGC 3627	11h20m15.3s	+12d59m32s	10.0	0.23×0.55	0.54×1.08	Sb	10.38	L	5.92	2.90	0.76	1.45	12.95	1
NGC 3628	11h20m17.4s	+13d35m19s	10.0	0.23×0.55	0.54×1.08	Sb	10.25	L	4.72	1.78	0.78	0.95	0.23	1
NGC 3675	11h26m09.0s	+43d35m04s	12.7	0.29×0.70	0.68×1.37	Sab	9.92	L	3.20	1.29	0.68	1.48	3.21	1
NGC 3726	11h33m19.9s	+47d01m49s	14.5	0.33×0.79	0.78×1.57	Sc	9.78	HII	3.44	0.14	0.22	0.31	2.52	1
NGC 3938	11h52m49.2s	+44d07m14s	14.8	0.34×0.81	0.80×1.60	Sc	9.93	HII	2.82	1.78	0.83	0.52	1.19	1
NGC 3949	11h53m42.0s	+47d51m31s	13.6	0.31×0.75	0.73×1.47	Sbc	9.87	HII	3.51	0.22	0.44	0.40	1.24	1
NGC 4013	11h58m31.5s	+43d56m54s	13.8	0.31×0.76	0.74×1.49	Sb	9.76	L	2.05	0.71	0.83	1.12	1.01	1

Continued on Next Page…

NGC 4051	12h03m09.8s	+44d31m50s	13.1	0.30×0.72	0.70×1.42	Sbc	9.90	S2 (1.5)	3.30	4.47	0.36	0.65	726.25	1
NGC 4085	12h05m23.3s	+50d21m08s	14.6	0.33×0.80	0.79×1.58	Sc	9.66	HII	4.71	0.63	0.19	0.32	172.71	6
NGC 4088	12h05m35.1s	+50d32m24s	13.4	0.31×0.73	0.72×1.45	Sbc	10.25	HII	7.04	0.21	0.18	0.32	1.40	1
NGC 4157	12h11m04.2s	+50d29m04s	13.3	0.30×0.73	0.72×1.44	Sab	10.12	HII	10.69	0.22	0.24	0.34	0.43	1
NGC 4490	12h30m34.9s	+41d38m47s	10.5	0.24×0.58	0.57×1.14	Sd	10.21	L	6.39	2.57	0.71	0.25	1.83	1
NGC 4536	12h34m28.5s	+02d11m08s	14.9	0.34×0.82	0.80×1.61	Sbc	10.32	HII	5.23	0.33	0.36	0.47	5.42	1
NGC 4559	12h35m57.0s	+27d57m37s	9.7	0.22×0.53	0.52×1.05	Scd	9.56	HII	3.59	0.35	0.40	0.42	0.90	1
NGC 4631	12h42m07.1s	+32d32m33s	7.7	0.18×0.42	0.41×0.83	Sd	10.22	HII	3.07	1.51	0.23	0.24	1.85	1
NGC 4666	12h45m07.7s	+00d27m41s	12.8	0.29×0.70	0.69×1.38	Sc	10.36	L	5.13	1.20	0.60	1.29	558.28	3
NGC 4736	12h50m52.9s	+41d07m15s	4.8	0.11×0.26	0.26×0.52	Sab	9.73	L	3.14	1.47	1.39	2.15	9.59	1
NGC 4818	12h56m50.0s	–08d31m38s	9.4	0.21×0.51	0.51×1.02	Sab	9.75	HII	2.95	0.15	0.18	0.63	-	2
NGC 4945	13h05m27.6s	–49d28m09s	3.9	0.09×0.21	0.21×0.42	Scd	10.48	HII	1.20	< 0.90	0.15	0.30	< 1.00	5
NGC 5033	13h13m27.2s	+36d35m40s	13.8	0.31×0.76	0.74×1.49	Sc	10.13	S2 (1.9)	4.48	4.68	1.07	2.34	96.28	1
NGC 5055	13h15m49.5s	+42d01m39s	8.0	0.18×0.44	0.43×0.86	Sbc	10.09	L	5.42	1.86	0.74	1.48	3.61	1
NGC 5128	13h25m27.6s	–43d01m12s	4.0	0.09×0.22	0.22×0.43	S0	10.11	HII	5.50	0.55	0.28	0.45	12.06	4
NGC 5194	13h29m53.5s	+47d11m42s	8.6	0.20×0.47	0.46×0.93	Sbc	10.42	S2	8.44	8.91	0.85	2.88	90.87	1
NGC 5195	13h30m00.0s	+47d16m00s	8.3	0.19×0.45	0.45×0.90	Irr	9.50	L	1.90	1.22	2.00	5.37	6.76	1
NGC 5236	13h36m58.8s	–29d51m46s	3.6	0.08×0.20	0.19×0.39	Sc	10.10	HII	6.05	0.29	0.21	1.33	35.36	4
NGC 5643	14h32m41.1s	–44d10m30s	13.9	0.32×0.76	0.75×1.50	Sc	10.24	S2	7.80	10.67	0.71	1.15	607.36	4
NGC 5907	15h15m58.9s	+56d18m36s	12.1	0.28×0.66	0.65×1.31	Sc	9.85	HII	11.81	1.07	0.34	0.60	0.44	1
NGC 6300	17h17m00.3s	–62d49m13s	13.1	0.30×0.72	0.70×1.42	Sb	10.09	S2	7.44	15.14	0.14	0.95	38.69	4
NGC 6744	19h09m45.9s	–63d51m27s	9.9	0.23×0.54	0.53×1.07	Sbc	9.99	L	0.90	1.30	2.44	-	6.75	4
NGC 6946	20h34m52.6s	+60d09m12s	5.3	0.12×0.29	0.29×0.57	Scd	10.16	HII	9.03	0.38	0.32	0.64	3.17	1

Continued on Next Page…

NGC 7331	22h37m04.6s	+34d24m56s	14.7	0.33×0.81	0.79×1.59	Sb	10.58	L	3.92	2.79	0.55	1.44	7.77	1
UGCA 127	06h20m56.9s	–08d29m42s	10.2	0.23×0.56	0.55×1.10	Scd	9.82	-	-	-	-	-	-	-

NOTES: (1) Common galaxy name. (2–3) *2MASS* near-IR position of galactic nucleus. (4) Luminosity distance to source in Mpc from the RBGS (Sanders et al. 2003; see footnote 2). (5–6) Projected spectral apertures (SH and LH respectively) in kiloparsecs. (7) Morphological classification from RC3 (de Vaucouleurs et al., 1991). (8) Logarithm of IR luminosity (8–1000 μm) from RBGS. (9) Optical spectral class from BPT diagnostics (S2: Seyfert 2; broad-line sub-class in parentheses, HII: Star-forming galaxy, and L: LINER). (10–13) Optical emission line ratios. (14) Observed [OIII] flux in units of $10^{-15}\,\mathrm{erg\,cm^{-2}\,s^{-1}}$. (15) References for published optical data.

REFERENCES: (1) Ho et al. (1997a); (2) Kewley et al. (2001b); (3) Veilleux et al. (1995); (4) Veron-Cetty et al. (1986); (5) Moorwood et al. (1996); (6) Moustakas and Kennicutt (2006); (7) Kirhakos and Steiner (1990); (8) Ganda et al. (2006); (9) Barth et al. (2009).

Table 3.2: $D < 15$ Mpc IR-bright galaxies not included in sample

Common Name (1)	Morph Class (2)	Dist (Mpc) (3)	L_{IR} ($L_\odot$) (4)	Spectral Class (5)	*Spitzer*-IRS Spec? (6)	$L_{[OIV]}$ ($\mathrm{erg\,s^{-1}}$) (7)
NGC 3486	Sc	9.2	9.31	Sy2	1	38.52
NGC 4565	Sb	10.0	9.66	Sy2	2	38.40
NGC 5248	Sbc	13.8	10.20	HII	3	-
NGC 5457	Scd	6.7	10.20	HII	2	-

NOTES: (1) Common galaxy name. (2) Morphological classification from RC3. (3) Luminosity distance in Mpc from RBGS. (4) Logarithm of IR luminosity (8–1000 μm) from RBGS. (5) Optical spectral class from Ho97 using BPT diagnostics; see Table 3.1. (6) Status of *Spitzer*-IRS data: 1. High-resolution observations are publicly available but signal-to-noise is not sufficient for analysis; 2. High-resolution observations available only for extranuclear regions; 3. No high-resolution observations available. (7) Logarithm of [OIV] $\lambda 25.89$ μm luminosity from low-resolution ($R \sim 100$) *Spitzer*-IRS spectroscopy in units of $\mathrm{erg\,s^{-1}}$ (Diamond-Stanic et al. 2009).

After extraction of the raw spectra, the ends of each echelle order were trimmed to remove the additional spectral noise caused by the poor response of the grating.[4] Using the redshifts given in the RBGS, each extracted spectrum was shifted to rest-wavelength for further spectral analysis. Solely for presentation purposes, single continuous spectra of each slit were produced. Echelle orders were matched by fitting each spectral continuum from a given order with either a first or second order polynomial. Each echelle order continuum was then combined by matching and calibrating to the 1st echelle order of the relevant slit to construct the final SH and LH continua. Due to the different aperture sizes (and hence continuum fluxes), we have not attempted to match the SH and LH spectra. Fig. 3.2 shows the reduced spectra for each of the sources using the SH and LH slits (left and right panels respectively).

3.2.3 Measuring Emission-line Properties

Second-order polynomials were used to model the continuum and gaussian profiles were simultaneously fit to spectral features to determine emission-line fluxes. These were calculated using the IDL-based spectral analysis tool SMART (Higdon et al., 2004).[5] Fluxes or 3σ upper-limits are given in Table 3.3 for the following emission lines: [NeII] $\lambda 12.81$ μm, [NeV] $\lambda 14.32$ μm, [NeIII] $\lambda 15.56$ μm, [NeV] $\lambda 24.32$ μm, [OIV] $\lambda 25.89$ μm, [FeII] $\lambda 25.99$ μm, [SIII] $\lambda 33.48$ μm and [SiII] $\lambda 34.82$ μm. Polycyclic Aromatic Hydrocarbon (PAH; e.g., Draine 2003) features are detected in many of the galaxies; we use the 11.3 μm PAH equivalent width in our analyses and report these values in Table 3.3. Due to their broad profiles, the strength of the PAH features are measured using multiple gaussians. The results obtained from our continuum and emission-line fitting procedure are shown in Fig. 3.3 for all [NeV] $\lambda 14.32$ μm detected galaxies.

Of the 64 galaxies in the $D < 15$ Mpc sample, 16 have published *Spitzer*-IRS data in S08 and 18 have published *Spitzer*-IRS data in Dale et al. (2009; hereafter D09). However, due to differing data-reduction routines and approaches in the detection of emission lines (e.g., we measured emission-line properties in apertures centred on the near-IR nucleus, S08 searched for emission lines in small apertures across the circumnuclear region of each galaxy, and D09 constrained emission-line properties in large apertures across the extent of each galaxy), we have re-analysed all of the galaxies to provide self-consistent results. However, despite these differing approaches, we find average emission-line flux

[4] Wavelength trim ranges are given in Table 5.1 of the *Spitzer*-IRS Observers Manual.

[5] SMART was developed by the IRS Team at Cornell University and is available through the SSC.

variances of only $\approx$ 10–30% between our study and that of S08 and D09 for those galaxies with with detected [NeII] $\lambda 12.81$ μm, [NeIII] $\lambda 15.56$ μm, and [OIV] $\lambda 25.89$ μm emission; when comparing to D09 we linearly scaled our emission-line fluxes by the difference in aperture size between D09 and our study.

3.2.4 [NeV] as an unambiguous AGN indicator

Due to the very high-ionization potential of [NeV] (97.1 eV) we consider its detection coincident with the galactic nucleus in mid-IR spectroscopy to be an almost unambiguous identifier of AGN activity. Theoretically, Schaerer and Stasińska (1999) have predicted that extremely hot O and B stars, in particular galaxies containing dense populations of Wolf-Rayet (WR) stars, may produce ionization spectra capable of exciting lines such as [OIV] (54.9 eV) and [NeV]. However, two WR galaxies are present in our volume-limited sample (IIZw40 and NGC 1569). We find that whilst [OIV] is clearly detected in these types of systems, [NeV] emission remains absent to the detection limits of this survey, and their mid-IR continuum and spectral features are clearly distinct from those of AGNs. Complimentary to this, Hao et al. (2009) find from a *Spitzer*-IRS study of 12 Blue Compact Dwarf galaxies that the mid-IR spectroscopy for eight of their sample contain [OIV] emission, however none appear to be producing [NeV] despite having sufficient sensitivity to detect the emission line. Similarly, extreme starburst driven shocks have also been predicted to excite some high-ionization lines such as [NeV] (Allen et al., 2008), however these require exceptionally high velocities, and based on the [NeV] $\lambda 14.32$ μm–[NeII] $\lambda 12.81$ μm and [NeIII] $\lambda 15.51$ μm–[NeII] $\lambda 12.81$ μm emission line ratios presented in Table 3.3, the [NeV] identified AGNs in this study are not consistent with shock models.

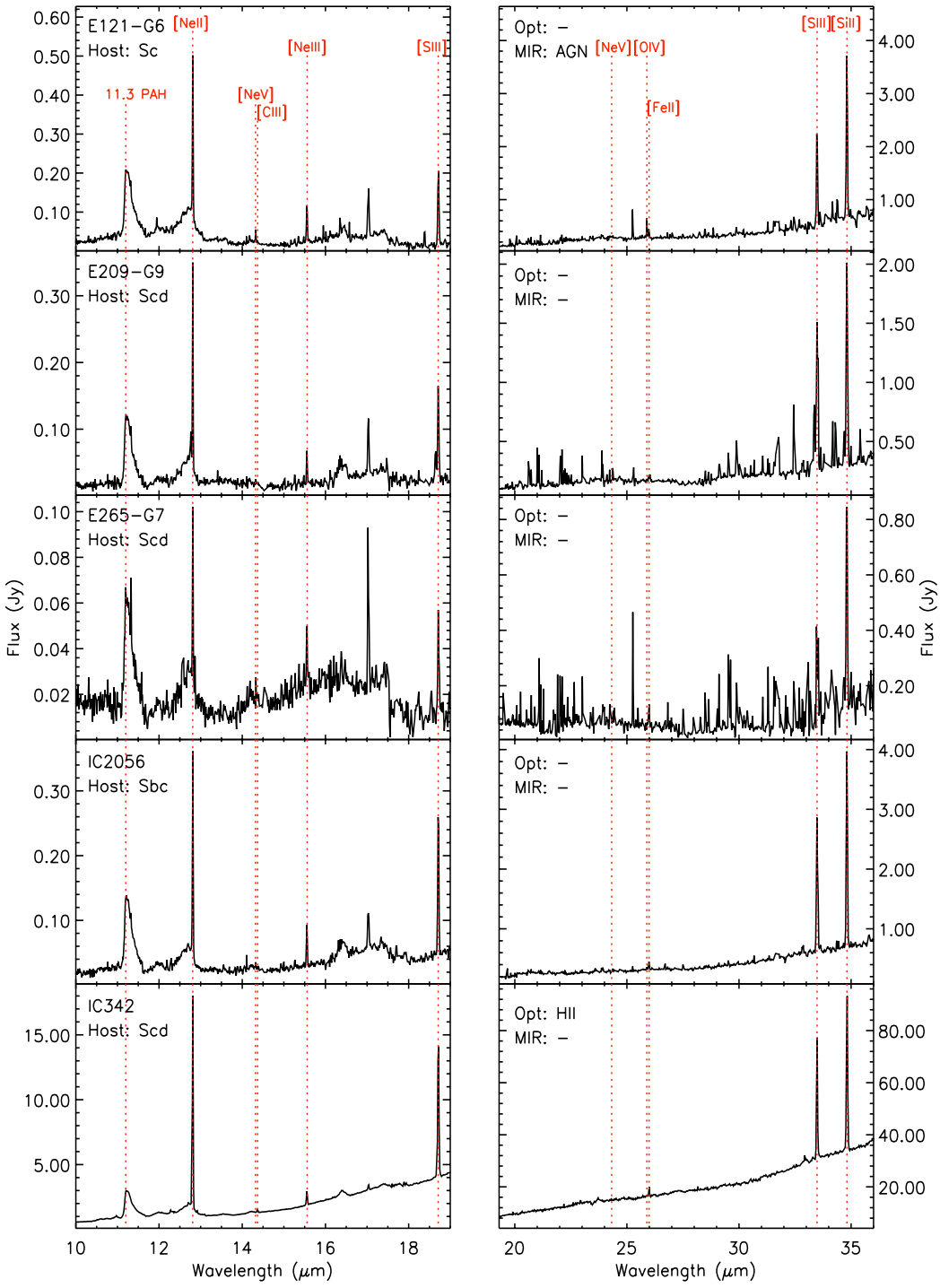

Figure 3.2: *Spitzer*-IRS high-resolution spectra for the SH and LH modules (left and right panels respectively) of all galaxies with *Spitzer*-IRS observations in our $D < 15$ Mpc IR-bright sample. The most prominent spectral features are labeled and indicated with dotted lines. The galaxy name, host-galaxy classification, optical spectral classification, and mid-IR classification are indicated.

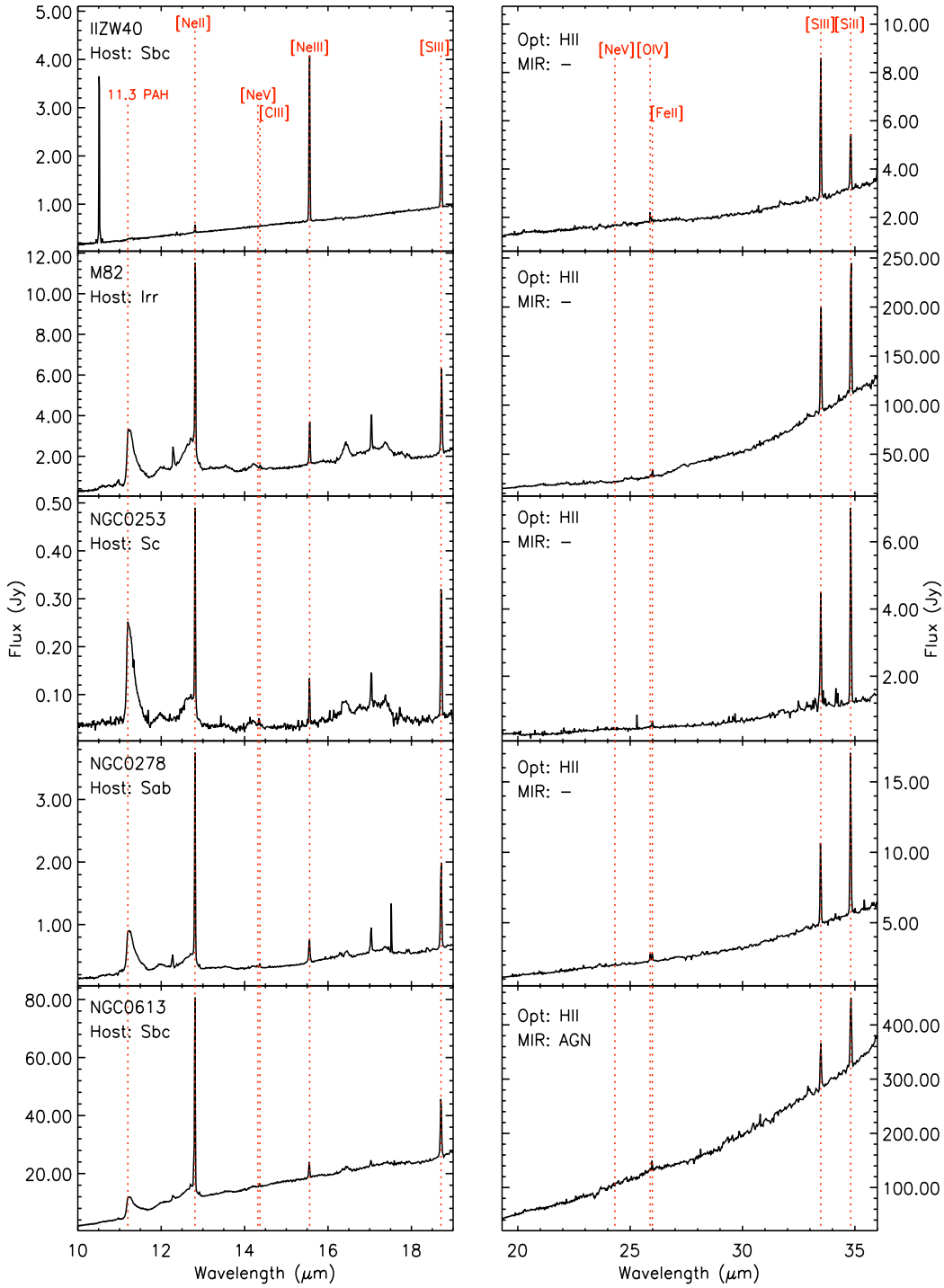

Figure 3.2: *continued..*

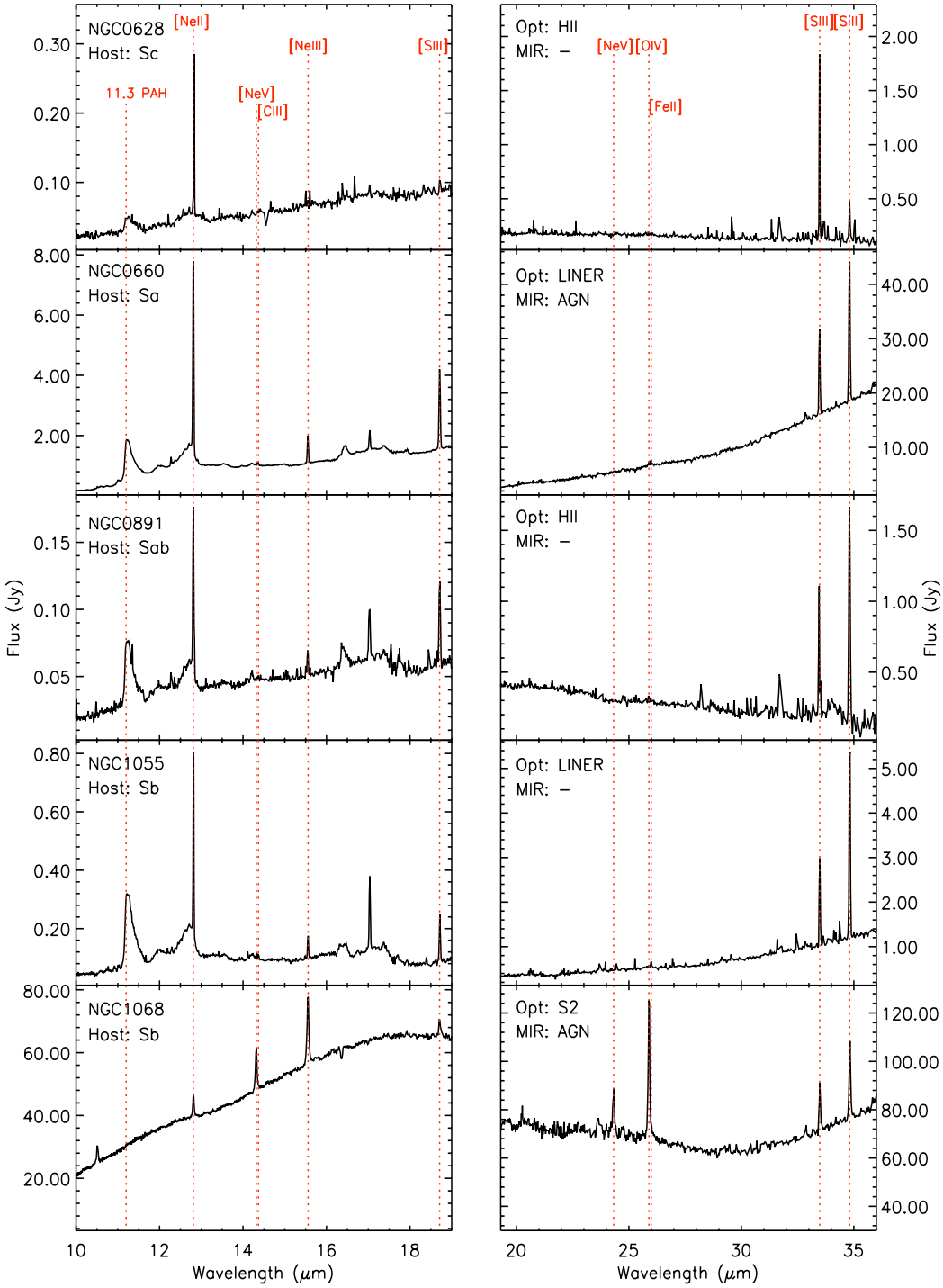

Figure 3.2: *continued..*

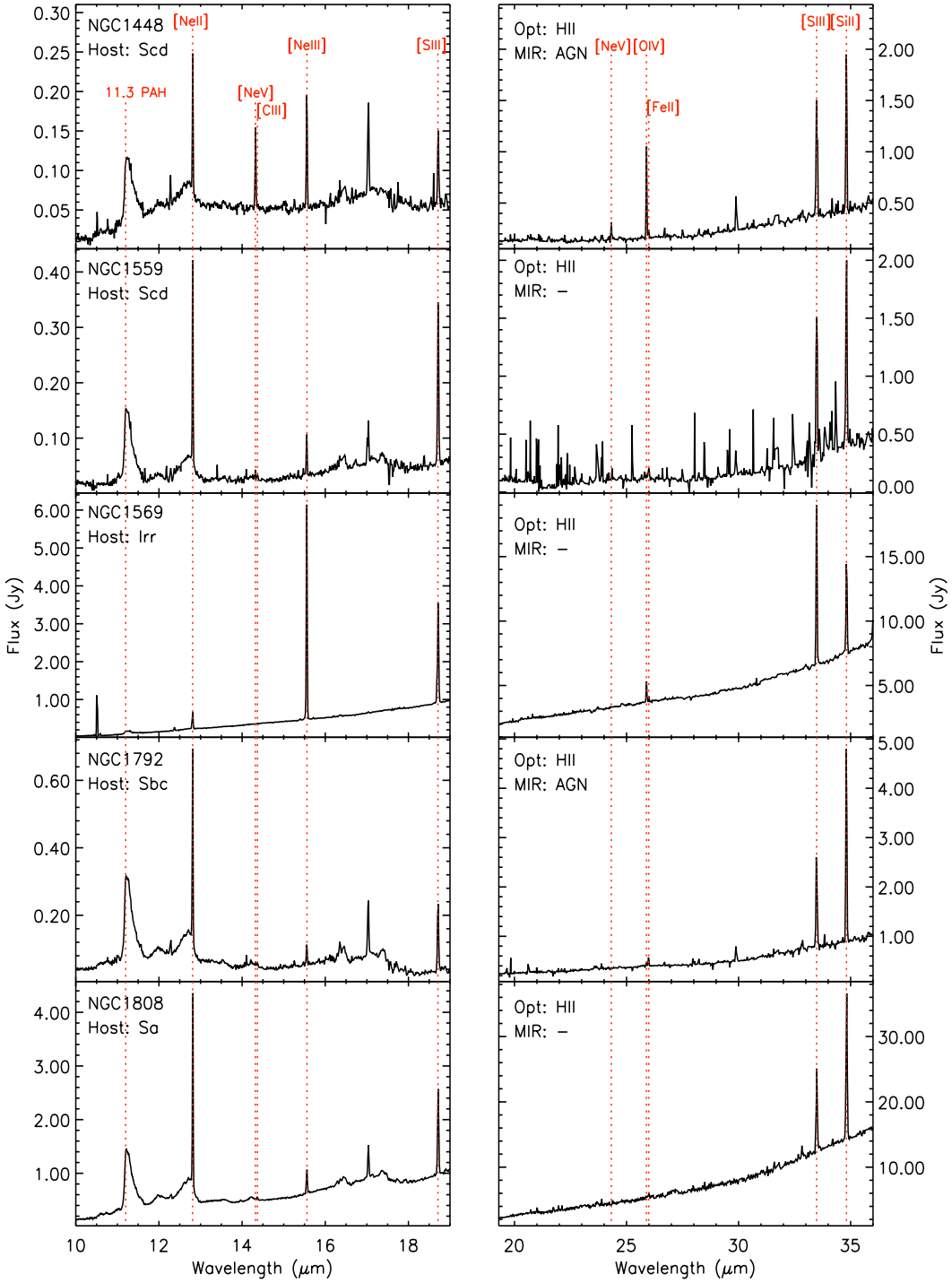

Figure 3.2: *continued..*

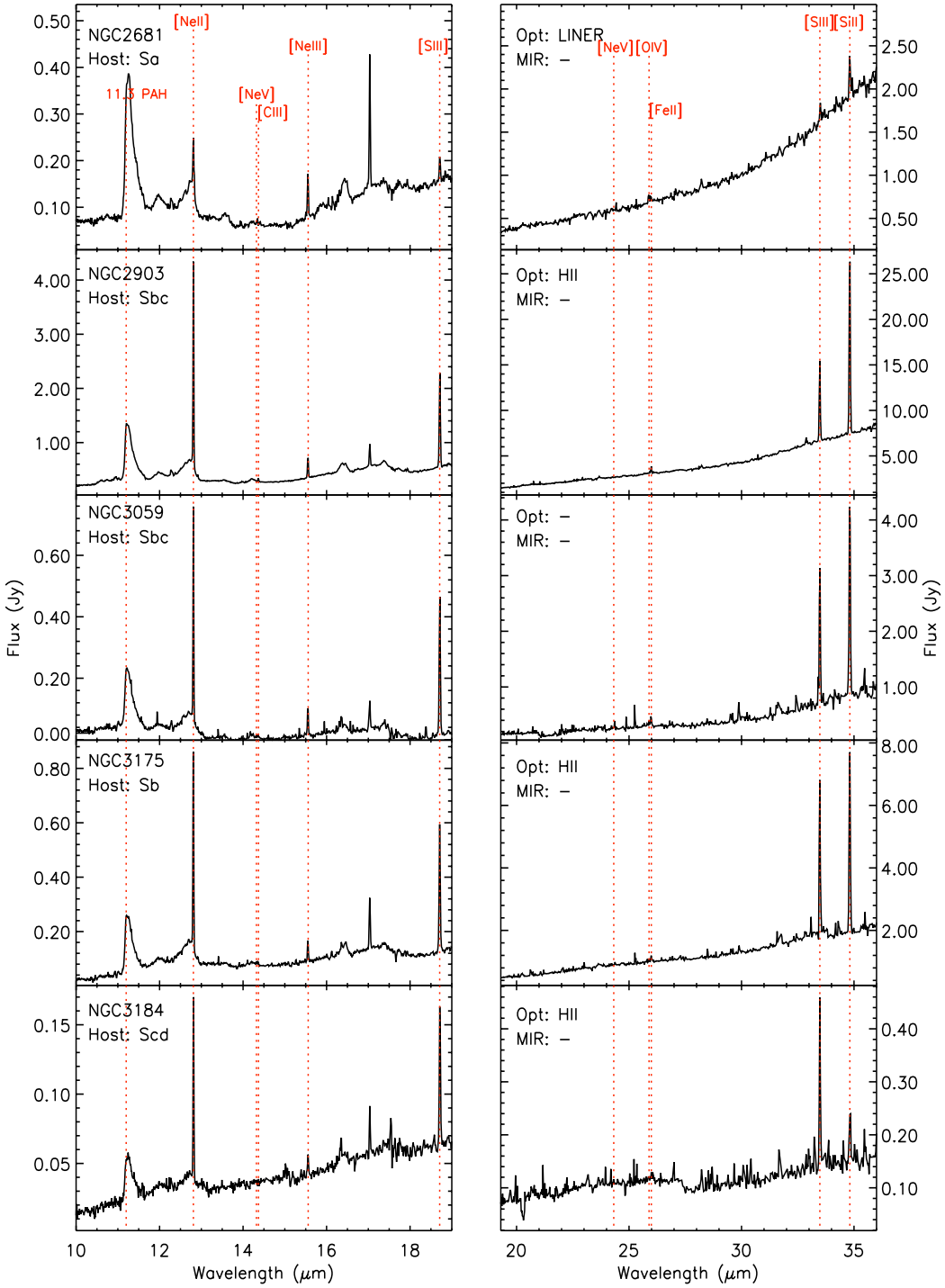

Figure 3.2: *continued..*

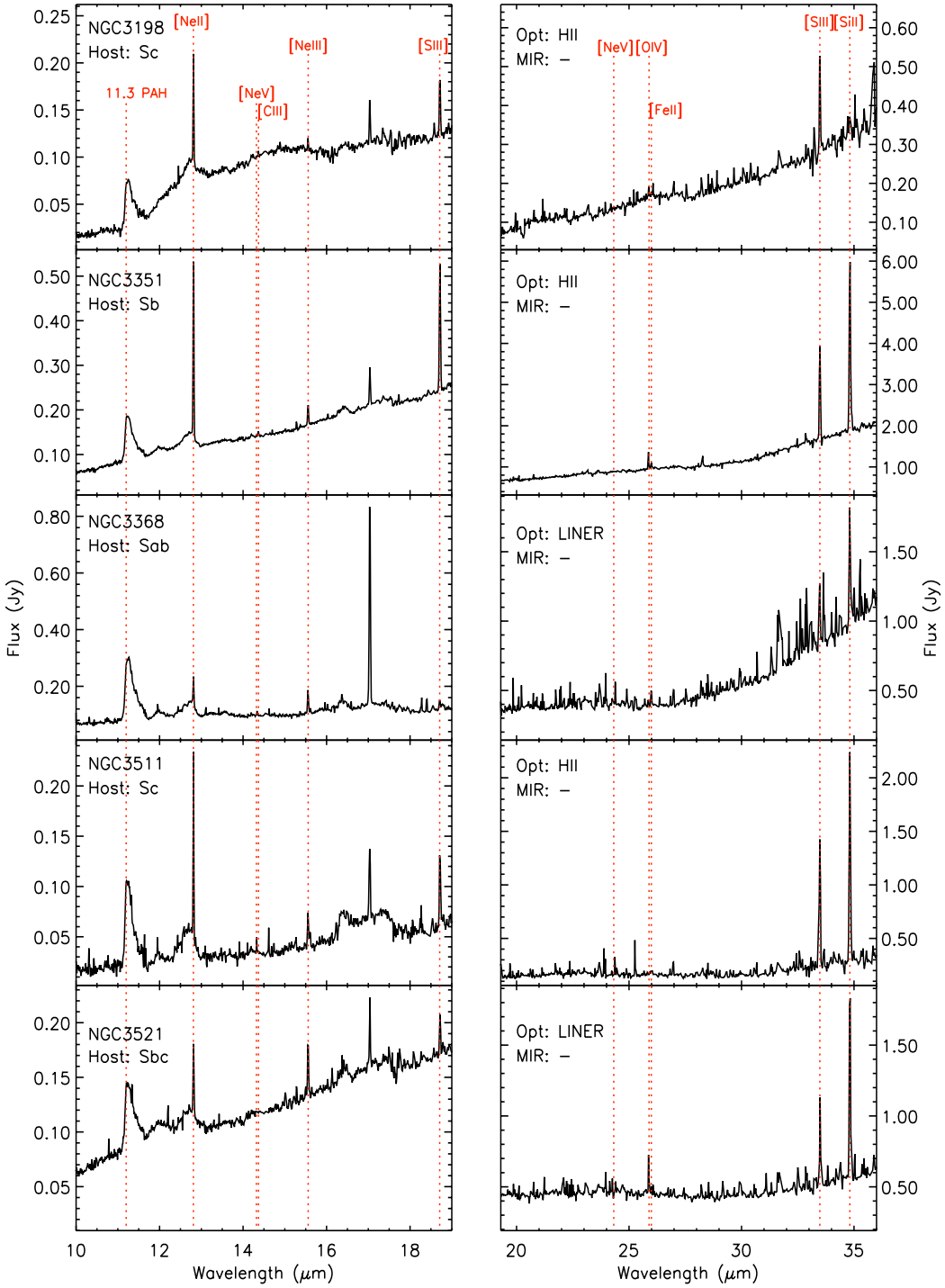

Figure 3.2: *continued..*

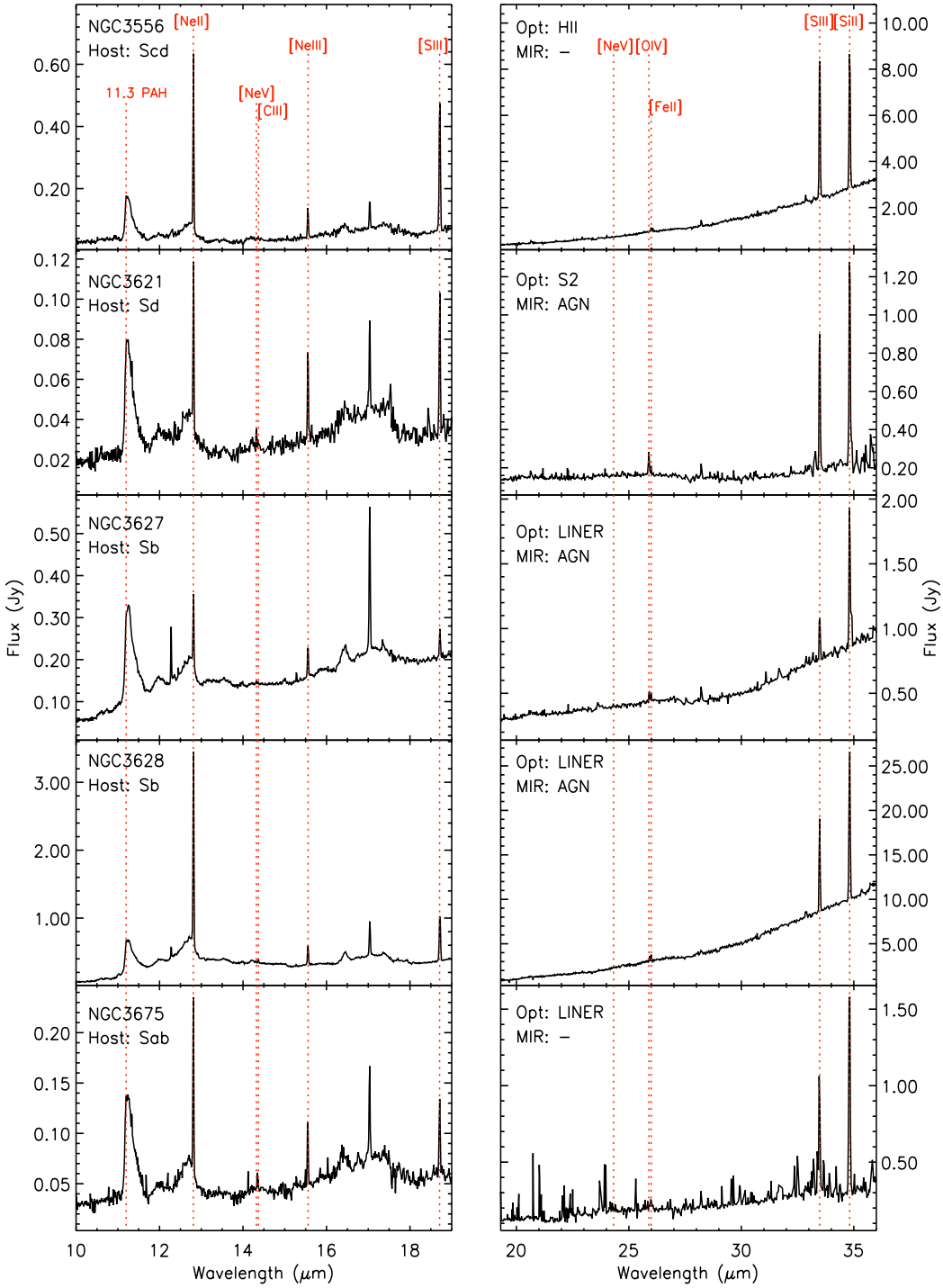

Figure 3.2: *continued..*

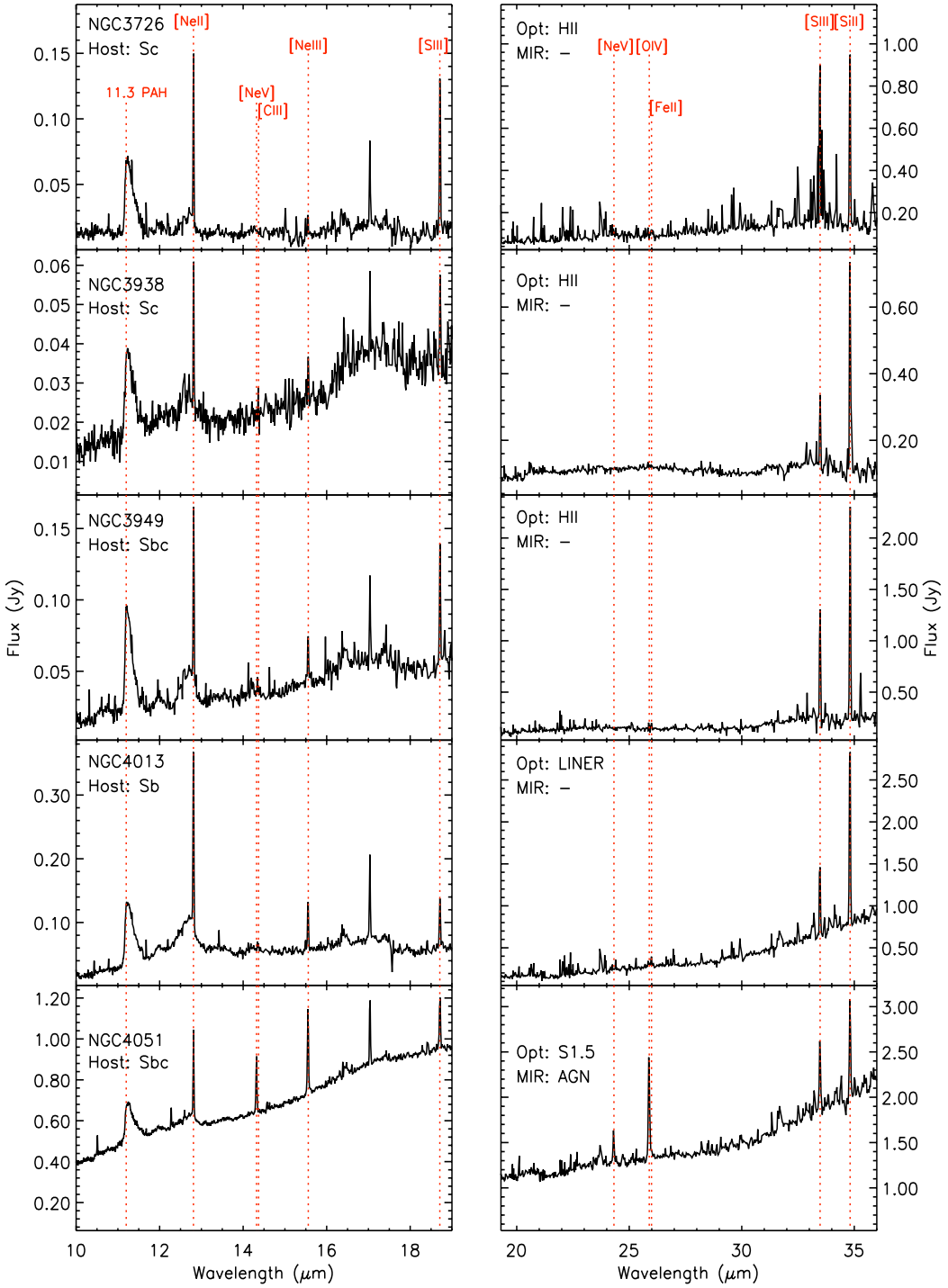

Figure 3.2: *continued..*

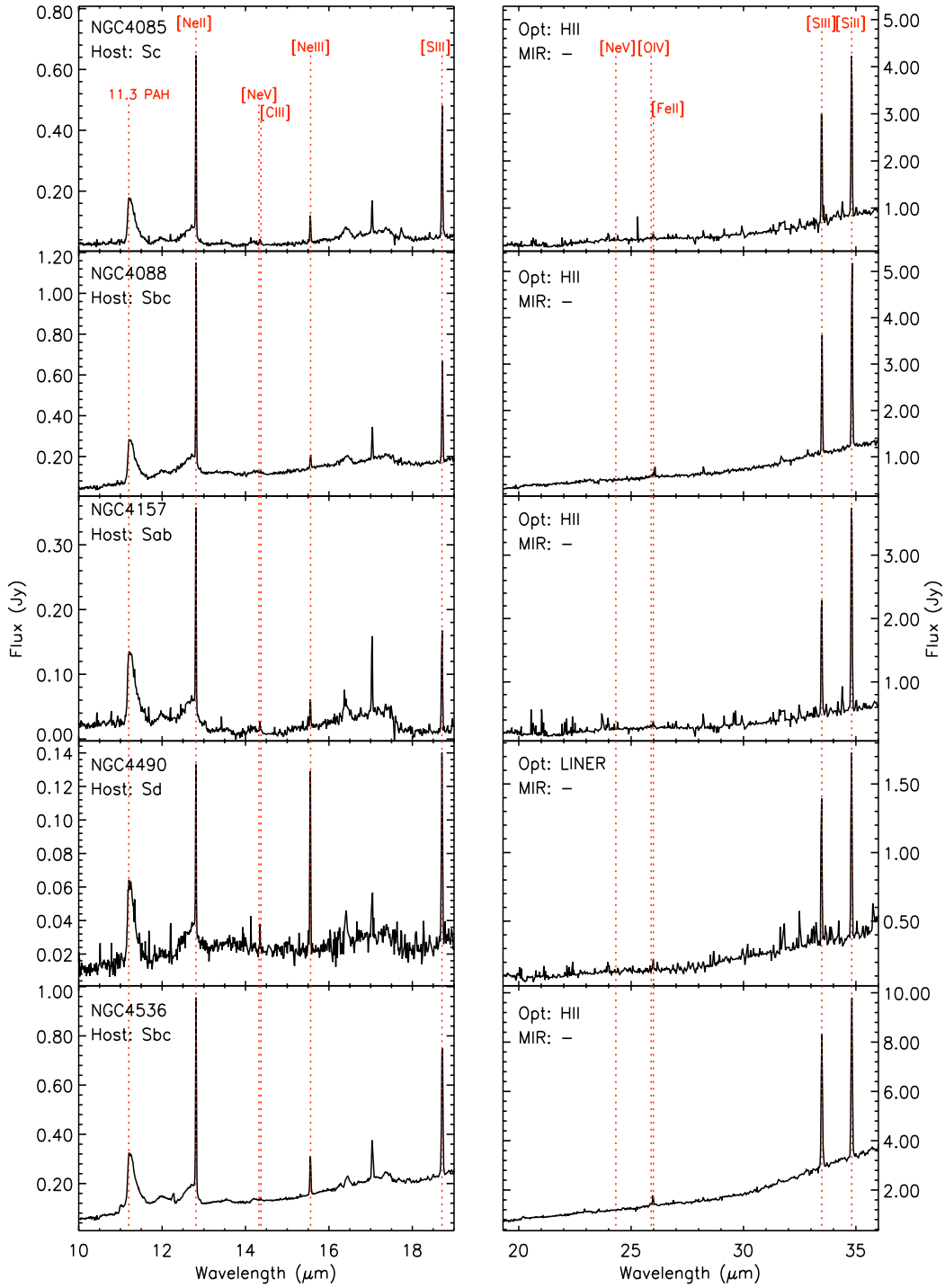

Figure 3.2: *continued..*

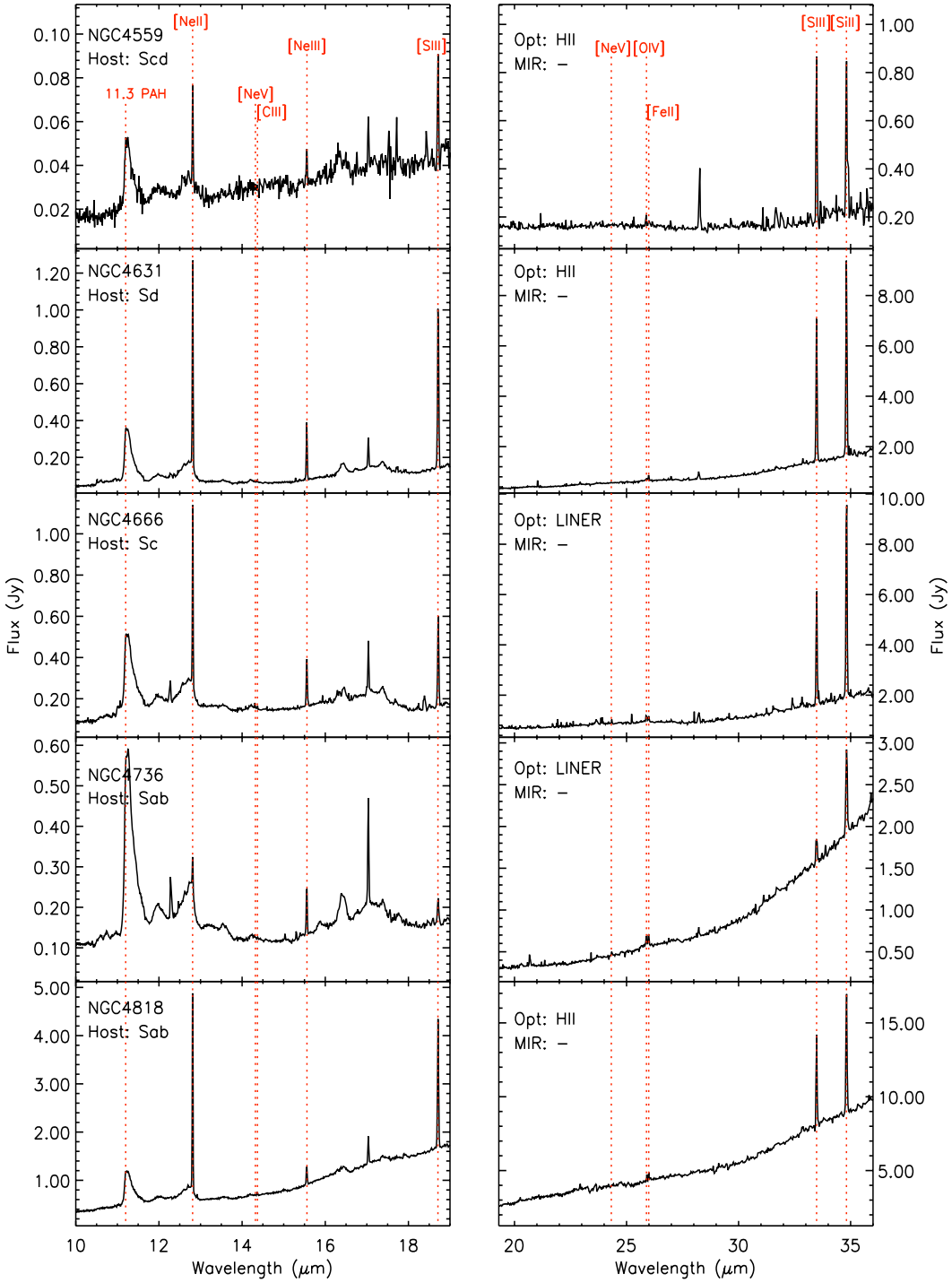

Figure 3.2: *continued..*

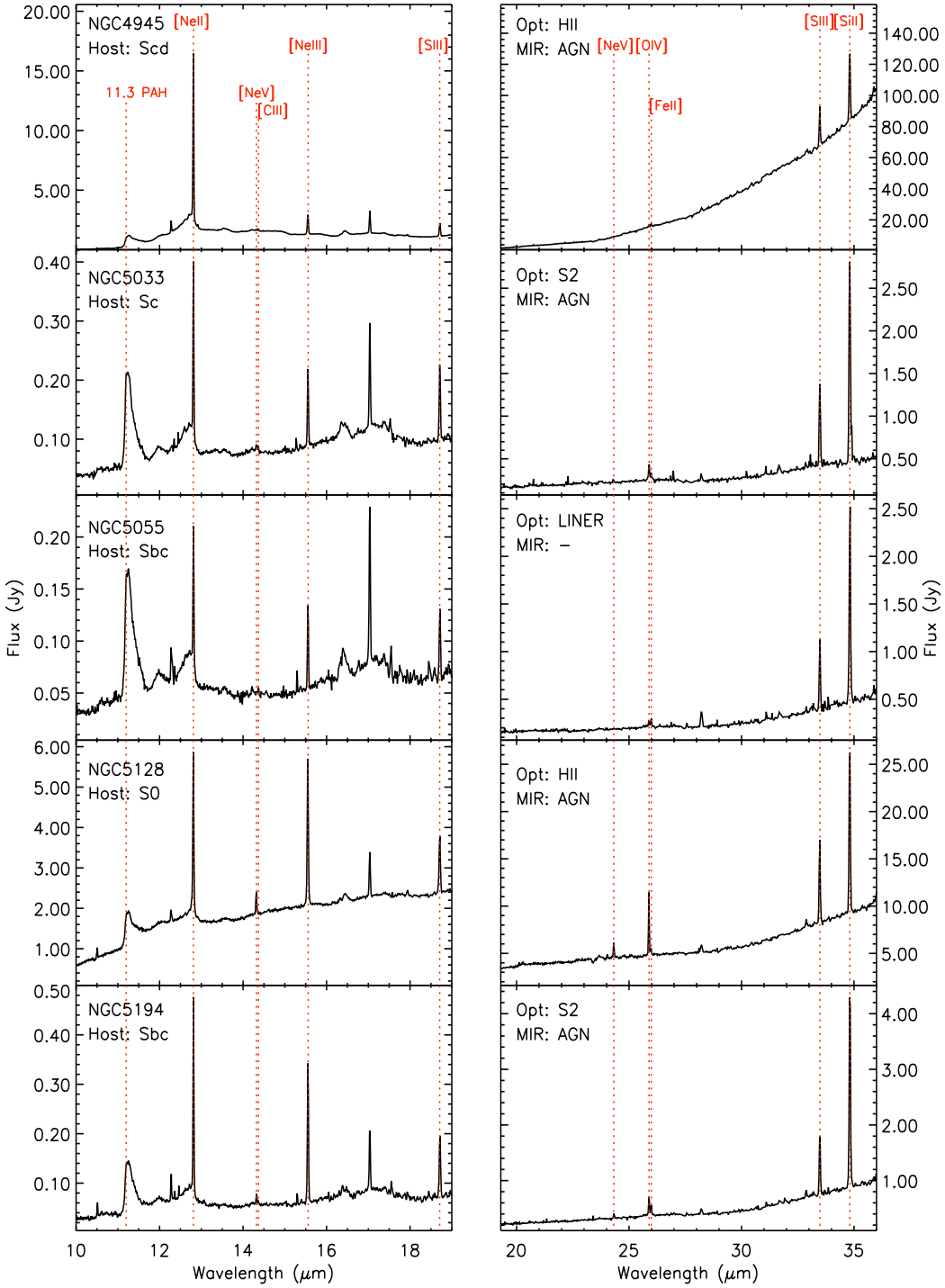

Figure 3.2: *continued..*

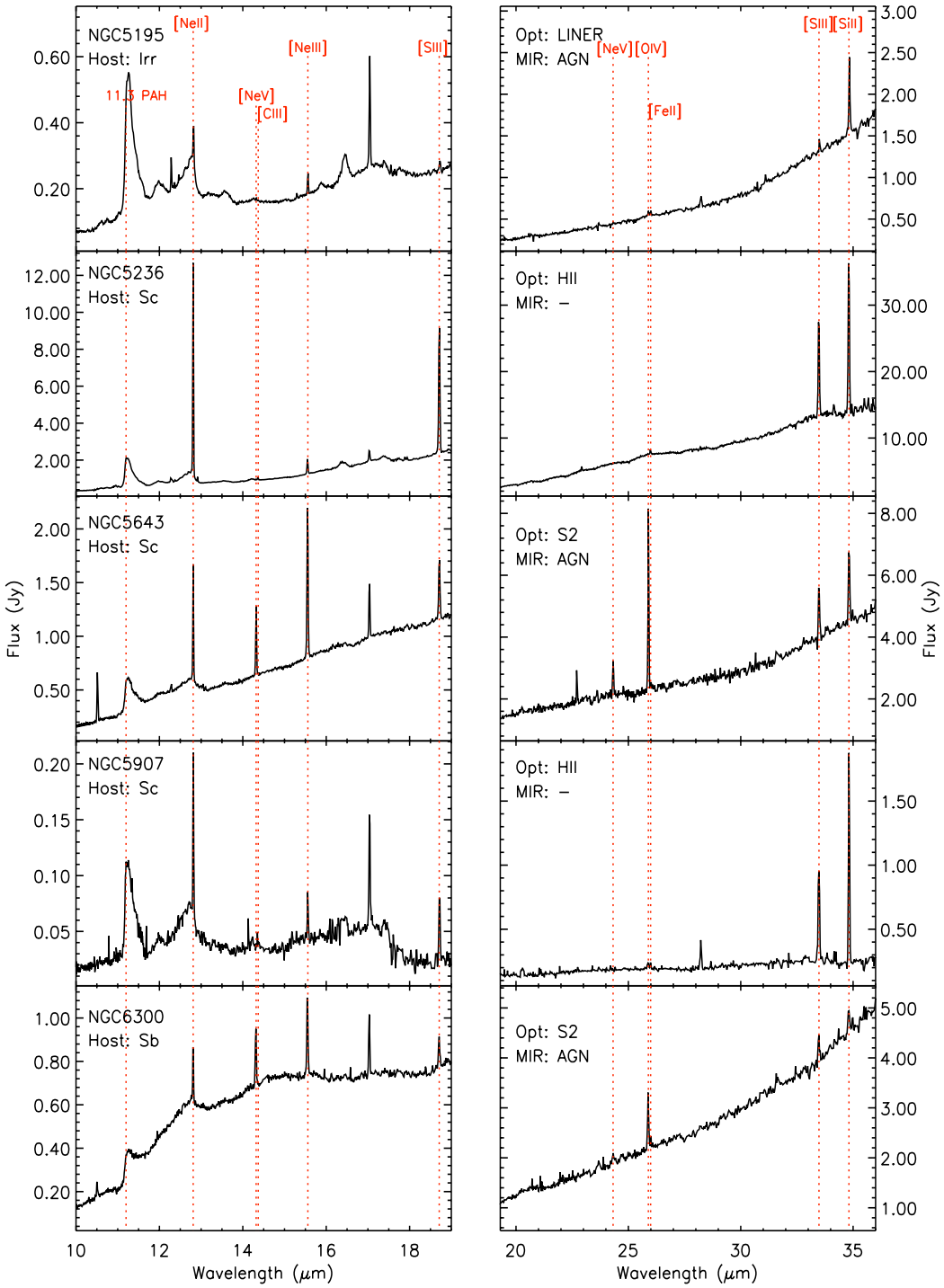

Figure 3.2: *continued..*

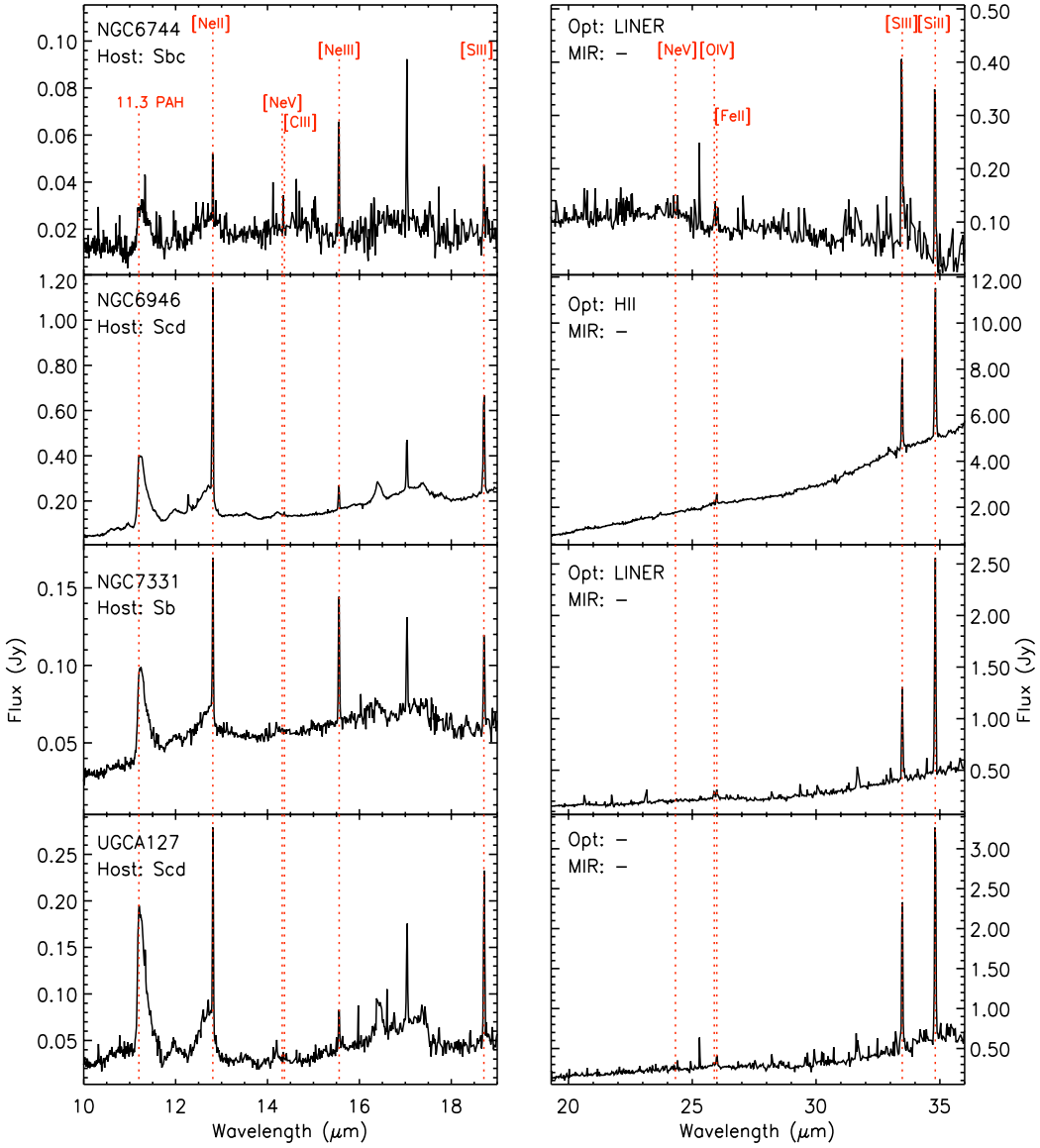

Figure 3.2: *continued..*

Table 3.3: Mid-IR Spectral Emission Lines (10^{-14} erg s^{-1} cm^{-2})

Common Name	EW PAH λ11.3 μm (μm)	[NeII] λ12.81 μm 21.6 eV	[NeV] λ14.32 μm 97.1 eV	[NeIII] λ15.56 μm 41.0 eV	[NeV] λ24.32 μm 97.1 eV	[OIV] λ25.89 μm 54.9 eV	[FeII] λ25.99 μm 7.9 eV	[SIII] λ33.48 μm 23.3 eV	[SiII] λ34.82 μm 8.2 eV	Mid-IR AGN?
(1)	(2)	(3)	(4)	(5)	(6)	(7)	(8)	(9)	(10)	(11)
ESO 121-G006	0.816	16.48 ± 0.50	0.65 ± 0.08	3.24 ± 0.24	< 0.59	4.57 ± 0.40	3.03 ± 0.26	28.59 ± 2.80	45.88 ± 1.87	Y
ESO 209-G009	1.127	9.81 ± 0.59	< 0.26	1.43 ± 0.20	< 0.12	< 0.29	< 0.99	22.86 ± 2.53	31.56 ± 1.70	-
ESO 265-G007	19.155	2.62 ± 0.32	< 0.41	1.13 ± 0.23	< 1.18	< 1.04	1.59 ± 0.17	8.47 ± 0.92	11.83 ± 1.08	-
IC 2056	1.072	12.77 ± 0.26	< 0.16	2.15 ± 0.15	< 0.10	0.75 ± 0.16	2.95 ± 0.21	42.00 ± 6.98	52.60 ± 2.00	-
IC 342	0.498	669.38 ± 5.01	< 0.64	39.21 ± 0.73	< 13.71	< 6.83	60.45 ± 4.95	652.93 ± 18.77	953.15 ± 13.71	-
IIZW40	0.015	6.04 ± 1.12	< 0.28	117.34 ± 2.34	< 1.14	8.49 ± 2.28	1.92 ± 0.49	86.92 ± 2.02	36.05 ± 1.41	-
M 82	0.843	506.22 ± 45.04	< 0.89	80.98 ± 1.99	< 14.65	45.67 ± 6.61	137.77 ± 0.66	1812.9 ± 36.8	2166.0 ± 25.5	-
NGC 0253	0.295	3099.10 ± 126.60	< 5.13	207.89 ± 9.05	< 113.68	< 83.66	245.20 ± 0.93	1463.4 ± 69.7	2411.8 ± 64.0	-
NGC 0278	0.851	17.84 ± 0.37	< 0.07	2.95 ± 0.16	< 0.59	< 0.62	3.82 ± 0.64	49.55 ± 3.37	86.82 ± 1.07	-
NGC 0613	0.501	130.73 ± 1.55	0.67 ± 0.11	15.96 ± 0.50	3.18 ± 0.56	9.09 ± 1.53	12.47 ± 1.25	84.23 ± 2.70	162.49 ± 2.11	Y
NGC 0628	0.175	2.31 ± 0.36	< 0.15	< 0.08	< 0.46	< 0.13	< 0.11	12.35 ± 0.94	4.78 ± 0.40	-
NGC 0660	0.730	379.81 ± 13.96	3.88 ± 0.25	37.46 ± 0.69	< 4.59	28.26 ± 8.24	22.03 ± 3.61	250.60 ± 11.47	435.29 ± 4.03	Y
NGC 0891	0.364	8.57 ± 0.78	< 0.04	0.84 ± 0.07	< 0.62	< 1.03	< 0.84	10.74 ± 2.02	28.11 ± 0.92	-
NGC 1055	0.747	26.42 ± 0.79	< 0.19	2.58 ± 0.20	< 0.58	1.22 ± 0.26	3.32 ± 0.47	28.26 ± 2.46	71.16 ± 0.98	-
NGC 1068	0.008	538.34 ± 37.3	898.04 ± 42.25	1432.2 ± 76.9	815.96 ± 58.78	2066.9 ± 154.9	169.76 ± 41.70	378.51 ± 34.07	616.32 ± 21.94	Y
NGC 1448	0.378	8.17 ± 0.72	3.68 ± 0.29	5.02 ± 0.12	3.60 ± 0.62	16.02 ± 0.49	1.60 ± 0.26	23.76 ± 5.08	22.55 ± 1.13	Y

Continued on Next Page...

NGC 1559	0.652	14.88 ± 0.24	< 0.44	2.34 ± 0.18	< 0.36	< 0.69	2.91 ± 0.21	23.25 ± 4.32	26.00 ± 0.88	-
NGC 1569	0.089	19.06 ± 1.28	< 0.38	188.15 ± 2.69	< 1.37	29.32 ± 0.16	6.43 ± 0.27	188.06 ± 4.38	111.08 ± 2.59	-
NGC 1792	0.492	23.32 ± 0.32	0.41 ± 0.13	2.10 ± 0.17	< 0.25	0.96 ± 0.06	3.38 ± 0.38	31.01 ± 0.93	57.43 ± 0.72	Y
NGC 1808	0.682	177.36 ± 16.36	< 0.91	17.26 ± 0.68	< 8.38	< 9.54	16.62 ± 2.78	205.83 ± 20.27	354.26 ± 15.15	-
NGC 2681	0.883	6.88 ± 0.28	< 0.15	3.43 ± 0.21	< 0.36	2.17 ± 0.70	1.56 ± 0.43	< 4.01	7.77 ± 0.66	-
NGC 2903	0.699	181.62 ± 13.59	< 0.82	13.52 ± 0.18	< 0.94	< 1.70	13.38 ± 2.73	124.25 ± 1.85	298.89 ± 2.03	-
NGC 3059	0.882	26.79 ± 0.93	< 0.18	3.13 ± 0.25	< 0.69	< 1.48	4.07 ± 0.64	40.41 ± 5.92	59.18 ± 0.82	-
NGC 3175	0.752	34.08 ± 0.46	< 0.35	2.46 ± 0.22	< 0.86	1.15 ± 0.07	3.91 ± 1.54	71.51 ± 2.47	92.40 ± 1.28	-
NGC 3184	0.324	5.70 ± 0.15	< 0.10	0.67 ± 0.08	< 0.20	0.50 ± 0.09	< 0.27	4.31 ± 0.35	5.05 ± 0.52	-
NGC 3198	0.423	4.75 ± 0.11	< 0.03	0.30 ± 0.08	< 0.16	0.45 ± 0.10	< 0.31	3.39 ± 0.45	4.34 ± 0.59	-
NGC 3351	0.263	18.87 ± 1.09	< 0.13	1.71 ± 0.08	< 0.14	4.71 ± 3.19	2.91 ± 0.32	38.47 ± 1.41	70.25 ± 1.19	-
NGC 3368	0.488	4.29 ± 0.29	< 0.29	2.85 ± 0.25	< 0.74	0.99 ± 0.29	2.58 ± 0.12	< 5.88	13.22 ± 2.53	-
NGC 3511	0.647	6.37 ± 0.18	< 0.34	1.39 ± 0.11	< 0.64	< 1.11	< 1.25	20.19 ± 3.06	31.35 ± 0.79	-
NGC 3521	0.172	3.02 ± 0.22	< 0.11	1.77 ± 0.17	< 0.31	1.53 ± 0.11	< 0.82	7.14 ± 1.08	21.79 ± 1.11	-
NGC 3556	0.771	26.43 ± 1.79	< 0.26	3.44 ± 0.11	< 0.32	< 0.69	2.79 ± 0.18	100.28 ± 1.09	95.50 ± 1.14	-
NGC 3621	0.555	3.69 ± 0.16	0.29 ± 0.00	1.51 ± 0.16	0.53 ± 0.05	2.86 ± 0.39	0.86 ± 0.73	12.27 ± 0.62	17.66 ± 1.08	Y
NGC 3627	0.579	8.14 ± 0.29	0.30 ± 0.08	2.79 ± 0.15	0.47 ± 0.04	1.99 ± 0.53	1.30 ± 0.28	5.78 ± 0.96	16.84 ± 1.90	Y
NGC 3628	0.798	155.28 ± 8.38	0.95 ± 0.06	10.38 ± 0.19	< 2.39	5.35 ± 2.89	12.12 ± 0.27	155.61 ± 6.44	264.07 ± 2.31	Y
NGC 3675	0.588	8.07 ± 0.13	< 0.23	2.21 ± 0.20	< 0.48	< 0.58	< 1.39	12.65 ± 3.29	25.12 ± 0.89	-
NGC 3726	1.408	5.47 ± 0.13	< 0.41	0.43 ± 0.06	< 0.52	< 0.44	< 0.45	12.60 ± 0.11	11.82 ± 0.27	-
NGC 3938	0.314	1.43 ± 0.14	< 0.09	0.31 ± 0.09	< 0.14	< 0.29	< 0.17	3.20 ± 0.29	9.84 ± 2.57	-
NGC 3949	0.528	5.82 ± 0.29	< 0.11	1.11 ± 0.15	< 0.11	1.48 ± 0.67	1.15 ± 0.03	17.12 ± 1.28	29.25 ± 0.89	-
NGC 4013	0.639	13.12 ± 0.26	< 0.09	2.77 ± 0.24	< 0.89	< 1.01	< 2.44	13.49 ± 2.33	34.23 ± 0.90	-

Continued on Next Page...

NGC 4051	0.085	16.78 ± 0.48	11.26 ± 0.43	16.02 ± 0.47	11.82 ± 1.20	36.42 ± 2.41	< 1.93	13.74 ± 1.17	17.17 ± 1.73	Y
NGC 4085	1.159	23.03 ± 0.31	< 0.15	2.92 ± 0.21	< 0.92	< 0.44	1.91 ± 0.43	36.63 ± 2.09	53.22 ± 1.66	-
NGC 4088	0.575	43.67 ± 1.61	< 0.19	2.54 ± 0.13	< 0.47	< 0.53	1.69 ± 0.31	36.31 ± 0.80	61.27 ± 0.59	-
NGC 4157	0.832	11.63 ± 0.18	< 0.07	1.44 ± 0.12	< 0.70	1.10 ± 0.32	2.51 ± 0.75	29.70 ± 3.13	54.72 ± 2.79	-
NGC 4490	0.396	3.55 ± 0.45	< 0.10	3.50 ± 0.12	< 0.10	1.08 ± 0.17	1.75 ± 0.35	16.87 ± 2.97	22.26 ± 0.87	-
NGC 4536	0.434	35.46 ± 0.39	< 0.06	6.11 ± 0.06	< 0.13	1.72 ± 0.25	9.74 ± 1.50	100.48 ± 4.53	114.02 ± 1.53	-
NGC 4559	0.214	1.89 ± 0.13	< 0.05	0.53 ± 0.08	< 0.07	< 1.62	0.54 ± 0.15	10.61 ± 0.93	10.03 ± 0.44	-
NGC 4631	0.647	45.92 ± 0.71	< 0.07	10.15 ± 0.13	< 0.27	< 1.47	< 3.67	85.16 ± 0.76	114.74 ± 1.89	-
NGC 4666	0.517	35.65 ± 2.01	< 0.57	8.32 ± 0.15	< 0.89	6.77 ± 1.94	5.14 ± 0.32	68.92 ± 1.84	124.15 ± 2.25	-
NGC 4736	0.734	3.74 ± 0.34	< 0.12	4.25 ± 0.07	< 0.76	2.01 ± 0.36	3.22 ± 0.44	6.38 ± 1.50	20.28 ± 1.13	-
NGC 4818	0.314	195.95 ± 14.93	< 0.38	13.37 ± 0.73	< 1.62	< 4.39	8.86 ± 0.50	86.31 ± 3.67	125.45 ± 3.74	-
NGC 4945	0.712	698.41 ± 60.43	7.06 ± 0.31	68.07 ± 2.27	< 2.12	28.35 ± 1.39	49.26 ± 13.00	359.62 ± 20.42	732.76 ± 7.84	Y
NGC 5033	0.644	13.26 ± 0.18	0.42 ± 0.05	5.08 ± 0.15	0.48 ± 0.08	5.08 ± 0.51	2.02 ± 0.47	17.38 ± 0.85	45.35 ± 1.52	Y
NGC 5055	0.606	6.04 ± 0.22	< 0.11	3.08 ± 0.10	< 0.89	1.75 ± 0.16	2.19 ± 0.47	11.90 ± 0.65	34.10 ± 1.84	-
NGC 5128	0.165	202.71 ± 3.97	21.96 ± 0.88	149.98 ± 5.04	27.88 ± 0.71	123.63 ± 2.72	24.99 ± 5.72	140.69 ± 6.05	297.43 ± 1.52	Y
NGC 5194	0.591	17.03 ± 0.26	0.74 ± 0.10	10.91 ± 0.24	1.61 ± 0.11	7.93 ± 0.25	4.33 ± 0.87	18.39 ± 0.81	60.42 ± 2.08	Y
NGC 5195	0.842	5.54 ± 0.72	0.20 ± 0.06	2.17 ± 0.11	< 0.39	0.94 ± 0.23	< 0.96	3.22 ± 0.39	12.21 ± 1.26	Y
NGC 5236	0.602	503.33 ± 19.88	< 0.61	29.30 ± 0.77	< 1.19	5.75 ± 1.08	18.57 ± 3.42	263.50 ± 9.21	391.40 ± 8.55	-
NGC 5643	0.227	46.41 ± 3.56	24.63 ± 1.03	56.47 ± 1.16	31.33 ± 1.77	118.28 ± 4.74	< 4.00	33.26 ± 3.05	42.67 ± 2.84	Y
NGC 5907	0.791	6.07 ± 0.22	< 0.01	1.28 ± 0.16	< 0.07	1.57 ± 0.51	0.94 ± 0.20	14.21 ± 1.41	23.94 ± 0.60	-
NGC 6300	0.125	11.52 ± 0.63	12.54 ± 0.66	15.28 ± 0.57	8.33 ± 1.29	29.45 ± 2.26	< 3.49	< 7.63	11.31 ± 0.82	Y
NGC 6744	0.245	1.06 ± 0.26	< 0.03	1.53 ± 0.17	< 0.13	< 0.73	0.84 ± 0.25	3.57 ± 0.98	3.24 ± 0.41	-
NGC 6946	0.768	38.45 ± 0.66	< 0.17	3.77 ± 0.10	< 0.59	4.00 ± 0.68	8.42 ± 0.60	61.00 ± 3.70	112.25 ± 1.57	-

Continued on Next Page...

NGC 7331	0.337	4.47 ± 0.15	< 0.16	3.08 ± 0.10	< 0.39	1.88 ± 0.14	1.61 ± 0.28	13.81 ± 0.41	30.58 ± 0.93	-
UGCA 127	0.982	9.34 ± 0.38	< 0.15	1.53 ± 0.24	< 0.97	3.37 ± 0.16	3.43 ± 0.12	29.37 ± 2.41	44.08 ± 1.68	-

NOTES: (1) Common galaxy name. (2) Equivalent width of the $11.3\ \mu\mathrm{m}$ PAH feature in units of $\mu\mathrm{m}$. (3–10) Fluxes and their statistical uncertainties for the measured mid-IR narrow emission lines in units $10^{-14}\,\mathrm{erg\,cm^{-2}\,s^{-1}}$. The mean uncertainty of the fluxes is approximately 10 percent. 3σ upper limits are quoted for non-detections. The ionisation potential of each emission line is given underneath the name. (11) Mid-IR AGN on the basis of [NeV] $\lambda 14.32\ \mu\mathrm{m}$ emission.

3.3 Results and Discussion

3.3.1 The Discovery of a Significant Population of Optically Unidentified AGNs

Of the 64 objects in our $D < 15$ Mpc sample (presented in Tables 3.1 and 3.3), 17 have 3σ detections of the [NeV] $\lambda 14.32$ μm emission line, and therefore have unambiguous evidence for AGN activity. We therefore find an overall AGN fraction of $\approx 27^{+8}_{-6}$ percent in the most bolometrically luminous galaxies to $D < 15$ Mpc ($L_{IR} \approx (0.3-20)\times10^{10}$ $L_{\odot}$).[6]

Of the 16 galaxies in common between S08 and our sample, S08 identified [NeV] (14.32 or 24.32 μm) in four systems (NGC 3556; NGC 3938; NGC 4536; NGC 5055). We do not detect significant [NeV] in any of these four galaxies, which may be due to differences in the positions and sizes of the apertures used to extract the spectra within CUBISM. Of the 18 galaxies in common between D09 and our sample, D09 identified [NeV] $\lambda 14.32$ μm in three systems (NGC 3621; NGC 5033; NGC 5194), all of which we also identify here; however, we also identified [NeV] emission in two systems where D09 quote [NeV] upper limits (NGC 3627; NGC 5195), which could be due to dilution of the [NeV] emission by the host galaxy in the large apertures used by D09. We note that differences in the identification of weak [NeV] emission can also be due to the adopted emission-line detection procedure and signal-to-noise ratio threshold.

Seven ($\approx 11^{+6}_{-4}$ percent) of the 64 galaxies in our sample are unambiguously identified as AGNs using classical optical emission-line diagnostics (i.e., optically classified as Seyfert galaxies; e.g., Baldwin et al. 1981; Veilleux and Osterbrock 1987; Kauffmann et al. 2003b); see Table 3.1. All of these optically identified AGNs are classified as AGNs at mid-IR wavelengths in our analysis. In Fig. 3.4, we plot the optical emission-line ratios of the 53 galaxies with good-quality optical spectra; of the other 11 galaxies in the sample, three do not have a sufficient number of detected emission lines to classify at optical wavelengths using emission-line diagnostics, and eight do not have published optical spectroscopy. Ten of our mid-IR classified AGNs are not unambiguously identified as AGNs at optical wavelengths: five are classified as HII galaxies (NGC 0613, NGC 1448, NGC 1792, NGC 4945, and NGC 5128), four are classified as LINERS (NGC 0660, NGC 3627, NGC 3628, and NGC 5195), and one does not have good-quality optical spectroscopic data (ESO121-G006). Although ESO121-G006 does

[6]Small-number Poisson statistical errors are calculated for upper and lower limits based on the 1σ confidence levels given in Gehrels (1986).

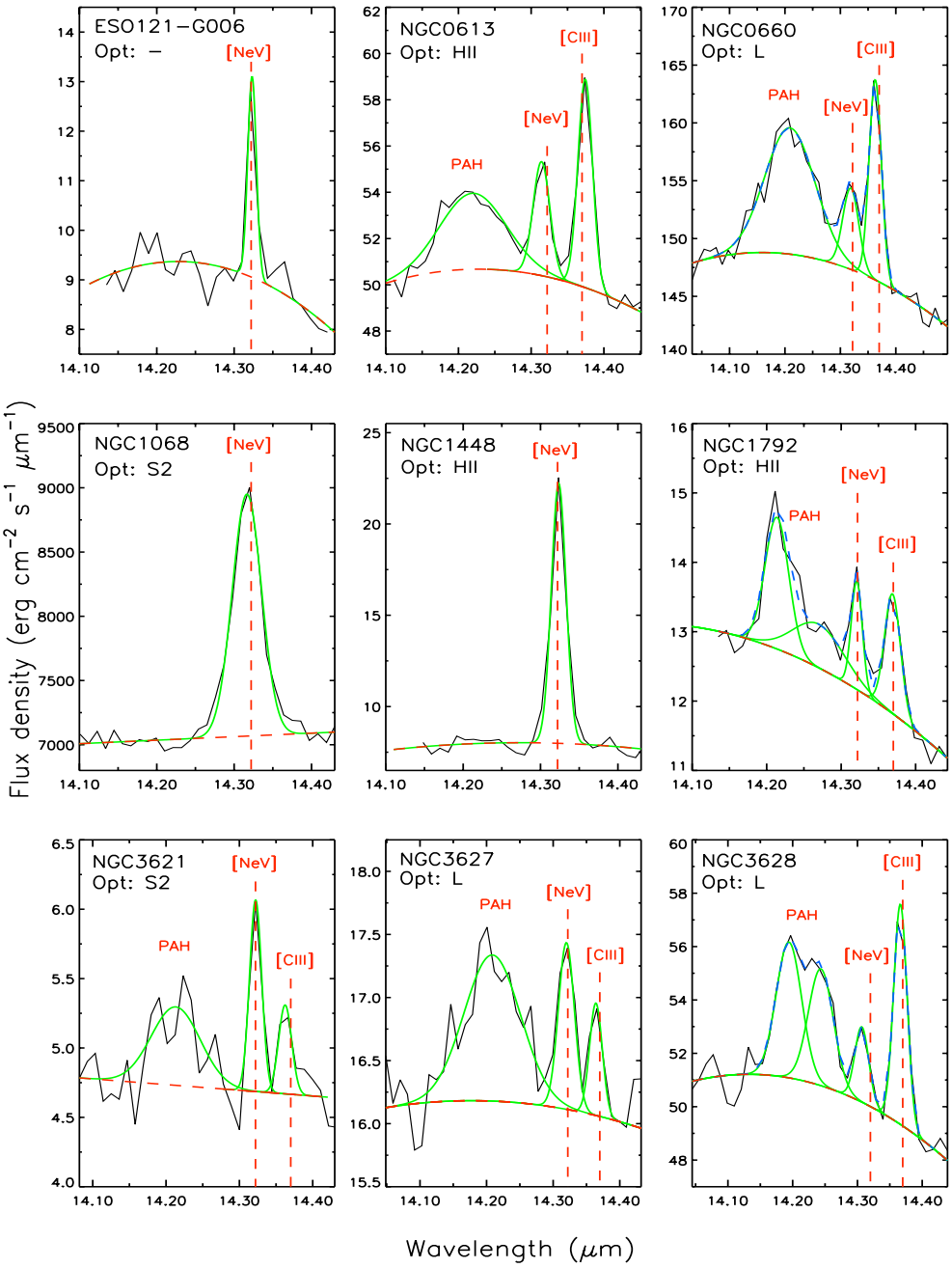

Figure 3.3: Mid-IR spectra expanded around the [NeV] $\lambda 14.32$ μm emission-line region for all [NeV] detected galaxies covering a broad range of optical and mid-IR spectral properties. The dotted line indicates the second-order polynomial fit to the continuum and the solid lines indicate the gaussian fit to the emission-line features; the [NeV] $\lambda 14.32$ μm , $\lambda 14.2$ μm PAH, and [ClII] $\lambda 14.37$ μm emission features are labeled when detected. The identification of AGN activity from the [NeV] $\lambda 14.32$ μm emission-line in ten objects is complicated by the PAH and [ClII] star-forming signatures and thus high signal-to-noise data is required.

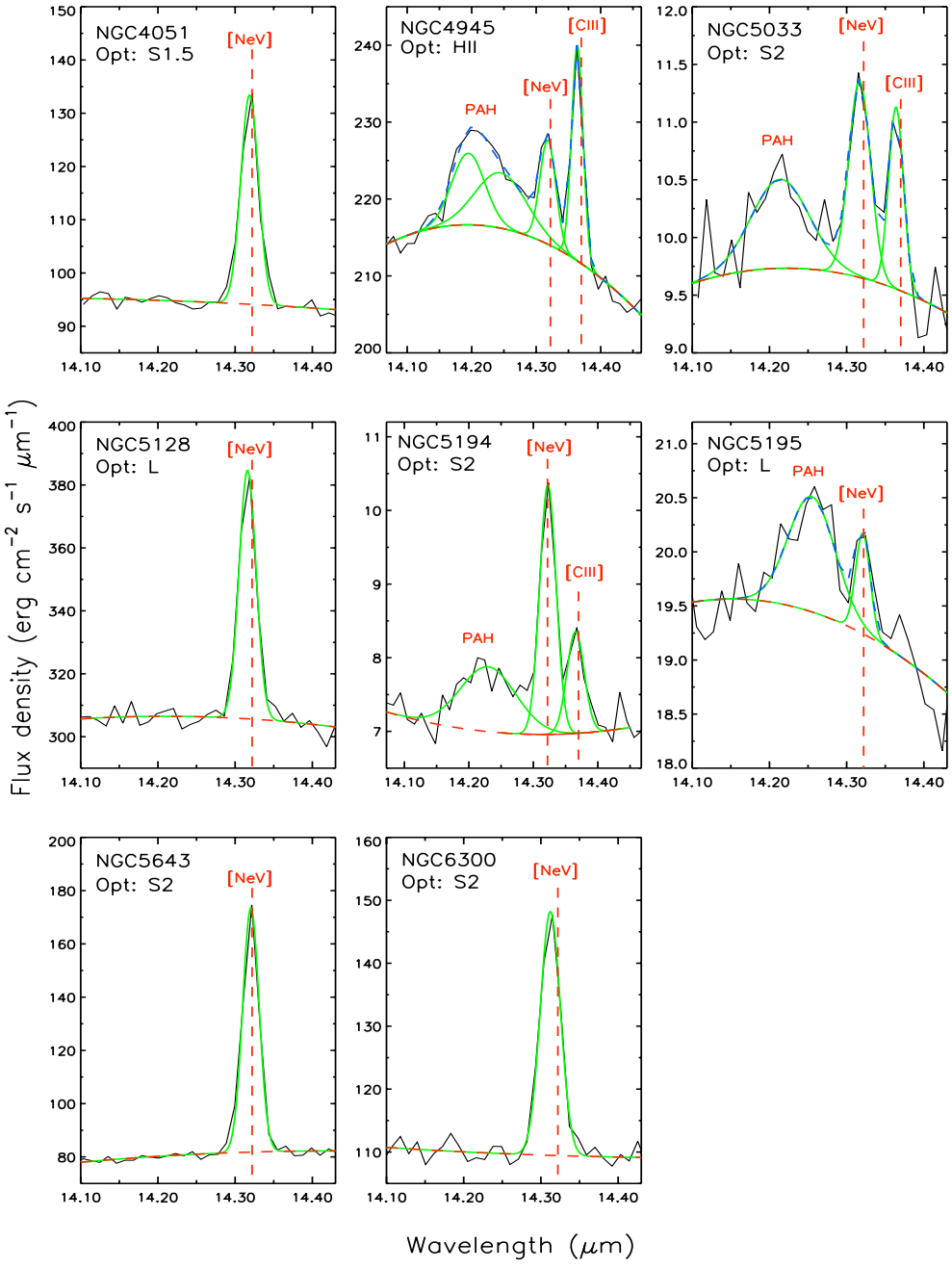

Figure 3.3: *continued*

not have a good-quality optical spectrum, since it is hosted in a highly inclined galaxy we would expect it to be an optically unidentified AGN; see § 3.3.3 and Fig. 3.10. Large optical spectroscopic studies (e.g., Veilleux et al. 1995; Ho97) have speculated that the central regions of many LINERs are likely to be powered by AGN activity. Indeed, using *Chandra* X-ray observations, Ho et al. (2001) suggest ≈ 60 percent of all LINERs host AGNs. By contrast, using our mid-IR diagnostics, we find only ≈ 25 percent of IR-bright LINERs appear to be AGNs, which could be due to a number of factors (e.g., different sample selection and ambiguous evidence for AGN activity at X-ray energies; i.e., X-ray binaries).

The optical spectroscopy for the galaxies in our sample comes from a variety of different studies with a range in emission-line sensitivities. However, the majority of the galaxies are in Ho97, which arguably comprises the most sensitive optical spectroscopy of a large number of nearby galaxies. Of the 38 galaxies present in both our sample and Ho97, we find that eight are mid-IR identified AGNs (NGC 0660, NGC 1068, NGC 3627, NGC 3628, NGC 4051, NGC 5033, NGC 5194 and NGC 5195), only four of which are unambiguously identified as AGN at optical wavelengths. One of the optically unidentified AGNs is NGC 5195, which may be a binary AGN system with NGC 5194 in the Whirlpool galaxy. Potential AGN activity has also been found in NGC 5195 using *Chandra* observations (Terashima and Wilson, 2004).

Optical spectroscopic surveys have found that AGNs typically reside in moderately massive bulge-dominated galaxies (Hubble-type: E–Sbc; $M_{\star} \approx$ (0.1–3) $\times 10^{11}\,\mathrm{M}_{\odot}$; e.g., Ho97; Heckman et al. 2004). In Fig. 3.5 we show the histogram of galaxy morphology for our $D < 15$ Mpc sample. We find that the host galaxies of our mid-IR identified AGNs cover a wide range of galaxy type (S0–Ir). However, in contrast to Ho97 and Heckman et al. (2004), we find that a large fraction of Sc–Sd-type galaxies host AGN activity at mid-IR wavelengths ($\approx 22^{+13}_{-9}$ percent; i.e., a comparable AGN fraction to that found in Sab–Sbc galaxies). This shows that late-type galaxies typically assumed to host pseudo bulges (Sc–Sd) can harbour AGN activity, and therefore must host a SMBH. As found in previous studies, this indicates that galaxies without classical bulges can host SMBHs (e.g., Greene et al. 2008; Barth et al. 2009).

In Fig. 3.5 we also show the incidence of AGN activity as a function of IR luminosity. In the moderate-luminosity IR bin ($\mathrm{L_{IR}} \approx$ (1–3) $\times 10^{10}\,\mathrm{L}_{\odot}$), we find a large AGN fraction of $\approx 39^{+16}_{-12}$ percent, suggesting that the overall AGN fraction for our sample may be a lower limit. The smaller AGN fractions found in the lower ($\mathrm{L_{IR}} < 10^{10}\,\mathrm{L}_{\odot}$; $\approx 16^{+11}_{-7}$ per-

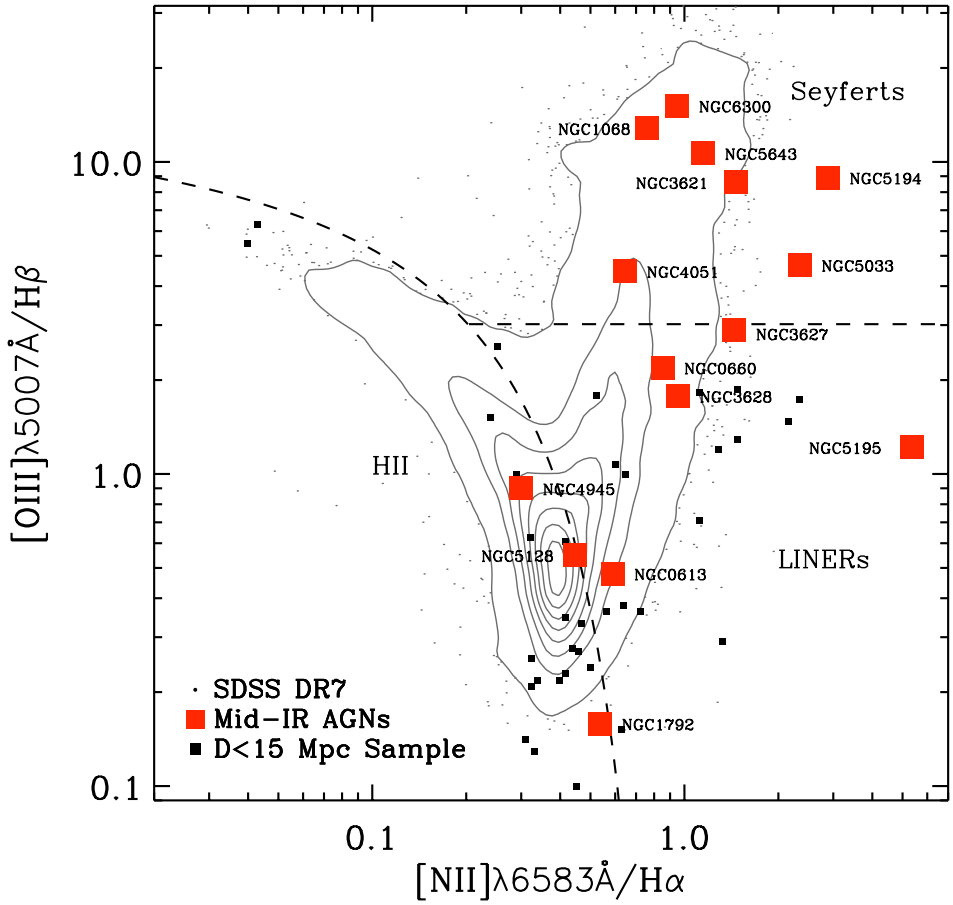

Figure 3.4: Emission-line diagnostic diagram showing [OIII]λ5007Å/Hβ versus [NII]λ6583Å/Hα for our $D < 15$ Mpc galaxy sample (squares) and the SDSS-DR7 (dots and contours). Kauffmann et al. (2003) demarcation lines are shown to isolate the Seyfert, LINER and star-forming HII regions (dashed lines). Those galaxies with 3σ [NeV] $\lambda 14.32$ μm detections (i.e., mid-IR identified AGNs) are labeled and highlighted with large squares. Seven of the $D < 15$ Mpc galaxies are optically classified as Seyferts, all of which are identified as mid-IR AGNs, while the other objects are optically classified either as HII galaxies or LINERs. Two additional mid-IR AGNs (NGC 1448; ESO121-G006) are not shown in the figure. NGC 1448 is classified as an HII galaxy (Veron-Cetty et al. 1986) but cannot be plotted on this figure since both [OIII]λ5007 and Hβ are undetected. ESO121-G006 lacks good-quality optical spectroscopy but since it is hosted in a highly inclined galaxy, it is likely to be an optically unidentified AGN; see § 3.3.3 and Fig. 3.10.

cent) and higher ($L_{IR} > 3 \times 10^{10} L_{\odot}$; $\approx 25^{+58}_{-21}$ percent) IR luminosity bins could be due to relatively weaker AGN sensitivity limits (i.e., a higher $L_{[NeV]}/L_{IR}$ emission-line ratio) and large uncertainties due to small-number statistics, respectively. Indeed, we find similar AGN fractions (of order ≈ 10 percent) in both the lower IR luminosity and moderate IR luminosity bins if we only consider AGNs identified with $L_{[NeV]}/L_{IR} < 10^{-5}$, suggesting that further AGNs remain to be detected in the lower IR luminosity; see Fig. 3.6. This may indicate that the overall AGN fraction in our IR-bright sample may be closer to ≈ 40 percent.

The large AGN fraction found in our study indicates a tighter connection between AGN activity and IR luminosity for galaxies in the local Universe than previously found, exceeding the AGN fraction obtained with optical spectroscopy by up-to an order of magnitude (e.g., compared to the results for $L_{IR} < 10^{11} L_{\odot}$ galaxies in Veilleux et al. 1999). This may indicate a close association between AGN activity and star formation, as is typically expected given the tight relationship between SMBH and spheroid mass in the local Universe (e.g., Magorrian et al. 1998; Gebhardt et al. 2000). There are probably two reasons why we identify a significantly larger AGN fraction than previously found: (1) mid-IR spectroscopy provides a more sensitive probe of AGN activity than optical spectroscopy, and (2) our galaxies are very nearby, allowing us to identify faint AGN signatures.

3.3.2 Why are AGN signatures often absent at optical wavelengths?

Of the seventeen galaxies in our $D < 15$ Mpc sample that unambiguously host AGN activity, ten ($\approx 60^{+25}_{-18}$ percent) lack AGN signatures at optical wavelengths. Here we explore the three most likely reasons why the AGN signatures are absent in the optical spectra of these galaxies: (1) the optically unidentified AGNs are intrinsically lower luminosity systems, (2) the optically unidentified AGNs have a larger fraction of star formation/stellar light that dilutes the optical AGN signatures, or (3) the optically unidentified AGNs are more heavily obscured at optical wavelengths.

3.3.2.1 Are optically unidentified AGNs intrinsically low luminosity?

The non detection of optical AGN signatures in the optically unidentified AGNs may be due to the AGNs being lower luminosity systems. In Fig. 3.7, we show the [NeV] $\lambda 14.32$ μm luminosities of the mid-IR identified AGNs and a sample of well-studied local

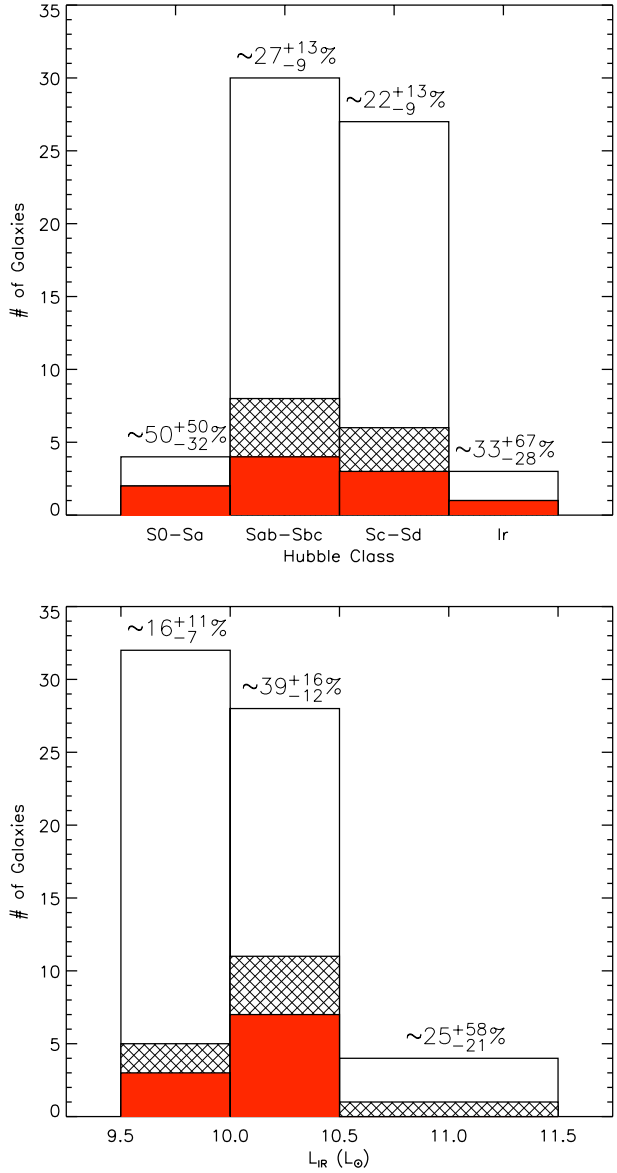

Figure 3.5: Fraction of AGNs identified in the $D < 15$ Mpc sample shown as a function of host-galaxy morphological classification and IR luminosity; the AGN fraction and associated 1σ errors are given for each sample bin. We further sub-divide the AGNs into [NeV] $\lambda 14.32\ \mu$m detected sources which are also optically observed to have AGN signatures (cross hatching), [NeV] $\lambda 14.32\ \mu$m detected sources which lack optical AGN signatures (solid colour), and combining these to give all galaxies with detected [NeV] $\lambda 14.32\ \mu$m emission, i.e. total number of AGN (cross-hatch+solid colour).

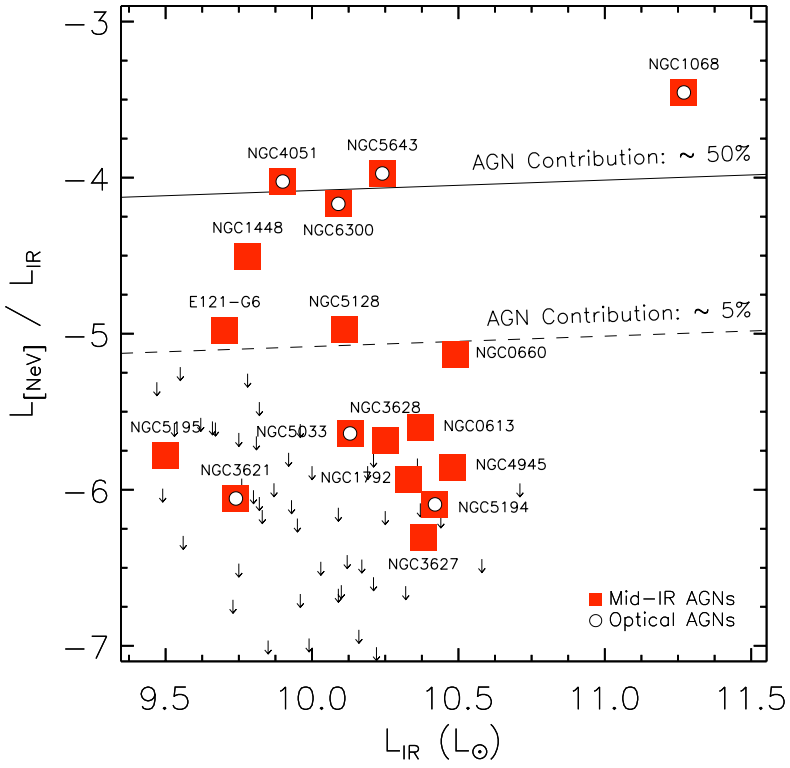

Figure 3.6: [NeV] $\lambda 14.32$ μm –IR luminosity ratio versus IR luminosity. Mid-IR identified AGNs (filled squares) and optically identified AGNs (open circles) are indicated. The solid and dashed lines show the expected luminosity ratio for a ≈ 50 percent and ≈ 5 percent AGN contribution to the IR emission, respectively; adapted from Satyapal et al. (2007). Both the optically identified and unidentified AGNs span a wide range of [NeV]–IR luminosity ratios. However, clearly the *Spitzer*-IRS observations are comparatively less sensitive towards the detection of [NeV] $\lambda 14.32$ μm emission in the lowest IR luminosity bin ($L_{IR} < 10^{10}$ $L_{\odot}$), indicating that the overall AGN fraction given in Fig. 3.5 should be considered a lower limit.

AGNs from Panessa et al. (2006) as a function of their [OIII] λ5007Å luminosity. We characterise the [NeV]–[OIII] luminosity relationship using a regressional fit.[7]

$$\log[\mathrm{NeV}] = (1.19 \pm 0.12)\log[\mathrm{OIII}] - (8.65 \pm 4.60) \quad (3.1)$$

The tightness in the [NeV]–[OIII] luminosity relationship indicates that the [NeV] luminosity provides a reliable measurement of the intrinsic luminosity of the AGN; the optically identified AGNs lie on this relationship if we correct the [OIII] luminosity for extinction as measured using the Balmer decrement (see § 3.3.2.3).

The optically identified AGNs in our sample cover a broader range of [NeV] $\lambda 14.32\ \mu\mathrm{m}$ luminosities than the optically unidentified AGNs ($\mathrm{L_{[NeV]}} \approx 10^{37}$–$10^{41}\ \mathrm{erg\,s^{-1}}$ and $\mathrm{L_{[NeV]}} \approx 10^{37}$–$10^{39}\ \mathrm{erg\,s^{-1}}$, respectively). However, since there are optically identified AGNs with similar luminosities to the optically unidentified AGNs, this indicates that the dominant reason for the non detection of the optically unidentified AGNs cannot be due to them hosting intrinsically lower-luminosity AGN activity. Fig. 3.7 also shows that the non identification of optical AGN signatures in the optically unidentified AGNs is not due to low-sensitivity optical spectroscopy since the [OIII]/[NeV] luminosity ratios are lower than that given in Equation 3.1.

3.3.2.2 Are optically unidentified AGNs star-formation dominated?

The non-identification of AGNs at optical wavelengths could be due to dilution from star-formation signatures, which we can test with our data. The mid-IR continua of starburst galaxies are typically characterised by strong PAH features at $\lambda \sim$ 3.3, 6.2, 7.7, 8.6, 11.3, 12.7, 14.2 and $17.0\ \mu\mathrm{m}$ combined with a steep spectral slope at far-IR ($\lambda > 25\ \mu\mathrm{m}$) wavelengths (Brandl et al., 2006). By contrast, PAH features tend to be weak or absent in AGN-dominated systems (e.g., NGC 1068; Rigopoulou et al. 2002). It is apparent from the *Spitzer*-IRS spectroscopy presented in Fig. 3.3 and 3.2, that most of the optically unidentified AGNs exhibit star-formation signatures at mid-IR wavelengths, indicating that they host joint AGN–starburst activity. However, to test whether the lack of AGN signatures at optical wavelengths is due to dilution from star-formation, we need to compare the relative AGN–star-formation contributions for both the optically identified and unidentified AGNs.

[7]The fit to the data was obtained using the IDL-based robust bi-sector linefit algorithm ROBUST_LINEFIT.

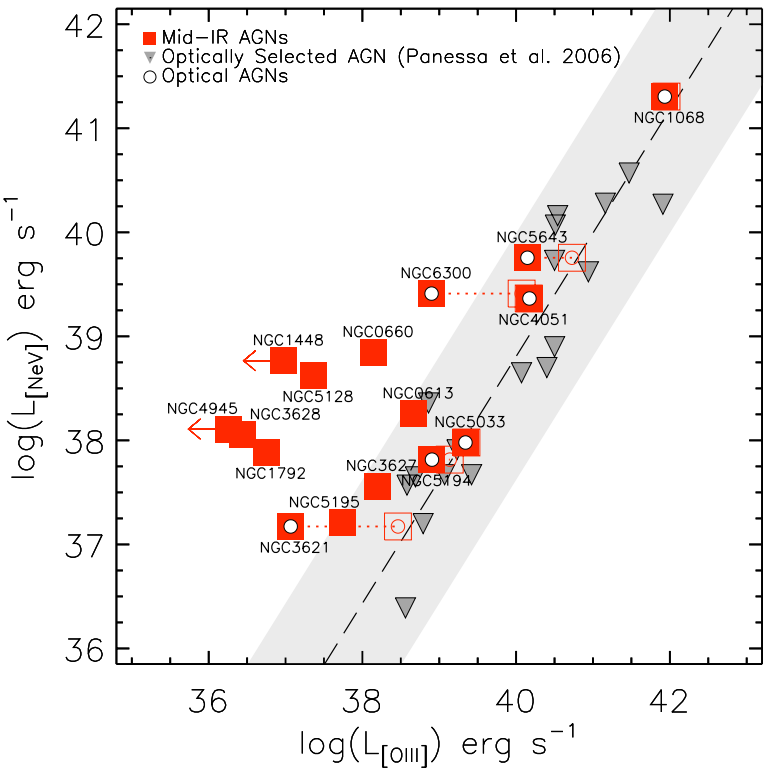

Figure 3.7: [NeV] $\lambda 14.32\ \mu$m luminosity versus [OIII] $\lambda 5007$Å luminosity. Mid-IR identified AGNs (filled squares), optically identified AGNs (open circles), and optically selected AGNs from Panessa et al. (2006; filled triangles) are indicated. The [OIII] luminosities for the Panessa et al. (2006) AGNs are corrected for extinction, and the *Spitzer*-IRS data is reduced and analysed following § 3.2.2. The dashed line was obtained using a robust bi-sector linefit algorithm for the Panessa et al. (2006) sample (see Equation 3.1) and shows that the [NeV] $\lambda 14.32\ \mu$m luminosity provides a reliable measurement of the intrinsic luminosity of the AGN. The shaded region indicates the intrinsic scatter within the relation. The [NeV]–[OIII] luminosity ratios of the optically identified AGNs in our $D < 15$ Mpc sample are in good agreement with the [NeV]–[OIII] luminosity relationship when the [OIII] luminosities are corrected for extinction using the Balmer decrement (dotted lines; see § 3.3.2.3). Three of the optically unidentified AGNs (NGC 613, NGC 3627 and NGC 5195) are within the scatter of the relation indicating that these galaxies may not necessarily be extinguished in [OIII] flux, but could have enhanced Hβ flux from young stars as suggested in Figs. 3.8 and 3.9. The symbols have the same meaning as in Fig. 3.6.

As the sources in the sample are well resolved, we can use the *Spitzer*-IRS spectra to quantify the relative strengths of the star-formation and AGN activity in the circumnuclear regions of the mid-IR identified AGNs. Previous studies have shown that the equivalent width of the IR-detected PAH features at 6.2 and 7.7 μm are well correlated with the AGN-starburst activity occurring within a galaxy (e.g., Genzel et al. 1998; Laurent et al. 2000; Peeters et al. 2004; Dale et al. 2006). However, given the spectral coverage of the *Spitzer*-IRS spectroscopy for the $D < 15$ Mpc sample ($\lambda \sim 9.9$–37.2 μm), here we calibrate and use the equivalent width of the 11.3 μm PAH feature ($\mathrm{EW}_{11.3,\mathrm{PAH}}$, which is detected in every galaxy) to indicate the relative AGN–star-formation contribution of each galaxy. Martín-Hernández et al. (2006) find that for a starburst-dominated circumnuclear region $\mathrm{EW}_{11.3,\mathrm{PAH}}$ (100 percent SF) ≈ 0.7 μm. Comparing this to an AGN-dominated system (i.e., NGC 1068) we find $\mathrm{EW}_{11.3,\mathrm{PAH}}$ (100 percent AGN) ≈ 0.008 μm. The mid-IR emission line ratios can also be used to constrain the relative contributions of AGN and stellar emission (e.g., Dale et al. 2006). Since [NeII] $\lambda 12.82$ μm emission is primarily produced by star-formation activity within a galaxy, and [NeV] $\lambda 14.32$ μm is solely attributed to AGN activity, the ratio of these emission lines is also a strong tracer of the relative strengths of these two processes (e.g., Sturm et al. 2002).

In Fig. 3.8 we present the predicted $\mathrm{EW}_{11.3,\mathrm{PAH}}$ and [NeII] $\lambda 12.82$ μm – [NeV] $\lambda 14.32$ μm flux ratios for different AGN–star-formation contributions; this is similar in principal to the approach adopted by Genzel et al. (1998). Both of the AGN–star-formation ratio estimates are in good agremment for the majority of the mid-IR AGNs, with a mean dispersion of ≈ 20 percent. We note that the predicted AGN–star-formation contributions for four (≈ 25 percent) of the AGNs (NGC 1068, NGC 4051, NGC 5128 and NGC 5643) differ by more than a factor of two from the mixing model, whilst the other mid-IR identified AGNs lie within a factor of 40 percent. One of these such outliers is the FR-1 radio galaxy, NGC 5128 ($\mathrm{EW}_{11.3,\mathrm{PAH,model}} > 4\times\mathrm{EW}_{11.3,\mathrm{PAH,obs}}$), which could be due to dilution of the PAH feature by an underlying synchrotron component (related to the radio emission) that is emitting at mid-IR wavelengths. On the basis of Fig. 3.8, the IR emission for five (29^{+20}_{-13} percent) of the mid-IR identified AGNs (NGC 1068, NGC 6300, NGC 4051, NGC 5643 and NGC 1448) has a significant contribution from AGN activity (> 25 percent), only one of which is an optically unidentified AGN (NGC 1448). As may be expected, these five galaxies also host the most luminous AGNs, as shown in Fig. 3.7. The IR emission for the other twelve ($\approx 71^{+26}_{-20}$ percent) mid-IR identified AGNs appears to be star-formation dominated (AGN contribution < 25 percent), nine of which are op-

tically unidentified AGNs. These analyses have been performed using the SH module of *Spitzer*-IRS, which traces only the circumnuclear region of these galaxies. However, we get qualitatively similar results if we consider the $L_{[\mathrm{NeV}]}/\mathrm{L_{IR}}$ ratios, which should provide a measure of the contribution of the AGN to the *total* IR luminosity of the galaxy (i.e., as measured by *IRAS*); see Fig. 3.6.

On the basis of these analyses we therefore conclude that relative AGN–star-formation contributions cannot give a complete explanation for the lack of optical AGN signatures. Clearly, there is a difference in the distribution of relative AGN–star formation strengths, with the optically unidentified AGNs being typically more star-formation dominated than the optically identified AGNs. However, since approximately half of the optically identified AGNs are also star-formation dominated, dilution from star-formation signatures is unlikely to be the dominant cause for the lack of optical AGN signatures in all of the optically unidentified AGNs. Indeed, as we show in § 3.3.2.3 and § 3.3.3, strong Hβ emission produced by young stars is likely to be the primary reason for the lack of AGN optical signatures (i.e., a low [OIII]–Hβ ratio) in only three of the optically unidentified AGNs.

3.3.2.3 Are optically unidentified AGNs heavily dust obscured?

The dominant reason for the lack of AGN optical signatures could be due to dust obscuration. A good measure of dust obscuration within a host galaxy is the so-called Balmer decrement (the Hα/Hβ flux ratio; e.g., Ward et al. 1987; see section 1.4). In Table 3.1 we show that both the optically identified and optically unidentified AGNs cover similar ranges in Balmer decrements (Hα/Hβ $\approx$ 3–7 and 2–13, respectively), apparently indicating no difference in optical extinction between the two populations. However, many late-type galaxies are found to be very dust/gas rich, and for galaxies such as these, the Balmer decrement may be a poor measure for high-levels of extinction or it may not trace a direct line-of-sight to the AGN. For example, NGC 4945 is an optically unidentified AGN (optically classified as an HII galaxy), and using analyses at near-IR wavelengths it is estimated to have a V-band extinction of $A_V \approx 6$–20 magnitudes (Moorwood et al., 1996); however, the optical Balmer decrement of the galaxy would suggest that it is relatively unobscured ($A_V \approx 0$ mags). To remove this ambiguity of additional attenuation to the optical emission and provide a more direct line-of-sight to the AGN, we require a measure of dust-obscuration that is capable of probing greater optical depths than optical spectroscopy alone.

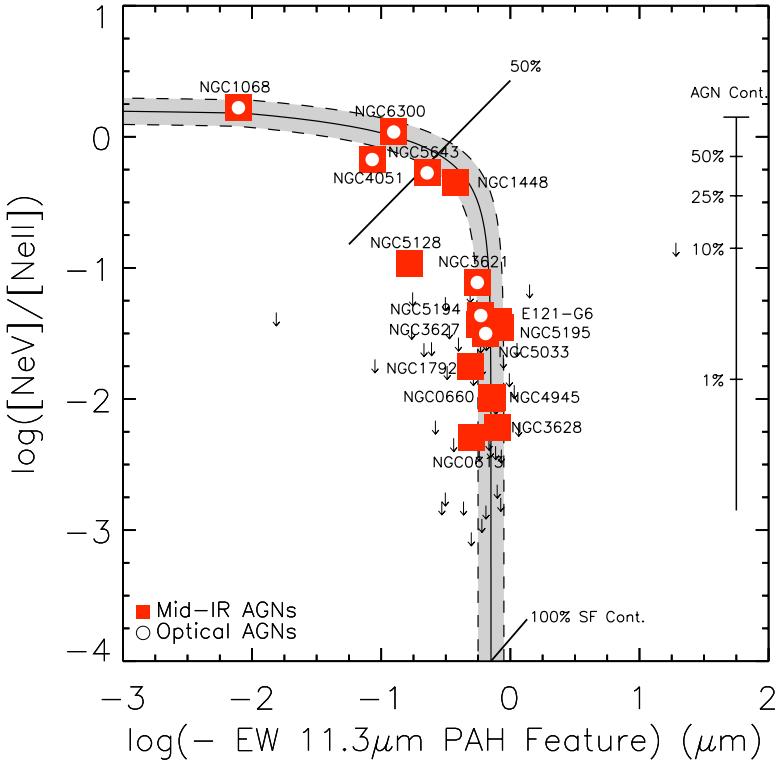

Figure 3.8: Flux ratio of the [NeV] $\lambda 14.32\ \mu$m and [NeII] $\lambda 12.82\ \mu$m emission lines versus equivalent width of the $11.3\ \mu$m PAH feature ($EW_{11.3,PAH}$). Both the $EW_{11.3,PAH}$ and the [NeV]–[NeII] flux ratio give relative measures of the AGN–starburst contribution. The vertical scale indicates the fraction of AGN activity for the [NeV]–[NeII] flux ratio (Sturm et al., 2002). A linear mixing model curve (solid line) and 0.1 dex errors (dashed) are shown: a 100% AGN is assumed to have [NeV]/[NeII] ~ 1.4, $EW_{11.3,PAH} \sim 0.008\ \mu$m, while a 100% starburst is assumed to have [NeV]/[NeII] ~ 0.001, $EW_{11.3,PAH} \sim 0.7\ \mu$m.

Here we estimate the extinction towards the AGNs using [OIV] $\lambda 25.89\ \mu$m at mid-IR wavelengths and [OIII] $\lambda 5007$Å at optical wavelengths.[8] [OIV] $\lambda 25.89\ \mu$m has often been used as a relatively dust-obscuration independent indicator of the AGN luminosity (e.g., Genzel et al. 1998; D06), and we show in § 3.3.4 that it is reliable for [NeV]–identified AGNs; however, see § 3.3.4 for caveats in using [OIV] $\lambda 25.89\ \mu$m to directly identify AGN activity. By contrast, the optically detected [OIII] $\lambda 5007$Å emission lines produced in the narrow-line regions of AGNs can be subject to strong reddening by dust/gas, and therefore the [OIV]–[OIII] emission-line ratio should provide a good indicator for the presence of heavy obscuration. There could be some dependence of the [OIV]–[OIII] ratio on the hardness of the radiation field (e.g., as measured using the [NeIII]–[NeII] ratio; Brandl et al. 2006); however, as we show below, we find no strong dependence in our sample.

In Fig. 3.9 we relate the two different measures of dust-extinction within the host galaxies obtained using the Balmer decrement and our [OIV]–[OIII] flux ratio estimate. We calibrate the extinction correction factor in A_V magnitudes by assuming $f_{[\mathrm{OIII}]} \propto {f_{[\mathrm{OIV}]}}^{1.8}$, as found for Seyfert 2 galaxies (e.g., Meléndez et al. 2008a), combined with the expected dust-reddening at $\lambda \approx 5007$Å and $25.9\ \mu$m (e.g., Osterbrock and Ferland 2006). Although the [OIII] emission-line constraints are typically obtained in a narrower slit than the [OIV], since the majority of the [OIII] and [OIV] emission is likely to be produced close to the AGN (i.e., the ionising source), aperture effects are unlikely to be significant. Good agreement in the levels of optical extinction are found for the optically identified AGNs on the basis of both the Balmer decrement and the [OIV]–[OIII] flux ratios, implying moderate levels of dust obscuration ($A_V \sim 0$–3 mags). However, by contrast, although optically unidentified AGNs have similar Balmer decrements to the optically identified AGNs, many have significantly higher [OIV]–[OIII] flux ratios. This suggests that the optically unidentified AGNs are so heavily extincted at optical wavelengths the Balmer decrement no longer provides a reliable estimate of the amount of obscuration or a direct line-of-sight to the AGN, suggesting $A_V > 3$ mags. Indeed, on the basis of the [OIV]–[OIII] flux ratio for NGC 4945 we estimate that the AGN is obscured behind a screen of $A_V \sim 9$ magnitudes, which is in good agreement with the de-

[8] We note that it would also be useful to determine the amount of extinction using the [NeV] emission lines at $14.32\ \mu$m and 3426Å. Unfortunately, this is not currently possible due to the lack of available data at ultra-violet wavelengths for the majority of our sample. Also, the intrinsic ratio is dependent on temperature variations of the photoionised gas within the narrow line region of the AGN.

tailed constraints of Moorwood et al. (1996). Additionally, the extinction estimated from the [OIV]–[OIII] flux ratio ($A_V \sim 5$ magnitudes) for NGC 5128 is in good agreement with the value derived by Alexander et al. (1999) from near-IR spectroscopy ($A_V \sim 7$ magnitudes). We also find that if the [OIII] emission was adjusted for the additional absorption within the narrow line region (NLR) found by our diagnostic, these heavily extinguished optically unidentified AGNs would be moved into the Seyfert region of an optical BPT diagram. For example, assuming there is no further reddening to the Hβ emission, an additional NLR extinction of $A_V \sim 3$ is consistent with an increase by a factor of 6 in [OIII] flux (i.e., the correction required for NGC 5128 to be optically classified as a Seyfert galaxy; see Fig. 3.4).

In Fig. 3.7, we show that three of the optically unidentified AGNs (NGC 0613, NGC 3627 and NGC 5195) are within the intrinsic scatter of the [OIII]-[NeV] relation (shaded region), and consequently do not appear to be deficient in [OIII] flux. Indeed, in Fig. 3.9 we find that these particular objects do not appear to be heavily extinguished at optical wavelengths ($A_V < 3$ mags). It is therefore likely that these are not classified as AGNs in optical surveys due to enhanced Hβ flux from young stars, which lowers their [OIII]/Hβ flux ratios in the BPT diagram (see Fig. 3.4). This is in agreement with the AGN–star-formation ratios estimated for these objects with *Spitzer*-IRS; see Fig. 3.8. However, it is clear from Figs. 3.7 and 3.9 that the majority of the optically unidentified AGNs are highly extinguished in [OIII] λ5007Å flux.

3.3.3 First-order constraints on the source of the optical extinction

The obscuration towards some of the AGNs implied by Figs. 3.7 and 3.9 may be due to either a dusty torus (as predicted by the unified model for AGNs; e.g., Antonucci 1993; see section 1.2) or extinction through the host galaxy (e.g., Malkan et al. 1998; Matt 2000). Here we can test the latter hypothesis by looking for evidence of host-galaxy extinction (i.e., a highly inclined galaxy or obscuring dust lanes) using available optical imaging. To test the former hypothesis we would require sensitive X-ray observations for all of the AGNs identified in our sample; given the predicted intrinsic luminosity for some of these AGNs, they would require unfeasibly long exposures (of the order ≈ 100 kiloseconds) to identify the central source.

In Fig. 3.10 we show the optical images of the optically identified and optically unidentified AGNs. It is clear that the optically identified AGNs in our sample are hosted by relatively face-on galaxies while, by contrast, many of the optically uniden-

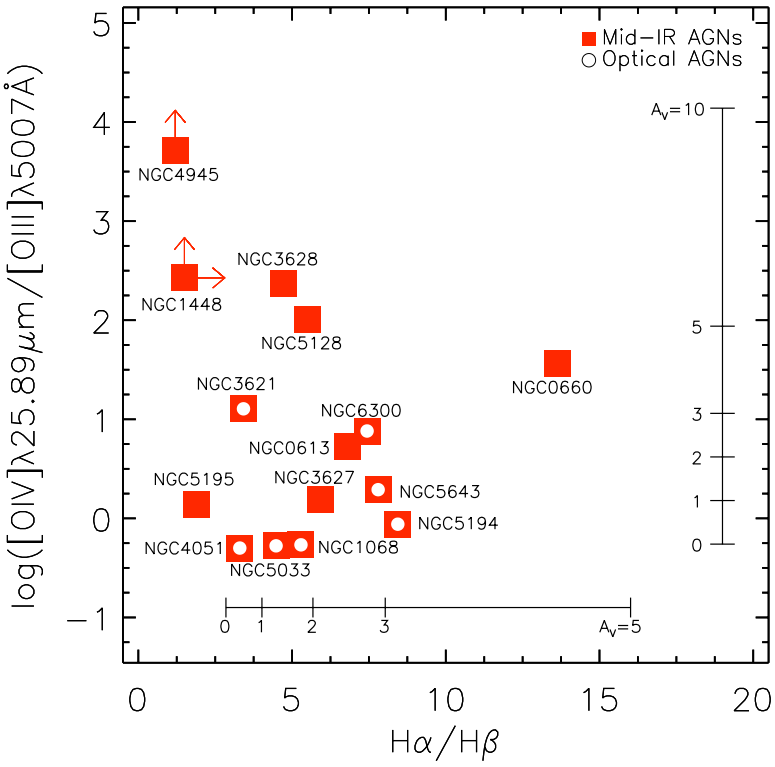

Figure 3.9: [OIV] λ25.89 μm and [OIII] λ5007Å flux ratio versus Balmer decrement (Hα/Hβ flux ratio). These ratios are indicators of the relative dust/gas extinction within the host galaxies, although the [OIV]–[OIII] flux ratio should be more sensitive towards high levels of extinction and provide a more direct probe of the extinction along the line-of-sight towards the NLR (see § 3.3.2.3); the solid lines indicate the relationship between the flux ratios and extinction in A_V. The symbols have the same meaning as in Fig. 3.6.

tified AGNs are hosted in either highly inclined galaxies or have dust lanes that obscure the central regions. Indeed, the four optically unidentified AGNs with the highest [OIV]–[OIII] flux ratios, which imply $A_V > 3$ mags, are all hosted by galaxies that are either highly inclined or have obscuring dust lanes; ESO121-G006 does not have good-quality optical spectroscopy, however, since it resides in a highly inclined host galaxy, it is likely to be an optically unidentified AGN with a high [OIV]–[OIII] flux ratio. Furthermore, three of the optically unidentified AGNs are found to be hosted in relatively face-on galaxies (NGC 0613, NGC 3627 and NGC 5195), similar to that of the optically identified AGNs, suggesting there is little extinction from the host galaxy towards these AGNs. This is consistent with our findings in the previous section that these galaxies do not appear to have heavily extinguished [OIII] emission (see Fig. 3.7).

Our findings extend the analyses of Malkan et al. (1998), who found that dust lanes can dictate the observed optical AGN type, by now showing that the host galaxy can have a large effect on even the *identification* of AGN activity. We find that four ($\approx 40^{+31}_{-19}$ percent) of the ten optically unidentified AGNs reside in highly inclined galaxies, compared to ≈ 4 percent (Sy1) and ≈ 7 percent (Sy2) of the optically identified AGNs in Malkan et al. (1998), respectively. Four ($\approx 40^{+31}_{-19}$ percent) of the optically unidentified AGNs also appear to have obscuring dust lanes, compared to ≈ 10 and ≈ 20 percent of the Sy1 and Sy2 galaxies in Malkan et al. (1998), respectively.[9] Whilst these findings are empirical and may be subject to small number statistics, there appears to be strong evidence to suggest that the non-identification of optical AGN signatures in the majority of these galaxies is due to extinction through the host galaxy, indicating that obscuration of the nucleus is not necessarily due to an obscuring torus. We also note that similar conclusions have been proposed for the non-identification of optical AGN signatures in $z \approx 0.5$–1 X-ray identified AGNs (e.g., Rigby et al. 2006).

3.3.4 Can further AGNs be identified using other mid-IR emission-line diagnostics?

In our analyses thus far we have conservatively identified AGNs using the [NeV] $\lambda 14.32$ μm emission line. However, there may be further AGNs in our sample that can be identified using different mid-IR emission lines. Other studies have used the high-excitation emission line [NeV] $\lambda 24.32$ μm, as well as intermediate-excitation emission lines such as [OIV]

[9] We note that high spatial-resolution *HST* observations are required for the optically unidentified AGNs to provide a consistent comparison to Malkan et al. (1998).

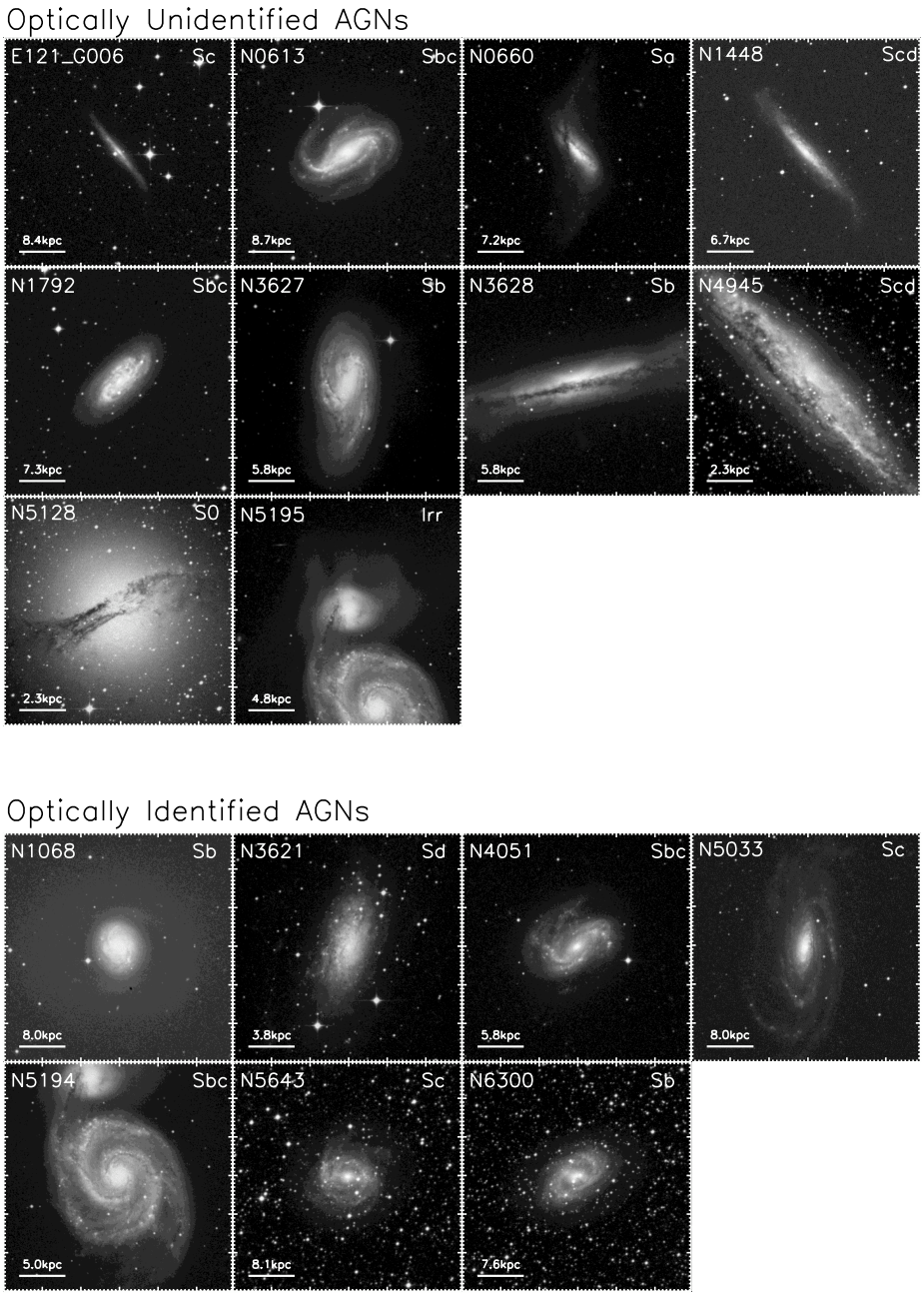

Figure 3.10: 10×10 arcmin ESO Digital Sky Survey images (combined B and R band) of the optically unidentified and optically identified AGNs. Optically unidentified AGNs are generally found to be hosted in either highly inclined galaxies (E121-G006, NGC 660, NGC 1448, NGC 3628 and NGC 4945) or galaxies with obscuring dust lanes (NGC 1792, NGC 3628, NGC 4945 and NGC 5128). This suggests that the lack of optical AGN signatures in these galaxies could be due to extinction through the host galaxy, indicating that obscuration of the nucleus is not necessarily due to an obscuring torus. Three of the optically unidentified AGNs (NGC 613, NGC 3627 and NGC 5195) appear to be hosted in relatively face-on galaxies; we suggest that the AGN optical signatures are diluted in these galaxies due to strong star-formation activity (see § 3.3.2.2).

$\lambda 25.89$ μm (54.9 eV) and [NeIII] $\lambda 15.56$ μm (41.0 eV). To explore whether we can identify further AGNs in our sample, we investigate these other potential AGN indicators here.

[NeV] $\lambda 24.32$ μm has the same ionisation potential as [NeV] $\lambda 14.32$ μm but it has a higher critical electron density ($n_e \approx 5 \times 10^5$ versus $n_e \approx 5 \times 10^4$ cm^{-3}; Sturm et al. 2002). [NeV] $\lambda 24.32$ μm is detected in 11 of the 64 galaxies in our sample, all of which are also detected at [NeV] $\lambda 14.32$ μm. The smaller AGN identification fraction found using [NeV] $\lambda 24.32$ μm may be due to the lower relative sensitivity of data in the LH module in some cases. We also note that a large number of pixels around $\lambda \approx 24.3$ μm were damaged by solar flares early in the *Spitzer* mission, and are flagged by the *Spitzer* pre-processing pipeline as either damaged or unreliable ('hot' pixels). In our custom reduction pipeline we removed these pixels from the analysis and fitting routines to reduce the potential for spurious detections. For example, from analysis of the BCD images for NGC 3938 before and after cleaning using a custom version of IRSCLEAN, we find that the possible [NeV] $\lambda 24.32$ μm emission reported by S08 falls below our detection threshold of 3σ. Furthermore, an additional 'hot' pixel at $\lambda \sim 24.3594$ μm (in the observed frame) is not removed by default in IRSCLEAN due to the high incidence of adjacent cleaned pixels. During the reduction process, care must be taken to remove such pixels to ensure reliable detections. Additionally, we do not find any further AGNs in our $D < 15$ Mpc sample on the basis of the [NeV] $\lambda 24.32$ μm emission line and urge caution when identifying AGNs at low redshifts (i.e., $z \lesssim 0.005$) solely on the detection of weak [NeV] $\lambda 24.32$ μm emission in high-resolution *Spitzer*-IRS observations. Certainly, at higher redshifts (i.e., where the observed [NeV] $\lambda 24.32$ μm emission is not affected by the spurious pixels at $\lambda \sim 24.35$ μm) detections of weak [NeV] $\lambda 24.32$ μm without complimentary [NeV] $\lambda 14.32$ μm will be possible for systems with high levels of relative dust extinction; however, this is likely to be rare as $A_{14.32}/A_{24.32} \sim 1.03$ (Chiar and Tielens, 2006).

[OIV] $\lambda 25.89$ μm is often attributed to AGN activity. However, since it is an intermediate excitation emission line it can also be detected in galaxies experiencing heightened starburst activity (D06). [OIV] $\lambda 25.89$ μm is detected in 41 of the 64 galaxies in our sample, including all of the 17 AGNs identified using [NeV]. For the mid-IR identified AGNs, we find that [OIV] $\lambda 25.89$ μm and [NeV] $\lambda 14.32$ μm emission are well correlated, suggesting that [OIV] $\lambda 25.89$ μm is a good proxy for the intrinsic AGN luminosity in [NeV]–identified AGNs; see Fig. 3.11. The regressional fit is characterised by the equation given below, with a spread in the data of only 0.24 dex (see also Footnote 9). We highlight the caveat that this relation may only hold for the emission-line and IR lumi-

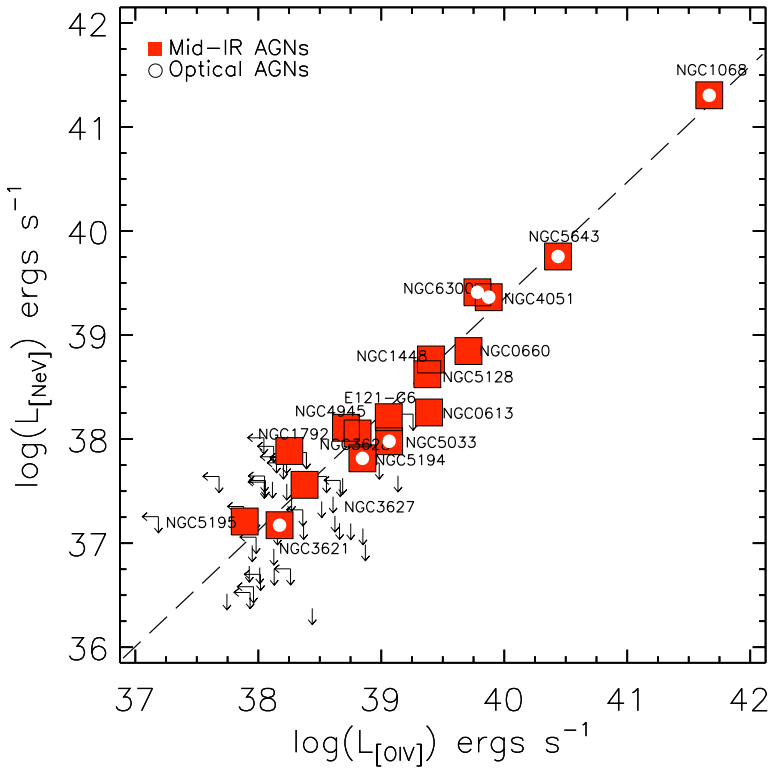

Figure 3.11: [NeV] $\lambda 14.32\ \mu$m luminosity versus [OIV] $\lambda 25.89\ \mu$m luminosity. The dashed line was obtained using a robust bi-sector linefit algorithm and indicates that for [NeV]–detected objects, [OIV] $\lambda 25.89\ \mu$m provides a good proxy for the intrinsic luminosity of the AGN (see Equation 3.2) for those galaxies with $10^{39} < \mathrm{L}_{[\mathrm{OIV}]} < 10^{42}\,\mathrm{erg\,s^{-1}}$. The symbols have the same meaning as in Fig. 3.6.

nosity range explored here. However, using a sample of AGNs which is a factor ≈ 3 greater than that considered here, Weaver et al. (2010) find a consistent relation with that derived in this work.

$$\log[\mathrm{NeV}] = (1.09 \pm 0.06)\,\log[\mathrm{OIV}] - (4.34 \pm 2.53) \tag{3.2}$$

Our finding of a tight relationship between [OIV] $\lambda 25.89\ \mu$m and [NeV] $\lambda 14.32\ \mu$m suggests that any AGN activity with bright [NeV] $\lambda 14.32\ \mu$m emission should also have bright [OIV] $\lambda 25.89\ \mu$m emission. Contrary to this, S08 identified two AGNs (NGC 4321 and NGC 4536) using [NeV] $\lambda 14.32\ \mu$m that had undetected [OIV] $\lambda 25.89\ \mu$m emission. NGC 4536 is present in our sample but we do not identify [NeV] $\lambda 14.32\ \mu$m using our conservative reduction and analysis techniques. Four of the galaxies (IC2056; NGC 3175; NGC 3184; NGC 3368) in our sample with [OIV] $\lambda 25.89\ \mu$m detections lie above the regressional fit in Fig. 3.11 and more sensitive mid-IR spectroscopy may identify AGN activity with [NeV] $\lambda 14.32\ \mu$m in these systems. A further 20 galaxies undetected in [NeV] $\lambda 14.32\ \mu$m lie below the regressional fit and, therefore, unless AGNs can have weak [NeV] $\lambda 14.32\ \mu$m and bright [OIV] $\lambda 25.89\ \mu$m emission (contrary to that found here and in Weaver et al. 2010), these do not appear to host AGN activity. However, we note that the 13 galaxies in our sample that are undetected in both [OIV] $\lambda 25.89\ \mu$m and [NeV] $\lambda 14.32\ \mu$m may host AGN activity substantially below our detection limits. Furthermore, for galaxies with $\mathrm{L}_{[\mathrm{OIV}]} < 10^{39}\,\mathrm{erg\,s^{-1}}$, the source of the [OIV] emission becomes uncertain as a non-negligible fraction may be produced by star formation (e.g., the starburst–AGN, NGC 4945). Therefore, the [OIV] emission may not be a strong tracer of the intrinsic luminosity of the AGN (i.e., the [NeV] luminosity) for galaxies with $\mathrm{L}_{[\mathrm{OIV}]} \ll 10^{39}\,\mathrm{erg\,s^{-1}}$. Further probes of the AGN luminosity (e.g., hard X-ray luminosities) are required to test this further.

[NeIII] $\lambda 15.56\ \mu$m is also an intermediate excitation emission line and could be produced by AGN or star-formation activity. Previous surveys (e.g., Farrah et al. 2007; Groves et al. 2008; Meléndez et al. 2008b) have selected potential AGNs on the basis of high [NeIII]–[NeII] flux ratios ([NeIII]/[NeII]> 1.03; Meléndez et al. 2008b). In Fig. 3.12 we show that while this diagnostic identifies many of the AGN-dominated systems in our sample, it does not find all of the AGNs. The production of [NeIII] appears to be complex and may have strong dependences on star-formation, gas density, temperature, metallicity and AGN activity (Brandl et al. 2006); for example, there is a similar range of [NeIII]–[NeII] ratios for both the optically unidentified AGNs and the galaxies without

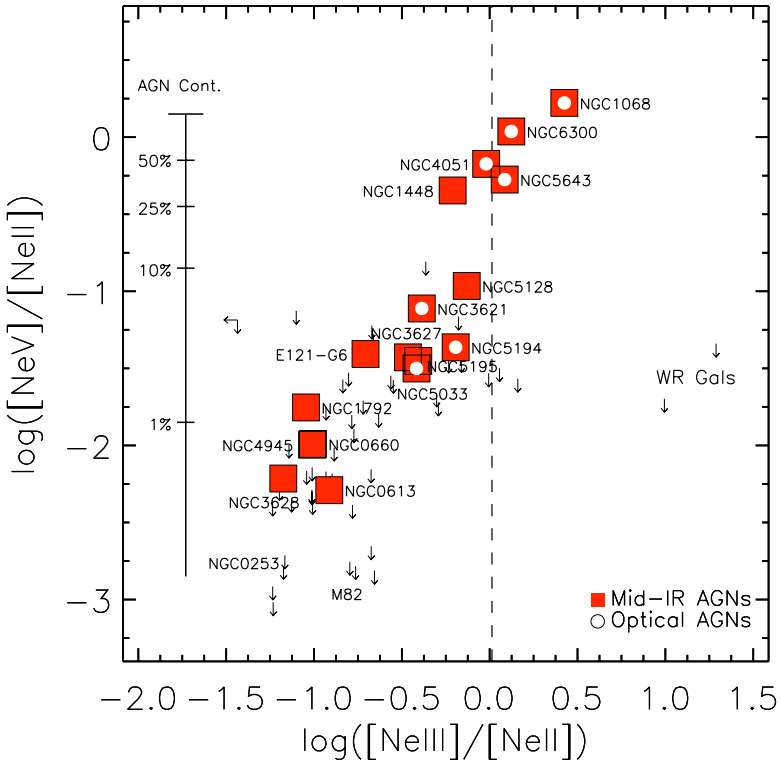

Figure 3.12: Logarithm of the ratio of the fluxes of [NeIII] $\lambda 15.51$ μm and [NeII] $\lambda 12.82$ μm emission lines are plotted against the logarithm of the ratio of the fluxes of [NeV] $\lambda 14.32$ μm and [NeII] $\lambda 12.82$ μm emission lines. The dashed line represents the demarcation for Seyfert 2 galaxies given in Melendez et al. (2008). Those AGNs which dominate the luminosity output of the galaxy have preferentially higher [NeIII]/[NeII] ratios, and appears to be a good proxy for AGN activity in these cases; however, we note that WR-galaxies can also have large [NeIII]/[NeII] ratios. By contrast, lower luminosity AGNs exhibit similar ratios to that of star-forming galaxies. The symbols have the same meaning as in Fig. 3.6.

clear signatures of AGN activity. Furthermore, the two WR galaxies in our sample also have high [NeIII]–[NeII] flux ratios, suggesting that further criteria (e.g., optical data; [NeV]/[NeII] ratio) are required to unambiguously identify AGN activity. However, three of our galaxies not identified as AGNs (NGC 4490; NGC 4736; NGC 6744) have high [NeIII]–[NeII] flux ratios and may host AGN activity below our [NeV] $\lambda 14.32$ μm sensitivity limit.

3.4 Summary

In this chapter we have presented the initial results of a sensitive volume-limited *Spitzer*-IRS spectral survey of all ($\approx$ 94 percent) bolometrically luminous ($L_{IR} \gtrsim 3 \times 10^9 L_\odot$) galaxies to $D < 15$ Mpc. We place direct constraints on the ubiquity of AGN activity in the local universe. Our main findings are the following:

(1). By conservatively assuming that the detection of the high-excitation [NeV] $\lambda 14.32$ μm emission line indicates AGN activity, we identified AGNs in 17 of the 64 galaxies in our sample. This corresponds to an AGN fraction of $\approx 27^{+8}_{-6}$ percent, a factor $\gtrsim 2$ greater than found using optical spectroscopy alone; further AGNs are likely to be identified below our [NeV] $\lambda 14.32$ μm sensitivity limit. The large AGN fraction indicates a tighter connection between AGN activity and IR luminosity for galaxies in the local Universe than previously found, potentially indicating a close association between AGN activity and star formation.

(2). We explored whether the absence of optical AGN signatures in the optically unidentified AGNs is due to either an intrinsically low-luminosity AGN or dilution from star formation. We found that the optically unidentified AGNs are typically characterised as star-formation dominated galaxies hosting modest-luminosity AGNs ($L_{[NeV]} \approx 10^{37}$–$10^{39}$ erg s^{-1}). However, since about half of the optically identified AGNs also have these properties, it appears unlikely that the dominant reason for the absence of optical AGN signatures is due to either (a) an intrinsically low-luminosity AGN or (b) strong star-formation dilution. Indeed, we find that only three of the optically unidentified AGNs may have enhanced Hβ emission from young stars which could dilute the optical AGN signatures. We also showed that the absence of optical AGN signatures is not due to low-sensitivity optical data. See § 3.3.2.1, § 3.3.2.2, & § 3.3.2.3.

(3). We explored whether the absence of optical AGN signatures in the optically unidentified AGNs is due to optical extinction. We found that the optically unidentified AGNs typically have larger [OIV] $\lambda 25.89$ μm–[OIII] $\lambda 5007$Å flux ratios than the optically identified AGNs, indeed suggesting that their emission is typically heavily extinguished at optical wavelengths ($A_{\rm V} \approx$ 3–9 mags). Examination of optical images revealed that seven of the optically unidentified AGNs are hosted in highly inclined galaxies or galaxies with dust lanes, indicating that obscuration of the AGN is not necessarily due to an obscuring torus. See § 3.3.2.3 and § 3.3.3.

We therefore conclude that optical spectroscopic surveys miss approximately half of the AGN population mostly due to extinction through the host galaxy. Sensitive X-ray observations are required to determine what fraction of the optically unidentified AGNs are heavily obscured due to nuclear obscuration intrinsic to the AGN.

Chapter 4

The incidence of growing black holes to $D < 15$ Mpc

This chapter is based on the work published in Goulding et al. (2010).

4.1 Introduction

While optical emission-line diagnostics alone cannot reliably characterise the properties of a non-negligable fraction of the AGN population, they are readily characterised at obscuration independent wavelengths (e.g., X-ray; mid-IR). Hence, the identification of AGNs made at X-ray and mid-IR wavelengths complements traditional UV/optical methods to yield a more complete census of AGN activity. In the previous chapter (see also Goulding and Alexander 2009; hereafter, GA09), we concluded that ≈ 50 percent of AGNs are missed (even at $D < 15$ Mpc) in sensitive optical surveys simply due to host-galaxy extinction. Furthermore, ≈ 30 percent of the optically unidentified AGNs were found to reside in late-type spiral galaxies (Sc–Sd; i.e., those likely to host the smallest SMBHs, $\mathrm{M_{BH}} \approx 10^{6}\,\mathrm{M_{\odot}}$). With the inclusion of these new optically unidentified AGNs, it is natural to ask, what are the masses of local active SMBHs, what are their Eddington ratios, and hence, how rapidly are these SMBHs growing in the local Universe?

In this chapter, we investigate the growth rates and space density of actively accreting SMBHs using the 17 AGNs identified in the volume-limited survey of GA09. Whilst the source statistics considered here are significantly smaller than those studies using the SDSS (e.g., H04; Schawinski et al. 2007), this work compliments previous studies by (1) significantly improved data quality over a broader wavelength range, and (2)

including a relatively large number (given the considered small volume) of optically unidentified AGNs which would not be reliably identified or characterised in the SDSS survey. Furthermore, by including a significant population of bolometrically luminous (but dust-obscured) late-type spiral galaxies (Sc–Sd) we are able to extend the SMBH density function to $\mathrm{M_{BH}} \lesssim 10^7\,\mathrm{M_\odot}$ further extending beyond the previous work of H04.

As many of the late-type spiral galaxies in the GA09 sample are predicted to host small galactic bulges, and hence comparatively low mass SMBHs, particular attention is paid to obtaining accurate mass estimates. Given their proximity, many of the sources in GA09 are well-studied and have multiple estimates of SMBH mass ($\mathrm{M_{BH}}$) from a variety of methods (i.e., reverberation mapping techniques; mapping of water maser spots; gas kinematical estimates; the M–σ_* relation; correlation of $\mathrm{M_{BH}}$ with the luminosity of the galactic bulge); we discuss the relative accuracy of each SMBH mass estimate technique in Section 4.3.1. Furthermore, to determine the relative mass accretion rates, and hence average growth times of the SMBHs in our sample, we require the best available estimates of the AGN bolometric luminosity ($L_{\mathrm{Bol,AGN}}$). Here we adopt two approaches: 1) for the AGNs with currently published data, we use high-quality well-constrained sensitive hard X-ray (2–10 keV) luminosities to directly measure $L_{\mathrm{Bol,AGN}}$; and 2) we accurately infer $L_{\mathrm{Bol,AGN}}$ using a well-constrained hard X-ray to high-ionisation mid-IR emission line relation. Using our well-defined estimates for SMBH mass and AGN bolometric luminosity, we then investigate the relative mass accretion rates of our sample of active SMBHs. We use these estimates to provide new constraints on the volume-average SMBH growth rates in the local Universe. We further compare these results to the previous works of H04 and Greene and Ho (2007) by producing a local AGN population density function.

4.2 The Sample

4.2.1 Selection and Data-reduction

The sample of local AGNs is derived from the *Spitzer*-IRS spectral investigation of a volume-limited sample of IR-bright galaxies to $D < 15$ Mpc by GA09 (see Chapter 3): High-resolution *Spitzer*-IRS spectroscopy ($R \sim 600$) was obtained for sixty-four of the sixty-eight (≈ 94 percent) galaxies detected in the RBGS with $\mathrm{L_{IR}} \gtrsim 3 \times 10^9\,\mathrm{L_\odot}$ within the considered volume. A particular advantage to a volume-limited sample is that, unlike magnitude-limited surveys, they do not suffer from radial selection effects and thus can

be used to construct volume-averaged statistics. By contrast, volume-limited samples yield limited source number statistics due to their inability to probe both the faintest and most luminous systems. We remind the reader than unlike many other local surveys, to $D < 15$ Mpc our sample does not include galaxies from local over densities such as the Virgo cluster at $D \sim 16$ Mpc (see § 4.5.4.1 for a detailed analysis and validation of the considered space-volume in this survey).

The *Spitzer*-IRS spectroscopic data presented in GA09 was reduced using a custom IDL pipeline which utilises the *Spitzer* Science Center data-processing packages SPICE, IRSCLEAN and CUBISM. For further detailed information on the reduction processes and spectral analyses see Chapters 2 and 3 of this thesis and §§2.1 and 2.2 of GA09 and references there-in. The mid-IR spectra of seventeen of the sixty-four galaxies ($\approx 27^{+8}_{-6}$ percent) presented in the previous chapter (see also GA09) were found to contain the [NeV] $\lambda 14.32$ μm emission line, and hence, host AGN activity. These seventeen sources are the main focus of this chapter. See Table 4.1.

4.3 Black Hole Mass Determination

4.3.1 Archival Data

To accurately determine the relative mass accretion rates and space density of active SMBHs in the local Universe requires reliable SMBH mass ($\mathrm{M_{BH}}$) estimates for the seventeen AGNs within our volume-limited sample. Here we outline the construction of the heterogeneous database of the most reliable available SMBH masses for these AGNs, derived from a variety of archival sources and $\mathrm{M_{BH}}$ estimation methods.

Many of the sources in the sample are late-type galaxies hosting relatively small bulges, and hence low-mass SMBHs. In such systems, SMBH mass estimates are often challenging to determine as: 1) characteristically low velocity dispersions can be difficult to measure as they are often at the resolution limit of published observations, 2) modeling of the contamination from composite stellar populations can often lead to inconsistencies between published measurements and 3) SMBH mass relations are poorly constrained at $\mathrm{M_{BH}} \sim 10^6\,\mathrm{M_\odot}$.

Given the varying degrees of accuracy associated with $\mathrm{M_{BH}}$ measurements estimated from differing methodologies, we have chosen to prioritise the archival data (which we further expand on here) based upon two broad categories: (i) physically motivated AGN modeling techniques (i.e., reverberation mapping, water maser mapping and gas

kinematics of the central engine) and (ii) indirect estimations from observational relations (the M–σ_* and $\mathrm{M_{BH}}$–$\mathrm{L_{bul}}$ relations). The adopted $\mathrm{M_{BH}}$ for the sources and their associated measurement methodologies are given in columns 12 and 13 of Table 4.1. The database contains four SMBH measurements determined from physically motivated AGN modeling and 13 from indirect methods.

4.3.1.1 Direct SMBH mass constraints from reverberation mapping, maser mapping and gas kinematics

Under the assumption that the gas in the broad-line region (BLR) is virialised by the SMBH and the orbital motion of the gas is Keplerian, $\mathrm{M_{BH}}$ estimations are possible through reverberation mapping techniques (Blandford and McKee, 1982). The time-lag between changes in the AGN continuum flux and the response of the broad-line region is used to directly infer the size of the virial radius and hence the mass of the SMBH (for an in-depth review see Peterson 2001). To date, reverberation mapping is widely accepted to be the most reliable of $\mathrm{M_{BH}}$ estimation methodologies (e.g., Wandel et al. 1999; Peterson and Wandel 1999; Onken et al. 2003; Bentz et al. 2009b). Only a minority of the galaxies in the sample (NGC 1068, NGC 4051 and NGC 5033) are known to have detected BLRs. However, the BLRs of NGC 1068 and NGC 5033 (both are Seyfert 1.9) are extremely weak and are therefore likely to suffer from optical extinction. Thus, reliable $\mathrm{M_{BH}}$ estimates using the BLR are not possible for these two AGNs. Hence, only one object (NGC 4051; Wandel 1999) in our sample has archival reverberation mapping data giving $\mathrm{M_{BH}} \approx 1.4^{+1.5}_{-0.9} \times 10^6\,\mathrm{M_\odot}$.

Complimentary to reverberation mapping, and also assuming Keplerian motion, mapping of megamaser spots and observations of gas kinematics within the gravitational sphere of influence of the SMBH are thought to yield relatively precise measurements of $\mathrm{M_{BH}}$. Again, due to the nature of the observations (i.e., a relatively edge-on inclination to the observer) and the requirement of a suitable gas disc, few $\mathrm{M_{BH}}$ estimations using these methods exist in the current literature. Indeed, in our sample there are currently only two AGNs (NGC 1068 and NGC 4945) with $\mathrm{M_{BH}}$ estimations from the mapping of megamaser spots ($\mathrm{M_{BH}} \approx 1.6 \times 10^7$ and $1.1 \times 10^6\,\mathrm{M_\odot}$, respectively) and one AGN (NGC 5128) with a spatially resolved gas dynamical $\mathrm{M_{BH}}$ estimate ($\mathrm{M_{BH}} \approx 2.4 \times 10^8\,\mathrm{M_\odot}$).

4.3.1.2 Indirect SMBH mass constraints from the M–σ_* relation

Since the seminal discovery that the mass of the stellar spheroid is closely related to $\mathrm{M_{BH}}$ (Magorrian et al. 1998), indirect $\mathrm{M_{BH}}$ estimation methods have become ubiquitous in the literature (e.g., Ferrarese and Merritt 2000; Gebhardt et al. 2000; Nelson et al. 2004; Onken et al. 2004; Greene and Ho 2006). Comparisons of spatially resolved stellar dynamics with reverberation-based $\mathrm{M_{BH}}$ estimates (over the range of $\mathrm{M_{BH}} \approx 2 \times 10^6$–$10^9\,\mathrm{M_\odot}$) show that these are well-correlated with the effective stellar velocity dispersions (σ_*) within the galaxy bulge (i.e., the M–σ_* relation; Gebhardt et al. 2000),

$$\mathrm{M_{BH}} = (1.2 \pm 0.2) \times 10^8\,\mathrm{M_\odot} \left(\frac{\sigma_*}{200\,\mathrm{km\,s^{-1}}}\right)^{(3.75\pm0.30)} \tag{4.1}$$

with an intrinsic scatter of only 0.34 dex. Furthermore, with the inclusion of a sample of dwarf Seyfert 1 galaxies, the correlation may be reasonably extrapolated to SMBH masses in the range 10^5–$10^6\,\mathrm{M_\odot}$ (Barth et al., 2005). However, we acknowledge that to-date, the M–σ_* relation is still poorly constrained for $\mathrm{M_{BH}} < 10^6\,\mathrm{M_\odot}$ and suffers from systematic uncertainties. Specifically, these are caused by the lack of homogeneous source statistics in this mass region and also the poor understanding of the physical nature of the central region in very late-type (Scd–Sm) galaxies (e.g., the existence of either a pseudo- or classical bulge; Kormendy and Kennicutt 2004). However, of the three AGNs in our sample which are classified as Hubble-type Scd or later, only NGC 3621 (Sd) has an $\mathrm{M_{BH}}$ measurement estimated from the M–σ_* relation.[1] Specifically, using the Echellette spectrograph on Keck-II, Barth et al. (2009) measure an accurate line-of-sight stellar velocity dispersion of the Calcium II triplet lines (CaT; $\lambda\lambda 8498$, 8542, 8662) observed in the central nuclear star cluster. They find a velocity dispersion consistent with a SMBH mass of $\mathrm{M_{BH}} \approx 3 \times 10^6 \mathrm{M_{BH}}$. We find that all of the AGNs in our sample host SMBHs with $\mathrm{M_{BH}} \gtrsim 10^6\,\mathrm{M_\odot}$ and thus are unlikely to suffer significant systematic uncertainities arrising from the use of the M–σ_* relation to estimate $\mathrm{M_{BH}}$ even in the most late-type galaxies.

Ten of the 13 AGNs in our sample without direct $\mathrm{M_{BH}}$ measurements have published $\mathrm{M_{BH}}$ estimates using the M–σ_* relation. For consistency purposes (and where possible) we have used the central stellar velocity dispersions given in the recently published cat-

[1] The $\mathrm{M_{BH}}$ measurement for NGC 1448 (Scd) is estimated from the $\mathrm{M_{BH}}$–$\mathrm{L_{K,bul}}$ relation (see § 4.3.2) due to the lack of sufficient spectroscopic data to measure a stellar velocity dispersion. NGC 4945 (Scd) is an $\mathrm{H_2O}$ megamaser source, and hence has an accurate and direct measurement of $\mathrm{M_{BH}}$ (Greenhill et al. 1997). See also Table 4.1.

alogue of Ho et al. (2009). They measure the central σ_* for the 486 galaxies within the Palomar Survey (Ho et al. 1997a,b) using the averaged values derived from the fitting of stellar absorption templates (Valdes et al., 2004) to the blue (4230–5110 Å) and red (6210–6860 Å) spectral ranges (i.e., the published spectroscopy does not include standard velocity dispersion measurement features; e.g., CaT). Where available, Ho et al. (2009) compare σ_* values derived from the modeling of the stellar absorption features to previously published measurements from CaT lines which are available in the HyperLeda database.[2] Measured errors are compared between the Palomar σ_* measurements and the weighted average adopted by HyperLeda for the available published σ_* measurements. The final adopted measurement of σ_* by Ho et al. (2009) is that with the smallest overall error. Where the values assumed by Ho et al. (2009) are previously published or are from HyperLeda we quote these references in column 14 of Table 4.1 (6 objects). For the AGNs in our sample which are not part of the Palomar survey, values of σ_* derived from direct fitting analyses of the CaT lines are adopted from other published sources (see column 14 of Table 4.1; 4 objects). All final adopted σ_* measurements are converted to $\mathrm{M_{BH}}$ estimates using Equation 4.1.[3]

[2]The HyperLeda database is a continuously updated electronic catalogue of galactic measurements available at http://leda.univ-lyon1.fr/. Specifically, HyperLeda contains a consolidated list of archival velocity dispersions for many nearby galaxies.

[3]We note that NGC 6300 currently has two measurements of σ_* from fitting of the CaT lines (Garcia-Rissmann et al., 2005), which were obtained through direct-fitting and cross-correlation analyses. For consistency with other measurements, we adopt the direct-fitting value of σ_*. We find that the derived $\mathrm{M_{BH}}$ from the cross-correlation method is a factor two larger; however, using this larger $\mathrm{M_{BH}}$ measurement will have little impact on our overall results.

Table 4.1: Catalogue of $D < 15$ Mpc mid-infrared identified AGNs and derived quantities.

Common Name	D (Mpc)	Hubble Type	AGN ID	$\log(L_{[OIV]})$ ($\mathrm{erg\,s^{-1}}$)	$\log(L_X)$ ($\mathrm{erg\,s^{-1}}$)	Ref. L_X	$\log(L_{bol,[OIV]})$ ($\mathrm{erg\,s^{-1}}$)	$\log(L_{bol,X})$ ($\mathrm{erg\,s^{-1}}$)	K_{Tot} (mag)	K_{Bul} (mag)	$\log(M_{BH})$ ($M_\odot$)	Method	Ref. M_{BH}
(1)	(2)	(3)	(4)	(5)	(6)	(7)	(8)	(9)	(10)	(11)	(12)	(13)	(14)
E121-G006	14.5	Sc	IR	39.04	-	-	41.82	-	8.98	10.91	$6.10^{+0.11}_{-0.51}$	L_{Bul}	14
NGC 0613	15.0	Sbc	IR	39.38	-	-	42.26	-	7.03	-	$7.34^{+0.08}_{-0.15}$	M-σ_*	15
NGC 0660	12.3	Sa	IR	39.71	-	-	42.69	-	7.34	-	$7.35^{+0.08}_{-0.16}$	M-σ_*	21
NGC 1068	13.7	Sb	IR,O,X	41.66	43.48	1,9,2	45.26	44.85	5.79	-	$7.20^{+0.12}_{-0.12}$	M	16
NGC 1448	11.5	Scd	IR	39.40	-	-	42.28	-	7.66	10.64	$5.99^{+0.11}_{-0.52}$	L_{Bul}	14
NGC 1792	12.5	Sbc	IR	38.26	-	-	40.49	-	7.01	9.08	$6.83^{+0.12}_{-0.53}$	L_{Bul}	14
NGC 3621	6.6	Sd	IR,O	38.18	-	-	40.68	-	6.60	-	$6.50^{+0.13}_{-0.27}$	M-σ_*	22
NGC 3627	10.0	Sb	IR	38.38	-	-	40.95	-	5.99	-	$7.30^{+0.10}_{-0.19}$	M-σ_*	21
NGC 3628	10.0	Sb	IR	38.81	-	-	41.51	-	6.07	-	$6.53^{+0.07}_{-0.12}$	M-σ_*	20
NGC 4051	13.1	Sbc	IR,O,X	39.88	41.72	3,2,4,5	42.91	42.71	7.67	-	$6.15^{+0.16}_{-0.22}$	R	19
NGC 4945	3.9	Scd	IR,X	38.72	42.49	6,2,7,4,5	41.40	43.61	5.23	-	$6.04^{+0.05}_{-0.05}$	M	17
NGC 5033	13.8	Sc	IR,O,X	39.08	40.85	8,9	41.86	41.73	6.96	-	$7.62^{+0.09}_{-0.16}$	M-σ_*	21
NGC 5128	4.0	S0	IR,X,R[a]	39.38	41.85	2,9,4,5	42.26	42.86	3.94	-	$8.38^{+0.20}_{-0.26}$	G	18
NGC 5194	8.6	Sbc	IR,O,X	38.85	41.11	10,2	41.56	42.00	5.92	-	$6.88^{+0.13}_{-0.27}$	M-σ_*	15

Continued on Next Page...

NGC 5195	8.3	Irr	IR	37.89	-	-	40.30	-	6.25	-	$7.31^{+0.07}_{-0.13}$	M-σ_*	20
NGC 5643	13.9	Sc	IR,O,X	40.43	41.08	11,12,2	43.63	41.98	7.17	-	$6.44^{+0.11}_{-0.21}$	M-σ_*	23
NGC 6300	13.1	Sb	IR,O,X	39.78	41.63	13,4,5	42.79	42.60	6.93	-	$6.80^{+0.11}_{-0.22}$	M-σ_*	24

NOTES: (1) Common galaxy name. (2) Distance to source in megaparsecs from the Revised Bright Galaxy Survey (RBGS; Sanders et al. 2003). (3) Morphological type from RC3 (de Vaucouleurs et al., 1991). (4) Waveband of AGN identification; IR: Mid-Infrared spectroscopy (GA09); O: Optical spectroscopy (references presented in GA09); X: X-ray spectroscopy (2–10 keV; see column 7 for references); R: Radio observations. (5) Logarithm of [OIV] $\lambda 25.89\ \mu\mathrm{m}$ luminosity in $\mathrm{erg\,s^{-1}}$ calculated using [OIV] flux presented in GA09; mean uncertainty is approximately 10 percent. (6) Logarithm of absorption corrected hard X-ray luminosity (2–10 keV) in $\mathrm{erg\,s^{-1}}$ which have been converted to the distances given in column 2. (7) Reference for X-ray data; see references below. (8) Logarithm of bolometric luminosity of the AGN estimated from $L_{[\mathrm{OIV}]}$ using Equation 4.4. (9) Logarithm of bolometric luminosity of the AGN estimated from $L_{\mathrm{X,2-10keV}}$ using the bolometric corrections described in Marconi et al. (2004). (10) Total *K*-Band magnitude from 2MASS Large Galaxy Atlas (Jarrett et al. 2003). (11) *K*-Band magnitude of bulge produced using GALFIT (Peng et al. 2002; see section 3.2.1). (12) Logarithm of estimated black hole mass and associated 1-sigma errors in solar masses. (13) Method of $\mathrm{M_{BH}}$ measurement; M: Maser Mapping; G: Gas Kinematics; R: Reverberation Mapping; M-σ_*: Mass–Velocity Dispersion Correlation; $\mathrm{L_{Bul}}$: K-band Luminosity–Bulge Correlation. (14) Reference for $\mathrm{M_{BH}}$ measurement; see references below.

REFERENCES: (1) Matt et al. (1997); (2) Dadina (2007); (3) Pounds et al. (2004); (4) Tueller et al. (2008); (5) Winter et al. (2009); (6) Guainazzi et al. (2000); (7) Itoh et al. (2008); (8) Cappi et al. (2006); (9) Bird et al. (2007); (10) Fukazawa et al. (2001); (11) Maiolino et al. (1998); (12) Guainazzi et al. (2004); (13) Matsumoto et al. (2004); (14) This Paper; (15) HyperLeda; (16) Greenhill et al. (1996); (17) Greenhill et al. (1997); (18) Marconi et al. (2001); (19) Wandel (1999); (20) Ho et al. (2009); (21) Barth et al. (2002); (22) Barth et al. (2009); (23) Whittle (1992); (24) Garcia-Rissmann et al. (2005); [a] for a review see Israel (1998).

4.3.2 Galaxy Decompositions using GALFIT

4.3.2.1 Indirect SMBH mass constraints from the $\mathrm{M_{BH}}$–$\mathrm{L_{K,bul}}$ relation

Three of the AGNs within our sample (ESO121-G006, NGC 1448 and NGC 1792) currently lack archival direct or indirect SMBH mass constraints. Hence, for these three objects, we follow the formalism of Marconi & Hunt (2003; hereafter, MH03) and use 2MASS K-band imaging and GALFIT, the two-dimensional imaging analysis software of Peng et al. (2002), to constrain the bulge luminosities and therefore, $\mathrm{M_{BH}}$ for these three AGNs.

Near-IR (0.9–4.8 μm) emission is a strong tracer of stellar mass and is less susceptible to the effects of dust/gas extinction than optical emission. As a result of this, the *K*-band (2.2 μm) is shown to provide the strongest correlation of all near-IR bands between the luminosity of the bulge and $\mathrm{M_{BH}}$ (MH03).

For the bulge-disc decomposition image analysis, we have obtained archival *K*-band imaging for ESO 121-G006, NGC 1448 and NGC 1792. These images were retrieved from the Two Micron All-Sky Survey (2MASS) extended source catalogue and consist of pre-mosaicked (1 arcsecond per pixel resolution) all-sky atlas images. The *K*-band images of the three galaxies were modeled with a central point spread function (PSF) and a constant sky background contribution, whilst the bulge and host-galaxy components were modeled using variations of the Sersic profile:

$$\Sigma(r) = \Sigma_e e^{-\kappa[(r/r_e)^{1/n}-1]} \tag{4.2}$$

where r_e is the effective radius of the profile, Σ_e is the surface brightness at the effective radius, n is the power-law (Sersic) index, and κ is coupled to n such that half of the total flux of the object is within the effective radius. We employ two special forms of the Sersic profile in our GALFIT modeling, the exponential ($n = 1$) and the de Vaucouleurs ($n = 4$) profiles, which are classically used to model galactic discs and bulges, respectively.

Häussler et al. (2007) have shown that the reliability of the fitting parameters produced by GALFIT are strongly dependent on the initial estimates. GALFIT will, in general, fail to find the overall global chi-squared (χ^2) minimum to the fit if the initial estimates are poorly constrained. Thus, to reduce this systematic effect, and aid the fitting routine, we use a simplified 1-dimensional fit to produce initial estimates of the fitting parameters. A 1-dimensional surface-brightness slice of the *K*-band image was taken across the major axis of each of the galaxies. A surface brightness profile extending from the nu-

cleus was produced by averaging the two semi-major axes from the slice, and removing the measured background flux. Few spiral galaxies are found to host bulges with true de Vaucouleurs profiles, thus a global χ^2 reduction process was used to simultaneously fit a generalised Sersic profile and a fixed ($n = 1$) exponential disc to the 1-d surface brightness profile. From these, we calculate Sersic and disc radii, as well as the Sersic index of the bulge. Combining the 1-d parameter estimates with the total *K*-band magnitude from the 2MASS Large Galaxy Atlas (Jarrett et al., 2003), we generate an appropriate set of constraints and initial parameters to be input to GALFIT.

Using the derived parameter estimates, GALFIT is used to fit a generalised 2-d Sersic profile with an exponential disc to the *K*-band image. To again aid the GALFIT reduction analysis, particular attention is paid to simulating accurate PSFs for the 2MASS images using known standard stars (J. R. Lucey private communication).[4] Results of this bulge/disc reduction for the three objects are presented in Fig. 4.1 and column 11 of Table 4.1.

We have directly tested our robust GALFIT method using the late-type galaxies (i.e., S0 or later) presented in the dataset of MH03 and find close agreement (≈ 0.1 dex). We do note however, that we find a systematic offset of a factor ≈ 2 in bulge luminosity for the AGNs in MH03 that are hosted in low-inclination angle late-type galaxies, which based on our testing, is likely to be caused by GALFIT over-estimating the contribution of the bulge to the total flux of the galaxy. Indeed, when directly comparing a sample of reverberation mapped X-ray detected AGNs to $\mathrm{M_{BH}}$ estimations using the MH03 formalism, Vasudevan et al. (2009) find similar results. However, the three galaxies fitted in our sample are all moderately to highly-inclined and thus this systematic effect will be negligible.

In Fig. 4.1 we show the three GALFIT produced image cubes obtained following our bulge/disc fitting routines. Within each of the residual (observed – model) images it is clear that the bulge is well fitted by a Sersic profile. The edge-on galaxy ESO121-G006 is well fit by an exponential disc combined with a Sersic profile, with no distinguishing residual features. The residual of NGC 1448 highlights the existence of its spiral arms and shows the presence of a truncated disc combined with a possible bar structure which our simplified modeling technique is incapable of fitting; however, the bulge fit does not appear to be compromised. Indeed, our derived $\mathrm{M_{BH}}$ estimations for ESO121-G006 and

[4] A detailed discussion of GALFIT problems caused by poor PSF modeling can be found in Bentz et al. (2009a)

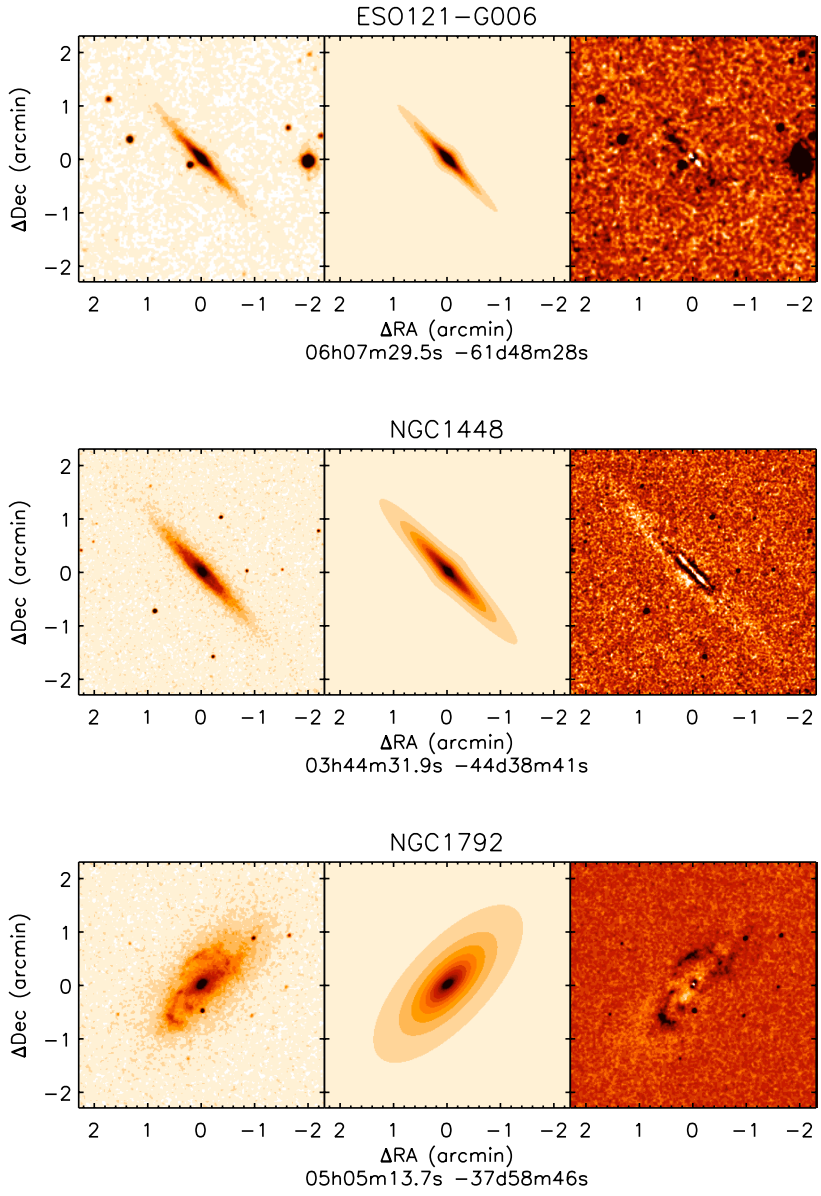

Figure 4.1: GALFIT (Peng et al., 2002) two-dimensional bulge/disc decompositions for the three AGNs (ESO121-G006, NGC 1448 and NGC 1792) with M_{BH} estimated from the M_{BH}–$L_{K,bul}$ relation. The panels show (left) *K*-band Two Micron All-Sky Survey (2MASS) extended source image of the galaxy, (middle) GALFIT model produced by fitting a Sersic profile, an exponential disc and a mean averaged background to the observed *K*-band image, (right) the residual image resulting from the subtraction of the model profile from the observed galaxy (i.e., $\mathrm{observation} - \mathrm{model}$). See § 4.3.2 for a brief explanation of the residual images.

NGC 1448 are consistent with the $\mathrm{M_{BH}}$ upper limits obtained from stellar mass-to-light ratio analyses (Ratnam and Salucci, 2000). The residual image of the moderately inclined galaxy, NGC 1792, contains strong spiral arms as well as a point-like nuclear source. We note that due to the inclination angle of this source, the derived $\mathrm{M_{BH}}$ may be systematically over-estimated by a factor of ≈ 2 (see above). Thus, our derived Eddington rate for NGC 1792, presented in § 4.5.1, should be considered a lower limit.

From the obtained *K*-band bulge magnitudes (column 11, Table 4.1) we calculate bulge luminosities ($L_{\mathrm{K,bul}}$). Using the well established $\mathrm{M_{BH}}$ to bulge *K*-band luminosity relation of MH03 (hereafter, $\mathrm{M_{BH}}$–$L_{\mathrm{K,bul}}$),

$$\log \mathrm{M_{BH}} = (8.08 \pm 0.10) + (1.21 \pm 0.13)\log\left(\frac{L_{\mathrm{K,bul}}}{8 \times 10^{10}}\right) \tag{4.3}$$

we calculate $\mathrm{M_{BH}}$ for ESO 121-G006, NGC 1448 and NGC 1792. The 1-σ uncertainties associated with the $\mathrm{M_{BH}}$ values are assessed by combining in quadrature the bulge magnitude errors as calculated by GALFIT with the intrinsic dispersion observed in the $\mathrm{M_{BH}}$–$\mathrm{L_{K,bul}}$ relation. The resultant $\mathrm{M_{BH}}$ estimates and 1-σ uncertainties are provided in column 12 of Table 4.1.

4.4 Bolometric Corrections

To determine the relative mass accretion rates, and hence the average growth times of SMBHs in the local Universe we require relatively accurate estimates of the bolometric luminosities of the AGNs ($L_{\mathrm{Bol,AGN}}$) in our sample. We use two methods to estimate $L_{\mathrm{Bol,AGN}}$: 1) a direct approach using the best available measured hard X-ray (2–10 keV) luminosities, and 2) a well-constrained $L_{\mathrm{Bol,AGN}}$–[OIV] luminosity relation to infer the intrinsic luminosity of the AGN (e.g., Dasyra et al. 2008; Meléndez et al. 2008, hereafter, M08).

4.4.1 Hard X-ray Luminosity as a Tracer of the Bolometric Luminosity of an AGN

High quality hard X-ray spectral analyses arguably provide the most unambiguous method for measuring the intrinsic luminosity of an AGN since X-rays are relatively unaffected by dust extinction, intrinsic absorption can be directly constrained from high S/N data, and star-formation contamination is often found to be negligible. We therefore divide our sample into two categories based on the quality and energy range of their available

published X-ray data: 1) AGNs with high S/N X-ray spectra where $N_{\rm H}$ has been accurately constrained and/or AGNs with $E > 10$ keV constraints where the observed X-ray emission will only be strongly absorbed for heavily Compton-thick ($N_{\rm H} > 10^{25}\,{\rm cm}^{-2}$) sources (8 AGNs); and 2) those AGNs with no or low S/N X-ray data, i.e., where there are insufficient counts to accurately determine $N_{\rm H}$ and the X-ray flux could have large contributions from star-formation (9 AGNs). Hence, we specifically do not estimate $L_{\rm Bol,AGN}$ for those AGNs with L_X measurements using *Chandra* that also have no further hard X-ray spectral constraints ($E > 10$ keV) due to relatively low count rates and the limited band-pass of the instrument at $z \sim 0$ (0.5–8 keV).

For the AGNs in our sample currently with either high S/N spectroscopy or $E > 10$ keV constraints, we estimate $L_{\rm Bol,AGN}$ using the Eddington ratio independent AGN bolometric corrections outlined in Equation 21 of Marconi et al. (2004). We note that Vasudevan and Fabian (2009) have suggested that the bolometric correction factor ($\kappa_{2-10{\rm keV}} = L_{\rm bol}/L_{2-10{\rm keV}}$) may be a function of the Eddington ratio of a considered source. Values of $\kappa_{2-10{\rm keV}} \sim 10$–30 are considered to be relatively low bolometric corrections and are generally found in AGNs with $\eta < 0.1$ (e.g., Vasudevan & Fabian 2009; Vasudevan et al. 2010). For the sample of X-ray detected AGNs considered here, we calculate similarly consistent values of $\kappa_{2-10{\rm keV}} \sim 8$–30, and thus conclude that the Eddington ratio is unlikely to be dominating the bolometric corrections adopted here from Marconi et al. (2004).

For further consistency, all archival X-ray luminosities were adjusted to the distances adopted in column 2 of Table 4.1. Final adopted L_X measurements, estimated $L_{\rm Bol,AGN}$ from L_X, and archival references for L_X are given in columns 6, 7 and 9 of Table 4.1, respectively.

4.4.2 [OIV] Luminosity as a Tracer of the Bolometric Luminosity of an AGN

For those galaxies in the sample without good-quality hard X-ray constraints we require an alternate approach to estimate the intrinsic luminosity of the AGN, and hence the relative mass-accretion rate. Here we build-upon an $L_{\rm Bol,AGN}$ estimation which relies on the AGN-produced [OIV] $\lambda 25.89\,\mu{\rm m}$ luminosities ($L_{\rm [OIV]}$) for the AGNs in our sample (e.g., Dasyra et al. 2008; M08).[5]

[5]We note that [NeV] may also provide a good proxy for $L_{\rm Bol,AGN}$; however, large samples of AGNs with [NeV] and hard X-ray measurements do not exist in the current literature, and hence, this relation is, to date, not well constrained.

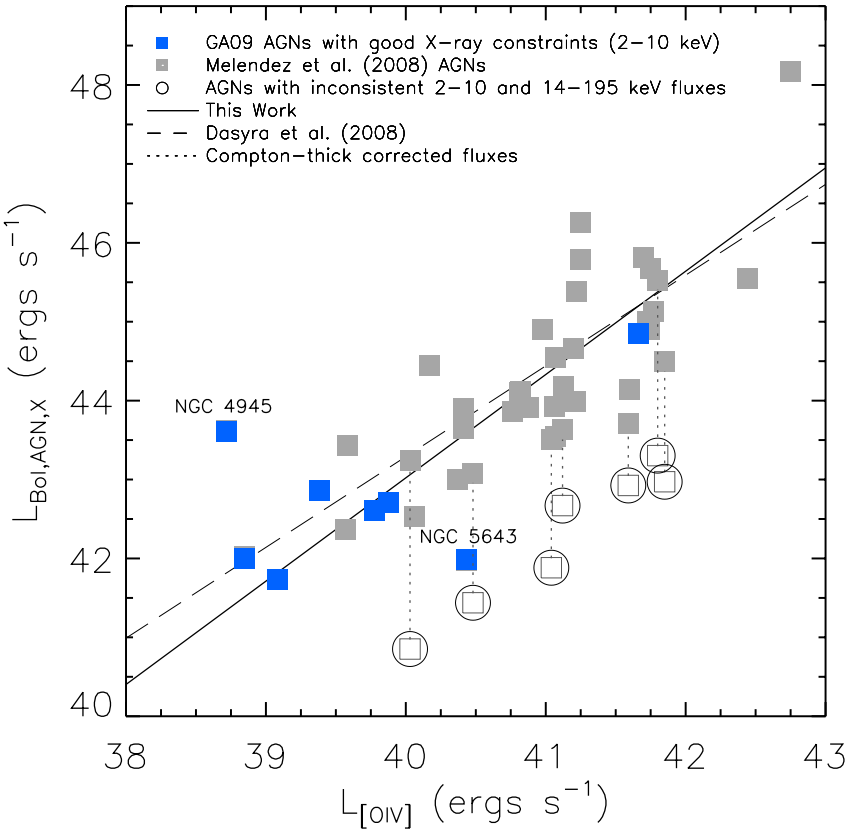

Figure 4.2: X-ray derived AGN bolometric luminosity ($L_{\rm Bol,AGN,X}$) versus [OIV] $\lambda 25.89$ μm luminosity ($L_{\rm [OIV]}$). The objects shown are from this work (black squares) and those in the *Swift*-BAT survey with detected [OIV] emission (M08; grey squares). The solid line is a best-fit bisector and was obtained using the IDL-based ROBUST_LINEFIT algorithm. The dashed line is the $L_{\rm Bol,AGN}$–$L_{\rm [OIV]}$ relation of Dasyra et al. (2008) derived from the optical luminosity at 5100Å. We also highlight those galaxies in M08 with inconsistent 2–10 and 14–195 keV luminosities (open circles). These seven galaxies and their alternatively published X-ray luminosities (which we adopt in our analysis; dotted line) are shown in Table 4.2; we find that five are identified as Compton thick AGNs in the literature and the other two are X-ray variable. The galaxies from our $D < 15$ Mpc sample which lie significantly off the derived correlation are labeled (NGC 4945 and NGC 5643); see text for further details.

Based on the simplest Unified Model of AGN (Antonucci, 1993), the hot dust within the predicted torus, close to the central engine, reprocesses absorbed UV, optical and X-ray emission into mid-IR emission. Hence, AGN emission detected at IR wavelengths is likely to be isotropic and independent of viewing angle. As discussed in § 3.2.4, the detection of high-ionisation [NeV] emission (97.1 eV) coincident with the nucleus of a galaxy is considered a robust indicator of AGN activity (e.g., Armus et al. 2006; GA09). Complimentary to this, GA09 find that [NeV] emission is also well correlated with [OIV] emission (54.9 eV) with an intrinsic scatter of only 0.24 dex. As [NeV] emission, and thus [OIV] emission, do not suffer from significant star-formation contamination and are both comparatively extinction-free, they may be used as relatively clean proxies for the bolometric luminosity of the AGNs presented here ($L_{\rm Bol,AGN}$).[6] Indeed, for a sample of 35 well-studied optically unobscured AGNs, Dasyra et al. (2008) show that both [NeV] and [OIV] emission are well correlated with the luminosity of the 5100 Å optical continuum, and hence $L_{\rm Bol,AGN}$ with an intrinsic scatter of 0.46 and 0.47 dex, respectively. However, the relation of Dasyra et al. (2008) is derived from AGNs with $L_{\rm [OIV]} > 2 \times 10^{40}\,{\rm erg\,s^{-1}}$ ($L_{\rm [NeV]} > 7 \times 10^{39}\,{\rm erg\,s^{-1}}$), and hence we test whether it may be reliably extrapolated to the more modest luminosity AGNs considered here (log-average $L_{\rm [OIV]} \approx 2 \times 10^{39}\,{\rm erg\,s^{-1}}$).

We combine our robustly adopted $L_{\rm Bol,AGN}$ from 2-10 keV flux measurements with the X-ray catalogue of nearby ($z < 0.08$) Seyfert galaxies in the *Swift*-BAT survey which have published [OIV] luminosities in M08. The catalogue of sources in M08 contain 2–10 keV luminosities obtained primarily from *ASCA* data, 14-195 keV luminosities from the *Swift*-BAT survey and [OIV] luminosities from *Spitzer*-IRS spectroscopy. Combining the M08 sample with our 8 AGNs with high-quality X-ray constraints, the range covered in $L_{\rm [OIV]}$ is $\approx$ (0.7–7000) $\times\, 10^{39}\,{\rm erg\,s^{-1}}$. For consistency, we convert the M08 2–10 keV luminosities to $L_{\rm Bol,AGN}$ using the same bolometric corrections adopted in § 4.4.1. In Fig. 4.2 we plot $L_{\rm Bol,AGN}$ versus $L_{\rm [OIV]}$ for the M08 sample and the 8 AGNs in our GA09 sample with good-quality hard X-ray constraints (grey filled squares and blue filled squares, respectively).

[6] We note that since star-formation can also produce [OIV] emission, the [NeV]–[OIV] relation may be unreliable for sources with exceedingly high star-formation rates (e.g., Ultra Luminous Infrared Galaxies with $L_{\rm IR} > 10^{12}\,{\rm erg\,s^{-1}}$; ULIRGs). However, there are no ULIRGs within the sample considered here.

Table 4.2: Catalogue of revised 2–10 keV luminosities for a subset of the M08 sample.

Common Name (1)	$\log(L_{2-10\mathrm{keV,M08}})$ ($\mathrm{erg\,s^{-1}}$) (2)	$\log(L_{2-10\mathrm{keV,alt.}})$ ($\mathrm{erg\,s^{-1}}$) (3)	C-thick AGN? (4)	Ref. (5)
Circinus	40.58	42.04	$\surd$	1
Mrk 3	41.95	43.20	$\surd$	2
NGC 1365	40.99	42.40	$\surd$	3
NGC 2992	41.69	42.50	$\times$	4
NGC 3079	40.02	42.18	$\surd$	5
NGC 4388	41.91	42.57	$\times$	6
NGC 6240	42.23	44.00	$\surd$	7

NOTES: (1) Common galaxy name. (2) Logarithm of 2–10 keV luminosity adopted by M08. (3) Logarithm of absorption corrected 2–10 keV luminosity adopted in this work from individual studies (2–10 keV luminosities were adjusted using our adopted distances). (4) Is the AGN a Compton thick source? (5) Reference for adopted $L_{2-10\mathrm{keV}}$ measurement.

REFERENCES: (1) Yang et al. (2009); (2) Awaki et al. (2008); (3) Risaliti et al. (2009); (4) Yaqoob et al. (2007); (5) Iyomoto et al. (2001); (6) Shirai et al. (2008); (7) Vignati et al. (1999)

As noted by M08, several of the AGNs in their sample have low 2–10 keV luminosities when compared to the 14-195 keV luminosities, most likely due to absorption of the 2–10 keV flux. These are highlighted with open circles in Fig. 4.2 and are shown in Table 4.2. Using high-quality X-ray spectral analyses from the current literature, five of the seven AGNs are identified as Compton thick (see column 4 of Table 4.2 in this paper, and Table 4 of M08). For the purpose of our analyses, we use absorption corrected measurements of $L_{2-10\mathrm{keV}}$ which are in good agreement with the M08 14–195 keV luminosities (see columns 2, 3 and 5 of Table 4.2; dotted-lines in Fig. 4.2). The other two AGNs (NGC 2992 and 4388) in M08 with inconsistent 2–10 and 14–195 keV fluxes are found to be highly variable (Beckmann et al. 2007 and Elvis et al. 2004, respectively).

With the inclusion of the obscuration-corrected 2–10 keV luminosities to infer $L_{\mathrm{Bol,AGN}}$, we find a strong correlation between $L_{[\mathrm{OIV}]}$ and $L_{\mathrm{Bol,AGN}}$ which is characterised by the equation:

$$\log\left(\frac{L_{\mathrm{bol,AGN}}}{10^{44}\,\mathrm{erg\,s^{-1}}}\right) = (0.38 \pm 0.09) + (1.31 \pm 0.09)\log\left(\frac{L_{[\mathrm{OIV}]}}{10^{41}\,\mathrm{erg\,s^{-1}}}\right) \tag{4.4}$$

with an intrinsic scatter in the data of ≈ 0.35 dex. We find good agreement with the Dasyra et al. (2008) relation (dashed-line) in the region $L_{[\mathrm{OIV}]} \approx 10^{40}$–$10^{43}\,\mathrm{erg\,s^{-1}}$ (i.e., where the Dasyra et al. (2008) relation is well sampled). However, for $L_{[\mathrm{OIV}]} < 10^{40}\,\mathrm{erg\,s^{-1}}$ we show that the Dasyra et al. (2008) relation will over estimate $L_{\mathrm{Bol,AGN}}$ by typically ≈ 0.5 dex.

In Fig. 4.2, we highlight two AGNs from the $D < 15$ Mpc sample (NGC 4945 and 5643) which appear to be significant outliers of the observed correlation. NGC 5643 possibly harbours a variable central source with variable levels of obscuration. From the detection of strong Fe Kα emission, Maiolino et al. (1998) suggest from using *BeppoSAX* data that NGC 5643 is possibly Compton thick ($\mathrm{N_H} > 10^{25}\,\mathrm{cm^{-2}}$); however, Guainazzi et al. (2004) find using *XMM-Newton* data, that it may be Compton thin with $\mathrm{N_H} \approx (6\text{–}10) \times 10^{23}\,\mathrm{cm^{-2}}$. Thus, from current available data, the true intrinsic luminosity of the AGN is highly uncertain. Here we conservatively adopt the Compton thin L_X value of Guainazzi et al. (2004); however, we note that if we use the value of Maiolino et al. (1998), then NGC 5643 would lie on our derived relationship. NGC 4945, by contrast, has observations using *Ginga*, *ASCA*, *OSSE*, the *Rossi X-ray Timing Explorer*, *BeppoSAX*, *Suzaku* and most recently *Swift*-BAT (Iwasawa et al. 1993, Tanaka et al. 1994, Done et al. 1996, Madejski et al. 2000, Guainazzi et al. 2000, Itoh et al. 2008 and Tueller et al. 2008, respectively) all of which provide excellent and consistent spectral constraints

over a wide X-ray band (1–200 keV) showing that the central source is Compton thick ($N_H \approx 4 \times 10^{24}\,\mathrm{cm}^{-2}$), with $L_{\mathrm{X,2-10keV}} \approx (3\text{–}10) \times 10^{42}\,\mathrm{erg\,s}^{-1}$ and an observed intrinsic variability of a factor ≈ 2. Here we adopt the luminosity from the most recent observation by *Swift*, $L_X \approx 3 \times 10^{42}\,\mathrm{erg\,s}^{-1}$. On the basis of our mid-IR constraints, it would therefore appear that NGC 4945 is under-luminous in [OIV] flux by a factor of ≈ 50 (see Table 4.1 and Fig. 4.2). We suggest this deficit in observed [OIV] flux is unlikely to be due to host galaxy extinction; the required absorption to account for a factor of ≈ 50 flux difference is $A_V \approx 240$ mags ($N_H \approx 5 \times 10^{23}\,\mathrm{cm}^{-2}$ assuming typical dust-to-gas ratios; using $A_V/\mathrm{E}(B-V) = 3.1$). Another possible explanation is a temporary decoupling of the X-ray emitting and narrow-line regions (i.e., the highly-luminous state of NGC 4945 may be a somewhat recent event). Given the spatial difference (and hence, the light-travel time) between the two emission regions: 10^{-4} pc and 1–10 pc, respectively, the photoionisation of the narrow-line region, and thus the observed [OIV] emission, may take ≈ 100 years to respond to the changes in the X-ray emitting region. We therefore suggest that the intrinsic scatter in the observed [OIV]–$L_{\mathrm{bol,AGN}}$ relation may be significantly reduced if it was possible to account for variability in the central region of all of the AGNs. Indeed, we find the average dispersion decreases to ≈ 0.31 dex if we remove NGC 4945 from our analysis.

Using Equation 4.4 and $L_{[\mathrm{OIV}]}$ from GA09 (column 5 of Table 4.1), we estimate $L_{\mathrm{Bol,AGN}}$ (column 7 of Table 4.1) for those AGNs in our sample currently without good hard X-ray measurements. We use these $L_{\mathrm{Bol,AGN}}$ estimates to assess the relative mass accretion rates ($\eta \sim \mathrm{L_{Bol,AGN}/L_{Edd}}$) of the SMBHs in our $D < 15$ Mpc sample.

4.5 Results and Discussion

We have estimated $\mathrm{M_{BH}}$ and $L_{\mathrm{Bol,AGN}}$ for the 17 AGNs with $\mathrm{L_{IR}} > 3 \times 10^9\,\mathrm{L_\odot}$ at $D < 15$ Mpc. We find the AGNs in our sample have $\mathrm{M_{BH}} \approx (0.1\text{–}30) \times 10^7\,\mathrm{M_\odot}$ and $L_{\mathrm{Bol,AGN}} \approx (0.03\text{–}700) \times 10^{42}\,\mathrm{erg\,s}^{-1}$. Here we use the SMBH mass and AGN bolometric luminosity estimates derived in Sections 4.3 and 4.4, to investigate the relative mass accretion rates of these seventeen AGNs and use them to derive the average present-day growth times of SMBHs in the very nearby Universe. Furthermore, we evaluate the unique contribution that our new optically unidentified AGNs make to the space density of active SMBHs in the local Universe, which have until now been previously derived from large-scale optical surveys (e.g., H04; Greene & Ho 2007).

4.5.1 Derived AGN Properties and Relative Mass Accretion Rates

In Fig. 4.3, we plot $L_{\rm Bol,AGN}$ against our adopted $\rm M_{BH}$ estimates (the associated 1-σ errors for $\rm M_{BH}$ measurements are described in section 4.3) for the 17 AGNs in our volume-limited sample. $L_{\rm Bol,AGN}$ is inferred from either accurate intrinsic high-quality hard X-ray (2–10 keV) constraints (where available) or AGN-produced [OIV] $\lambda 25.80\ \mu$m emission (see § 4.4.1 and 4.4.2). The $L_{\rm Bol,AGN}$ 1-σ errors for the sources with hard X-ray constraints are the result of combining the uncertainty in the $L_{X,2-10keV}$ measurement with that of the mean spread in the bolometric correction factor employed from Marconi et al. (2004). For those AGNs with $L_{\rm Bol,AGN}$ derived from $L_{\rm [OIV]}$, the error is derived from the uncertainty in $L_{\rm [OIV]}$ as quoted in GA09 combined in quadrature with the intrinsic scatter of the empirical [OIV]–$L_{\rm bol,AGN}$ relation (Equation 4.4). We find that with the exception of NGC 5128 (Centaurus A), our sample is dominated by AGNs with SMBHs in the mass range $\rm M_{BH} \approx (0.1\text{–}5) \times 10^7\,M_\odot$ (median of $\rm M_{BH} \approx 7 \times 10^6\,M_\odot$). Due to the irregular structure of one of the galaxies in the sample (NGC 5195), $\rm M_{BH}$ is poorly determined; in Fig. 4.3 we plot $\rm M_{BH}$ estimates from both the M-σ_* and $\rm M_{BH}$–$\rm L_{K,bul}$ relations (connected blue-dashed line).

We find the AGNs in our sample are spread over a wide range of bolometric luminosities, $L_{\rm Bol,AGN} \approx 10^{40}$–$10^{45}\,\rm erg\,s^{-1}$. To assess the relative mass-accretion rates of the sample ($L_{\rm Bol,AGN}/L_{\rm Edd} \sim \eta$), we over-plot lines of constant Eddington ratios ($\eta \approx 10^{-3}, 10^{-1}, 1.0$; derived following Rees 1984) and their associated mass-doubling times ($t \approx 30, 0.3, 0.03$ Gyrs, respectively). Given the large range in bolometric luminosities, it is not surprising that the AGNs in the sample are found to be accreting at rates covering over 5 orders of magnitude ($\eta \approx 10^{-5}$–1). With the exception of a few AGNs, the observed range in Eddington ratios is found to be roughly consistent with those found by H04 for active galaxies (solid contours in Fig. 4.3).

As our work is not limited by the spectral resolution of the SDSS (i.e., with a limit of $\rm M_{BH} \gtrsim 3 \times 10^6\,M_\odot$), we show in Fig. 4.3 that significant accretion, $\eta > 10^{-3}$ (i.e., radiatively efficient accretion systems; e.g., thin discs) occurs onto SMBHs with $\rm M_{BH} \approx (1\text{–}3) \times 10^6\,M_\odot$. The majority of these low-mass, rapidly-accreting SMBHs are hosted in late-type, disc-dominated spiral galaxies (Sc–Sd). This is somewhat in conflict with the general assumption that gas-rich late-type spirals are preferentially inactive galaxies and that a large bulge may be a necessary component for the existence of a SMBH, and thus a luminous AGN (e.g., Ho97; Kauffmann et al. 2003a). Furthermore, of the four

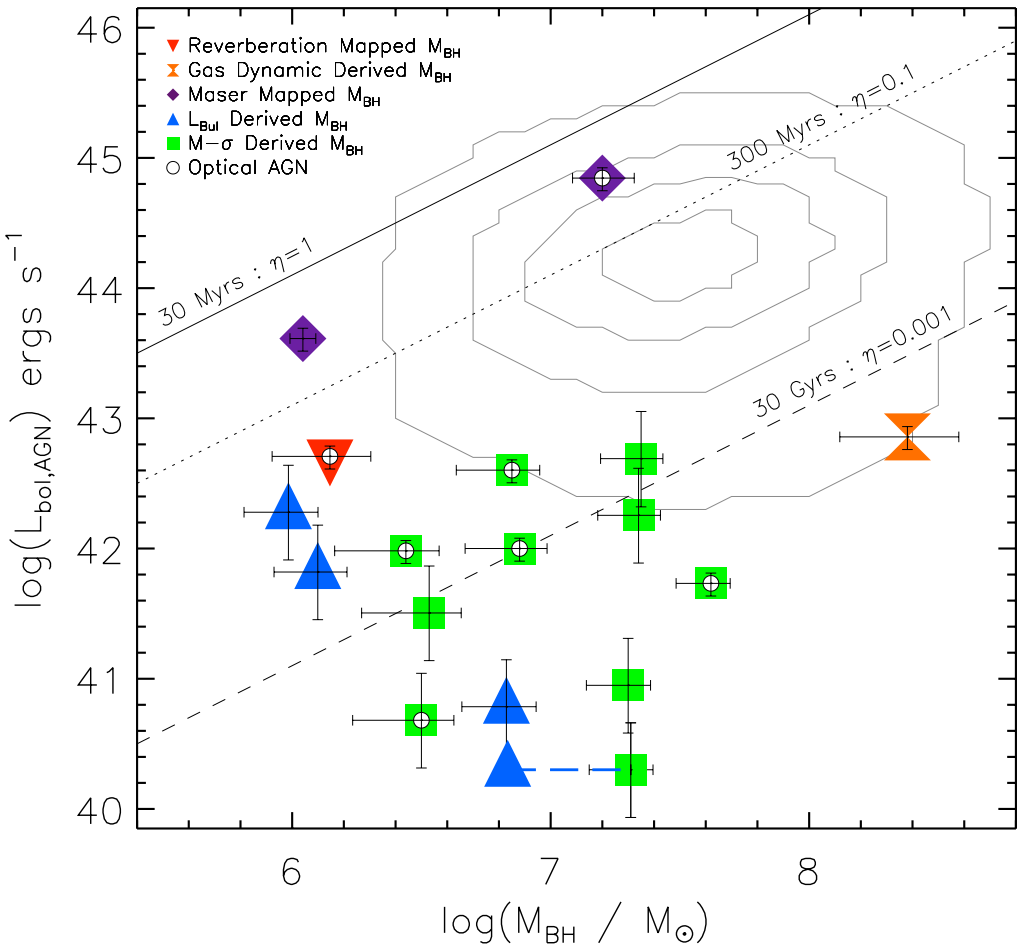

Figure 4.3: AGN bolometric luminosity ($L_{\rm Bol,AGN}$; in $\rm erg\,s^{-1}$) is plotted against SMBH mass ($\rm M_{BH}$) for the $D < 15$ Mpc mid-infrared identified AGNs presented in GA09 and Chapter 3. Associated 1–σ error bars for $\rm M_{BH}$ and $L_{\rm Bol,AGN}$ estimations are shown (see § 4.3.1 and § 4.5.1, respectively for details of their derivations). AGNs which are previously identified in optical surveys are highlighted with open circles. AGNs with $\rm M_{BH}$ estimates from reverberation mapping (downward triangles), gas dynamics (hour glass), maser mapping (diamond), the M–σ_* relation (squares) and the $\rm M_{BH}$–$\rm L_{K,bul}$ relation (upward triangles) are plotted. NGC 5195 is represented with both an upward triangle and square (with a dashed-line connector) as both of the $\rm M_{BH}$ estimates for this galaxy are highly uncertain given its irregular morphology. Constant ratios of Eddington luminosity and their implied SMBH mass-doubling times are illustrated for $\eta = 10^{-3}, 10^{-1}, 1$ (30 Gyrs, 300 Myrs and 30 Myrs; solid line, short-dash and long-dash, respectively). Contours are shown for the active galaxies in the SDSS optical survey of H04. In general, we probe lower SMBH masses and AGN luminosities than those of H04, and we find that the majority of these AGNs would not be detected using optical SDSS data alone.

AGNs within the sample with SMBHs consistent with $\mathrm{M_{BH}} \approx 10^6\,\mathrm{M_\odot}$, we find that three sources are not identified as AGNs in sensitive optical surveys. This suggests that significant SMBH growth occurs in low-mass systems without optical AGN signatures, which will be missed by statistically-large optical surveys such as H04 even if the spectral resolution was sufficient to identify SMBHs down to $\mathrm{M_{BH}} \approx 10^6\,\mathrm{M_\odot}$.

For the subset of our AGN sample which host SMBHs with $\mathrm{M_{BH}} \gtrsim 3 \times 10^6\,\mathrm{M_\odot}$, we find that many of the optically unidentified AGNs are accreting at relatively low Eddington ratios ($\eta \lesssim 10^{-3}$), and are unlikely to make a significant additional contribution to the present-day growth of SMBHs. However, these same AGNs may form part of a separate, underlying population of radiatively inefficient accretion systems such as advection dominated accretion flows (ADAFs; e.g., Narayan and Yi 1994) or those which contain optically-thick slim-discs. Further spectral analysis of the X-ray data may distinguish between these particular accretion systems, but is beyond the scope of these analyses.

4.5.2 The Present-Day Growth of SMBHs

Using the relative mass accretion rates estimated for our sample (Fig. 4.3), we can infer the volume-averaged growth time of SMBHs in the local Universe. Assuming a mean Kerr spin parameter (a) for our sample of $a \approx 0.67$ (e.g., Treister and Urry 2006; Hopkins et al. 2007), i.e., an accretion efficiency (ϵ) of ≈ 0.1, the characteristic mass doubling time (t_{2M}) of a SMBH accreting matter at the Eddington limit is $t_{2M} \approx 30$ Myrs (Rees 1984). Under the further assumption that a, and hence ϵ, does not vary significantly for changes in $\mathrm{M_{BH}}$ (King et al., 2008), we assess the present-day growth rate of SMBHs.[7] Following H04, we calculate and extend to lower masses ($\mathrm{M_{BH}} < 3 \times 10^6\,\mathrm{M_\odot}$) the integrated growth of SMBHs. Growth time errors are calculated from the log-normal standard deviations of the sample. We note here that we also include the optically unidentified AGNs which would not be identified in the SDSS.

In Fig. 4.4, we find that the mean growth time for low-mass SMBHs ($\mathrm{M_{BH}} \approx 10^6\,\mathrm{M_\odot}$) is $\approx 6^{+6}_{-3}$ Gyrs, which is consistent with these AGNs growing on time-scales similar to the age of the Universe. Our results are found to be broadly consistent with a simple extrapolation of the growth times calculated by H04 to $\mathrm{M_{BH}} \approx 10^6\,\mathrm{M_\odot}$ (dashed-line in Fig. 4.4). Thus, the AGNs hosting SMBHs in the mass range $\mathrm{M_{BH}} \approx 10^6$–$10^7\,\mathrm{M_\odot}$, which

[7] We note that the spin variation and spin directionality of SMBHs in AGNs is currently an ongoing area of research, and a consensus between groups has yet to be reached for an average value of the Kerr spin parameter; for example see Brenneman and Reynolds (2006), King et al. (2008) and Fabian et al. (2009).

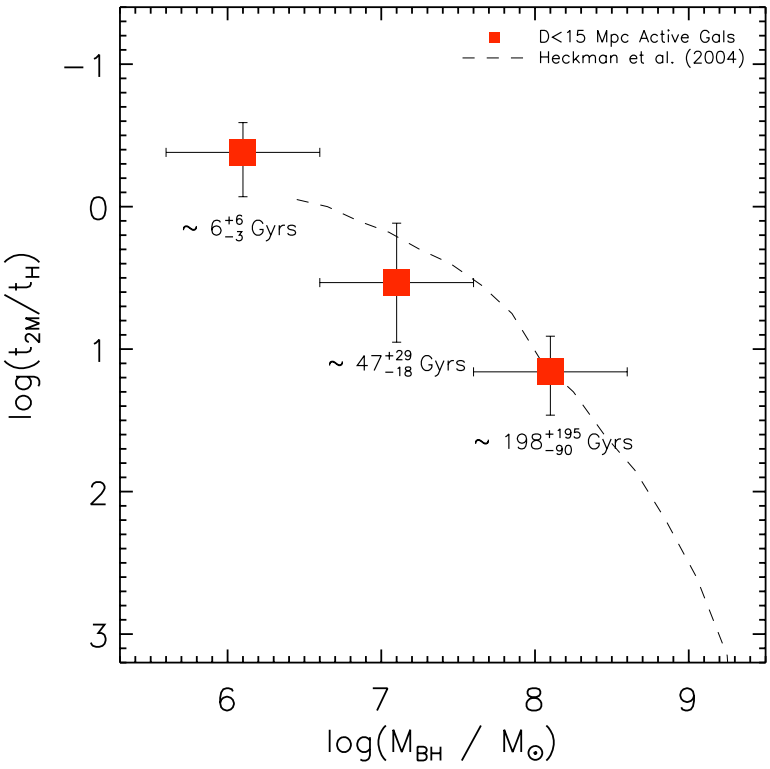

Figure 4.4: $\mathrm{M_{BH}}$ is plotted against the characteristic mean mass doubling time (t_{2M}) of a SMBH in units of Hubble-time (t_H) for the $D < 15$ Mpc AGNs. Growth time errors are calculated from the log-normal standard deviations of the sample. For comparison, the growth time function of H04 is shown (dashed curve). We find good agreement with H04 over the region $\mathrm{M_{BH}} \approx (0.3\text{–}10) \times 10^7\,\mathrm{M_\odot}$ and further extend the growth time constraints to lower SMBH masses ($\mathrm{M_{BH}} \approx 10^6\,\mathrm{M_\odot}$).

are dominated by optically unidentified AGNs (see Fig. 4.3), are acquiring a significant proportion of their mass in the present-day, and are amongst the most rapidly growing SMBHs in the local Universe. Furthermore, we find our derived growth times of SMBHs with $\mathrm{M_{BH}} \gtrsim 3 \times 10^6\,\mathrm{M_\odot}$ are in good agreement with those presented in H04, with mean growth times of $t_{2M} \approx 47^{+29}_{-18}$ and $\approx 198^{+195}_{-90}$ Gyrs for AGNs with $\mathrm{M_{BH}} \approx$ (0.3–3) and (3–30) $\times 10^7\,\mathrm{M_\odot}$, respectively.[8]

4.5.3 Space-Density of AGNs in the local Universe

An accurate active SMBH mass function, especially for lower mass SMBHs ($\mathrm{M_{BH}} \approx 10^6\,\mathrm{M_\odot}$), is crucial for determining the active SMBH mass density and the AGN fraction as a function of SMBH mass, these can then be used to extend our understanding of the role played by accretion in the growth of all SMBHs across cosmic time. In this section we calculate the space density of active SMBHs for our sample and compare it to complimentary optical studies of local narrow-line (NL; H04) and broad-line (BL; Greene & Ho 2007) AGNs, and the total mass function of local SMBHs by Marconi et al. (2004).

Following Greene & Ho (2007), in the top panel of Fig. 4.5 we plot the volume-weighted space density, Φ against $\mathrm{M_{BH}}$ in mass bins of 0.5 dex. The volume, V, encompassed by the GA09 sample to $D < 15$ Mpc is $V \approx 1.3 \times 10^4$ Mpc^3. In comparison to the active SMBH mass function containing the optically identified NL-AGNs of H04 (dotted line), we find a significantly larger space-density of SMBHs. We find that the space-density of active SMBHs identified in the mid-IR is roughly constant in the mass region $\mathrm{M_{BH}} \approx$ (0.9–90) $\times 10^6\,\mathrm{M_\odot}$ with a value of $\Phi \approx 6.3 \times 10^{-4}\,\mathrm{Mpc^{-3}\,logM_{BH}^{-1}}$. This space-density of AGNs is a factor of ≈ 10 greater than that estimated by H04 over the same $\mathrm{M_{BH}}$ range. Since we find only two (≈ 10 percent) of the 17 AGNs in our sample are sufficiently luminous/unobscured to be detected in the SDSS survey, we determine that this is consistent with our results. However, the space density derived here may still be a lower-limit for the abundance of NL-AGNs in the local Universe. A further examination of the (distance-model adjusted) Palomar survey suggests that at least four further NL-AGNs are not included in our volume-limited survey. Of these, two (NGC 3486; NGC 4565) lack high-resolution *Spitzer*-IRS spectroscopy of the central region (as noted in Table 3.2), one (NGC 3031; $\mathrm{L_{IR}} \approx 2.8 \times 10^9\,\mathrm{L_\odot}$) lies fractionally below our luminosity limit for this survey, and NGC 4258 is not included in the RBGS due to its extremely

[8] We note that our sample contains only one galaxy with $\mathrm{M_{BH}} \gtrsim 10^8\,\mathrm{M_\odot}$ (NGC 5128) and thus may not be representative for high $\mathrm{M_{BH}}$ systems.

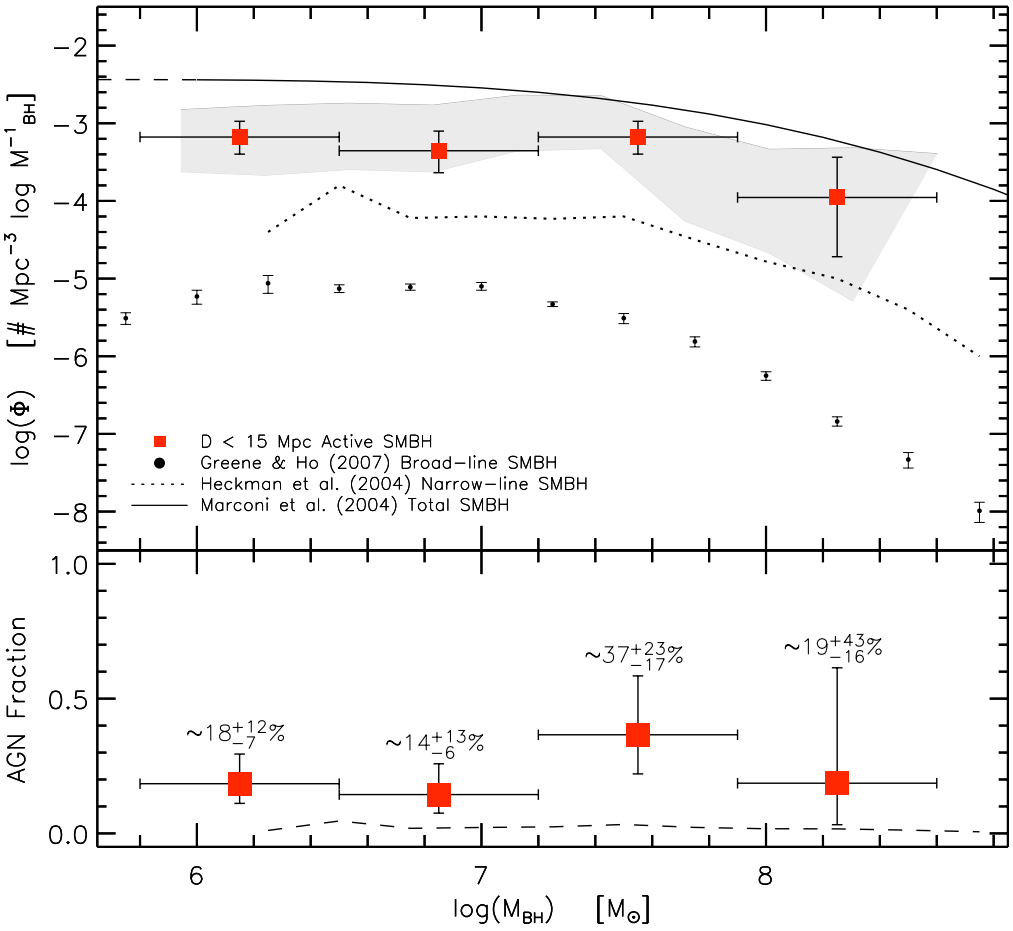

Figure 4.5: (Upper panel) Comparison of volume-weighted space densities of active SMBHs in the local Universe, Φ in units of number $\mathrm{Mpc}^{-3}\,\log \mathrm{M}_{\mathrm{BH}}^{-1}$. Mid-IR active SMBH function (filled squares; Goulding & Alexander 2009) is compared to the optically identified NL AGN function (dotted curve) of H04, the BL AGN function (filled circle) of Greene & Ho (2007), and total local SMBH mass function (active+inactive galaxies; solid curve; Marconi et al. 2004). Sample selection bias is analysed using a robust Monte-Carlo simulation (shaded region; see § 4.5.4.2). (Lower panel) Ratio of mid-IR active SMBHs to the total local SMBH mass function. The total SMBH mass function is extrapolated by 0.3 dex to $\mathrm{M}_{\mathrm{BH}} < 10^6\,\mathrm{M}_\odot$. For comparison the volume-weighted AGN fraction of H04 is also shown (dashed line). We estimate a mean volume-weighted local AGN fraction of $\approx 25^{+29}_{-14}$ percent over the range $\mathrm{M}_{\mathrm{BH}} \approx (0.5\text{–}500) \times 10^6\,\mathrm{M}_\odot$.

large angular size.

The derived volume-weighted space density for our active SMBHs (filled squares), which is dominated by NL-AGNs, is found to be significantly greater (a factor of ≈ 100) than the SMBH density of BL-AGNs (filled circles) presented in Greene & Ho (2007) in the mass region $\mathrm{M_{BH}} \approx (0.9\text{–}90) \times 10^6\,\mathrm{M_{\odot}}$. The significant increase in active SMBH density when compared to the BL-AGN density of Greene & Ho (2007) is partially to be expected due to the greater relative sensitivity of our *Spitzer*-IRS observations coupled with the greater abundance of observed Sy2 to Sy1 galaxies identified in the local Universe. However, this factor of ≈ 100 may not be a good indicator of the intrinsic Sy 1:Sy 2 ratio. Tommasin et al. (2010) find that the mid-IR spectroscopy of a small fraction of Seyfert 1 galaxies do not contain significant [NeV] $\lambda 14.32\ \mu\mathrm{m}$ emission. It is likely that the identification of low equivalent-width emission lines (such as [NeV] or [OIV]) in BL-AGNs is further complicated by a strong IR continuum emission which dominates the mid-IR regime. Hence, it is possible that by requiring the detection of [NeV] $\lambda 14.32\ \mu\mathrm{m}$ to infer AGN status, we may be rejecting broad-line objects, and thus finding a lower Sy 1:Sy 2 ratio than is representative in the local Universe.

4.5.4 Validation of derived space-density of active SMBHs

In this section we further consolidate our results by discussing possible limitations and additional sources of error which may exist in these analyses: 1) whilst the sensitivity of the data used in this survey is high, the volume considered is relatively small compared to that of the SDSS, thus our results may be subject to cosmic variance; 2) given the modest errors associated with the $\mathrm{M_{BH}}$ estimates, the adopted $\mathrm{M_{BH}}$ binning structure is likely to be subjective and thus degenerate towards objects scattering between the defined bins. Under these assumptions, in the following sub-sections we investigate whether the sample is indeed representative of the local Universe and discuss the construction of a Monte Carlo simulation to assess the effect of our adopted $\mathrm{M_{BH}}$ binning.

4.5.4.1 Is our sample representative of the local Universe?

Given the large incidence of AGNs within our sample it is possible that the volume considered in our sample is over-dense compared to other regions in the local Universe. The construction of the original sample of 64 bolometrically luminous galaxies in GA09 was designed to be complete down to the flux-limit of the Revised Bright Galaxy Sample.

This imposed a distance constraint of $D < 15$ Mpc (see Fig. 1 of GA09), and hence did not include the Virgo cluster at $D \approx 16$ Mpc, and thus our sample does not incorporate known local over-densities; however, this volume may still not be representative of the Universe at large.

To robustly test our considered volume ($V \approx 1.3 \times 10^4$ Mpc^3), we constructed the total SMBH space density function for all galaxies to $D < 15$ Mpc and compared this to the local total (active+inactive) SMBH mass function of Marconi et al. (2004) derived from the luminosity function of local galaxies. Given the large co-moving volume ($V_c \approx 1000$ Gpc^3) considered in Marconi et al. (2004), their derived SMBH mass function is unlikely to suffer from significant cosmic variance.

Our total SMBH mass function was formulated using all galaxies identified in the NASA/IPAC Extra-galactic Database (NED) to $D < 15$ Mpc with a total *K*-band luminosity of $L_{\rm K,gal} \gtrsim 1.5 \times 10^9\,{\rm L}_\odot$. The luminosity threshold is designed to include all galaxies which could potentially host a SMBH with ${\rm M_{BH}} \gtrsim 10^6\,{\rm M}_\odot$ (i.e., the lower limit of the SMBH masses for the AGNs in our sample) using the ${\rm M_{BH}}$–$L_{\rm K,bul}$ relation. This conservative lower limit assumes that $L_{\rm K,gal} = L_{\rm K,bul}$ (i.e., that all galaxies in the sample have an early-type galaxy classification). In reality, the majority of the sources identified in NED to $D < 15$ Mpc are late-type galaxies (i.e., $L_{\rm K,gal} \gg L_{\rm K,bul}$), and therefore some systems will have ${\rm M_{BH}} \ll 10^6\,{\rm M}_\odot$. To $D < 15$ Mpc, we identify 105 galaxies which potentially host a SMBH with ${\rm M_{BH}} \gtrsim 10^6\,{\rm M}_\odot$. To estimate ${\rm M_{BH}}$ in each of these galaxies, we relate the associated Hubble-type from the Third Reference Catalogue of Bright Galaxies (de Vaucouleurs et al., 1991) to a mean bulge/disc ratio (e.g., Benson et al. 2007) and establish an individual bulge luminosity based on galaxy-type and $L_{\rm K,bul}$. We convert the estimated bulge luminosity to ${\rm M_{BH}}$ using the ${\rm M_{BH}}$–$L_{\rm K,bul}$ relation and construct a total SMBH mass function. Whilst this rather crude estimation carries large associated errors, we still find very good agreement (a mean variance of 0.1 dex) with the SMBH mass function of Marconi et al. (2004) throughout the mass range ${\rm M_{BH}} \approx 10^6$–$10^9\,{\rm M}_\odot$. Thus, to first-order, our volume-limited sample does not appear to be over-dense and/or subject to strong cosmic variance, and hence, is broadly representative of the typical field-galaxy population in the local Universe.

We further validate this conclusion by estimating the active SMBH mass function for those AGNs which are sufficiently optically bright to be included in H04. Under this assumption, the derived space densities of active SMBHs for this sample and that of H04 should be comparable if our sample is indeed representative of a field-galaxy population.

We find that using the H04 detection limit inferred from Fig. 4.3, our new estimated space density is consistent with H04 ($\Phi \approx 10^{-4}$) throughout the mass range considered here ($\mathrm{M_{BH}} \approx (0.05\text{–}30) \times 10^8\,\mathrm{M_\odot}$), although there are still considerable uncertainties given the small number statistics inherent with our sample.

4.5.4.2 Monte Carlo Analysis of $\mathrm{M_{BH}}$ binning

We have established that our sample and the estimate of the SMBH mass density (both from active and inactive galaxies) do not appear to be subject to over-densities caused by cosmic variance. We therefore now investigate the effect of small-number statistics on our results, which are inherent in relatively small samples such as this.

In Fig. 4.5, the AGNs in the sample were placed into equal bins of $\mathrm{M_{BH}}$ with width 0.5 dex. However, this binning process does not allow for the error inherent to each individual $\mathrm{M_{BH}}$ measurement. Hence, some objects may scatter out of one defined bin and into another. The bin width we employ in our relatively modest sample (64 objects) may therefore be subjective and requires testing. Here we use a Monte Carlo analysis to assess the effect of the scattering of AGNs into different $\mathrm{M_{BH}}$ bins on the derived space density of active SMBHs in the local Universe (Φ).

Our Monte Carlo analysis calculates Φ by selecting a random set of SMBH masses from gaussian probability distributions constructed using our adopted $\mathrm{M_{BH}}$ masses and their associated 1-σ errors given in column 12 of Table 4.1. The binning structure was designed to incorporate at least one object in each bin from 250,000 realisations of the simulation across the considered mass range of the sample ($\mathrm{M_{BH}} \approx (0.5\text{–}500) \times 10^6\,\mathrm{M_\odot}$). We impose the upper mass limit as we have only one high-mass AGN (NGC 5128; $\mathrm{M_{BH}} \approx 2.4 \times 10^8\,\mathrm{M_\odot}$) in the sample. Thus, we determine that given our sample distribution the maximum number of equal width bins to be nine (i.e., equal bin sizes of 0.33 dex with $\gtrsim 1$ object). Hence, we use our simulation to conservatively assess the maximum error on our calculated space density of active SMBHs.

The error shown in Fig. 4.5 (shaded region) is the standard deviation of the 250,000 simulations in our volume-limited sample combined in quadrature with the Poisson error determined from the number counts in our real sample. We found 250,000 realisations to be sufficient, since at this level the maximum variation in the standard deviation over multiple runs was less than 10^{-6}.

We find that the mean spread in the derived value of Φ from our volume-limited sample is ≈ 0.85 dex, and as predicted appears to be subject to some scattering of $\mathrm{M_{BH}}$.

However, using our conservative error analyses, we show that the space density of active SMBHs found from our sample is consistently greater than that found for optical narrow-line AGNs (H04) with $\mathrm{M_{BH}} < 10^8\,\mathrm{M_\odot}$. Thus, to first-order, we find a significant increase (average factor of ≈ 9, a minimum factor of ≈ 2 and a maximum of ≈ 80) in the space density of active SMBHs in the local Universe in the mass range $\mathrm{M_{BH}} \approx (0.5\text{–}100) \times 10^6\,\mathrm{M_\odot}$ compared to H04; for $\mathrm{M_{BH}} > 10^8\,\mathrm{M_\odot}$ our errors increase significantly due to very limited source statistics (see § 4.4.1). We thus conclude that while this survey is subject to the scattering of objects through the $\mathrm{M_{BH}}$ bins, even in our most pessimistic case, we still find a significant increase in the space density of active SMBHs in the local Universe compared to that found in large-scale optical NL AGN studies.

4.5.5 The volume-weighted local AGN fraction

The ratio of the space densities of the active SMBH to total SMBH mass function (i.e., the volume-weighted local active SMBH fraction) is shown in the lower panel of Fig. 4.5. We calculate an overall active SMBH fraction of $\approx 25^{+29}_{-14}$ percent for SMBHs of $\mathrm{M_{BH}} \approx (0.5\text{–}500) \times 10^6\,\mathrm{M_\odot}$ down to our [NeV] completeness limit ($L_{[\mathrm{NeV}]} \gtrsim 10^{38}\,\mathrm{erg\,s^{-1}}$). We find that this fraction is consistent with being constant throughout this $\mathrm{M_{BH}}$ range. However, given our detection sensitivity limit, we are unable to probe lower Eddington ratios for AGNs hosting smaller SMBHs. Instead, we can also consider the effect of the AGN fraction for a fixed value of Eddington ratio (e.g., $\eta > 10^{-3}$; i.e., thin-disc accretion systems). We find an overall AGN fraction for sources with $\eta > 10^{-3}$ of $\approx 14^{+9}_{-5}$ percent. There is also tentative evidence that the AGN fraction ($\approx 16^{+9}_{-6}$ and $\approx 8^{+10}_{-5}$ percent) increases with decreasing SMBH mass ($\mathrm{M_{BH}} \approx 10^6$–$10^7\,\mathrm{M_\odot}$ and $\mathrm{M_{BH}} \approx 10^7$–$10^8\,\mathrm{M_\odot}$ bins, respectively) for SMBHs growing with $\eta > 10^{-3}$.

For the lowest-mass SMBHs ($\mathrm{M_{BH}} \approx (5\text{–}30) \times 10^5\,\mathrm{M_\odot}$), we estimate an overall non-negligible volume-weighted AGN fraction of 18^{+12}_{-7} percent, potentially showing that a considerable proportion of small bulge (and pseudo-bulge) galaxies (i.e., late-type spiral galaxies; Sc–Sd) host AGN activity. We assume here that the total SMBH mass function remains constant at $\mathrm{M_{BH}} < 10^6\,\mathrm{M_\odot}$.[9] It has been previously suggested by H04 and Greene & Ho (2007) that the AGN fraction may peak at $\mathrm{M_{BH}} \approx (0.7\text{–}2) \times 10^7\,\mathrm{M_\odot}$. However, with the inclusion of the additional low-mass optically unidentified AGNs (see

[9] We note that Page (2001) finds a marginal upturn in the SMBH mass function at $\mathrm{M_{BH}} < 10^6\,\mathrm{M_\odot}$ with the inclusion of a large population of dwarf spiral galaxies. This however, will have little impact on our resulting volume-weighted AGN fraction.

Fig. 4.3), we find that the AGN fractions are consistent with remaining constant or even increasing for $\mathrm{M_{BH}} < 10^7\,\mathrm{M_\odot}$. Hence, it appears that these low mass active SMBHs will not have been identified in optical AGN surveys.

As noted in § 4.5.3, the space-density of AGNs, and hence the local AGN fraction derived in this work, may only be a lower-limit given the nature of our volume-limited survey which by definition does not include IR-faint systems. To improve upon these current source statistics, a much larger sample of well-selected late-type spiral galaxies ($\gg 100$) would be required to investigate our findings further. Due to the demise of *Spitzer*-IRS this is no longer possible; however, with the greater sensitivity and resolving power of the next generation of space-based mid-IR spectrographs, for example the *Space Infrared Telescope for Cosmology and Astrophysics (SPICA)*[10] and the mid-IR instrument (MIRI) on-board the *James Webb Space Telescope (JWST)*[11], surveys such as these can be continued and extended to study more distant (i.e., greater volumes) and heavily obscured AGNs.

4.6 Summary

In this chapter we have presented the mean growth times and volume-weighted space density of active SMBHs in the local Universe. Our sample of 17 AGNs was derived from a sensitive volume-limited mid-IR spectral survey of all IR bright galaxies to $D < 15$ Mpc carried out using the NASA *Spitzer* Space Telescope (see GA09 and Chapter 3 for further details on the sample selection). The most accurate SMBH masses available for the objects are compiled from a variety of sources (i.e., reverberation mapping; maser mapping; gas kinematics; the M–σ_* relation). For the three AGNs without published $\mathrm{M_{BH}}$ estimates, we use a bulge/disc decomposition method to determine the bulge luminosity and hence a SMBH mass. The AGNs in our sample host SMBHs with $\mathrm{M_{BH}} \approx (0.1\text{–}30) \times 10^7\,\mathrm{M_\odot}$ (see § 4.3.1 and 4.3.2). Our main findings are the following:

(1). Using combined mid-IR emission line and high-quality hard X-ray constraints, we have derived accurate measurements of the intrinsic luminosities of our sample of AGNs (see § 4.4). In conjunction with the well-established SMBH measurements from previous studies and our own estimates from our aforementioned bulge/disc decomposition method, we have assessed the relative mass accretion rates of our

[10] See http://www.ir.isas.jaxa.jp/SPICA/

[11] See http://www.roe.ac.uk/uktac/consortium/miri/

sample. Due to our high sensitivity and the ability to probe low SMBH masses, we find that significant mass accretion ($\eta > 10^{-3}$) occurs onto SMBHs with $\mathrm{M_{BH}} \approx 10^{6}\,\mathrm{M_{\odot}}$, the majority of which would not be identified in even the most sensitive optical surveys. See § 4.5.1.

(2). Using our derived relative mass accretion rates for the sample and assuming a typical accretion efficiency of $\epsilon \approx 0.1$, we assessed the characteristic mean mass doubling times (t_{2M}) for AGNs in the very nearby Universe. For AGNs hosting SMBHs with $\mathrm{M_{BH}} \approx (0.5\text{–}50) \times 10^{7}\,\mathrm{M_{\odot}}$ we find consistent growth times ($t_{2M} \approx 47$–198 Gyrs) with those of the NL-AGNs identified in the SDSS (H04). However, we also find that SMBHs with $\mathrm{M_{BH}} < 5 \times 10^{6}\,\mathrm{M_{\odot}}$ (i.e., below the spectral resolution limit of the SDSS), are amongst the most rapidly growing SMBHs in the local Universe, with present-day growth times consistent with (and possibly less than) the current age of the Universe ($t_{2M} \approx 6^{+6}_{-3}$ Gyrs). See § 4.5.2.

(3). To assess the incidence of this population of low mass, rapidly growing SMBHs, we constructed a local space density function of active SMBHs. We find that active SMBHs may be at least a factor ≈ 2 more common than previously identified in NL-AGN surveys using SDSS data. Furthermore, we estimate a non-negligible space density for low mass active SMBHs ($\mathrm{M_{BH}} \approx 10^{6}\,\mathrm{M_{\odot}}$) of $\Phi \approx 6 \times 10^{-4}\mathrm{Mpc}^{-3}\,\log \mathrm{M_{BH}^{-1}}$ which is consistent with the space density of more massive active SMBHs ($\mathrm{M_{BH}} \approx 10^{7}\,\mathrm{M_{\odot}}$; i.e., those previously determined to be the most rapidly accreting population of SMBHs). See § 4.5.3

(4). Using a local total SMBH mass function (Marconi et al. 2004), we estimate a mean volume-weighted local AGN fraction of $\approx 25^{+29}_{-14}$ percent, which remains relatively constant in the mass range $\mathrm{M_{BH}} \approx (1\text{–}10) \times 10^{6}\,\mathrm{M_{\odot}}$. However, when only considering the SMBHs with $\eta > 10^{-3}$ (i.e., radiatively efficient thin-accretion disc systems), we find an overall AGN fraction of $\approx\approx 14^{+9}_{-5}$ percent and also tentative evidence for an increasing AGN fraction ($\approx 16^{+9}_{-6}$ and $\approx 8^{+10}_{-5}$ percent) with decreasing SMBH mass (for $\mathrm{M_{BH}} \approx 10^{6}$–$10^{7}\,\mathrm{M_{\odot}}$ and $\mathrm{M_{BH}} \approx 10^{7}$–$10^{8}\,\mathrm{M_{\odot}}$, respectively). See § 4.5.5

Chapter 5

The incidence of [NeV]λ3427Å detected active galactic nuclei in the Sloan Digital Sky Survey

5.1 Introduction

Optical emission line classification schemes, such as those proposed by Baldwin, Phillips & Terlevich (1981; hereafter, BPT diagrams) are widely used throughout the current literature. Galaxies which are classified as AGNs on the basis of their optical spectroscopy are found to produce strongly photoionised emission lines such as [OIII] λ5007Å, [OI] λ6300Å, [NII] λ6585Å and [SII] λ6731Å. Selection boundaries to separate strongly star-forming galaxies from AGNs and LINERs have been proposed by several groups (e.g., Kewley et al. 2001, 2006; Kauffmann et al. 2003a; Schawinski et al. 2007) based primarily on the use of wide-scale optical surveys (e.g., the SDSS). However, these optical AGN classification schemes are: (1) defined by theoretical modeling in radiative transfer codes (e.g., Kewley et al. 2001); and (2) potentially biased against smaller, dust-rich galaxies. Hence, they remain observationally and robustly untested for their completeness towards the identification of all potential AGNs (e.g., they may not include the most heavily-obscured and/or composite systems).

Recently, using sensitive mid-IR observations from *Spitzer*-IRS spectroscopy, GA09 (see also Chapter 3) conservatively used [NeV] λ14.32 μm as a robust indicator of AGN activity. They found a large population of AGNs which lie below the maximum starburst limit of Kewley et al. (2001), i.e., they are not unambiguously identified as AGNs based

on solely traditional optical BPT diagnostics. These AGNs were shown to be hosted in very late-type galaxies (Hubble-type Sc–Sd) with AGN signatures which appear to be strongly dust extinguished at optical wavelengths. These optically unidentified AGNs were identified in an extremely local ($D < 15$ Mpc) volume-limited sample of bolometrically luminous ($L_{\rm IR} \gtrsim (0.3\text{–}20) \times 10^{10}\,{\rm L}_{\odot}$) galaxies, and as such the locality of these AGNs suggests they cannot be rare objects (see Chapter 3). Indeed, similar results have also been found using *Spitzer*-IRS by Satyapal et al. (2008) and Bernard-Salas et al. (2009) for late-type spiral galaxies identified in the Palomar optical spectroscopic survey (Ho97) as HII or LINER galaxies. Taken together, these observations suggest that there may be a large population of AGNs which are currently being missed in large scale optical surveys using current emission-line selection methods.

Due to the extreme conditions required to produce the high ionisation emission line [NeV] (97.1 eV), its detection in a galaxy spectrum provides unambiguous evidence for the existence of nuclear accretion (e.g., Schmitt 1998). Despite [NeV] emission being a factor ≈ 9 weaker than [OIII] λ5007Å , the optical [NeV] λ3427Å emission line is commonly observed in nearby Seyfert galaxies (see Storchi-Bergmann et al. 1995; Erkens et al. 1997 and references there-in). More recently, Gilli et al. (2010) has used [NeV] λ3427Å to identify potential Compton-thick QSOs at $z \sim 1$ based on their apparent weakness at X-ray energies. Such techniques could be applied globally in order to understand the fraction of obscured AGN activity across cosmic time. However, sample biases due to selection on the basis of high ionisation emission are currently poorly understood. In this chapter, we use [NeV] λ3427Å detected in Sloan Digital Sky Survey spectroscopy to: (1) test the use of currently accepted optical AGN-selection processes; (2) identify the fraction of local Seyfert galaxies with detected [NeV] λ3427Å emission lines; and (3) attempt to reconcile the discrepancy between optical AGN selections and the large population of optically unidentified AGNs found in mid-IR spectroscopic studies. Throughout this chapter we adopt a standard ΛCDM cosmology of $H_0 = 71\,{\rm km\,s^{-1}}$ Mpc^{-1}, $\Omega_M = 0.30$ and $\Omega_{\Lambda} = 0.70$.

5.2 Sample Selection and Optical Classification

Our sample of local galaxies is selected from the SDSS-DR7 (Abazajian et al. 2009). We select all spectroscopically targeted galaxies in the redshift range $z \sim 0.14$–0.31. In this redshift region the [NeV] λ3427Å emission line is redshifted into the spectral range of

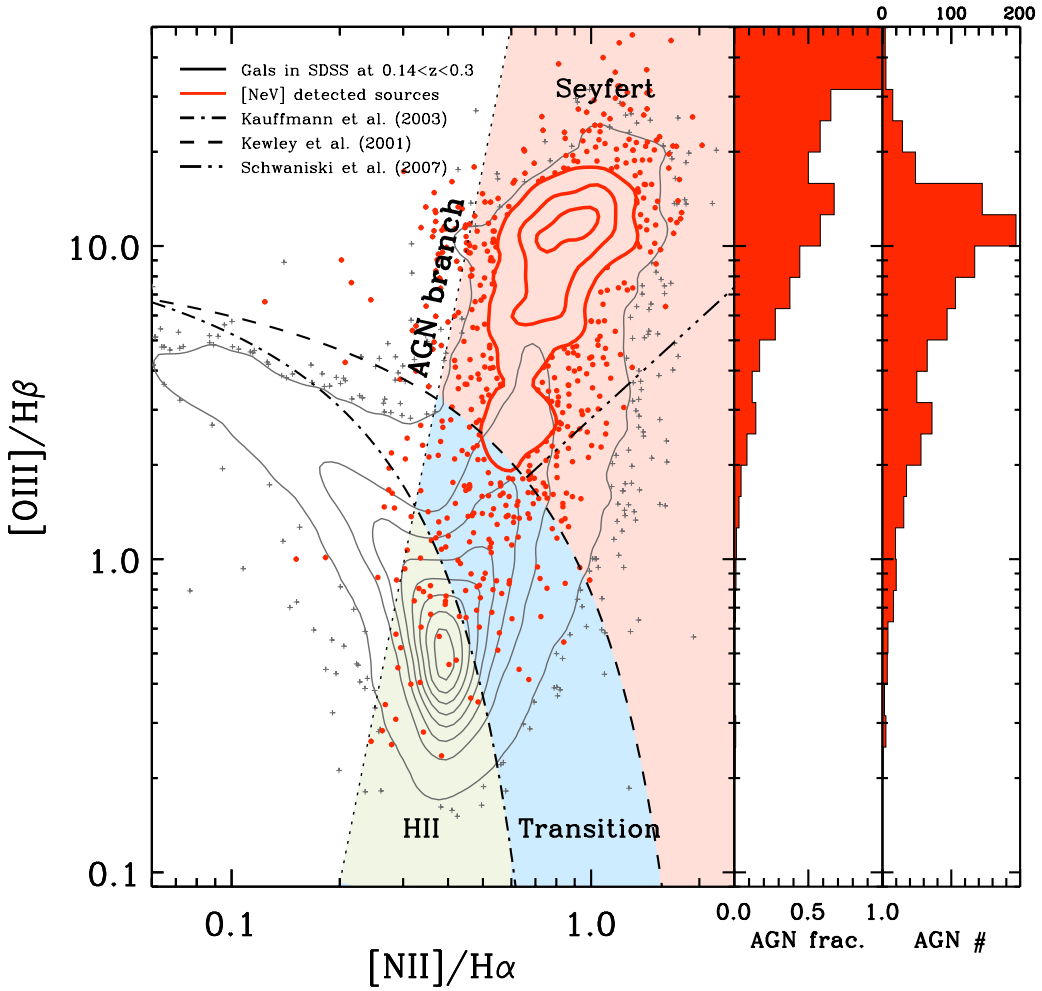

Figure 5.1: **Left panel:** Optical emission line diagnostic diagram presenting all galaxies which are spectroscopically identified (S/N $>$ 5) in the SDSS-DR7 at $z \sim 0.14$–0.31 (grey contours; small grey crosses). The empirical HII classification scheme presented by Kauffmann et al. (2003a), the theoretical maximum starburst limit of Kewley et al. (2001), and the AGN-LINER separation of Schawkinski et al. (2007) are shown with dash-dot, dashed and dot-dash-dot lines, respectively. We additionally over-plot all galaxies with 5σ detections of the AGN-produced [NeV] λ3427 emission-line (thick red contours; filled red dots). **Right panels:** Fraction and number of [NeV]λ3427 detected AGN as a function of the [OIII]/Hβ ratio rightward of the AGN-branch in the BPT diagram.

the SDSS ($\lambda \sim$ 3800–9200 Å), whilst the individual spectroscopy will also still contain the Hβ, [OIII] λ5007, [NII]$\lambda\lambda$6550,6585 and Hα complex used during our classification process. Additionally, in order to reduce the possibility for the inclusion of false detections of emission lines, which may occur due to the poor efficiency of the detector at the bluest wavelengths, we have chosen a wavelength range with good spectroscopic sensitivity, $\lambda \sim$ 3890–8600Å (i.e., an emission throughput of > 0.1). Our total sample contains 18,059 galaxies.

To robustly classify our sample of galaxies in the optical regime, we select only those galaxies with well-detected emission lines (signal-to-noise ratios $\gtrsim 5$ and equivalent width > 0) in a traditional BPT diagram. We remove from our sample all galaxies which may contain broad-emission features (here defined as full-width half-maximum $> 700\,\mathrm{km\,s^{-1}}$) in Balmer emission lines (i.e., Hα; Hβ), as these sources are very likely to be Type-1 AGNs and cannot be classified using BPT emission-line diagnostics.

5.2.1 The fraction of [NeV] detected galaxies in the SDSS-DR7

In Fig. 5.1 we show our parent sample of all narrow-line galaxies detected in the SDSS-DR7 at $z \sim 0.14$–0.31. We separate the BPT diagram into three distinct regions: (1) the HII region, i.e., those galaxies which lie below the canonical separation between star-forming and active galaxies (Kauffmann et al. 2003a); (2) the classical Seyfert galaxy region, here defined as all galaxies which lie above the theoretical maximum starburst limit of Kewley et al. (2001a); and (3) the intermediate 'transition' region bounded by the Kauffmann et al. (2003a) and Kewley et al. (2001) demarcations. We find 1226 ($\approx 6.8 \pm 0.2$) galaxies have significant detections (S/N > 5) of the [NeV] 3427Å emission line, we here define these [NeV]-detected sources as unambiguous AGNs.

We isolate all galaxies which lie rightward of the AGN-branch in the BPT diagram (i.e., those which do not follow the star-forming demarcation curve of Kauffmann et al. 2003a), we find a rising percentage of galaxies with detected [NeV] 3427Å emission originating from the maximum starburst limit and peaking significantly in the Seyfert region with an AGN fraction of ≈ 68 percent; whilst the [NeV] 3427Ådetected fraction in the HII and transition region is < 2 percent.[1] Hence, using [NeV] as unambiguous AGN indicator, we find good empirical evidence that the theoretical starburst limit of Kewley et al. (2001) provides a robust selection-cut for Seyfert galaxies. We find an overall [NeV]

[1]We note that the [NeV]-detected fraction presented in Fig. 5.1 does become consistent with ≈ 100 percent at [OIII] $/H\beta \gtrsim 30$, though source statistics become limited in this region of parameter space.

-detected AGN fraction in the Seyfert region of $\approx 27 \pm 4$ percent. In Section 5.3.2.1, we investigate the ≈ 70 percent of Seyfert galaxies which lack significant [NeV] detections.

In Fig. 5.1 we additionally show the separation line between LINER and Seyfert galaxies suggested by Schawinski et al. (2007). Whilst it is clear that this boundary does exclude the main population of [NeV] detected Seyfert galaxies, to within 0.1 dex of this cut, the fractional density of [NeV] detected AGNs is roughly equal. This suggests that based on the current empirical separation, a substantial fraction of Seyfert galaxies may be incorrectly classified as LINERs. However, given our poor source number statistics at the locus of the transition–Seyfert–LINER regions, revision of the Seyfert–LINER classification scheme is beyond the scope of these analyses.

In section 5.3 we investigate the nature of [NeV] detected AGNs throughout the BPT diagram using large source number spectral stacking analyses and emission-line diagnostics, as well as using these results to place further constraints on the population of [NeV] ($14.32\ \mu$m) detected AGNs which are not optically classified as Seyfert galaxies.

5.3 Results and Discussion

5.3.1 What are the spectral properties of [NeV] λ3427Å (un-)detected sources in BPT diagrams?

In the previous section we established that the majority of [NeV] detected sources in the SDSS-DR7 have optical emission-line ratios consistent with Seyfert galaxies. However, we also showed that ≈ 2 percent of sources in the transition and HII region also contain significant detections of [NeV] emission. Here we investigate the spectral properties of these [NeV] emitting sources in order to place new constraints on the ubiquity of optically classified AGNs in the the SDSS.

For each of the galaxies in our parent SDSS-DR7 sample (see section 5.2 and Fig. 5.1) we have retrieved the 1-dimensional spectral products from the SDSS-DR7 data archive server. In recent releases of the SDSS data products, significant improvements have been implemented for the wavelength calibrations of the available spectroscopy (see Adelman-McCarthy et al. 2008; Abazajian et al. 2009). These new calibrations allow us to produce accurate composite spectra (i.e., spectral stacks) of the average galaxy populations in the three highlighted regions of the BPT diagram (i.e., HII, transition and Seyfert) presented in Fig. 5.1. We normalize each individual spectrum to the average continuum emission at $\lambda \sim 3435$–3440Å and produce spectral stacks of sources in each BPT region

with and without 5σ detections of [NeV] λ3427. See Fig. 5.2.

5.3.1.1 Galaxies with detected [NeV] λ3427Å emission lines

In Fig. 5.3 we show the emission-line profiles produced in the spectral stacking process. We find that the relative flux of the [NeV] and [OIII] emission-lines in the [NeV] detected Seyferts are a factor $\gtrsim 5$ greater than the fluxes measured in the HII and transition regions galaxies with detected [NeV] emission lines. See Table 5.1. Furthermore, we find that the [NeV] and [OIII] line-profiles are relatively symmetric in the Seyfert galaxies; however, for the HII and transition galaxies, we find a systematic blue-wards shift in the [NeV] profiles (≈ 260 and $\approx 175\,\mathrm{km\,s^{-1}}$ for the HII and transition region AGNs, respectively) as well as asymmetric blue wings in both the [NeV] and [OIII] emission-lines. Although we stipulate for selection that the [NeV] emission line must be at least $S/N \gtrsim 5$ as defined by the SDSS fitting routines, we find that the stack of the [NeV]-detected HII region galaxies is not consistent with containing a formal 3σ detection of the [NeV] emssion line. Inspection of the individual SDSS spectra for the 32 galaxies with so-called [NeV] detections shows that a minority contain very narrow (≈ 1 pixel wide) noisy emission features at $\approx$ 3426–3428Å which have been incorrectly associated with [NeV] emission. The resulting spectral stack co-adds these noisy emission features with real [NeV] detections in other spectra to produce an artificially broadened [NeV] profile which is poorly fit by a gaussian profile, and hence we calculate only a 3σ upper-limit for the [NeV] -detected HII region galaxies. Both of these detected features are indicative of large outflowing winds being produced by a rapidly accreting central source often found in narrow-line Seyfert 1 galaxies (e.g., Boroson and Oke 1987; Bian et al. 2005). Indeed, when comparing the Hβ profiles between [NeV] detected Seyfert and HII region galaxies, we find that in order to model the profile of the [NeV] detected HII galaxies a second component with full-width half maximum of $\approx 1000\,\mathrm{km\,s^{-1}}$ is required, suggesting these sources may in fact be narrow-line Seyfert 1 galaxies which have been incorrectly modeled during spectral fitting by the SDSS-DR7 pipeline. Hence, the detection of [NeV] λ3427Å emission in non-Seyfert region galaxies may be an efficient method to select narrow-line Seyfert 1 systems in large-scale optical surveys.

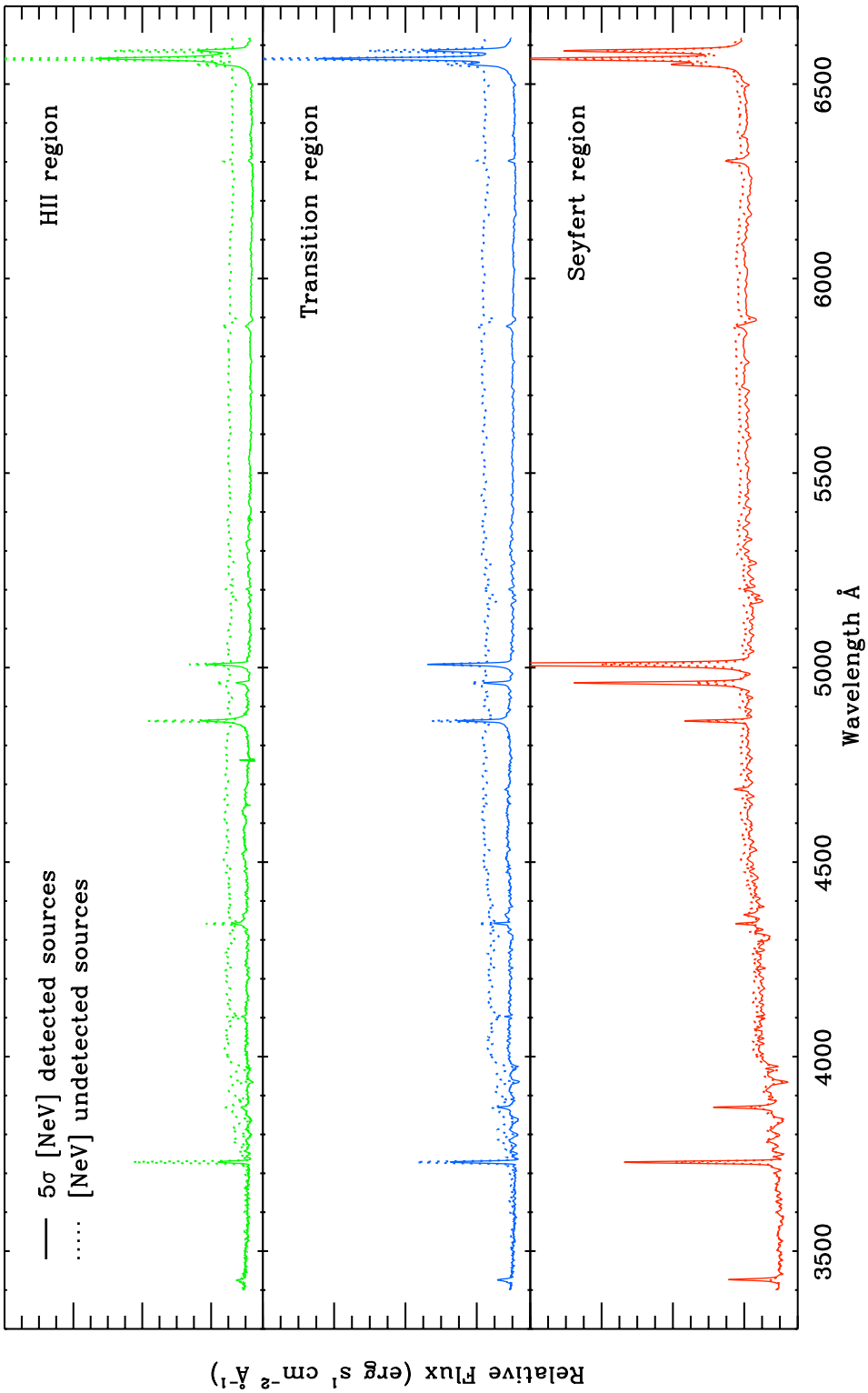

Figure 5.2: Composite optical spectra for the galaxies at $z \sim 0.14$–0.31 in our SDSS-DR7 sample. Stacked spectra for [NeV] detected (5σ) galaxies in the HII star-forming, transition and Seyfert regions of Fig. 5.1 are shown in the upper (green), middle (blue) and lower (red) panels, respectively.

Table 5.1: Stacking analysis results

Region	[NeV] detected?	#	z	$F_{[\mathrm{NeV}]}$ ($\mathrm{erg\,s^{-1}}$)	$F_{[\mathrm{OIII}]}$ ($\mathrm{erg\,s^{-1}}$)	$\frac{\mathrm{H}\alpha}{\mathrm{H}\beta}$	$L_{[\mathrm{NeV}]}$ ($\mathrm{erg\,s^{-1}}$)	$L_{[\mathrm{OIII}]}$ ($\mathrm{erg\,s^{-1}}$)
(1)	(2)	(3)	(4)	(5)	(6)	(7)	(8)	(9)
HII	$\surd$	32	0.19	< -15.34	-14.88	3.88	< 41.12	41.42
HII	$\times$	6280	0.17	< -15.76	-15.43	6.15	< 41.56	41.48
Transition	$\surd$	114	0.19	-15.42	-14.75	4.95	41.49	41.88
Transition	$\times$	5367	0.17	< -15.79	-15.32	7.52	< 41.92	41.85
Seyfert	$\surd$	1016	0.18	-15.28	-14.21	5.91	42.08	42.86
Seyfert	$\times$	2720	0.18	< -15.85	-14.88	7.86	< 42.02	42.35

NOTES: (1) Region of BPT diagram for stacked objects; (2) Based on the SDSS spectral analysis routine, are these objects determined to have [NeV]λ3427 in their spectroscopy at $S/N > 5$; (3) Number of objects in the stack; (4) Average redshift of objects in the stack; (5–6) Logarithm of observed measured flux from stack in $\mathrm{erg\,s^{-1}}$; (7) Average $H\alpha/H\beta$ ratio from stack; (8–9) Logarithm of dereddened luminosity based on our chosen cosmology and assuming an intrinsic ratio of $H\alpha/H\beta = 3$ in $\mathrm{erg\,s^{-1}}$.

5.3.1.2 Galaxies with non-detections of [NeV] λ3427Å emission lines

In Fig. 5.2 we additionally show the average spectral stacks of the galaxies in the HII, transition and Seyfert regions which lack significant detections of [NeV] emission. As with the [NeV] detected sources, we find that the Seyfert galaxies have rising continua towards higher wavelengths. In Fig. 5.3 we show that within the stacked spectrum we clearly recover a weak ($\approx 2.7\sigma$) [NeV] signal at λ3427Å for the optical Seyfert galaxies with formally undetected [NeV] emission. This suggests a lack of sensitivity possibly due to extinction or detector efficiency and/or low intrinsic AGN luminosity which prevents the detection of the relatively weak [NeV] emission line in the individual source spectroscopy; we investigate this further in the next section. By contrast to the Seyfert galaxies, we find little or no evidence for hidden [NeV] emission in the spectral stacks for transition (or HII) region galaxies where we find relatively flat continua with low RMS scatter at $\lambda \sim 3427$Å.

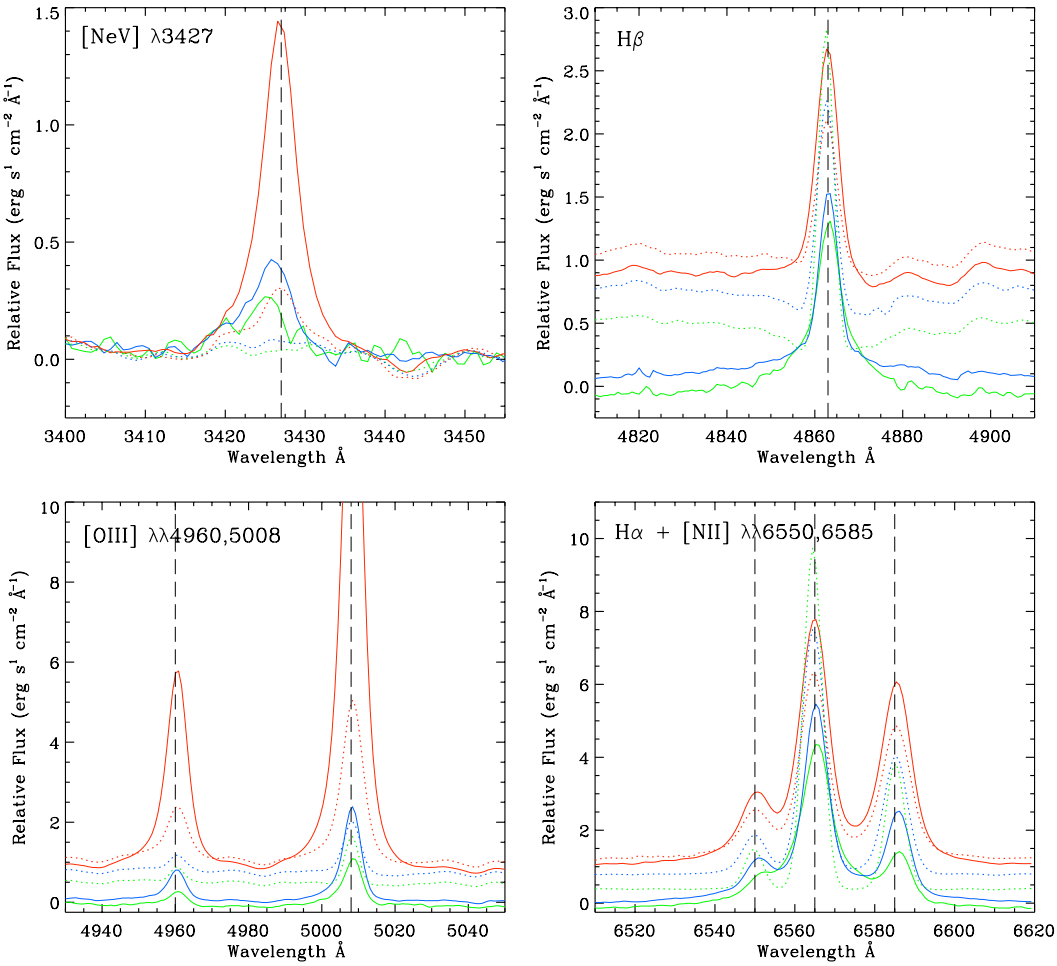

Figure 5.3: Optical spectral stacks expanded around the [NeV] λ3427 (top-left), Hβ (top-right), [OIII] $\lambda\lambda 4960, 5007$ (bottom-left) and Hα+[NII]$\lambda\lambda 6550, 6585$ (bottom-right) emission lines. Spectral stacks for [NeV] detected (non-detected) sources in the Seyfert, transition and HII regions are shown with solid (dotted) red, blue and green lines, respectively. Optical Seyferts with significantly detected [NeV] emission appear to produce strong [OIII] emission as well as narrow Balmer lines. By contrast, [NeV] detected sources in the transition and HII regions contain significantly weaker high-ionisation emission lines, and produce Balmer lines with broadened secondary components (FWHM $\approx 1000\,\mathrm{km\,s^{-1}}$), indicative of narrow-line Seyfert 1 galaxies.

5.3.2 Why do the SDSS spectra for the majority of Seyfert galaxies not contain significant [NeV] λ3427Å emission?

Approximately seventy percent of the Seyfert galaxies in our SDSS-DR7 parent sample lack significant [NeV] emission in their optical spectroscopy despite its expected production being relatively ubiquitous throughout AGNs (Veilleux and Osterbrock, 1987; Osterbrock and Ferland, 2006). Here we investigate whether the non-detection of high-ionisation signatures in these optical AGNs are due to: (1) observational sensitivity; (2) the AGNs being intrinsically less luminous; and/or (3) host-galaxy dust extinction.

5.3.2.1 Does poor observational sensitivity prevent the detection of [NeV] λ3427Å signatures in the majority of Seyfert galaxies?

Here we test the use of [OIII] emission to infer the expected [NeV] $\lambda3427\,$Å emission in [NeV] undetected Seyfert galaxies, and use this to place constraints on the fraction of optical Seyfert galaxies in the SDSS-DR7 which should have detected [NeV] $\lambda3427$Å emission lines, or alternately, estimate the fraction of AGNs which are not flux-limited. In Fig. 5.4 we present a luminosity-luminosity plot for the sources in our SDSS-DR7 parent sample with 5σ detected [NeV] and [OIII] emission lines. Distances are calculated using our chosen cosmology. As dust reddening is a function of wavelength, any dust present in these individual systems will affect the [NeV] emission more severely than the longer wavelength [OIII] emission lines. We have corrected the presented [NeV] and [OIII] luminosities for dust reddening using the Balmer decrement (i.e., the Hα/Hβ ratio), assuming an intrinsic ratio of 3.0 and a typical Cardelli et al. (1989) ISM extinction curve. Using the IDL ROBUST_LINEFIT regressional analysis routine we produce a best-fit to the data. For a fixed temperature, the extinction-corrected optical [NeV] $\lambda3427$ and mid-IR and [NeV] $\lambda14.32\ \mu$m emission lines are found to be in an $approx1:1$ ratio, hence we find excellent agreement with the analogous mid-IR relation given in Equation 3.1. This suggests that extinction-corrected [NeV] $\lambda3427$ is a good indicator of AGN luminosity as predicted by Gilli et al. (2010). Hence, we may use the measured [OIII] flux from the SDSS-DR7 fits and our regressional analysis for Type-2 AGNs to predict the fraction of sources formally lacking [NeV] detections which lie below the flux-limit of SDSS spectroscopy ($f_{[\mathrm{NeV}]} \gtrsim 1.3 \times 10^{-16}\,\mathrm{erg\,s^{-1}}$).

Based on the flux limit of the SDSS we would expect to detect [NeV] emission in only 1864 (≈ 50 percent) of the 3736 Seyfert galaxies in our sample. Therefore, we suggest

that the majority of Seyfert galaxies lacking significant detections of [NeV] emission at optical wavelengths are missed due to sensitivity limits within the SDSS spectroscopy. However, we also predict that the SDSS spectroscopy for the remaining ≈ 20 percent of sources should contain clear detections of the [NeV] emission line. Hence, whilst sensitivity limitations plausibly explain the lack of [NeV] in ≈ 50 percent of Seyfert galaxies it does not fully explain the non-identification of [NeV] in all Seyferts.

5.3.2.2 Do Seyfert galaxies which lack significant [NeV] emission host significantly less luminous AGNs?

The non-identification of [NeV] in a non-negligible fraction of Seyfert galaxies could be due to them being intrinsically less luminous AGNs, where-by the AGN emission is substantially diluted by the host-galaxy. In Fig. 5.4 we over-plot the average dereddened [OIII] and [NeV] luminosities (see Table 5.1) found from fitting the emission features in our spectral stacking analyses for the sources in the HII, transition and Seyfert regions of Fig. 5.1.

We find that based on our spectral stacks the mean [NeV] and [OIII] luminosities ($L_{[\mathrm{NeV}]} \approx 1.1\times10^{42}\,\mathrm{erg\,s^{-1}}$; $L_{[\mathrm{OIII}]} \approx 6.0\times10^{42}\,\mathrm{erg\,s^{-1}}$) for [NeV] detected Seyfert galaxies are in excellent agreement with the [NeV] –[OIII] relation. However, these luminosities are a factor ≈ 2 greater than the median luminosities of the whole Seyfert galaxy sample, suggesting that [NeV] detected Seyferts may be higher luminosity AGNs. Indeed, for those Seyfert galaxies lacking formal 5σ detections, we find a systematically lower [OIII] luminosity ($L_{[\mathrm{OIII}]} \approx 2.5 \times 10^{42}\,\mathrm{erg\,s^{-1}}$) which is more consistent with the bulk of the Type-2 Seyfert galaxy population.

We additionally find that the [NeV] undetected Seyferts are a factor ≈ 4 and 20 greater in [OIII] luminosity than the HII and transition region galaxies, respectively. Hence, as sources with much lower [NeV] and [OIII] luminosities are detected in galaxies with arguably greater contributions from star-formation activity (i.e., HII galaxies), we surmise that host-galaxy dilution is unlikely to be a dominant factor with regards to the detection of [NeV] emission.

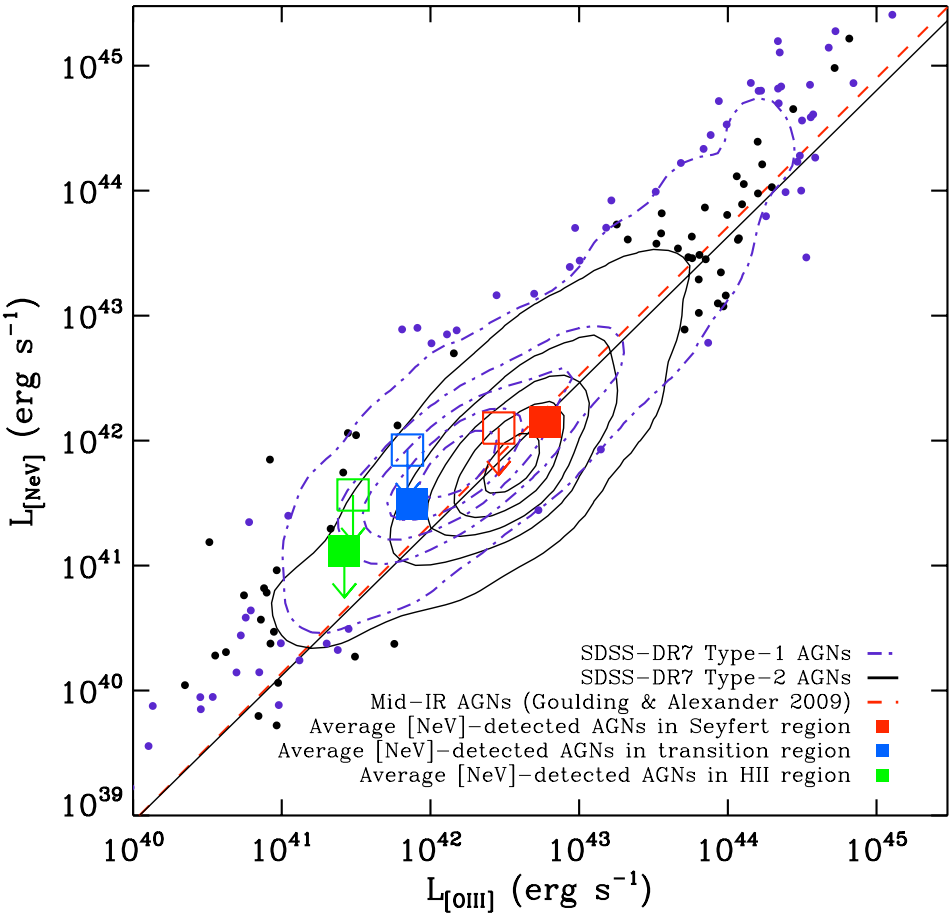

Figure 5.4: Luminosities of [NeV] λ3427Å versus [OIII] λ5007Å for Seyfert 1 (dot-dashed contours) and Seyfert 2 (solid contours) galaxies in the SDSS-DR7 at $z \sim 0.14$–0.31. Fluxes have been corrected for dust-extinction using the Balmer decrement. The [NeV] (14.32 μm)–[OIII] λ5007Å correlation (red dashed line) of Goulding & Alexander (2009) is found to be consistent with the [NeV] λ3427Å–[OIII] λ5007Å relation derived here from optical spectroscopy (solid line). We additionally show the luminosities derived from our composite spectra for Seyfert (red), transition (blue) and HII (green) galaxies with detected (filled square) and non-detected (open square) [NeV] λ3427Å emission lines.

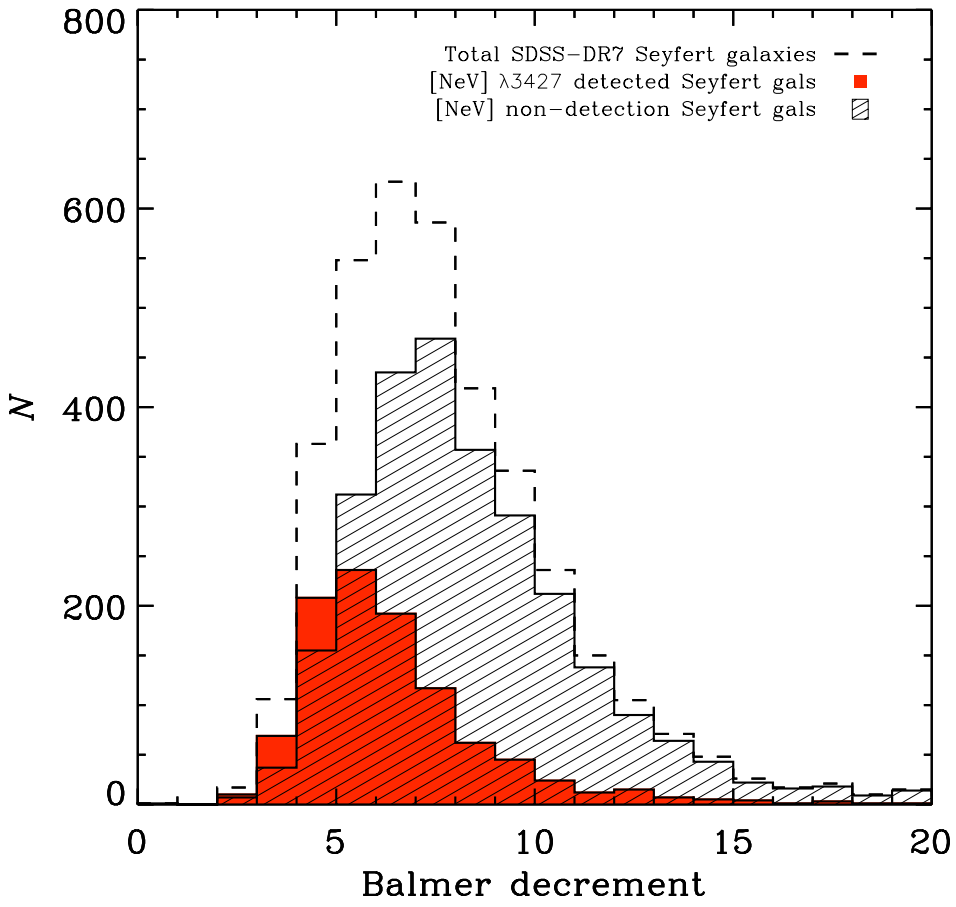

Figure 5.5: A histogram of the distributions of Balmer decrements for the Seyfert galaxies in our SDSS-DR7 parent sample (dashed-line), [NeV] λ3427Å (5σ) detected (filled histogram) and non-detected Seyfert galaxies (hashed histogram). The Seyfert galaxies lacking significant detections of [NeV] are systematically shifted to higher Balmer decrements, suggesting they are hosted by galaxies with greater dust content.

5.3.2.3 Are Seyfert galaxies which lack significant [NeV] λ3427Å emission strongly dust extinguished?

Assuming sufficiently sensitive observations, the dominant reason for the lack of optical [NeV] signatures in Type-2 Seyfert galaxies may be due to strong host-galaxy dust extinction. It is well-established that the Balmer decrement is a relatively good indicator of dust extinction in the optical regime. In Fig. 5.5 we show a histogram of the differing Balmer decrement distributions for both [NeV] detected and undetected Seyfert galaxies in our sample. We find that the distribution of Balmer decrements for [NeV] detected Seyferts is consistent to that of the whole SDSS-DR7 narrow-line parent sample with a median Balmer decrement of ≈ 5.3. By contrast, we find a systematic shift towards higher Balmer decrements (median of ≈ 7.2) for the [NeV] undetected Seyfert galaxies, equivalent to an increase in dust extinction of $A_V \approx 1$ magnitude.

Clearly, [NeV] detected Seyfert galaxies are systematically hosted in galaxies with lower dust content than those lacking [NeV] emission. This suggests that a large fraction of AGNs are hosted in massive galaxies with on-going young star-formation. Hence, we may infer that for the majority of Type-2 Seyfert galaxies with sufficient quality optical spectroscopy, the lack of significant high-ionisation emission is most likely due to systematically higher levels of dust within their host galaxies.

5.3.3 Are mid-IR detected AGNs a separate population of AGNs?

Recently, using *Spitzer*, focused mid-IR spectroscopic studies have identified a population of AGNs which are not unambiguously identified as AGNs at optical wavelengths (e.g., Satyapal et al. 2008; Goulding and Alexander 2009; Bernard-Salas et al. 2009). In this section, we compare the population of [NeV] detected Seyfert galaxies identified in the SDSS-DR7 to the optically unidentified AGNs found in the volume-limited sample of $D < 15$ Mpc galaxies by GA09 (see also Chapter 3).

A powerful diagnostic for understanding the general properties of galaxies (i.e., luminosity; mass; evolution) is from their distribution in colour and absolute magnitude parameter space. Previous studies have determined that a colour-magnitude diagram is bimodal (e.g., Strateva et al. 2001; Baldry et al. 2004). A colour–magnitude plot is separated into a red-sequence which is mainly comprised of large evolved elliptical galaxies, and a blue cloud of younger, actively star-forming, disk-dominated spiral galaxies, such as the majority of the population of emission-line galaxies studied here.

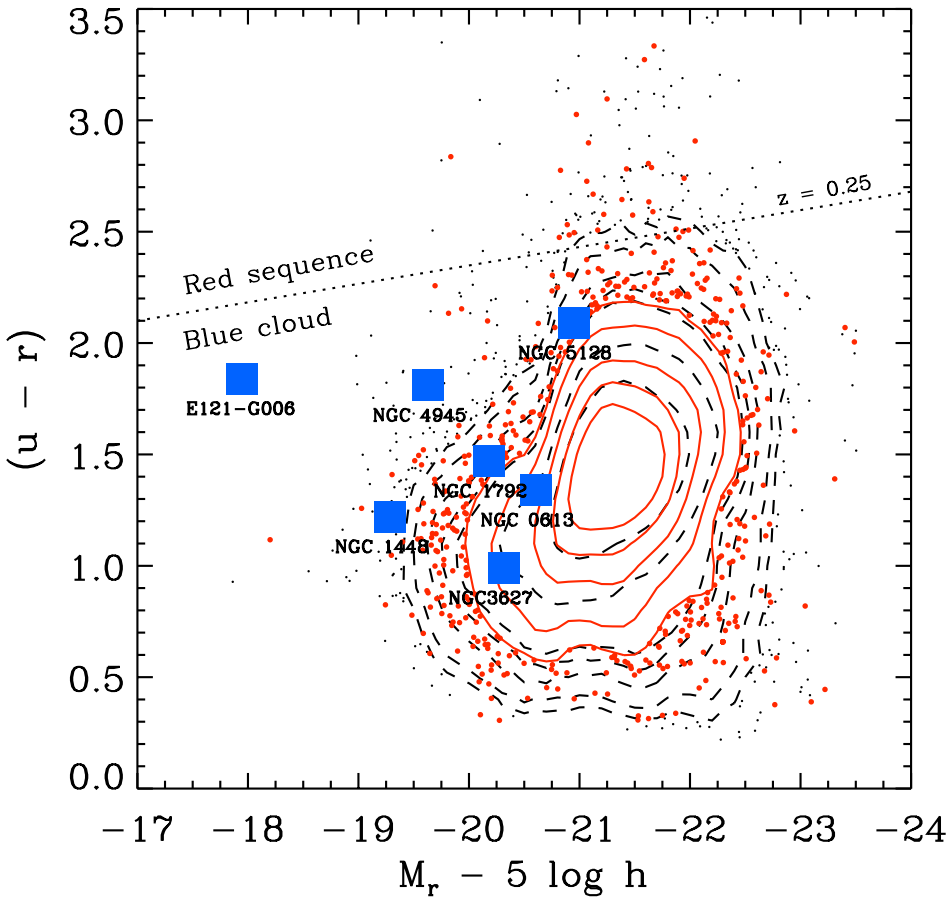

Figure 5.6: A rest-frame extinction-corrected $u - r$ colour versus absolute r-band magnitude ($M_{r,AB}$) diagram of the SDSS-DR7 narrow-line galaxies at $z \sim 0.14$–0.31 (black-dashed contours). [NeV] λ3427 detected Seyfert galaxies in the SDSS-DR7 are shown with red contours. For comparison all optically unidentified AGNs identified by GA09 (see Chapter 3) with available photometric constraints are shown with blue filled squares. Optically unidentified AGNs appear systematically hosted in lower luminosity (lower mass) galaxies than optically identified Seyfert galaxies.

In Fig. 5.6 we present a $u-r$ colour versus absolute r-band magnitude ($M_{r,AB}$) diagram of all narrow-line galaxies in the SDSS-DR7 at $z \sim 0.14$–0.31. We use the u and r $pertromag$ photometric measurements from the SDSS-DR7 catalogue. We correct these for galactic extinction and convert to AB magnitudes before applying K-corrections to compute rest-frame colours. K-corrections are performed using KCORRECT (v4.2).[2] Calculating rest-frame colours for these galaxies allows for simple comparison with the AGNs presented in GA09. We additionally calculate absolute r-band magnitudes from the corrected r-band photometry.

As predicted, given our selection criteria, Fig. 5.6 is dominated by galaxies which peak in the blue cloud and extends towards the red sequence (i.e., the so-called green-valley). We find very few evolved, red, elliptical galaxies in our sample. The [NeV] λ3427 detected Seyfert galaxies span a similar distribution in colour–magnitude space, peaking slightly more redwards than the parent sample.[3]. By contrast, we find that optically unidentified AGNs have similarly blue colours ($u-r \sim 1.1$–1.7) to the majority of our parent sample, however they are systematically hosted in less luminous and hence, less massive host galaxies with $M_r \gtrsim -20$, a region of parameter space which is not readily probed by large-scale optical surveys such as the SDSS.[4] GA09 find that the majority of the optically unidentified AGNs are indeed hosted in late-type spiral galaxies (Hubble-types Sc–Sd). These particular sources are found to be dust-rich systems.

Given our optical selection bias towards brighter, more massive galaxies (i.e., our inability to probe lower-mass systems) and that many optically-unidentified AGNs are found to be hosted in systems with large dust masses (i.e., high balmer decrements), we surmise that in the SDSS we would expect to detect very few optically unidentified AGNs such as those identified in mid-IR surveys. Indeed, the majority of [NeV] detected AGNs which lie in the HII or transitions appear to be dominated by narrow-line Seyfert 1 galaxies, and are not optically similar to the mid-IR AGNs identified by GA09. Therefore, we conclude that whilst the SDSS is an excellent resource for the derivation of large active-galaxy population properties (e.g., Kauffmann et al. 2003a; Heckman et al. 2004;

[2]KCORRECT is an IDL routine which uses galaxy photometry and redshifts to model the SED of the source in order to provide K-corrected photometry. It is available and maintained at http://howdy.physics.nyu.edu/index.php/Kcorrect

[3]We also note, that it is clear that our parent sample may also contain many quasar-like systems given the large concentration of sources with $u-r < 0.5$ and $M_r \lesssim -21$ in Fig. 5.6

[4]Photometry for the optically unidentified AGNs presented in GA09 are derived heterogeneously from the total Johnson magnitudes in the NASA Extra-galactic Database.

Wild et al. 2010), current sensitivity and sample bias limitations, even in the local Universe, prevent the identification of a significant fraction of AGNs which may currently host the majority of present-day accretion onto the smallest supermassive black holes (e.g., Goulding et al. 2010).

5.4 Summary

Using [NeV] λ3427Å as an unambiguous AGN indicator, we have presented the incidence of high-ionisation detected AGNs from a carefully selected sample of emission-line galaxies in the SDSS-DR7 catalogue at the redshift interval, $0.14 < z < 0.31$. Our main findings are the following:

(1). From a parent sample of 18,059 galaxies detected in the SDSS-DR7 at $0.14 < z < 0.31$, we find that 1226 ($\approx 6.8 \pm 0.2$ percent) have detected [NeV] λ3427Å emission. The majority of the [NeV] detected population have optical emission line ratios which are similar or greater than those predicted by the maximum starburst limit of Kewley et al. (2001). Hence, we empirically show that the Kewley et al. (2001) demarcation provides a good selection cut for optical Type-2 Seyfert galaxies. See section 5.2.

(2). Using spectral stacking analyses we investigated the average optical spectroscopic properties of [NeV] detected and undetected sources in the SDSS-DR7. We find that the optical spectra for [NeV] λ3427Å detected Seyfert galaxies contain [OIII] λ5007Å and [NeV] λ3427Å emission lines which are a factor ≈ 5 greater in flux than [NeV] detected sources in the HII and transitions regions. For the Seyfert galaxies lacking significant detections of [NeV] λ3427, we find evidence at the $\approx 2.7\sigma$ level for [NeV] emission in the spectral stacks of these galaxies. By contrast, we find no such [NeV] signal in the spectral stacks of either the HII or transition region galaxies. See section 5.3.1.

(3). In the optical Seyfert region of a traditional BPT diagram we find that only $\approx 27 \pm 4$ percent of optical AGNs have significant detections of [NeV] emission. Using a suite of optical emission-line diagnostics we determine that a lack of sensitivity towards lower fluxes and increased levels of dust extinction of $A_V \approx 1$ magnitude (i.e., a decrease in [NeV] flux by a factor ≈ 5) are the dominant reasons for the lack

of [NeV] signatures in the majority of Seyfert galaxies. See sections 5.3.2.1, 5.3.2.2 and 5.3.2.3.

Chapter 6

Searching for Compton-thick active galactic nuclei at $z \sim 0.1$

This chapter is based on work submitted for publication in MNRAS.

6.1 Introduction

Unbiased deep and wide-field X-ray surveys have been instrumental in the identification of a large proportion of the AGN population to high redshifts ($z \sim 5$; e.g., Alexander et al. 2001; Barger et al. 2003; Fiore et al. 2003; Tozzi et al. 2006; Brusa et al. 2010). Using the exceptional sensitivities of *XMM-Newton* and the *Chandra X-ray Observatory*, > 80 per cent of the X-ray background (XRB) has been resolved into discrete sources at soft energies (0.5–5 keV; e.g., Worsley et al. 2005; Hickox and Markevitch 2006, 2007). However, AGN synthesis models for the XRB predict that ~ 50 per cent of the AGN population may be heavily obscured and remains undetected at $E > 6$ keV in deep X-ray surveys (e.g., Gilli et al. 2007; Treister et al. 2009).

Using high-quality X-ray spectroscopic analyses of objects in the local Universe, it is now well-established that the majority of AGNs are obscured along the line-of-sight by large columns of gas and dust (e.g., Risaliti et al. 1999; Matt et al. 2000). The presence of this obscuring material results in strongly depressed nuclear X-ray emission observed at $E \sim 0.5$–10 keV. Identification of the most heavily obscured AGNs with $N_H \gtrsim 1.5 \times 10^{24}\,\mathrm{cm}^{-2}$ (i.e., Compton-thick AGNs; see Section 1.4) requires sensitive $E > 10$ keV data, or high-quality X-ray spectroscopy at $E \sim 0.5$–10 keV in order to identify a Fe K_α fluorescence line at $E \sim 6.4$ keV and/or a Compton-reflection component. Even at low

redshifts ($z \sim 0.05$) the observed X-ray flux required to detect FeK$_\alpha$ at a high significance often requires long exposure times even with the most sensitive X-ray observatories (of the order 100s of kiloseconds with *Chandra* and *XMM-Newton*).

Given the required X-ray sensitivity to directly identify Compton-thick AGNs using X-ray data alone, only a small fraction of this heavily-obscured population can be discovered using current instrumentation (e.g., *Chandra*; *XMM-Newton*; *Swift*). In recent years, new techniques have been developed to discover Compton-thick AGN candidates using X-ray data and optical spectroscopy combined with pointed mid-IR observations, allowing us to probe $\approx$ 2–3 orders of magnitude lower in the z–L_X plane than using X-ray data alone. These approaches are promising since the reprocessed mid-IR continuum emission and high-excitation optical– and mid-IR narrow-line emission (i.e., [OIII] $\lambda5007$; [NeV] $14.32\ \mu$m; [OIV] $25.89\ \mu$m) in AGN is relatively unaffected by the optically-thick X-ray obscuring material in the central region and, therefore, provide reliable measurements of the intrinsic luminosity of even the most heavily Compton-thick AGNs (e.g., Heckman et al. 2005; Panessa et al. 2006; Meléndez et al. 2008a; Diamond-Stanic et al. 2009; Goulding et al. 2010). For example, through examination of a local optically-selected AGN sample, Maiolino et al. (1998) and Bassani et al. (1999) find that those AGNs with X-ray–[OIII] flux ratios of $f_X/f_{[\rm OIII]} < 1$ almost invariably host intrinsically obscured central sources (many of which are Compton thick), and those with $f_X/f_{[\rm OIII]} < 0.1$ always appear to be Compton thick (see also Akylas and Georgantopoulos 2009; hereafter, AG09). Furthermore, this diagnostic has successfully identified new Compton-thick AGNs which have since been unambiguously confirmed using high-quality X-ray data (e.g., NGC 5135; Levenson et al. 2004).

Clearly, indirect AGN luminosity indicators provide good first-order approximations as to whether an AGN is Compton thick. Greater reliability in identifying Compton-thick AGNs can therefore be made when considering multiple diagnostics, particularly those which probe different regions of the AGN (e.g., the emission line region and the reprocessed continuum emission). Recently, Vignali et al. (2010) combined pointed *Chandra*-ACIS observations with optical emission-line *and* mid-IR continuum luminosities to identify six Compton-thick quasars ($L_{[\rm OIII]} > 2 \times 10^9\,{\rm L}_\odot$) at $z \sim 0.40$–0.73 in the Sloan Digital Sky Survey (SDSS). Somewhat similar approaches have also been adopted by Alexander et al. (2008); LaMassa et al. (2009); Bauer et al. (2010); Donley et al. (2010) using *Spitzer* IR spectroscopy and/or optical spectroscopy to identify high-redshift X-ray undetected Compton-thick AGNs in deep and wide-field surveys. Whilst each of

these studies have successfully identified Compton-thick AGNs using multi-wavelength analyses, they sample only the most luminous systems ($L_{\rm X,intr} \gtrsim 10^{44}\,{\rm erg\,s^{-1}}$) where the predicted space-density of Compton-thick AGNs, even at $z \sim 2$, is relatively low ($\phi \lesssim 10^{-5}$ Mpc^{-3}; Gilli et al. 2007). In order to clearly understand the evolution of these Compton-thick sources, it is vital to also identify the more modest luminosity population ($L_{\rm X,intr} \approx [0.1\text{–}1] \times 10^{43}\,{\rm erg\,s^{-1}}$), which comprise the most energetically dominant AGNs in the nearby Universe ($z \sim 0.1$; e.g., Ueda et al. 2003; Ebrero et al. 2009; Aird et al. 2010).

In this chapter, we identify a sample of nearby ($z \sim 0.03$–0.2) X-ray undetected optically-selected candidate Compton-thick AGNs from a large cosmological volume which is well-matched to that of the *Chandra* Deep Fields (CDFs; Giacconi et al. 2002; Alexander et al. 2003; Luo et al. 2008) at $z \sim 0.5$–2.5 ($V \approx 4.6 \times 10^6$ Mpc^3). We use pointed high signal-to-noise *Spitzer*-IRS spectroscopy and $24\,\mu$m photometry combined with the unprecedented wide-field coverage of the SDSS to explore the ubiquity of typical Compton-thick AGNs at $z \sim 0.1$. We outline the construction of our sample of 14 optical narrow-line AGNs derived from the population of galaxies in the SDSS which lie in the large overlap region with the *XMM-Newton* Serendipitous Survey (≈ 100 deg^2). These AGNs are all undetected to faint flux limits in $E \sim 2$–12 keV *XMM-Newton* observations, and based on their X-ray–[OIII] flux ratio limits are likely to be heavily obscured (and possibly Compton thick). We use mid-IR narrow-line emission and AGN-produced mid-IR continuum emission to determine the intrinsic luminosity of these obscured AGNs. We combine each of these AGN luminosity indicators in order to reliably identify which sources are Compton-thick AGNs. We use these results to further constrain the ubiquity of Compton-thick AGNs at $z \sim 0.1$. Throughout this chapter we adopt a standard ΛCDM cosmology of $H_0 = 71\,{\rm km\,s^{-1}}$ Mpc^{-1}, $\Omega_M = 0.30$ and $\Omega_\Lambda = 0.70$.

6.2 Sample Selection

We select our candidate Compton-thick AGN sample on the basis of their optical and X-ray properties. Sources that are identified to be AGNs using traditional optical emission line diagnostics (e.g., Baldwin et al. 1981) but are undetected to faint limits in wide-field *XMM-Newton* observations (i.e., $f_X/f_{\rm [OIII]} < 1$) are strong candidates for containing heavily obscured AGNs (e.g., Bassani et al. 1999; Panessa and Bassani 2002; Akylas and

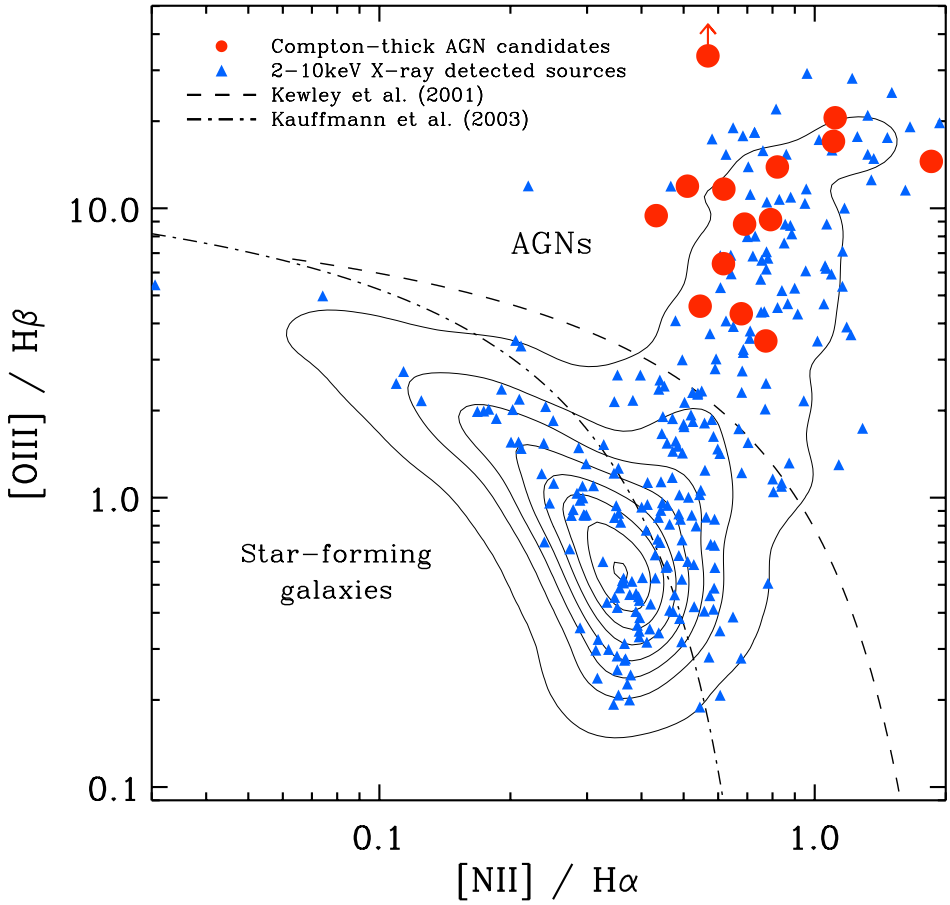

Figure 6.1: Optical emission line diagnostic diagram presenting the 2690 galaxies detected in the seventh data release of the Sloan Digital Sky Survey with serendipitous X-ray coverage from *XMM-Newton* at $0.03 < z < 0.2$ (solid contours). The fourteen X-ray undetected optical AGNs selected for our sample are shown with red circles. The 272 galaxies with hard-band X-ray detections ($E > 2$ keV) are shown with blue triangles. The empirical HII star-forming classification curve presented by Kauffmann et al. (2003) and the extreme starburst line of Kewley et al. (2001a) are also shown with dash-dotted and dashed curves, respectively.

Georgantopoulos 2009).[1] Here we provide the details behind the construction of our sample of X-ray undetected optically identified AGNs (i.e., candidate Compton-thick AGNs).

6.2.1 Construction of the optical–X-ray catalogue

We construct a parent sample of all optical spectroscopically detected galaxies in the ≈ 100 deg^2 overlap region between the seventh data release of the SDSS (Abazajian et al. 2009; hereafter SDSS-DR7) and the second source catalogue of the *XMM-Newton* Serendipitous survey (Watson et al. 2009; hereafter 2XMMi). We define the redshift range for our shallow wide-area sample based on the combined available cosmological volume in the deep 2Ms "pencil-beam" CDF-North (≈ 448 arcmin^2; Alexander et al. 2003) and CDF-South (≈ 436 arcmin^2; Giacconi et al. 2002; Luo et al. 2008) surveys. At $z \sim 0.5$–2.5, where the CDFs are complete towards X-ray luminous AGNs, the encompassed volume is $V \sim 4.57 \times 10^6$ Mpc^3, which is equivalent to the redshift range of $z \sim 0.03$–0.2 in our SDSS-2XMMi selected sample.

6.2.1.1 AGN identification in the SDSS-DR7

The SDSS-DR7 is currently the largest publicly available optical spectroscopic catalogue (≈ 9830 deg^2) containing 929,555 spectroscopic source redshifts.[2] Previous studies have used past data releases of the survey to show that through careful spectral analyses, general galaxy and AGN properties can be derived from these large datasets (e.g., Kauffmann et al. 2003a; Heckman et al. 2004; Greene and Ho 2007). We select all galaxies with well detected narrow [OIII]λ5007, Hα, [NII]λ6585 emission-lines (S/N > 5).[3] All galaxies with detected broad Balmer-lines (here defined as a full-width half maximum $> 700\,\mathrm{km\,s^{-1}}$) are removed as these sources are unlikely to be intrinsically obscured by a gas/dust-rich geometrically thick torus. AGNs which are heavily obscured are often found to be hosted in dust-rich galaxies, and thus are likely to be strongly reddened (i.e., Hα–Hβ ratios $\gg 3.1$; e.g., Goulding and Alexander 2009). Hence, whilst useful in unambiguously discriminating between the properties of galaxies (e.g., Kauffmann

[1] Throughout this chapter we define *X-ray undetected* as formally X-ray undetected sources in the hard band ($E > 2$ keV) unless otherwise stated.

[2] The SDSS-DR7 data archive server is available at http://www.sdss.org/dr7/

[3] SDSS spectra are obtained through 3 arcsecond fibers; at the median redshift of our sample ($z \sim 0.08$) this projected aperture is equivalent to a physical region of ≈ 5 kpc, and hence encompasses all of the narrow-line region emission as well as a large fraction of the host galaxy emission.

et al. 2003; Wild et al. 2010), we purposely do not limit our selection to only galaxies with well-detected Hβ emission. Sources are separated by classification based on their optical emission-line ratios in a traditional diagnostic diagram (hereafter, BPT diagram; e.g., Baldwin et al. 1981). We conservatively identify the narrow-line AGNs in the SDSS-DR7 as those which lie above the theoretical starburst limit of Kewley et al. (2001a). See Fig. 6.1.

6.2.1.2 SDSS AGNs in the *XMM-Newton* footprint

The 2XMMi catalogue identifies all X-ray sources detected in 3491 observations made during the first $\approx$ 8 years of *XMM-Newton* (Watson et al. 2009). Its unprecedented sky coverage (360 deg^2) and sensitivity (median *XMM-Newton* exposures of 20–50 ks) currently provides an exceptional resource for the unbiased identification of obscured AGN activity throughout the Universe. Using an automated reduction and analysis pipeline, the 2XMMi catalogue provides source positions, exposure times, X-ray fluxes and band ratios of all detected sources which serendipitously fall within the field-of-view of previous *XMM-Newton* observations.

All sources in our SDSS parent sample are matched to 2XMMi using a 3.7 arcsecond radius, which is chosen as a good compromise between maximising source numbers and minimising the probability of spurious matches (e.g., Watson et al. 2009). The matching algorithm is restricted to sources within 14 arc-minutes of the aim point of each *XMM-Newton* observation to minimise the likelihood of spurious matches due to the degradation of the X-ray PSF far off-axis. Based on the X-ray/optical positional analysis of SDSS quasars and the 2XMMi catalogue by Watson et al. (2009), if we assume no systematic offsets, then we expect our XMM–SDSS matching to be $\approx$ 92 percent complete. We identify all optical sources in the 2XMMi which have 3σ detections at $E \sim$ 2–12 keV using the PN detector. For all other matched sources (i.e., those which lie within the footprint of an *XMM-Newton* observation but are undetected in the hard-band of the 2XMMi catalogue), we use FLIX to compute robust 3σ (likelihood threshold of 6.6) X-ray upper-limits in this band.[4] Using a sub-sample of the matched sources that are formally undetected in the hard band in 2XMMi, we tested the use of FLIX to provide X-ray upper-limits. Broadly,

[4]FLIX is a purpose-built program provided by the *XMM-Newton* Survey Science Center. It provides robust estimates of the X-ray upper limit to a given point in the sky for a source which has not been detected in the 2XMMi catalogue. For a discussion of the upper limit algorithm see Carrera et al. (2007) and for further documentation see http://www.ledas.ac.uk/flix/flix_help.html.

we find that the upper-limits provided by FLIX are consistent with the fluxes within $\pm 3\sigma$ given by 2XMMi. For the sake of comparison with previous studies, we convert these 2–12 keV upper-limits to 2–10 keV limits assuming a powerlaw spectrum with spectral index of $\Gamma = 1.4$ where $F_\nu \propto \nu^{-(\Gamma-1)}$; $\Gamma = 1.4$ is the spectral slope of the X-ray background and similar to that of many absorbed AGNs. Our final combined parent sample of SDSS-DR7 galaxies at $z \sim 0.03$–0.2 with complimentary hard X-ray *XMM-Newton* coverage is 2690 objects (272 are hard X-ray detected sources). The median redshift of the sample is ≈ 0.09. Of these galaxies, 334 (≈ 12 percent) are classified as optical narrow-line (NL) AGNs (i.e., 101 are X-ray detected and 233 are X-ray undetected AGNs).

6.2.1.3 A sample of candidate Compton-thick AGNs

Assuming the optical emission-lines and X-ray AGN emission are well-correlated (e.g., Mulchaey et al. 1994; Alonso-Herrero et al. 1997), sources which are optically classified as AGNs but are undetected to faint limits in relatively deep X-ray observations are likely to be those with heavily attenuated X-ray emission, similar to the objects currently missed in deep X-ray surveys. From our well-defined parent sample of 334 optical NL AGNs, 233 are not detected in the hard-band of the 2XMMi catalogue. In this section, we outline the selection method for our sample of 14 hard-band undetected candidate Compton-thick AGNs.

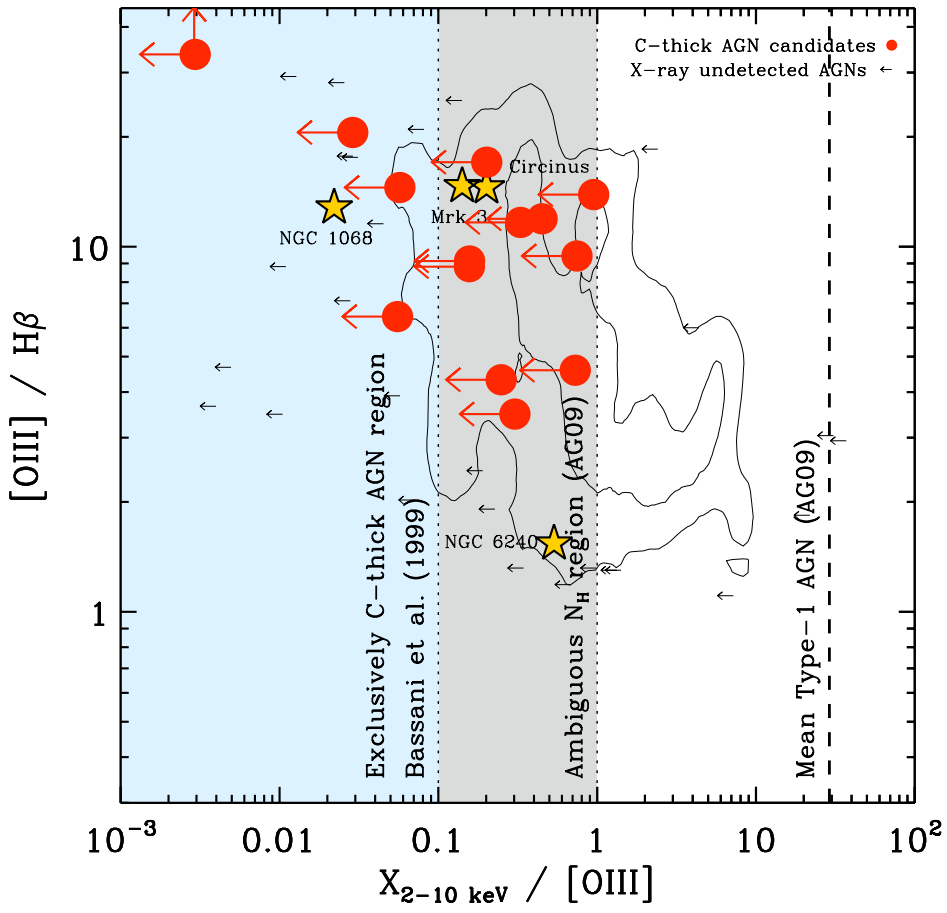

Figure 6.2: Intrinsic obscuration optical–X-ray diagnostic diagram for AGNs adapted from Bassani et al. (1999). Contours shown are all optical AGNs in the SDSS-DR7 which lie in the *XMM-Newton* footprint (i.e., those galaxies which lie above the Kewley et al. 2001 extreme starburst line presented in Fig. 6.1). These contours enclose 50% and 90% of the whole X-ray undetected parent sample. We select 14 candidate Compton-thick AGNs for *Spitzer* observations based on their $f_X/f_{[\rm OIII]}$ ratio (filled circles). Four of these sources lie in the region exclusively occupied by Compton-thick AGNs ($f_X/f_{[\rm OIII]} < 0.1$; e.g., Bassani et al. 1999), and 10 are selected from the heavily obscured N_H region ($f_X/f_{[\rm OIII]} \sim$ 0.1–1.0) which is often found to contain Compton-thick AGNs (e.g., Bassani et al. 1999; AG09). We also show the mean Type-1 (i.e., unobscured) AGN $f_X/f_{[\rm OIII]}$ ratio from AG09 and for comparison, four well-studied local 'bona-fide' Compton-thick AGNs (Circinus, Mrk 3, NGC 1068 and 6240; data is taken from Bassani et al. 1999; stars).

Table 6.1: Basic source properties of the candidate Compton-thick AGNs

ID	Source name	α_{J2000} (deg)	δ_{J2000} (deg)	z	$D_{\rm L}$ (Mpc)	$\log(M_{\rm BH})$ ($\rm M_{\odot}$)	$\frac{\rm [OIII]}{\rm H\beta}$	$\frac{\rm [NII]}{\rm H\alpha}$	$\frac{\rm H\alpha}{\rm H\beta}$	A_V (mags)	$\log(L_{\rm [OIII]})$ ($\rm erg\,s^{-1}$)	$\log(L_{\rm HX})$ ($\rm erg\,s^{-1}$)
(1)	(2)	(3)	(4)	(5)	(6)	(7)	(8)	(9)	(10)	(11)	(12)	(13)
1	SDSS J094046+033930	145.19287	3.65839	0.08730	392.8	7.94	20.55	1.11	16.61	4.86	42.94	< 41.40
2	SDSS J094506+035551	146.27664	3.93087	0.15593	733.6	7.68	11.93	0.51	4.68	1.20	42.73	< 42.39
3	SDSS J100328+554154	150.86636	55.69831	0.14602	682.8	7.53	13.89	0.82	4.72	1.22	42.39	< 42.36
4	SDSS J101757+390528	154.48708	39.09110	0.05392	237.0	7.29	4.59	0.55	4.94	1.35	41.33	< 41.19
5	SDSS J102142+130550	155.42455	13.09733	0.07650	341.7	6.93	4.32	0.68	9.69	3.30	41.83	< 41.23
6	SDSS J111521+424217	168.83784	42.70484	0.19714	950.9	-	> 33.63	0.57	> 33.30	> 6.88	44.68	< 42.15
7	SDSS J115658+550822	179.24117	55.13932	0.07980	357.2	7.72	17.04	1.10	7.40	2.52	42.96	< 41.62
8	SDSS J121355+024753	183.47861	2.79806	0.07429	331.3	6.77	6.44	0.62	6.30	2.05	42.49	< 41.23
9	SDSS J123026+414258	187.60876	41.71606	0.12486	576.0	7.50	8.82	0.70	8.53	2.93	42.58	< 41.77
10	SDSS J134133−002432	205.38905	−0.40892	0.07173	319.3	< 8.30	11.66	0.62	6.34	2.07	42.07	< 41.60
11	SDSS J135858+651546	209.61739	65.26288	0.03259	141.1	6.85	3.48	0.77	9.78	3.32	41.48	< 40.96
12	SDSS J142931+425149	217.37810	42.86364	0.15500	728.8	7.60	9.14	0.79	12.09	3.94	42.32	< 42.16
13	SDSS J215650−074533	329.20630	−7.75905	0.05541	243.8	7.14	9.43	0.43	4.41	1.02	41.61	< 41.49
14	SDSS J221742+000908	334.42340	0.15209	0.04514	197.2	6.36	14.53	1.85	11.15	3.71	41.80	< 40.56

NOTES: (1) Source-identification; (2) SDSS source name; (3–4) J2000 positional co-ordinates from the SDSS-DR7; (5) SDSS spectroscopic redshift; (6) luminosity distance in megaparsecs calculated using our adopted cosmology; (7) logarithm of black hole mass in units of solar masses derived from the stellar velocity dispersion (MPA-JHU DR7 release) using the M–σ relation (Gebhardt et al., 2000); (8–10) Emission-line ratios from SDSS-DR7; (11) Implied A_V in magnitudes derived from the Balmer decrement; (12) Logarithm of dust extinction corrected [OIII] luminosity; (13) Logarithm of the 3-σ upper limit of the 2-10 keV X-ray luminosity derived from fluxes produced using FLIX.

The de-reddened [OIII] luminosity is assumed to be a good tracer of AGN power (e.g., Heckman et al. 2005; Netzer et al. 2006; Panessa et al. 2006). In order to identify obscured AGN candidates, we follow Maiolino et al. (1998) and Bassani et al. (1999) by using the flux ratio of de-reddened (intrinsic) [OIII] and observed (absorbed) 2–10 keV X-ray emission, and compare it to the [OIII]/H_{β} ratio in a new diagnostic diagram analogous to a BPT figure; see Fig. 6.2. Optical luminosities are corrected for dust-reddening towards the AGN NL-region using the Balmer decrement (i.e., the observed Hα–Hβ ratio; Ward et al. 1987), an intrinsic ratio of 3.1 (Osterbrock and Ferland, 2006) and a standard $R = 3.1$ Cardelli et al. (1989) extinction curve. The parent AGN sample are found to have de-reddened [OIII] luminosities in the range $L_{[\mathrm{OIII}]} \approx (0.03\text{–}500) \times 10^{42}\,\mathrm{erg\,s^{-1}}$ (median $L_{[\mathrm{OIII}]} \approx 10^{42}\,\mathrm{erg\,s^{-1}}$). AG09 find that the average X-ray–[OIII] flux ratio for unobscured AGNs (i.e., Type 1s; $N_H < 10^{22}\,\mathrm{cm^{-2}}$) is ≈ 30, whilst heavily obscured AGNs (Type 2s) typically exhibit lower values of $f_X/f_{[\mathrm{OIII}]}$. AGNs with $f_X/f_{[\mathrm{OIII}]} < 0.1$ are invariably found to be Compton thick and a significant proportion of Compton-thick AGNs have $f_X/f_{[\mathrm{OIII}]} \sim 0.1\text{–}1.0$ in addition to heavily absorbed Compton-thin AGNs. One-hundred and forty-seven (≈ 63 percent) of the 233 X-ray undetected AGNs have $f_X/f_{[\mathrm{OIII}]} < 1.0$ (24 have $f_X/f_{[\mathrm{OIII}]} < 0.1$) from which we select a representative subsample of 14 (≈ 10 percent) to be further investigated using pointed mid-IR spectroscopic and photometric observations. Our sample of 14 AGNs are well-matched to the parent sample of X-ray undetected AGNs with a redshift distribution of 0.03–0.2 (median ~ 0.08) and $L_{[\mathrm{OIII}]} \approx (0.2\text{–}500) \times 10^{42}\,\mathrm{erg\,s^{-1}}$ (median $L_{[\mathrm{OIII}]} \approx 2 \times 10^{42}\,\mathrm{erg\,s^{-1}}$). For completeness, we also note that 11/14 of our sources are detected in at least one of the softer X-ray bands ($E < 2$ keV) in 2XMMi. These detections, in many cases, may be due to a scattered or reprocessed soft X-ray component (e.g., Matt et al. 2000) or star-formation (e.g., Boller et al. 2003). Clearly, this softer component may partially contribute to the flux at $E > 2$ keV. However, any correction which could be made to our 3σ upper-limits would only serve to reduce the current hard-band limits. The basic source properties for our sample of 14 candidate Compton-thick AGNs are shown in Table 6.1.

6.3 Mid-IR Spectroscopy and Photometry

We have used the *Spitzer* Infra-Red Spectrograph (IRS) and Multi-band Imaging Photometry for *Spitzer* (MIPS) to observe the 14 candidate Compton-thick AGNs selected in Section 2 (PID:50818; PI: D.Alexander). In this section, we present the reduction

methodology and resulting spectroscopy and photometry for these 14 targets. In order to robustly assess the intrinsic luminosity of the central sources in these AGNs, we also present mid-IR spectral decomposition analyses to isolate the AGN continuum and star-formation emission.

6.3.1 *Spitzer*-IRS Spectral Reduction and Analysis

Each of the 14 candidate Compton-thick AGNs were observed in spectral staring mode with the low-resolution modules (short-low [SL; 5.2–$14.5\ \mu$m] and long-low [LL; 14.0–$38.0\ \mu$m]; $R \approx 57$–127) of the *Spitzer*-IRS instrument (Houck et al., 2004). The sources were observed between 30th November 2008 and 24th February 2009 using ramp durations of 60 seconds $\times$ 10 (4) cycles and 120 seconds $\times$ 4 cycles for the SL1 (SL2) and LL modules, respectively. The total integration time for each of the sources was 0.5 hours.

The two-dimensional Basic Calibrated Data (BCDs) images produced by the S18.7.0 *Spitzer* Science Center (SSC) pipeline were retrieved and further analyzed using our custom IDL reduction routine (see section 2.2). Briefly, individual BCDs were rigorously cleaned of rogue 'hot' pixels using a customised version of IRSCLEAN. Individual rows were fit as a function of time to remove latent charge which exists on the detector after bright and/or long observations. The cleaned BCDs were averaged in the differing nod positions, which were then used to perform alternate background subtractions of the source in each nod position.

Spectral extraction was performed using SPICE. The spectroscopy was extracted using an optimally calibrated 2-pixel wide spectral window to maximize the signal-to-noise ratio of each spectrum. Errors were estimated for each of the spectra using a second spectral window offset from the source in the spatial direction. The spectra for each of the modules for an individual object were corrected for their differing apertures and normalized to the flux level of the 1st LL module. Orders were clipped of spectral noise (see the *Spitzer*-IRS handbook for further information) and stitched together by fitting low-order polynomials to produce the final spectra.

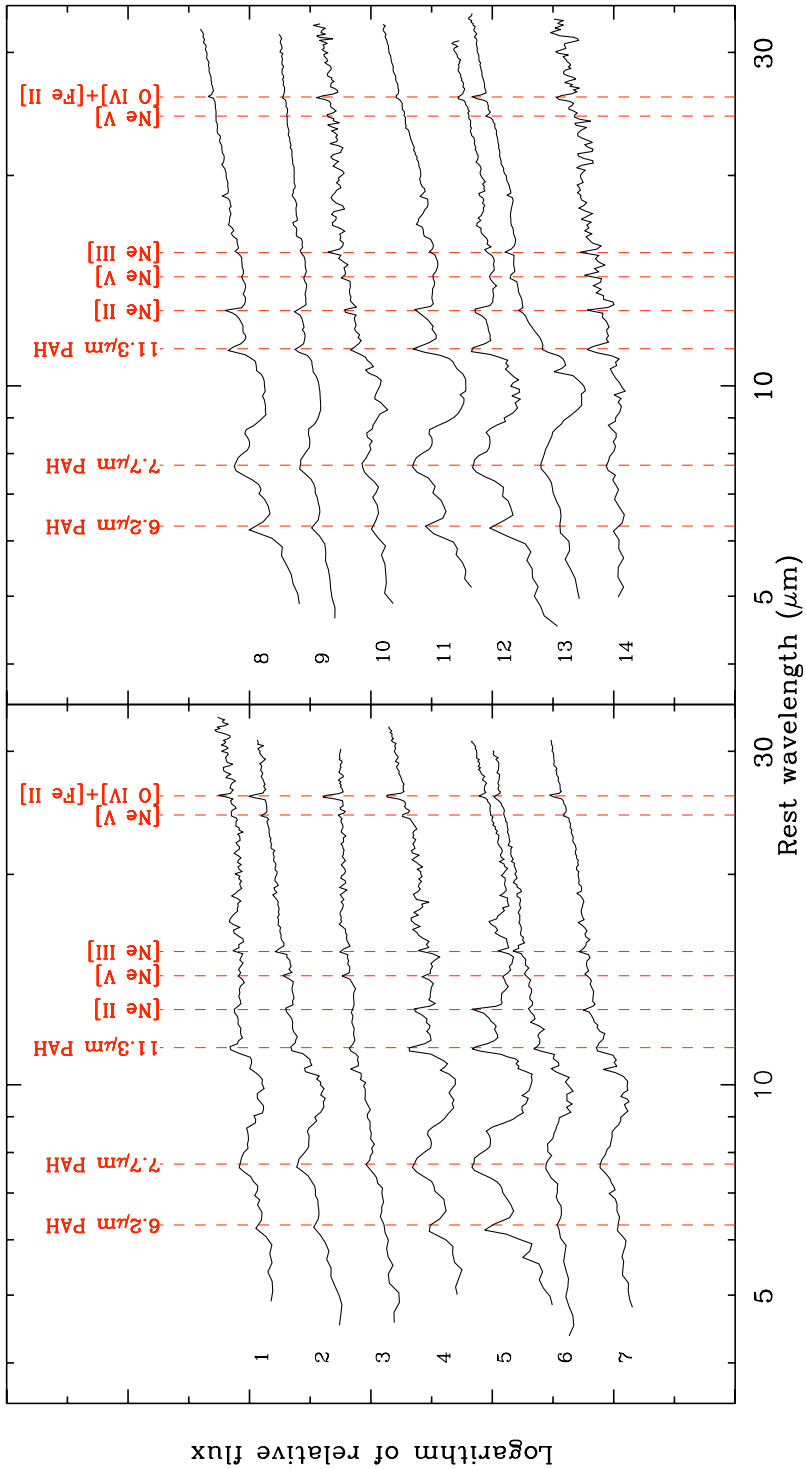

Figure 6.3: Rest-frame low-resolution *Spitzer*-IRS spectroscopy of the 14 X-ray undetected SDSS AGNs in our sample. The prominent emission-line and PAH features that may be detected are highlighted.

6.3.2 *Spitzer*-MIPS Reduction and Analysis

In order to measure accurate emission-line and continuum fluxes we use *Spitzer*-MIPS $24\ \mu\mathrm{m}$ photometry to flux calibrate the IRS spectroscopy. Eleven of our 14 *Spitzer*-IRS targets were observed with the MIPS photometer. The remaining three sources were scheduled but were not observed before the depletion of the instrument's cryogenic liquid coolant.

BCDs were retrieved and the data reduced using the SSC analysis program MOPEX. We post-process individual BCD frames to remove common MIPS artifacts (i.e., "jailbars", latents etc.) and suppress large and small-scale gradients using master-flat images generated from the initial data. Processed frames are then background matched, stacked, mosaicked and median filtered using MOPEX to create the final background-subtracted reduced image.

Point source extraction was performed using the SSC provided *Spitzer* Astronomical Point Source EXtraction (APEX) software to produce $24\ \mu\mathrm{m}$ aperture photometric fluxes of the sources in the reduced MIPS frames (see column 5 of Table 6.2). These fluxes were then convolved with the $24\ \mu\mathrm{m}$ MIPS response curve to produce absolute flux calibrated IRS spectra of each source. The average upwards photometric correction required to the spectroscopy was a factor of ≈ 1.3. For the three objects lacking MIPS observations (see Table 6.2) we did not attempt to correct these spectra. Hence, we consider the emission-line and continuum fluxes (derived in sections 6.3.3 and 6.3.4) for these three AGNs to be less accurate and most likely conservative lower-limits.

6.3.3 Mid-IR Emission-line Fluxes

The reduced and flux-calibrated mid-IR spectra produced in the previous sections were further analyzed (i.e., fitting of emission-lines and polycyclic aromatic hydrocarbon features) using the *Spitzer* spectral analysis program, SMART (Higdon et al., 2004). Typical AGN dominated emission lines present in the spectra of these sources included [NeV] ($\lambda\lambda 14.32, 24.32\ \mu\mathrm{m}$) and [OIV]+[FeII] ($\lambda\lambda 25.89, 25.99\ \mu\mathrm{m}$).[5] Additionally, AGN and star-formation produced lines such as [NeII] ($\lambda 12.82\ \mu\mathrm{m}$) and [NeIII] ($\lambda 15.51\ \mu\mathrm{m}$) were also present. See Table 6.2 for the *Spitzer*-IRS derived properties and see Fig 6.3 for the final *Spitzer*-IRS spectra.

[5] We note that due to the spectral resolution of the LL modules, [OIV] and [FeII] emission lines cannot be individually resolved.

Mid-IR high-excitation narrow-line emission such as [NeV] and [OIV] (ionisation potentials of 97.1 eV and 54.9 eV, respectively) have been shown to be excellent extinction-free unambiguous indicators of the bolometric luminosity of an AGN (e.g., Meléndez et al. 2008a; Diamond-Stanic et al. 2009; Goulding et al. 2010). From analysis of our *Spitzer*-IRS spectroscopy, we find that six of the AGNs in our sample have detected [NeV] emission and all 14 have detected [OIV]+[FeII].[6] The [NeV] and [OIV] luminosities for the six AGNs with detected [NeV] are well correlated and lie within the intrinsic scatter of Equation 3.2 and the more recent calibration of Weaver et al. (2010); for the sources with [NeV] 3σ upper-limits, we find that the majority of the fluxes are also consistent with these relationships. Hence, we confirm that the [OIV] emission in these particular sources is likely to be a good indicator of the intrinsic luminosity of the AGN. For AGNs with strong contributions from star-formation, the [FeII] emission may contaminate the measured [OIV] flux measured from low-resolution *Spitzer*-IRS spectroscopy (Meléndez et al., 2008b). For those galaxies which we find to be dominated by star formation at mid-IR wavelengths (i.e., AGN contributions of < 50 percent; see Section 6.3.4), we conservatively apply a small downwards correction factor of ≈ 1.5 (Meléndez et al., 2008b) to our measured [OIV] flux to account for the [Fe II] contamination. Our final adopted [OIV] luminosities cover the range, $L_{[\mathrm{OIV}]} \approx (0.15\text{–}20 \times 10^{41}\,\mathrm{erg\,s^{-1}}$.

6.3.4 Spectral Decompositions

The low-resolution mid-IR spectra of typical Type-2 AGNs at rest-frame $\lambda \approx 4\text{–}15\ \mu\mathrm{m}$ are composed of three primary components: 1) a power-law like thermal AGN dust continuum; 2) a star-formation component which arises from the super-position of PAH features; and 3) a silicate absorption feature at $\lambda \approx 9.7\ \mu\mathrm{m}$ produced by the hot dust continuum being absorbed by cooler dust on parsec scales (e.g., Goulding and Alexander 2009; Tommasin et al. 2010; Mullaney et al. 2010; Gallimore et al. 2010). Therefore, as expected, we find that the mid-IR spectra for the majority of our candidate Compton-thick AGNs contain both an AGN produced continuum and strong polycyclic aromatic hydrocarbon (PAH) features, which are associated with starburst activity in the circumnuclear photodissociation regions of the host galaxy. Here we outline our spectral decomposition routine to determine the relative contributions of starburst (SB) activity and the

[6] We note that the reliable identification of some AGNs even in the very nearby Universe can often require extremely high signal-to-noise, high-resolution mid-IR spectroscopy (e.g., Satyapal et al. 2008; Goulding and Alexander 2009).

AGN continuum in our 14 Compton-thick AGN candidates (i.e., the SB:AGN ratio), and measure the intrinsic luminosity of the central source from the AGN produced mid-IR continuum at $6\ \mu\mathrm{m}$ (e.g., Lutz et al. 2004).

Using a purpose-built IDL-based routine, we fit the IRS spectroscopy for each of the 14 candidate Compton-thick AGNs with a combined standard starburst template and an AGN power-law component (with spectral index, k) convolved with a Draine and Li (2007) extinction curve ($\rho(\lambda)$) of the form,

$$f_{AGN}(\lambda) = a\lambda^{k}\exp[-b\tau\rho(\lambda)] \tag{6.1}$$

where a, b and k are constants, and τ is the optical depth.[7] Within the fitting we use four possible starburst templates which cover a realistic range of physical and theoretical scenarios: 1) low-resolution *Spitzer*-IRS spectroscopy of the archetypal starburst galaxy, M82; 2) a combined *Spitzer*-IRS starburst template of local pure star-forming galaxies presented in Brandl et al. (2006);[8] 3) a theoretical radiative transfer model of a pure circumnuclear starburst region at $r \approx 3$ kpc with $L_{\mathrm{IR}} \approx 10^{10}\,\mathrm{L}_{\odot}$ (Siebenmorgen and Krügel 2007; hereafter, SK07); and 4) a theoretical radiative transfer model of a nuclear star cluster at $r < 0.35$ kpc with $L_{\mathrm{IR}} \approx 10^{10}\,\mathrm{L}_{\odot}$ (SK07).

The best resulting model parameters derived from the minimum Chi-squared fit to the IRS data are given in Table 6.2 and shown in Fig. 6.4. We note that none of the AGNs in our sample have mid-IR spectral features which are consistent with the theoretical nuclear star cluster model, and hence, the best-fit spectral model for each are that of an AGN combined with one of the three circumnuclear starburst templates. Based on the mid-IR spectral-fits, we also derive the approximate contribution of the AGN to the mid-IR emission for each of the sources; see column (7) of Table 6.2. We find that although these AGNs were selected to be strong [OIII] and [NII] emitters (i.e., optically-dominated Seyfert galaxies), the mid-IR spectra of ≈ 50 percent of the sources are consistent with being dominated by star-formation activity. Indeed, on the basis of these spectral decompositions, the mid-IR spectroscopy for one source (SDSS J102142+130550) is consistent with there being no AGN component, despite this source clearly being identified as an AGN at optical wavelengths.

[7] Our IDL routine makes use of the Markwardt 1-dimensional Chi-squared analysis library, see http://cow.physics.wisc.edu/∼craigm/idl/ for further details.

[8] We note that as we require only starburst emission in these templates, we do not include galaxies in the combined Brandl starburst template which have any previous evidence for AGN activity (i.e., Mrk 266, NGC 660, 1097, 1365, 3628 and 4945).

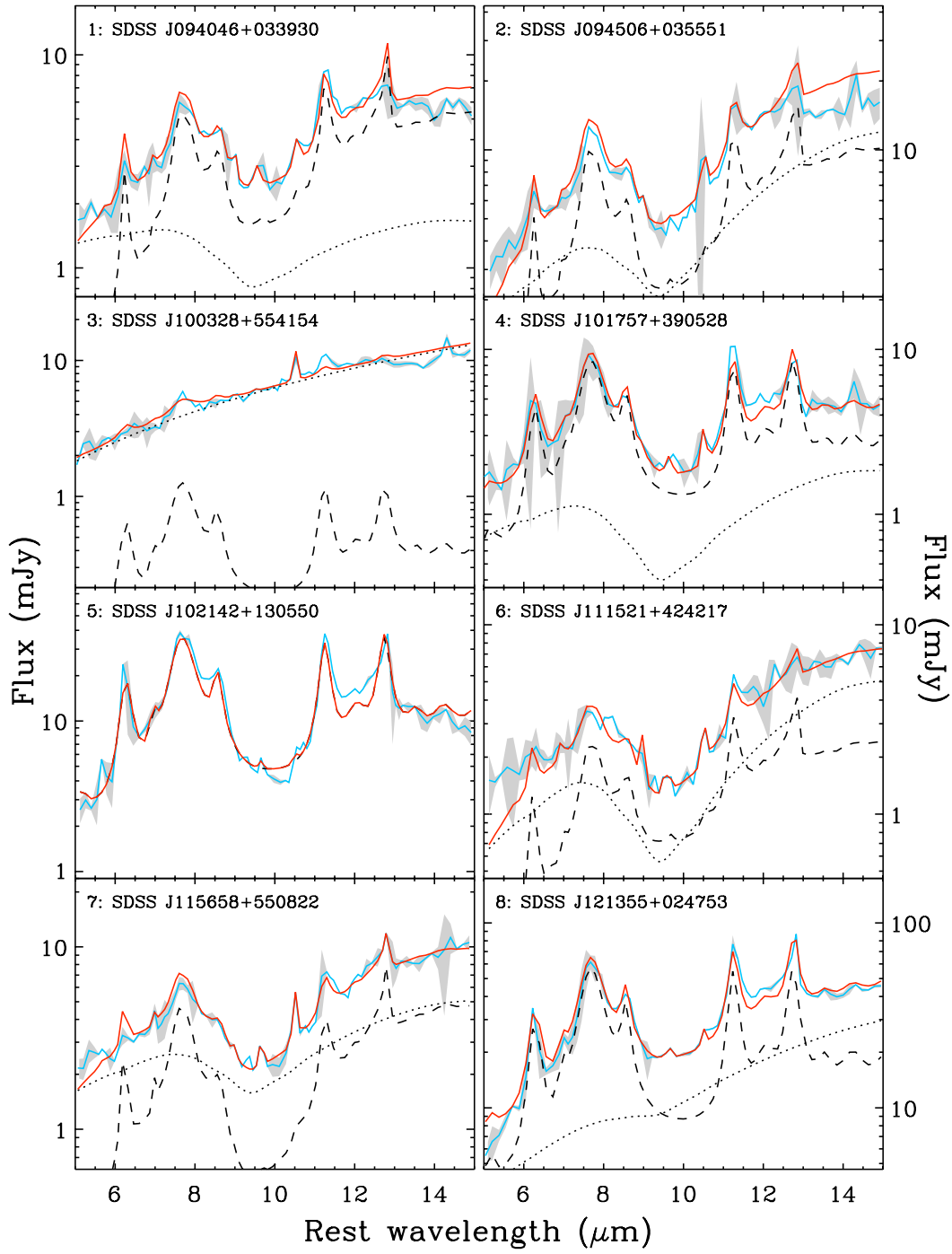

Figure 6.4: Spectral decompositions of the *Spitzer*-IRS spectra (blue solid curve) for our candidate Compton-thick AGNs produced by our spectral analysis program as described in section 6.3.4. The grey shaded region indicates the 1σ error to the observed spectrum. The best-fit absorbed power-law and starburst template are shown with dotted and dashed curves, respectively. See Table 6.2 for best-fitting parameters. The total best-fit spectrum (i.e., power-law+starburst+emission-lines) is shown with a solid red curves.

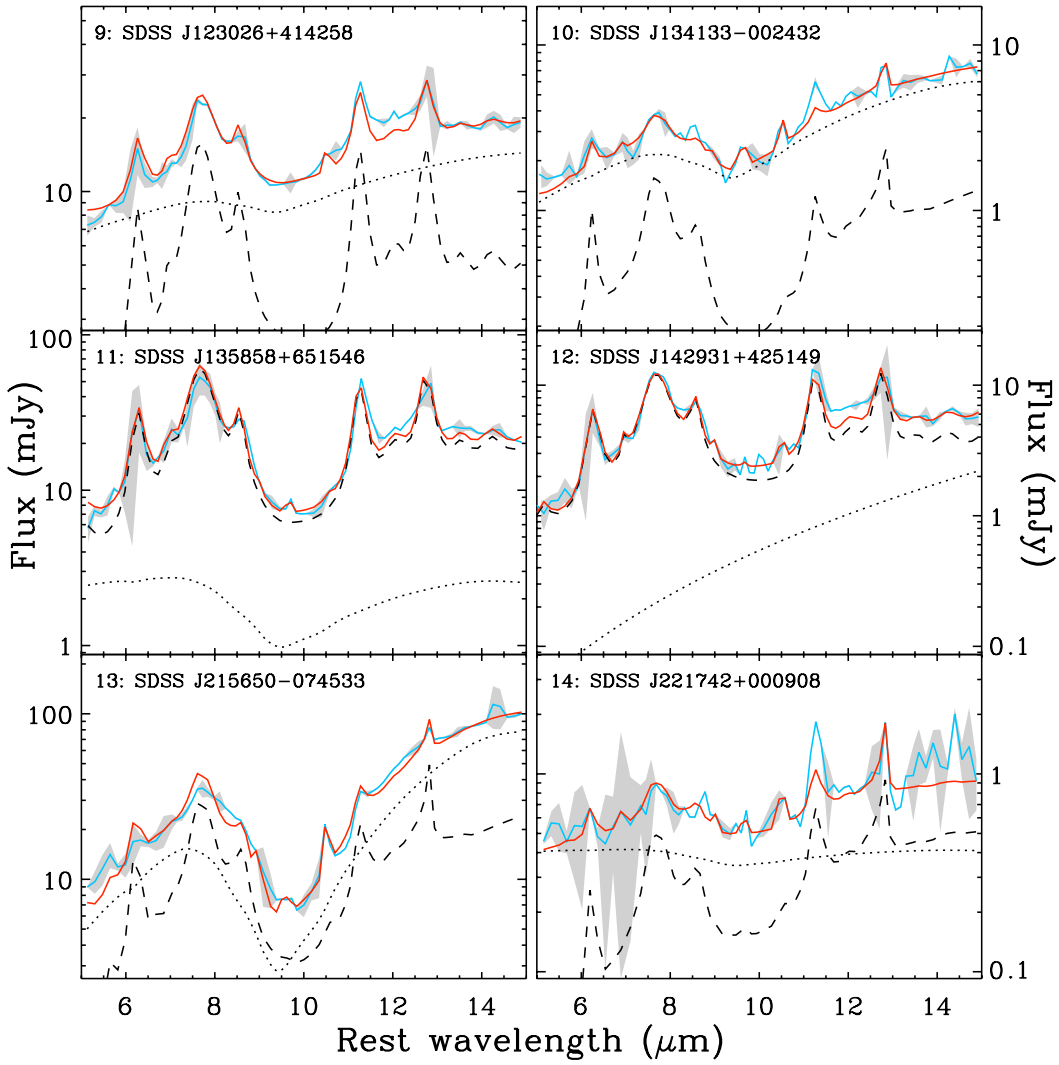

Figure 6.4: *continued*...

Table 6.2: Measured AGN properties for candidate Compton-thick AGNs

ID	[NeV]λ14.32	[NeV]λ24.32	[OIV]λ25.89	$S_{24\mu m}$	SB	AGN	$S_{6\mu m}$	log($L_{X,[OIV]}$)	log($L_{X,6\mu m}$)	C-thick?	
	(erg s^{-1} cm^{-2})	(erg s^{-1} cm^{-2})	(erg s^{-1} cm^{-2})	(mJy)	Model	cont.	(mJy)	(erg s^{-1})	(erg s^{-1})	[OIV]	6 μm
(1)	(2)	(3)	(4)	(5)	(6)	(7)	(8)	(9)	(10)	(11)	(12)
1	< 0.98	< 0.77	3.91 ± 0.81	3.98 ± 0.04	2	40%	1.71 ± 0.14	42.67	42.74	y	y
2	10.51 ± 1.43	6.60 ± 2.09	29.39 ± 1.05	17.82 ± 0.05	2	55%	3.27 ± 0.19	44.42	43.58	Y	y
3	4.07 ± 0.78	4.07 ± 0.78	6.45 ± 2.03	8.49 ± 0.03	3	92%	2.49 ± 0.02	43.63	43.30	y	?
4	3.58 ± 0.55	3.65 ± 0.54	12.89 ± 0.64	-	3	38%	1.30 ± 0.76	42.76	42.08	Y	?
5	< 2.94	< 1.00	6.79 ± 1.62	8.90 ± 0.05	3	$< 0.1\%$	< 0.01	42.80	-	Y	-
6	< 1.67	< 0.78	5.64 ± 0.91	6.80 ± 0.03	2	72%	1.42 ± 0.17	43.88	43.34	Y	y
7	3.33 ± 0.98	2.95 ± 0.95	10.90 ± 1.38	10.72 ± 0.10	2	53%	2.53 ± 0.31	43.26	42.74	Y	y
8	7.40 ± 1.81	< 2.19	19.07 ± 1.03	65.36 ± 0.06	3	38%	5.47 ± 0.99	43.26	43.01	Y	Y
9	< 2.07	< 1.47	5.24 ± 0.90	-	3	66%	8.36 ± 0.33	43.45	43.69	Y	Y
10	< 1.08	< 1.32	6.52 ± 0.92	6.93 ± 0.04	1	85%	1.95 ± 0.11	42.91	42.52	y	?
11	< 2.46	< 3.39	12.89 ± 1.92	39.94 ± 0.03	3	12%	3.47 ± 2.71	42.26	42.06	y	y
12	< 1.07	< 0.63	4.68 ± 0.76	6.33 ± 0.03	3	9%	0.09 ± 0.40	43.35	41.91	?	?
13	57.16 ± 3.16	42.17 ± 6.52	180.77 ± 6.01	106.90 ± 0.55	1	81%	16.42 ± 3.20	44.24	43.23	Y	Y
14	< 1.44	< 0.96	3.06 ± 0.51	-	2	62%	0.43 ± 0.09	42.09	41.44	Y	?

NOTES: (1) SDSS source-identification. (2-4) Fluxes and their 1σ uncertainty for the AGN-produced mid-IR emission lines in units of 10^{-15} erg s^{-1} cm^{-2}. (5) MIPS 24 μm flux density in units of mJy. (6) Best-fit starburst model in the mid-IR spectral modeling analysis (see section 6.3.4) - 1: M82; 2: Combined SB (Brandl et al. 2006); 3: Circumnuclear starburst at 3 kpc (SK07). (7) Inferred AGN contribution to the mid-IR emission at $\lambda \sim 5$–15 μm. (8) Unabsorbed AGN 6 μm flux and 1σ uncertainty in units of mJy. (9-10) Logarithm of the estimated 2–10 keV luminosity from the AGN-produced [OIV] and 6 μm emission (see sections 6.3.3, 6.3.4 and 6.4.1 for further details). (11-12) Indication for whether the source is consistent with being Compton-thick ($N_H > 1.5 \times 10^{24}$ cm^{-2}) on the basis of the mid-IR indicators: 'Y' - conservatively identified to be Compton-thick, 'y' - less-conservatively identified to be Compton-thick, '?' - inconclusive due to X-ray upper-limits (see section 6.4.1).

In order to estimate the intrinsic AGN luminosity and hence place limits on the X-ray absorption in these sources, we use the measured AGN power-law parameters to derive $6\ \mu\mathrm{m}$ luminosities ($L_{6\mu m}$). The uncertainties of these $6\ \mu\mathrm{m}$ fluxes are established by considering a weighted spread in the measured $6\ \mu\mathrm{m}$ fluxes from all statistically valid starburst template fits (i.e., we reject all statistically poor fits at the 95 per cent level). The mean 1σ uncertainty is ≈ 0.1 dex. See column (8) of Table 6.2.

We estimate the $6\ \mu\mathrm{m}$ continuum luminosities for 13 of our 14 candidate Compton-thick AGNs and conservatively estimate an upper limit for the $6\ \mu\mathrm{m}$ continuum flux of $< 10^{-2}$ mJy for SDSS J102142+130550. We find using our adopted cosmology, that the AGNs cover more than 2 decades in $6\ \mu\mathrm{m}$ luminosity, with $\nu L_{6\mu m} \approx (0.1\text{–}20) \times 10^{43}\,\mathrm{erg\,s^{-1}}$.

6.4 Results and Discussion

We have selected a sample of 14 [OIII] bright, X-ray undetected AGNs from the $\approx 100\,\mathrm{deg}^2$ overlap region between the SDSS-DR7 and 2XMMi surveys. These sources lie at $z \sim 0.03$–0.2 and host moderately luminous AGNs with $L_{[\mathrm{OIII}]} \approx (0.2\text{–}500) \times 10^{42}\,\mathrm{erg\,s^{-1}}$ (i.e., similar to those of typical nearby Seyfert galaxies). Our 14 targets all have $f_X/f_{[\mathrm{OIII}]} < 1$, implying strong intrinsic absorption of their X-ray flux; i.e., many are likely Compton-thick AGNs. In the absence of X-ray spectroscopic data, in section 6.3 we derived AGN-produced emission line and continuum luminosity measurements in order to independently constrain the intrinsic luminosity of these candidate Compton-thick AGNs. In this section, we use these intrinsic luminosities in conjunction with X-ray constraints from *XMM-Newton* data to test whether these objects are indeed Compton-thick AGNs. We then use these results to place new constraints on the space density and relative mass-accretion rates of Compton-thick AGNs in the nearby Universe ($z \sim 0.1$).

6.4.1 Identifying Compton-thick AGNs at $z \sim 0.1$

Previously, strong, relatively high-excitation emission lines, such as [OIII]λ5007 (35.1 eV), have been used as proxies for hard X-ray emission in AGNs, and hence, their intrinsic luminosity (L_{AGN}; e.g., Mulchaey et al. 1994; Alonso-Herrero et al. 1997; Heckman et al. 2005; Panessa et al. 2006). However, such emission may also be readily excited by strong star-formation as well as being subject to significant dust-extinction within the host galaxy. By contrast, mid-IR high-excitation narrow-line emission (e.g., [NeV]; [OIV])

is an excellent extinction-free indicator of $L_{\rm AGN}$ (see Section 6.3.3) and, when combined with sensitive X-ray data, can provide good first order constraints on whether an AGN in Compton thick.

In Fig. 6.5 we present the observed 2–10 keV X-ray upper-limit luminosities from the *XMM-Newton* data versus the mid-IR [OIV] luminosity for our candidate Compton-thick AGNs and compare them to the intrinsic properties found for local 'bona-fide' Compton-thick AGNs. We find that the candidate Compton-thick AGNs are spread over a wide range of [OIV] luminosities, $L_{\rm [OIV]} \approx (0.13\text{–}20) \times 10^{41}\,{\rm erg\,s^{-1}}$; for the sources in our sample which we find to be dominated by SF at mid-IR wavelengths (column 7 of Table 6.2), [OIV] fluxes have conservatively been adjusted for contamination from [FeII] emission (see section 6.3.3). We find that based on the observed X-ray upper-limits, none of the objects in our sample are consistent with the local intrinsic relation of AGNs from Goulding et al. (2010), suggesting that the X-ray emission is heavily obscured. However, as we illustrate in Fig. 6.5, the observed $L_X/L_{\rm [OIV]}$ for our sample (mean ratio ≈ 3.6) is consistent with the observed $L_X/L_{\rm [OIV]}$ ratio for a sample of well-studied local 'bona-fide' Compton-thick AGNs (i.e., Circinus, Mrk 3, NGC 1068 and NGC 6240). Furthermore, the $L_X/L_{\rm [OIV]}$ luminosity ratio of these four Compton-thick AGNs is consistent with the Goulding et al. (2010) relationship when the X-ray data is corrected for the absorption implied from high-quality X-ray spectroscopy. Assuming the [OIV] emission is indeed an isotropic AGN indicator (e.g., Melendez et al. 2008; Diamond-Stanic et al. 2009; Goulding et al. 2010), this suggests that by comparing the observed X-ray upper-limit to the intrinsic X-ray luminosity as predicted by our [OIV] measurements ($L_{\rm x,[OIV]}$), we may infer whether the sources in our sample are indeed Compton-thick AGNs.

Based on Compton reflection models, Alexander et al. (2008) predict that the observed–intrinsic X-ray flux ratio for a Compton-thick AGN with $N_H \sim 1.5 \times 10^{24}\,{\rm cm^{-2}}$ is $f_{\rm X,intr}/f_{\rm X,obs} \approx 15$ in the 2–10 keV band. Hence, we predict that sources with $f_{\rm X,intr}/f_{\rm X,obs} \gtrsim 15$ are likely to be obscured by Compton-thick material. For the 14 candidate Compton-thick AGNs in our sample, we calculate $f_{\rm X,[OIV]}$ using the local X-ray–[OIV] relation of Goulding et al. (2010). We predict intrinsic X-ray luminosities of $L_{X,\rm predict} \approx (0.1\text{–}26) \times 10^{43}\,{\rm erg\,s^{-1}}$ (see Column 9 of Table 6.2). We find that 13 (≈ 90 percent) of the sources exhibit $f_{\rm X,[OIV]}/f_{\rm X,obs} \gtrsim 15$ (see Column 11 of Table 6.2). The intrinsic scatter within the local X-ray–[OIV] relation is ≈ 0.3 dex, hence the average uncertainty on the estimated intrinsic X-ray luminosities is a factor of ≈ 2. Therefore, if we conservatively assume that none of the AGNs in our sample with $f_{\rm X,intr}/f_{\rm X,obs} \approx 15\text{–}30$ are

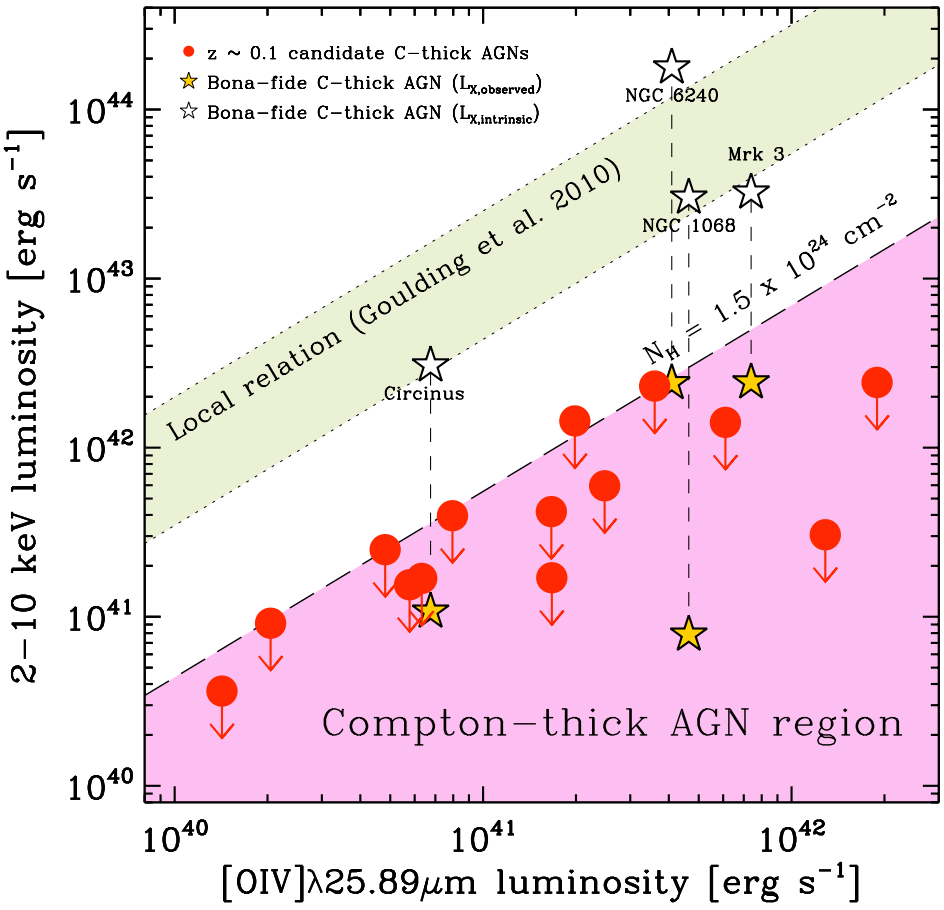

Figure 6.5: Rest-frame 2–10 keV X-ray luminosity versus mid-IR [OIV] ($\lambda 25.89\ \mu$m) luminosity ($L_{[\mathrm{OIV}]}$) for our sample of Compton-thick AGN candidates (filled circles). We show the local X-ray–[OIV] relation of Goulding et al. (2010) and find on the basis of $L_{[\mathrm{OIV}]}$ that the majority of our sample are consistent with the observed X-ray luminosity being absorbed by a factor ≥ 20 (i.e., $N_H > 1.5 \times 10^{24}\,\mathrm{cm}^{-2}$). For comparison, we additionally highlight the observed (filled stars) and absorption-corrected (open stars) X-ray luminosities for 4 well-studied 'bona-fide' Compton-thick AGNs (Circinus, Mrk 3, NGC 1068 and 6240). The observed X-ray luminosities for these 'bona-fide' Compton-thick AGNs occupy roughly the same region of parameter space as our sample but our objects are $\approx$ 10–100 times more distant. However, their intrinsic X-ray luminosities are consistent with the local relations.

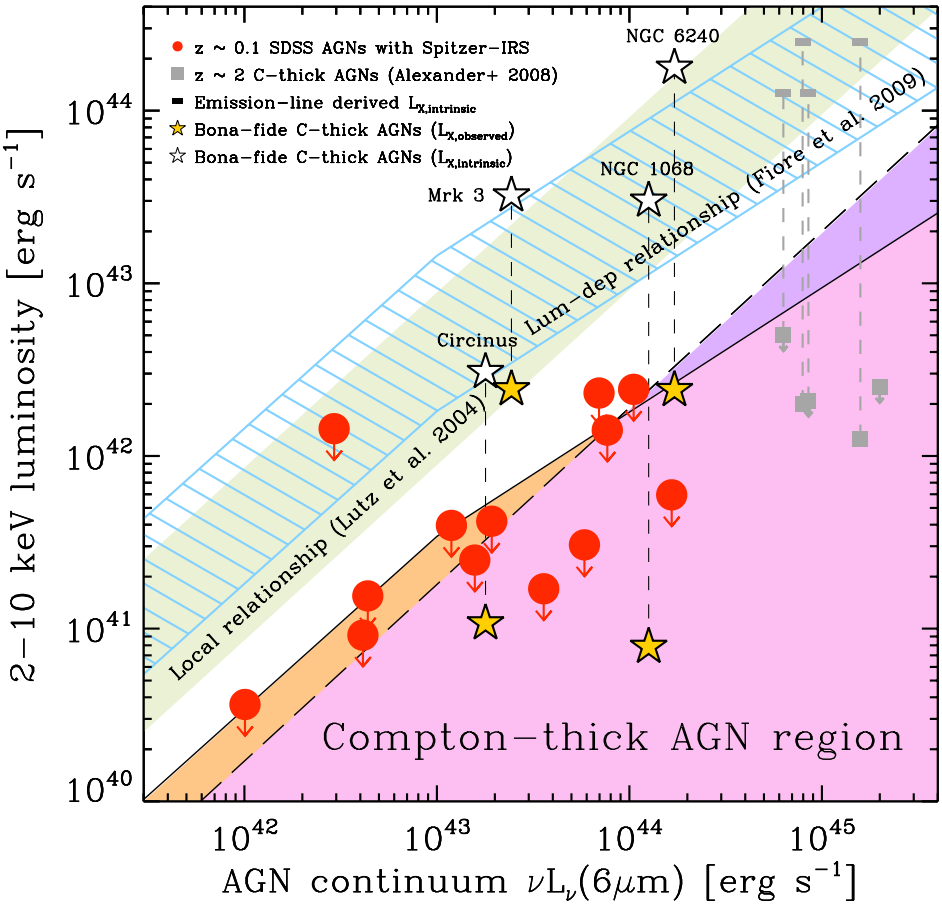

Figure 6.6: Rest-frame 2–10 keV X-ray luminosity versus the mid-IR AGN continuum luminosity at 6 μm for the Compton-thick AGN candidates with measured 6 μm luminosities (filled circles). A comparison sample of $z \sim 2$ Compton-thick quasars is additionally shown (Alexander et al. 2008; grey squares). We use the local X-ray–6 μm relation of Lutz et al. (2004) and the luminosity-dependent relation of Fiore et al. (2009) to predict the region of parameter space where Compton-thick AGN lie. We find that on the basis of 6 μm luminosities, many of the sources in our sample are likely to be Compton-thick AGNs. For comparison, we additionally highlight the observed (filled stars) and absorption-corrected (open stars) X-ray luminosities for 4 well-studied 'bona-fide' Compton-thick AGNs (Circinus, Mrk 3, NGC 1068 and 6240).

Compton thick, but instead apply a more conservative Compton-thick AGN threshold of $f_{\rm X,intr}/f_{\rm X,obs} \gtrsim 30$, we still estimate that at least 9/14 (≈ 65 percent) of our candidate Compton-thick AGNs could be genuine Compton-thick AGNs. It is also prudent to note that as the observed X-ray constraints for all of these sources are upper-limits, the implied $f_{\rm X,[OIV]}/f_{\rm X,obs}$ ratio is also a lower-limit, and hence, we cannot exclude the possibility that all of the sources in our sample are Compton-thick AGNs.

By combining multiple indirect AGN luminosity indicators, particularly those which probe different regions of the central engine, we can place even stronger constraints on whether the AGNs in our sample are Compton thick than using narrow-line emission alone. The $6\ \mu$m continuum luminosity has been shown to provide a good proxy for the intrinsic AGN luminosity (e.g., Lutz et al. 2004; Maiolino et al. 2007; Treister et al. 2008; Fiore et al. 2009). In Fig. 6.6 we again present the observed 2–10 keV X-ray upper-limit luminosities from *XMM-Newton* data but now compare these luminosities to the AGN continuum luminosity at $6\ \mu$m derived in Section 6.3.4 and the luminosity-dependent (Fiore et al., 2009) and luminosity-independent (Lutz et al. 2004) relations derived using high-quality X-ray data and mid-IR *Spitzer* IRAC photometry and ISO spectroscopy, respectively. As noted in Section 6.3.4, one of our 14 candidate Compton-thick AGNs is consistent with there being little or no mid-IR emission from an AGN continuum at $\lambda \sim 5$–$15\ \mu$m, and we remove this AGN from further analyses in this section.

We conservatively adopt the slightly lower-luminosity X-ray–$6\ \mu$m relationship of Lutz et al (2004) to infer the intrinsic X-ray luminosities of the candidate Compton-thick AGNs. We estimate intrinsic X-ray luminosities of $L_{X,\rm predict} \approx (0.2$–$30) \times 10^{42}\,{\rm erg\,s^{-1}}$ (see Column 10 of Table 6.2). Eight out of the 13 (≈ 60 percent) $6\ \mu$m detected sample members lie in the region expected for Compton-thick AGNs (i.e., $N_H \gtrsim 1.5 \times 10^{24}\,{\rm cm^{-2}}$; see Column 12 of Table 6.2). However, if we were to adopt the relationship of Fiore et al. (2009) this Compton-thick AGN fraction would increase to 9/13 sources (≈ 80 percent; i.e., consistent with that found when using [OIV] as a N_H diagnostic). Furthermore, if we account for the intrinsic scatter of within the Lutz et al (2004) relationship (≈ 0.5 dex), and (as above) conservatively assume that none of the sources which lie within this region of scatter are genuine Compton thick AGNs, we still find that at least 3 of the 13 (≈ 20 percent) sources must be Compton thick.

In Columns 11 and 12 of Table 6.2 we summarise whether we identify the sources to be Compton-thick AGNs on the basis of their combined X-ray and mid-IR properties. We consider those AGNs which are conservatively identified as Compton-thick AGNs

(i.e., those which lie below the region of intrinsic scatter derived from the L_X–$L_{[\rm OIV]}$ and L_X–$L_{6\mu m}$ relationships) in at least one of the mid-IR diagnostics and are also below the standard Compton thick threshold in the other mid-IR diagnostic to be genuine Compton-thick AGNs (i.e., in the nomenclature of Table 6.2, only those AGNs with Y-Y, Y-y or y-Y). This is a reasonable and conservative assumption to make if we consider the 'bona-fide' Compton-thick AGNs shown in Figs. 6.5 and 6.6; all of these AGNs would be identified to be Compton-thick AGNs (y/Y) on the basis of [OIV] emission and 3/4 on the basis of $6\ \mu$m emission. Hence, using our adopted definition, we find that 6/14 (≈ 43 percent) of our candidate Compton-thick AGNs are very likely genuine Compton-thick AGNs on the basis of their combined mid-IR properties. Under the reasonable assumption that our sample of candidate Compton-thick AGNs is a representative subsample of the parent X-ray undetected population of AGNs in the SDSS-DR7 (i.e., in both redshift and luminosity parameter space; see section 6.2), these results imply that $\approx 43 \pm 21$ percent of the sources with $f_X/f_{[\rm OIII]} < 1$ are Compton thick.[9]

Of the four AGNs which were selected because they lie in the Compton-thick AGN exclusive region of Fig. 6.2 (i.e., those with $f_X/f_{[\rm OIII]} < 0.1$), three have mid-IR emission-line and continuum AGN indicators consistent with the X-ray emission being absorbed by at least a factor $\gtrsim 15$. Hence, these are very likely to be Compton-thick AGNs. Whilst the [OIV] emission from the fourth AGN (SDSS J221742+000908) is consistent with a Compton-thick AGN (see Fig. 6.5) we find little evidence for this on the basis of its $6\ \mu$m continuum luminosity. Indeed, the observed $L_{X,2-10keV}$ appears to be comparatively unabsorbed on the basis of AGN continuum luminosity. However, we note that we would also find a similar result for the 'bona-fide' Compton-thick AGN, Mrk 3. We find that five of the 10 AGNs with $f_X/f_{[\rm OIII]} \sim 0.1$–$1.0$ exhibit mid-IR emission features consistent with Compton-thick AGNs. All five AGNs have strong [OIV] and $6\ \mu$m luminosities suggesting strong absorption of the X-ray emission, as well as evidence for silicate absorption at $9.7\ \mu$m. By contrast, for the AGN which does not appear to be clearly Compton-thick on the basis of either of our mid-IR AGN indicators (SDSS J142931+425149), we find that the underlying AGN continuum in this sources is consistent with an unabsorbed power-law (i.e., no evidence for silicate absorption).

[9] Uncertainties are calculated using standard Poisson counting statistics.

6.4.2 The space-density of Compton-thick AGNs at $z \sim 0.1$

Based on the mid-IR emission-line and continuum emission diagnostics, we find that at least six ($\gtrsim 43 \pm 21$ percent) of our sample of 14 X-ray undetected optical narrow-line AGNs with $L_X/L_{[\rm OIII]} < 1$ appear to suffer from heavy intrinsic absorption with $N_H \gtrsim 1.5 \times 10^{24}\,{\rm cm}^{-2}$ (i.e., they are Compton-thick AGNs). Assuming that our sample of candidate Compton-thick AGNs is representative of the parent population, we may use our derived Compton-thick AGN fraction to infer at least a lower limit for the number, and hence space density, of Compton-thick AGNs at $z \sim 0.03$–0.2.

The total number of Type-2 AGNs in the SDSS-2XMMi overlap region is 334 at $z \sim 0.03$–0.2, 147 (≈ 45 percent) of these AGNs are X-ray undetected in 2XMMi with $L_X/L_{[\rm OIII]} < 1$ (i.e., our parent sample). Based on our derived AGN fraction, we would expect that $\gtrsim 63$ of the sources in our parent sample with $L_X/L_{[\rm OIII]} < 1$ to be Compton-thick AGNs, i.e., at least ≈ 20 percent of all Type-2 AGNs in the SDSS-2XMMi overlap region. The volume encompassed by our survey is $V \approx 4.6 \times 10^6$ Mpc^3. Hence, we estimate a lower limit to the space-density of Compton-thick AGNs at $z \sim 0.1$ of $\log(\Phi) \gtrsim -5.2$ Mpc^{-3} in the luminosity range of $L_X \approx (0.1\text{–}10) \times 10^{43}\,{\rm erg\,s^{-1}}$. In Fig. 6.7 we compare our estimated space-density lower-limit to that of the XRB synthesis models and to the similar study of SDSS-selected Compton-thick quasars of Vignali et al. (2010). At the median predicted intrinsic X-ray luminosity of our sample of Compton-thick AGNs ($L_X \approx 10^{43}\,{\rm erg\,s^{-1}}$), we find good agreement with that predicted by the XRB model at $0.03 < z < 0.2$. Furthermore, by comparison to wide-field derived hard X-ray luminosity functions (e.g., Ueda et al. 2003), we suggest that these Compton-thick sources may comprise a significant fraction ($\approx$ 20–100 percent) of X-ray undetected accretion in the nearby Universe.

6.4.3 The mean growth rate of Compton-thick AGNs at $z \sim 0.1$

In this section we consider the implied Eddington ratios ($\eta \sim L_{\rm AGN}/L_{\rm Edd}$; where $L_{\rm Edd} \approx 1.26 \times 10^{38} ({\rm M_{BH}}/{\rm M_\odot})\,{\rm erg\,s^{-1}}$) for the Compton-thick AGNs identified in our sample with publicly available black-hole mass ($\rm M_{BH}$) estimates. Stellar velocity dispersion measurements have been computed for 13 out of the 14 AGNs in our sample, at least five of which we identify as Compton-thick AGNs. These measurements are publicly available in the MPA-JHU release of SDSS-DR7 and are derived from the fitting of stellar

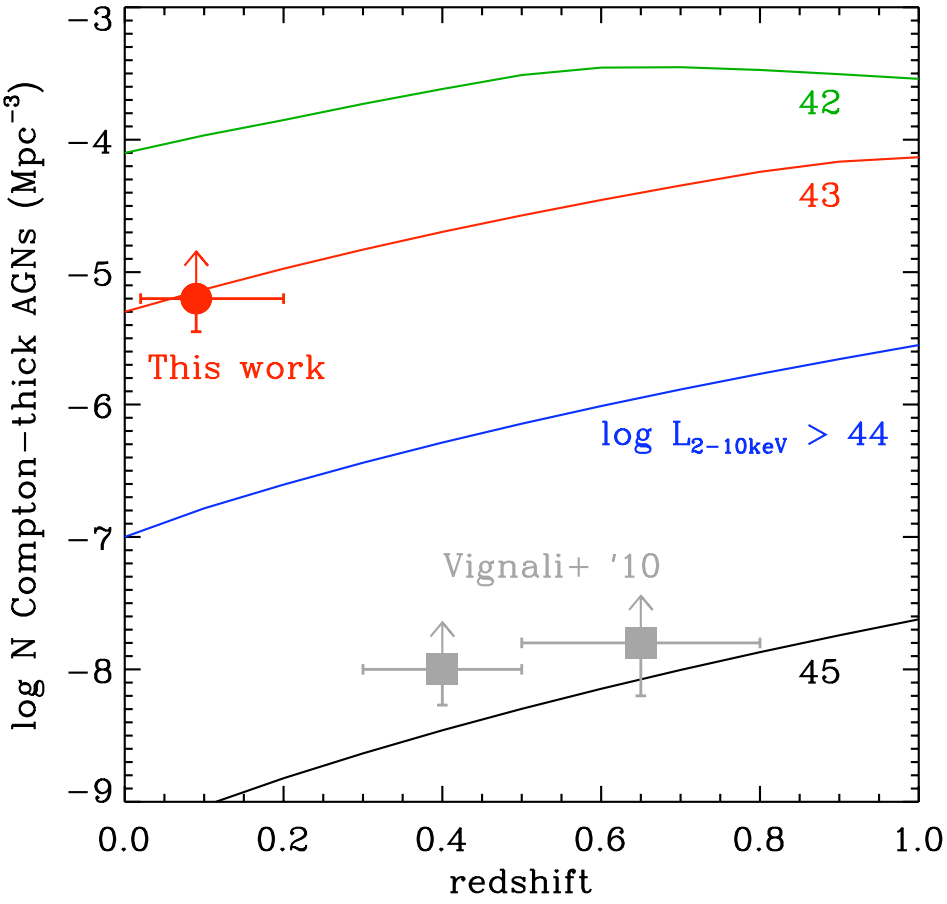

Figure 6.7: Space density of Compton-thick AGNs compared with the XRB synthesis models for intrinsic X-ray luminosities of $L_X > 10^{42}$,10^{43},10^{44} and $10^{45}\,\mathrm{erg\,s^{-1}}$ (Gilli et al. 2007). Data points refer to this work (circle) and those from a comparable study of luminous Compton-thick quasars at $z \sim 0.3$–0.8 derived from the SDSS (Vignali et al. 2010; squares).

population synthesis models to the SDSS 1-D spectra.[10] Using the M–σ relation of Gebhardt et al. (2000) we convert the stellar velocity dispersions to $\mathrm{M_{BH}}$ (see Column 7 of Table 6.1) in order to calculate L_{Edd} for these sources. The median SMBH mass for our sample is $\mathrm{M_{BH}} \approx 3 \times 10^{7}\,\mathrm{M_{\odot}}$ (i.e., these AGNs host SMBHs similar to those identified in H04; see Chapter 4).

In order to estimate η for our Compton-thick AGNs, we use $L_{[\mathrm{OIV}]}$ to infer L_{X} using the relation of Goulding et al. (2010) and we assume the bolometric corrections of Marconi et al. (2004) to calculate L_{AGN}. On the basis of their [OIV] luminosities we find that the Compton-thick AGNs are spread over a wide-range of Eddington ratio, $\eta \approx 0.006$–4 (median ≈ 0.2).[11] By comparison to the total population of Type-2 AGNs identified in the SDSS, Heckman et al. (2004) find that < 0.5 percent of Type-2 AGNs hosting SMBHs with $\mathrm{M_{BH}} \approx 3 \times 10^{7}\,\mathrm{M_{\odot}}$ are accreting above $\eta \approx 0.1$. Hence, these results suggest that the Compton-thick AGNs identified here harbour some of the most rapidly growing black holes in the nearby Universe. This would further suggest that not taking account of Compton-thick AGNs in deep-field X-ray surveys may exclude the most rapid growth phases of SMBHs as predicted by many models (e.g., Fabian 1999; Granato et al. 2006; Hopkins et al. 2008).

6.5 Summary

We have presented a sample of 14 local ($z \sim 0.03$–0.2) X-ray undetected optical AGNs selected from the large overlap region between the SDSS-DR7 and 2XMMi catalogues. These sources were selected as candidate Compton-thick AGNs on the basis of their X-ray–[OIII] emission line ratios (i.e., $f_X/f_{[\mathrm{OIII}]} < 1.0$; e.g., Bassani et al. 1999; see Section 6.2). We have employed a suite of optical (e.g., [OIII] emission-line) and mid-IR (e.g., [OIV] emission-line; 6 μm AGN continuum) diagnostics to infer the intrinsic AGN luminosity in these sources. Assuming any deficit in X-ray flux compared to these es-

[10] The MPA-JHU SDSS catalogue is maintained by a large collaboration of SDSS researchers and is a complementary dataset providing additional information for the SDSS-DR7 data-release including measurements of velocity dispersions, stellar masses, star-formation rates etc. It is available at http://www.mpa-garching.mpg.de/SDSS/

[11] It is important to note the large uncertainties involved with calculating bolometric luminosities and subsequent Eddington ratios; the large scatter in the X-ray–[OIV] relation combined with a possible Eddington ratio dependent bolometric correction (e.g., Vasudevan and Fabian 2007) could a yield an uncertainty factor of the order $\gtrsim 10$ for the highest Eddington ratio sources.

timates is due to Compton-thick absorption, we assess the ubiquity of Compton-thick AGN activity in the nearby Universe. Our main findings are the following:

(1). Using *Spitzer*-IRS low resolution spectroscopy, we find that six of our 14 candidate Compton-thick AGNs have 3σ detections of [NeV] and all 14 have [OIV]. We performed mid-IR spectral decompositions of our sample to establish $6\ \mu\mathrm{m}$ AGN continuum luminosities. Using established X-ray to mid-IR continuum and emission-line relationships, we infer the intrinsic X-ray luminosity of these AGNs and conservatively find that $6/14$ (≈ 50 percent) of the sources in our sample appear to be heavily obscured with $N_H \gtrsim 1.5 \times 10^{24}\,\mathrm{cm}^{-2}$ (i.e., are Compton-thick AGNs). We predict an overall Compton-thick AGN fraction of $\gtrsim 43 \pm 21$ percent. See sections 6.3.3, 6.3.4 and 6.4.1.

(2). We used our results to infer the ubiquity of Compton-thick AGNs in our SDSS–2XMMi parent sample. We predict that on the basis of the analyses presented here that at least $\gtrsim 20$ percent of the 334 optical Type-2 AGNs in the SDSS-DR7 at $z \sim 0.03$–0.2 are obscured by Compton-thick material. This implies a space-density of $\log(\Phi) \gtrsim -5.2$ Mpc^{-3} for Compton-thick AGNs with $L_X \approx (0.1\text{–}10) \times 10^{43}\,\mathrm{erg\,s}^{-1}$ at $z \sim 0.1$ which we find is consistent with the number density of Compton-thick AGNs predicted by XRB synthesis models. See sections 6.4.1 and 6.4.2.

(3). We establish that (allowing for uncertainties and associated optical selection effects) the Compton-thick AGNs identified in our sample appear to be rapidly accreting. Using [OIV] luminosity to infer the L_{AGN} and the stellar velocity dispersion to estimate $\mathrm{M_{BH}}$, we find for these sources a median Eddington ratio of $\eta \approx 0.2$. By comparison to studies of local Type-2 AGNs with similar SMBH masses ($\mathrm{M_{BH}} \approx 3 \times 10^7\,\mathrm{M_\odot}$ e.g., Heckman et al. 2004), we find that Compton-thick AGNs may harbour some of the most rapidly growing black holes in the nearby Universe ($z \sim 0.1$). See section 6.4.3.

In summary, we have established that about half of these sources have optical and mid-IR AGN indicators consistent with their observed X-ray emission being heavily obscured by Compton-thick material. Indirect multi-wavelength analyses, such as those employed here, are currently the best technique to identify Compton-thick AGNs which are 2–3 orders of magnitude further down the $L_X - z$ plane than can be achieved using X-ray spectroscopy alone. Using the next generation of X-ray satellites (e.g., *NuStar*;

IXO; *WFXT*), high-quality X-ray spectroscopy and $E > 10$ keV detections will allow us to directly and unambiguously classify many of these sources as Compton-thick AGNs.

Chapter 7

Conclusions & Future Work

In this thesis we have attempted to address questions that stem from a common thread: how many SMBHs are actively accreting in the nearby Universe? In this section, we summarise the main results of this in-depth investigation. We conclude this chapter by outlining a new project which uses high spatial resolution, ground-based mid-IR analyses to provide first order measurements of the absorption towards the central engine in a sample of optically unidentified seemingly X-ray weak AGNs.

7.1 An overview of presented work

7.1.1 A census of AGN activity to $D < 15$ Mpc

In Chapters 3 and 4 we presented the results of a sensitive volume-limited *Spitzer*-IRS spectral survey of all (≈ 94 percent) bolometrically luminous ($L_{IR} \gtrsim 3 \times 10^9\,L_\odot$) galaxies to $D < 15$ Mpc. We placed direct constraints on the ubiquity of AGN activity in the local Universe by conservatively assuming that the detection of the high-excitation [NeV] $\lambda 14.32\,\mu$m emission line indicates AGN activity. We identified AGNs in 17 of the 64 galaxies in our sample, i.e., an AGN fraction of $\approx 27^{+8}_{-6}$ percent; a factor $\gtrsim 2$ greater than found using optical spectroscopy alone. We found that the optically unidentified AGNs are typically characterised as star-formation dominated galaxies hosting modest-luminosity AGNs ($L_{[NeV]} \approx 10^{37}$–$10^{39}\,erg\,s^{-1}$). However, we find that the lack of optical AGN signatures are most likely due to dust extinction in the host galaxy. The majority of the optically unidentified AGNs are hosted in highly inclined galaxies or galaxies with dust lanes, indicating that obscuration of the AGN is not necessarily due to an obscuring torus.

For the 17 AGNs identified using *Spitzer*-IRS, we presented the mean growth times and volume-weighted space density of active SMBHs in the local Universe. The most accurate SMBH masses available for the objects are compiled from a variety of sources. We combined mid-IR emission line and high-quality hard X-ray constraints to derive accurate measurements of the intrinsic luminosities of the 17 AGNs. Due to our high sensitivity and the ability to probe low SMBH masses, we find that significant mass accretion ($\eta > 10^{-3}$) occurs onto SMBHs with $\mathrm{M_{BH}} \approx 10^{6}\,\mathrm{M_{\odot}}$, the majority of which would not be detected in even the most sensitive optical surveys. For AGNs hosting SMBHs with $\mathrm{M_{BH}} \approx (0.5\text{–}50)\times10^{7}\,\mathrm{M_{\odot}}$ we find consistent growth times ($t_{2M} \approx 47$–198 Gyrs) with those of the narrow-line AGNs identified in the Sloan Digital Sky Survey. However, we find that SMBHs with $\mathrm{M_{BH}} < 5 \times 10^{6}\,\mathrm{M_{\odot}}$, are amongst the mast rapidly accreting in the nearby Universe with $t_{2M} \approx 6^{+6}_{-3}$ Gyrs. To assess the incidence of this population of low mass, rapidly growing SMBHs, we constructed a local space density function of active SMBHs. We calculated a non-negligible space density for low mass active SMBHs ($\mathrm{M_{BH}} \approx 10^{6}\,\mathrm{M_{\odot}}$) of $\Phi \approx 6 \times 10^{-4}\mathrm{Mpc^{-3}}\,\log\,\mathrm{M_{BH}^{-1}}$ which is consistent with the space density of more massive active SMBHs ($\mathrm{M_{BH}} \approx 10^{7}\,\mathrm{M_{\odot}}$; i.e., those previously determined to be the most rapidly accreting population of SMBHs from optical surveys). Hence, we find no direct evidence for a turnover at low masses as has been previously suggested. Using a local total SMBH mass function, we estimated a mean volume-weighted local AGN fraction of $\approx 25^{+29}_{-14}$ percent, which remains relatively constant in the mass range $\mathrm{M_{BH}} \approx (1\text{–}10) \times 10^{6}\,\mathrm{M_{\odot}}$.

7.1.2 The incidence of [NeV] $\lambda3427$Å detected AGNs in the SDSS-DR7

In Chapter 5 we used [NeV] $\lambda3427$Å emission as an unambiguous AGN indicator to assess the incidence of AGN activity in the SDSS and to further understand the nature of the population of optically unidentified AGNs investigated in chapters 3 and 4. We find that only $\approx 27 \pm 4$ percent of optical AGNs (i.e., those identified using BPT diagnostics) have significant detections of [NeV] $\lambda3427$Å emission, and that only ≈ 2 percent of HII and transition region galaxies appear to host AGNs on the basis of [NeV] $\lambda3427$Å (i.e., are optically unidentified AGNs). Using spectral stacking analyses we investigated the average optical spectroscopic properties of [NeV] $\lambda3427$Å detected and undetected sources in the SDSS-DR7. We found that the optical spectra for [NeV] $\lambda3427$Å detected sources are characterised by strong [OIII] $\lambda5007$Å emission lines, and that optical AGNs which lack [NeV] $\lambda3427$Å emission are most likely dust extinguished. By contrast, [NeV]

$\lambda 3427$Å detected HII and transition region galaxies are most likely to be NLS1s based on their broad-based Balmer lines. We compared the populations of [NeV] $\lambda 3427$Å detected galaxies in the SDSS-DR7 to the sample of [NeV] $\lambda 14.32\ \mu\mathrm{m}$ detected optically unidentified AGNs presented in Chapters 3 and 4. We found that in colour-magnitude space, optically unidentified AGNs are hosted in significantly bluer and lower mass galaxies than those which are readily identified in the SDSS. Hence, we conclude that large-scale optical surveys such as the SDSS are likely to miss a significant fraction of present-day accretion onto the lowest mass supermassive black holes.

7.1.3 Searching for Compton-thick AGNs at $z \sim 0.1$

In Chapter 6 we combined the unprecedented wide-field coverages of the SDSS and the 2XMMi surveys to select 14 candidate Compton-thick AGNs to be observed with *Spitzer*-IRS spectroscopy. On the basis of their observed X-ray and optical emission-line fluxes, these AGNs were selected to contain heavily absorbed central sources. We found that six of our 14 candidate Compton-thick AGNs have 3σ detections of [NeV] and all 14 have [OIV] in mid-IR spectroscopy. We performed mid-IR spectral decompositions of our sample to establish $6\ \mu\mathrm{m}$ AGN continuum luminosities. Using established X-ray to mid-IR continuum and emission-line relationships, we inferred the intrinsic X-ray luminosity of these AGNs and conservatively found that 6/14 (≈ 43 percent) of the sources in our sample appeared to be heavily obscured with $N_H \gtrsim 1.5 \times 10^{24}\,\mathrm{cm}^{-2}$ (i.e., are Compton-thick AGNs). We predict that at least $\gtrsim 20$ percent of the 334 optical Type-2 AGNs in the SDSS-DR7 at $z \sim 0.03$–0.2 are obscured by Compton-thick material. This implies a space-density of $\log(\Phi) \gtrsim -5.2$ Mpc^{-3} for Compton-thick AGNs with $L_X \approx (0.1$–$10) \times 10^{43}\,\mathrm{erg\,s}^{-1}$ at $z \sim 0.1$ which we find is consistent with the number density of Compton-thick AGNs predicted by XRB synthesis models. Furthermore, we established that the Compton-thick AGNs identified in our sample appear to be rapidly accreting (median Eddington ratio ~ 0.2) and that Compton-thick AGNs may harbour some of the most rapidly growing black holes in the nearby Universe ($z \sim 0.1$).

7.2 Future work

Mid-IR emission line diagnostics, based on the identification of the AGN-produced high-excitation mid-IR emission-lines (e.g., [OIV] 54.9eV; [NeV] 97.1eV) from recent *Spitzer*-IRS spectroscopy suggest that ≈ 27 percent of bolometrically-luminous galaxies at $D < 15$ Mpc host intrinsically luminous AGNs (Goulding & Alexander 2009; see Chapter 3), despite the fact that many have weak optical and X-ray nuclei. Such AGNs are presumably heavily obscured and may be surrounded by potentially Compton-thick central regions. This result implies that sensitive optical surveys may be missing ≈ 50 percent of the AGN population in the nearby Universe, possibly skewing our understanding of various AGN-related phenomena. However, measurements of the intrinsic AGN luminosity through mid-IR narrow-line emission are both in-direct (e.g., some portion could be due to high mass star-formation) and subject to light time-travel inconsistencies (e.g., the X-ray nucleus could have recently dimmed but there is a response delay to the extended line emission). Hence, based on *Spitzer*-IRS spectroscopy alone, the intrinsic AGN properties of this significant population of optically-unidentified AGN cannot be reliably measured.

The most direct measurements of the intrinsic AGN properties are made at hard X-ray energies ($E > 10$ keV), which are capable of penetrating high column densities in the most heavily-obscured and mildly Compton-thick AGNs. Goulding et al (2010) find that for the 8 AGNs in their $D < 15$ Mpc sample with excellent-quality X-ray data, the absorption-corrected X-ray luminosities are consistent with the AGN-luminosities predicted using the mid-IR [OIV] ($\lambda 25.89 \mu m$) emission (see Chapter 4). The other 9 AGNs in the $D < 15$ Mpc sample have poor quality X-ray spectral constraints, but the X-ray emission is a factor $\lesssim 100$ below that predicted using $L_{\rm OIV}$, suggesting they are heavily obscured (possibly by Compton-thick material). If confirmed, these results would indicate that a much larger fraction (a factor ≈ 2) of SMBH growth was more obscured than previously thought. Given the observed X-ray faintness of these targets, unreasonably long individual X-ray exposures (of the order ≈ 100 ks) would be required to directly test this scenario at X-ray energies.

An alternative method to infer the intrinsic AGN properties is from the mid-IR AGN continuum emission (3–15 μm) which is radiated directly from hot-dust in the torus. This emission will react on significantly shorter time-scales ($\lesssim 1$ year; i.e., the physical size of the sublimation region) than the narrow-line emission, and has been shown to pro-

vide an excellent unambiguous proxy for the absorption-corrected L_X in even the most heavily Compton-thick Seyferts (e.g., Krabbe et al. 2001; Horst et al. 2006, 2008; Gandhi et al. 2009; see Chapter 6). Therefore, the mid-IR continuum luminosity can be used to identify Compton-thick AGNs in seemingly X-ray weak objects, and thus presents the best, currently available method, to definitively identify the intrinsic properties of X-ray faint optically-unidentified AGNs. See Fig. 7.1.

The existing mid-IR observations of the $D < 15$ Mpc AGNs from high-resolution *Spitzer*-IRS spectroscopy, however, are not sufficient for these analyses. The spectral range of the hi-res *Spitzer*-IRS spectroscopy (10–37 μm) is insufficient to (1) accurately measure the contamination from circumnuclear star-formation, which is present in many of the $D < 15$ Mpc AGNs, and (2) measure the Silicate absorption feature (at ≈ 9.7 μm) which is often indicative of heavily obscured AGNs. With the demise of *Spitzer*-IRS, these analyses now require ground-based mid-IR instruments (e.g., Gemini-S T-ReCS; Gemini-N Michelle; VLT-VISIR) capable of probing linear scales of ≈ 15 parsecs at the diffraction-limit.

We have successfully proposed for 14 hours of observing time to use the superior spatial resolution and spectral range of T-ReCS on Gemini-South. We are using these to obtain diffraction-limited mid-IR imaging and spectroscopy of the central regions of the five optically-unidentified AGNs in GA09 which are observable in the 2010B semester. With the new observations, we will:

1. use the high-spatial resolution imaging data to measure the N-band (≈ 10.5 μm) continuum emission from the unresolved nuclear core.

2. use the proposed N-band spectroscopy to identify potential contaminants to the ≈ 10.5 μm continuum emission from Si absorption and nuclear star-formation emission.

3. compare the observed L_X to the intrinsic ≈ 10.5 μm continuum emission to constrain the intrinsic L_X and hence estimate the absorption towards the X-ray emission.

Overall, our proposed observations of a complete sample of candidate heavily-obscured (and possibly Compton-thick) AGNs, are required to provide first order measurements of the absorption towards the central engine and unambiguously determine the AGN intrinsic luminosities. These data will provide the best constraints on the incidence of Compton-thick AGNs out to $D < 15$ Mpc.

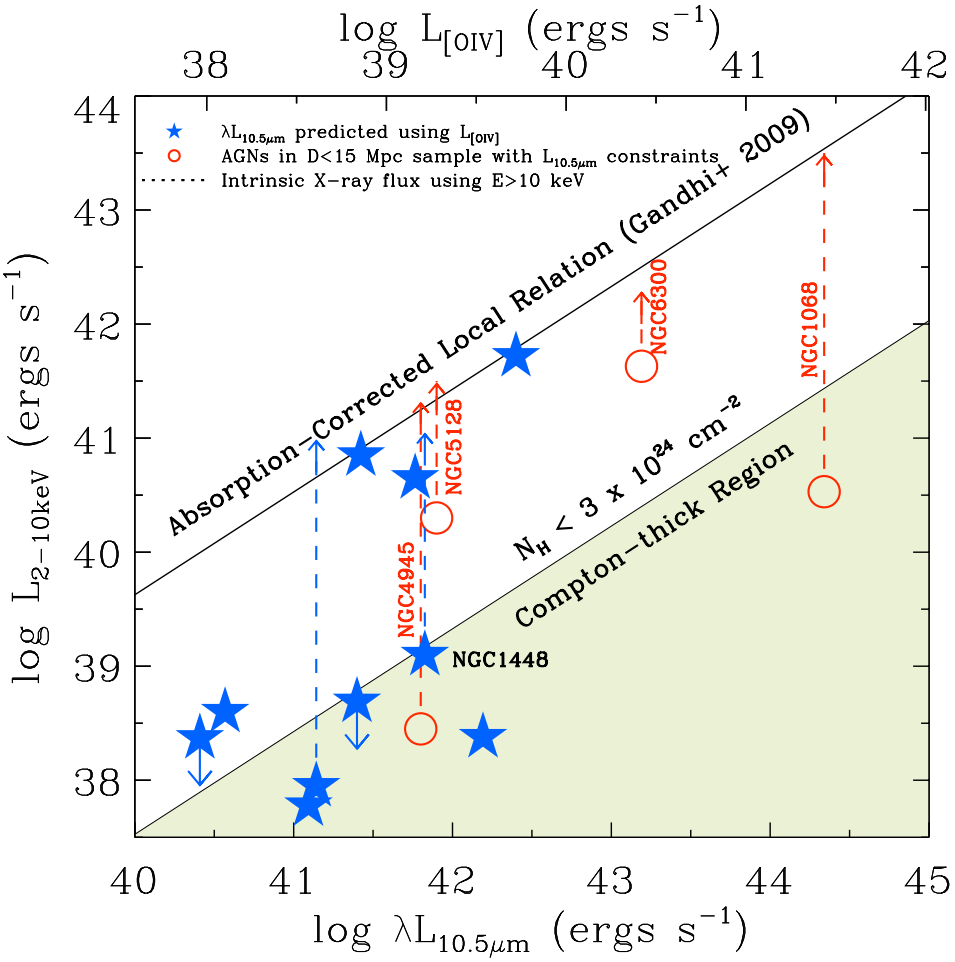

Figure 7.1: $L_{\mathrm{X,2-10keV}}$ versus predicted $\lambda L_{10.5\mu m}$ for the $D < 15$ Mpc AGNs (filled stars). For the four AGNs in GA09 currently with good measurements of $\lambda L_{10.5\mu m}$ from high-resolution mid-IR imaging (open circles), the absorption-corrected X-ray fluxes are consistent with the local relation found by Gandhi et al. (2009). On the basis of $L_{[\mathrm{OIV}]}$ we predict that at least five of the AGNs lacking mid-IR imaging are likely to be Compton-thick. High-resolution mid-IR imaging observations will provide a good test of whether these AGNs are intrinsically X-ray weak or heavily obscured before the next generation of $E > 10$ keV telescopes (> 2012).

7.3 Final remarks

How we choose to observe the AGN population will always place a bias on our interpretation and understanding of their incidence, accretion rates and role in galaxy evolution. Throughout this thesis we have used multi-wavelength analyses (from mid-IR, X-ray and optical observations) to place the strongest available constraints on the ubiquity of AGN activity in the nearby Universe. Whilst wide-scale optical surveys are now providing an excellent resource for the derivation of large active-galaxy population properties, dust-obscuration may still be preventing the identification of a significant fraction of AGNs. Obscuration-independent wavelengths (e.g., IR; X-ray) are beginning to provide a window for us to identify these heavily obscured central sources but are currently limited by technologies which are, by comparison to optical instrumentation, still in a stage of infancy.

Looking towards the coming decade, we can only be excited at the prospect of proposed future observatories. The next generation of X-ray satellites e.g., *NuStar* ($\approx$ 2012); *Astro-H* ($\approx$ 2015); *International X-ray Observatory* (subject to funding, $\approx$ 2021); *Wide-field X-ray Telescope* (subject to funding, $\approx$ 2025) will provide the greatest constraints yet on the environments and demographics of Compton-thick AGNs across cosmic time. Complimentary to this, the *James Webb Space Telescope* (*JWST*) will become a fantastic joint-successor to *Hubble* and *Spitzer*. Coupled with the *Space Infra-Red Telescope for Cosmology and Astrophysics* (*SPICA*; $\approx$ 2017), the new mid-IR imaging and spectroscopic instruments onboard these observatories will allow us to peer through obscuring dust columns to greater depths, over longer wavelength ranges and with higher resolutions than ever before. With the advent of these new missions we may become one step closer to truly providing a complete census of AGN activity throughout the Universe.

Bibliography

K. N. Abazajian et al. The Seventh Data Release of the Sloan Digital Sky Survey. *ApJS*, 182:543–558, June 2009.

J. K. Adelman-McCarthy et al. The Sixth Data Release of the Sloan Digital Sky Survey. *ApJS*, 175:297–313, April 2008.

J. Aird, K. Nandra, E. S. Laird, A. Georgakakis, M. L. N. Ashby, P. Barmby, A. L. Coil, J.-S. Huang, A. M. Koekemoer, C. C. Steidel, and C. N. A. Willmer. The evolution of the hard X-ray luminosity function of AGN. *MNRAS*, 401:2531–2551, February 2010.

A. Akylas and I. Georgantopoulos. XMM-Newton observations of Seyfert galaxies from the Palomar spectroscopic survey: the X-ray absorption distribution. *A&A*, 500:999–1012, June 2009. [AG09]

D. M. Alexander, J. H. Hough, S. Young, J. A. Bailey, C. A. Heisler, S. L. Lumsden, and A. Robinson. Searching for the hidden broad-line region in Centaurus A. *MNRAS*, 303:L17–L22, February 1999.

D. M. Alexander, W. N. Brandt, A. E. Hornschemeier, G. P. Garmire, D. P. Schneider, F. E. Bauer, and R. E. Griffiths. The Chandra Deep Field North Survey. VI. The Nature of the Optically Faint X-Ray Source Population. *AJ*, 122:2156–2176, November 2001.

D. M. Alexander, F. E. Bauer, W. N. Brandt, D. P. Schneider, A. E. Hornschemeier, C. Vignali, A. J. Barger, P. S. Broos, L. L. Cowie, G. P. Garmire, L. K. Townsley, M. W. Bautz, G. Chartas, and W. L. W. Sargent. The Chandra Deep Field North Survey. XIII. 2 Ms Point-Source Catalogs. *AJ*, 126:539–574, August 2003.

D. M. Alexander, R.-R. Chary, A. Pope, F. E. Bauer, W. N. Brandt, E. Daddi, M. Dickinson, D. Elbaz, and N. A. Reddy. Reliable Identification of Compton-thick Quasars at z ˜ 2: Spitzer Mid-Infrared Spectroscopy of HDF-oMD49. *ApJ*, 687:835–847, November 2008.

M. G. Allen, B. A. Groves, M. A. Dopita, R. S. Sutherland, and L. J. Kewley. The MAPPINGS III Library of Fast Radiative Shock Models. *ApJS*, 178:20–55, September 2008.

A. Alonso-Herrero, M. J. Ward, and J. K. Kotilainen. [OIII]5007, near-IR and X-ray properties of Seyfert 2 galaxies. *MNRAS*, 288:977–987, July 1997.

A. Alonso-Herrero, P. G. Pérez-González, G. H. Rieke, D. M. Alexander, J. R. Rigby, C. Papovich, J. L. Donley, and D. Rigopoulou. The Host Galaxies and Black Holes of Typical z˜0.5-1.4 AGNs. *ApJ*, 677:127–136, April 2008.

R. Antonucci. Unified models for active galactic nuclei and quasars. *ARA&A*, 31:473–521, 1993.

R. R. J. Antonucci and J. S. Miller. Spectropolarimetry and the nature of NGC 1068. *ApJ*, 297:621–632, October 1985.

L. Armus, J. Bernard-Salas, H. W. W. Spoon, J. A. Marshall, V. Charmandaris, and et al. Detection of the Buried Active Galactic Nucleus in NGC 6240 with the Infrared Spectrograph on the Spitzer Space Telescope. *ApJ*, 640:204–210, March 2006.

H. Awaki, K. Koyama, H. Inoue, and J. P. Halpern. X-ray implications of a unified model of Seyfert galaxies. *PASJ*, 43:195–212, April 1991.

H. Awaki, N. Anabuki, Y. Fukazawa, L. C. Gallo, S. Ikeda, N. Isobe, T. Itoh et al. Wide-Band Spectroscopy of the Compton Thick Seyfert2 Galaxy Markarian 3 with Suzaku. *PASJ*, 60:293–+, January 2008.

I. K. Baldry, K. Glazebrook, J. Brinkmann, Ž. Ivezić, and et al. Quantifying the Bimodal Color-Magnitude Distribution of Galaxies. *ApJ*, 600:681–694, January 2004.

J. A. Baldwin, M. M. Phillips, and R. Terlevich. Classification parameters for the emission-line spectra of extragalactic objects. *PASP*, 93:5–19, February 1981.

A. J. Barger, L. L. Cowie, P. Capak, D. M. Alexander, F. E. Bauer, E. Fernandez, W. N. Brandt, G. P. Garmire, and A. E. Hornschemeier. Optical and Infrared Properties of the 2 Ms Chandra Deep Field North X-Ray Sources. *AJ*, 126:632–665, August 2003.

A. J. Barth, L. C. Ho, and W. L. W. Sargent. A Study of the Direct Fitting Method for Measurement of Galaxy Velocity Dispersions. *AJ*, 124:2607–2614, November 2002.

A. J. Barth, J. E. Greene, and L. C. Ho. Dwarf Seyfert 1 Nuclei and the Low-Mass End of the M_{BH}–σ Relation. *ApJ*, 619:L151–L154, February 2005.

A. J. Barth, L. E. Strigari, M. C. Bentz, J. E. Greene, and L. C. Ho. Dynamical Constraints on the Masses of the Nuclear Star Cluster and Black Hole in the Late-Type Spiral Galaxy NGC 3621. *ApJ*, 690:1031–1044, January 2009.

L. Bassani, M. Dadina, R. Maiolino, M. Salvati, G. Risaliti, R. della Ceca, G. Matt, and G. Zamorani. A Three-dimensional Diagnostic Diagram for Seyfert 2 Galaxies: Probing X-Ray Absorption and Compton Thickness. *ApJS*, 121:473–482, April 1999.

F. E. Bauer, L. Yan, A. Sajina, and D. M. Alexander. X-ray Constraints on the Active Galactic Nuclei Properties in Spitzer-Infrared Spectrograph Identified z ˜ 2 Ultraluminous Infrared Galaxies. *ApJ*, 710:212–226, February 2010.

V. Beckmann, S. D. Barthelmy, T. J.-L. Courvoisier, N. Gehrels, S. Soldi, J. Tueller, and G. Wendt. Hard X-ray variability of active galactic nuclei. *A&A*, 475:827–835, December 2007.

A. J. Benson, D. Džanović, C. S. Frenk, and R. Sharples. Luminosity and stellar mass functions of discs and spheroids in the SDSS and the supermassive black hole mass function. *MNRAS*, 379:841–866, August 2007.

M. C. Bentz, B. M. Peterson, H. Netzer, R. W. Pogge, and M. Vestergaard. The Radius-Luminosity Relationship for Active Galactic Nuclei: The Effect of Host-Galaxy Starlight on Luminosity Measurements. II. The Full Sample of Reverberation-Mapped AGNs. *ApJ*, 697:160–181, May 2009a.

M. C. Bentz, B. M. Peterson, R. W. Pogge, and M. Vestergaard. The Black Hole Mass-Bulge Luminosity Relationship for Active Galactic Nuclei From Reverberation Mapping and Hubble Space Telescope Imaging. *ApJ*, 694:L166–L170, April 2009b.

J. Bernard-Salas, H. W. W. Spoon, V. Charmandaris, V. Lebouteiller, D. Farrah, D. Devost, B. R. Brandl, Y. Wu, L. Armus, L. Hao, G. C. Sloan, D. Weedman, and J. R. Houck. A Spitzer High-resolution Mid-Infrared Spectral Atlas of Starburst Galaxies. *ApJS*, 184: 230–247, October 2009.

W. Bian, Q. Yuan, and Y. Zhao. The blueshift of the [OIII] emission line in narrow-line Seyfert 1 galaxies. *MNRAS*, 364:187–194, November 2005.

A. J. Bird, et al., and . The Third IBIS/ISGRI Soft Gamma-Ray Survey Catalog. *ApJS*, 170: 175–186, May 2007.

R. D. Blandford and C. F. McKee. Reverberation mapping of the emission line regions of Seyfert galaxies and quasars. *ApJ*, 255:419–439, April 1982.

A. J. Blustin, M. J. Page, S. V. Fuerst, G. Branduardi-Raymont, and C. E. Ashton. The nature and origin of Seyfert warm absorbers. *A&A*, 431:111–125, February 2005.

T. Boller, R. Keil, G. Hasinger, E. Costantini, R. Fujimoto, N. Anabuki, I. Lehmann, and L. Gallo. XMM-Newton observation of the ULIRG NGC 6240. The physical nature of the complex Fe K line emission. *A&A*, 411:63–70, November 2003.

T. A. Boroson and J. B. Oke. Spectroscopy of the galaxy components of N and Seyfert galaxies. *PASP*, 99:809–815, August 1987.

B. R. Brandl, J. Bernard-Salas, H. W. W. Spoon, D. Devost, G. C. Sloan, and et al. The Mid-Infrared Properties of Starburst Galaxies from Spitzer-IRS Spectroscopy. *ApJ*, 653: 1129–1144, December 2006.

L. W. Brenneman and C. S. Reynolds. Constraining Black Hole Spin via X-Ray Spectroscopy. *ApJ*, 652:1028–1043, December 2006.

M. Brusa, F. Civano, A. Comastri, T. Miyaji, M. Salvato, and et al. The XMM-Newton Wide-field Survey in the Cosmos Field (XMM-COSMOS): Demography and Multiwavelength Properties of Obscured and Unobscured Luminous Active Galactic Nuclei. *ApJ*, 716:348–369, June 2010.

M. Cappi, et al., and . X-ray spectral survey with XMM-Newton of a complete sample of nearby Seyfert galaxies. *A&A*, 446:459–470, February 2006.

J. A. Cardelli, G. C. Clayton, and J. S. Mathis. The relationship between infrared, optical, and ultraviolet extinction. *ApJ*, 345:245–256, October 1989.

F. J. Carrera, J. Ebrero, S. Mateos, M. T. Ceballos, A. Corral, X. Barcons, M. J. Page, S. R. Rosen, M. G. Watson, J. A. Tedds, R. Della Ceca, T. Maccacaro, H. Brunner, M. Freyberg, G. Lamer, F. E. Bauer, and Y. Ueda. The XMM-Newton serendipitous survey. III. The AXIS X-ray source counts and angular clustering. *A&A*, 469:27–46, July 2007.

J. E. Chiar and A. G. G. M. Tielens. Pixie Dust: The Silicate Features in the Diffuse Interstellar Medium. *ApJ*, 637:774–785, February 2006.

A. Comastri. Compton-Thick AGN: The Dark Side of the X-Ray Background. In A. J. Barger, editor, *Supermassive Black Holes in the Distant Universe*, volume 308 of *Astrophysics and Space Science Library*, pages 245–+, August 2004.

L. L. Cowie, A. J. Barger, M. W. Bautz, W. N. Brandt, and G. P. Garmire. The Redshift Evolution of the 2-8 keV X-Ray Luminosity Function. *ApJ*, 584:L57–L60, February 2003.

S. M. Croom, R. J. Smith, B. J. Boyle, T. Shanks, L. Miller, P. J. Outram, and N. S. Loaring. The 2dF QSO Redshift Survey - XII. The spectroscopic catalogue and luminosity function. *MNRAS*, 349:1397–1418, April 2004.

M. Dadina. BeppoSAX observations in the 2-100 keV band of the nearby Seyfert galaxies: an atlas of spectra. *A&A*, 461:1209–1252, January 2007.

D. A. Dale, J. D. T. Smith, L. Armus, B. A. Buckalew, G. Helou, R. C. Kennicutt, Jr., J. Moustakas, H. Roussel, and et al. Mid-Infrared Spectral Diagnostics of Nuclear and Extranuclear Regions in Nearby Galaxies. *ApJ*, 646:161–173, July 2006. [D06]

D. A. Dale, J. D. T. Smith, and et al. The Spitzer Infrared Nearby Galaxies Survey: A High-Resolution Spectroscopy Anthology. *ApJ*, 693:1821–1834, March 2009. [D09]

K. M. Dasyra, L. C. Ho, L. Armus, P. Ogle, G. Helou, B. M. Peterson, D. Lutz, H. Netzer, and E. Sturm. High-Ionization Mid-Infrared Lines as Black Hole Mass and Bolometric Luminosity Indicators in Active Galactic Nuclei. *ApJ*, 674:L9–L12, February 2008.

G. de Vaucouleurs, A. de Vaucouleurs, H. G. Corwin, Jr., R. J. Buta, G. Paturel, and P. Fouque. *Third Reference Catalogue of Bright Galaxies*. Volume 1-3, XII, 2069 pp. 7 figs.. Springer-Verlag Berlin Heidelberg New York, 1991.

R. Della Ceca, P. Severgnini, A. Caccianiga, A. Comastri, R. Gilli, F. Fiore, E. Piconcelli, P. Malaguti, and C. Vignali. Heavily obscured AGN with BeppoSAX, INTEGRAL, SWIFT, XMM and Chandra: prospects for Simbol-X . *Memorie della Societa Astronomica Italiana*, 79:65–+, 2008.

L.-B. Desroches and L. C. Ho. Candidate Active Nuclei in Late-Type Spiral Galaxies. *ApJ*, 690:267–278, January 2009.

A. M. Diamond-Stanic, G. H. Rieke, and J. R. Rigby. Isotropic Luminosity Indicators in a Complete AGN Sample. *ApJ*, 698:623–631, June 2009.

C. Done. Observational characteristics of accretion onto black holes. *ArXiv e-prints*, August 2010.

C. Done, G. M. Madejski, and D. A. Smith. NGC 4945: The Brightest Seyfert 2 Galaxy at 100 keV. *ApJ*, 463:L63+, June 1996.

J. L. Donley, G. H. Rieke, D. M. Alexander, E. Egami, and P. G. Pérez-González. The AGN, Star-forming, and Morphological Properties of Luminous IR-bright/optically-faint Galaxies. *ApJ*, 719:1393–1407, August 2010.

B. T. Draine. Interstellar Dust Grains. *ARA&A*, 41:241–289, 2003.

B. T. Draine and A. Li. Infrared Emission from Interstellar Dust. IV. The Silicate-Graphite-PAH Model in the Post-Spitzer Era. *ApJ*, 657:810–837, March 2007.

J. Ebrero, F. J. Carrera, M. J. Page, J. D. Silverman, X. Barcons, M. T. Ceballos, A. Corral, R. Della Ceca, and M. G. Watson. The XMM-Newton serendipitous survey. VI. The X-ray luminosity function. *A&A*, 493:55–69, January 2009.

M. Elvis, B. J. Wilkes, J. C. McDowell, R. F. Green, J. Bechtold, S. P. Willner, M. S. Oey, E. Polomski, and R. Cutri. Atlas of quasar energy distributions. *ApJS*, 95:1–68, November 1994.

M. Elvis, G. Risaliti, F. Nicastro, J. M. Miller, F. Fiore, and S. Puccetti. An Unveiling Event in the Type 2 Active Galactic Nucleus NGC 4388:A Challenge for a Parsec-Scale Absorber. *ApJ*, 615:L25–L28, November 2004.

U. Erkens, I. Appenzeller, and S. Wagner. The nature of the FHIL winds from AGN. *A&A*, 323:707–716, July 1997.

A. C. Fabian. The obscured growth of massive black holes. *MNRAS*, 308:L39–L43, October 1999.

A. C. Fabian, A. Zoghbi, R. R. Ross, P. Uttley, L. C. Gallo, and et al. Broad line emission from iron K- and L-shell transitions in the active galaxy 1H0707-495. *Nature*, 459:540–542, May 2009.

X. Fan, J. F. Hennawi, and et al. A Survey of $z > 5.7$ Quasars in the Sloan Digital Sky Survey. III. Discovery of Five Additional Quasars. *AJ*, 128:515–522, August 2004.

D. Farrah, J. Bernard-Salas, H. W. W. Spoon, B. T. Soifer, L. Armus, B. Brandl, V. Charmandaris, V. Desai, S. Higdon, D. Devost, and J. Houck. High-Resolution Mid-Infrared Spectroscopy of Ultraluminous Infrared Galaxies. *ApJ*, 667:149–169, September 2007.

E.A. Fath. Bulletin number 149 - the spectra of some spiral nebulae and globular star clusters. *Lick Observatory Bulletin*, 5:71–77, 1908.

L. Ferrarese and D. Merritt. A Fundamental Relation between Supermassive Black Holes and Their Host Galaxies. *ApJ*, 539:L9–L12, August 2000.

F. Fiore, M. Brusa, F. Cocchia, A. Baldi, N. Carangelo, P. Ciliegi, A. Comastri, F. La Franca, R. Maiolino, G. Matt, S. Molendi, M. Mignoli, G. C. Perola, P. Severgnini, and C. Vignali. The HELLAS2XMM survey. IV. Optical identifications and the evolution of the accretion luminosity in the Universe. *A&A*, 409:79–90, October 2003.

F. Fiore, S. Puccetti, M. Brusa, M. Salvato, G. Zamorani, and et al. Chasing Highly Obscured QSOs in the COSMOS Field. *ApJ*, 693:447–462, March 2009.

A. Franceschini, G. Hasinger, T. Miyaji, and D. Malquori. On the relationship between galaxy formation and quasar evolution. *MNRAS*, 310:L5–L9, November 1999.

Y. Fukazawa, N. Iyomoto, A. Kubota, Y. Matsumoto, and K. Makishima. Excess hard X-ray emission from the obscured low luminosity AGN in the nearby galaxy M 51 (NGC 5194). *A&A*, 374:73–82, July 2001.

J. F. Gallimore, A. Yzaguirre, J. Jakoboski, M. J. Stevenosky, D. J. Axon, S. A. Baum, C. L. Buchanan, M. Elitzur, M. Elvis, C. P. O'Dea, and A. Robinson. Infrared Spectral Energy Distributions of Seyfert Galaxies: Spitzer Space Telescope Observations of the 12 μm Sample of Active Galaxies. *ApJS*, 187:172–211, March 2010.

K. Ganda, J. Falcón-Barroso, R. F. Peletier, M. Cappellari, E. Emsellem, R. M. McDermid, P. T. de Zeeuw, and C. M. Carollo. Late-type galaxies observed with SAURON: two-dimensional stellar and emission-line kinematics of 18 spirals. *MNRAS*, 367:46–78, March 2006.

P. Gandhi, H. Horst, A. Smette, S. Hönig, A. Comastri, R. Gilli, C. Vignali, and W. Duschl. Resolving the mid-infrared cores of local Seyferts. *A&A*, 502:457–472, August 2009.

A. Garcia-Rissmann, L. R. Vega, N. V. Asari, R. Cid Fernandes, H. Schmitt, R. M. González Delgado, and T. Storchi-Bergmann. An atlas of calcium triplet spectra of active galaxies. *MNRAS*, 359:765–780, May 2005.

K. Gebhardt, R. Bender, G. Bower, A. Dressler, S. M. Faber, A. V. Filippenko, R. Green, C. Grillmair, L. C. Ho, J. Kormendy, T. R. Lauer, J. Magorrian, J. Pinkney, D. Richstone, and S. Tremaine. A Relationship between Nuclear Black Hole Mass and Galaxy Velocity Dispersion. *ApJ*, 539:L13–L16, August 2000.

N. Gehrels. Confidence limits for small numbers of events in astrophysical data. *ApJ*, 303:336–346, April 1986.

R. Genzel, D. Lutz, E. Sturm, E. Egami, D. Kunze, A. F. M. Moorwood, D. Rigopoulou, H. W. W. Spoon, A. Sternberg, L. E. Tacconi-Garman, L. Tacconi, and N. Thatte. What Powers Ultraluminous IRAS Galaxies? *ApJ*, 498:579–+, May 1998.

I. Georgantopoulos, A. Akylas, A. Georgakakis, and M. Rowan-Robinson. The Compton-thick AGN in the Chandra Deep Field North. *A&A*, 507:747–756, November 2009.

G. Ghisellini, F. Haardt, and G. Matt. The Contribution of the Obscuring Torus to the X-Ray Spectrum of Seyfert Galaxies - a Test for the Unification Model. *MNRAS*, 267: 743–+, April 1994.

R. Giacconi, A. Zirm, J. Wang, P. Rosati, M. Nonino, P. Tozzi, R. Gilli, V. Mainieri, G. Hasinger, L. Kewley, J. Bergeron, S. Borgani, R. Gilmozzi, N. Grogin, A. Koekemoer, E. Schreier, W. Zheng, and C. Norman. Chandra Deep Field South: The 1 Ms Catalog. *ApJS*, 139:369–410, April 2002.

R. Gilli, A. Comastri, and G. Hasinger. The synthesis of the cosmic X-ray background in the Chandra and XMM-Newton era. *A&A*, 463:79–96, February 2007.

R. Gilli, C. Vignali, M. Mignoli, K. Iwasawa, A. Comastri, and G. Zamorani. The X-ray to [Ne V]3426 flux ratio: discovering heavily obscured AGN in the distant Universe. *ArXiv e-prints*, May 2010.

A. D. Goulding and D. M. Alexander. Towards a complete census of AGN in nearby Galaxies: a large population of optically unidentified AGN. *MNRAS*, 398:1165–1193, September 2009. [GA09]

A. D. Goulding, D. M. Alexander, B. D. Lehmer, and J. R. Mullaney. Towards a complete census of active galactic nuclei in nearby galaxies: the incidence of growing black holes. *MNRAS*, 406:597–611, July 2010.

G. L. Granato, L. Silva, A. Lapi, F. Shankar, G. De Zotti, and L. Danese. The growth of the nuclear black holes in submillimetre galaxies. *MNRAS*, 368:L72–L76, May 2006.

J. E. Greene and L. C. Ho. The M_{BH}–σ_* Relation in Local Active Galaxies. *ApJ*, 641: L21–L24, April 2006.

J. E. Greene and L. C. Ho. The Mass Function of Active Black Holes in the Local Universe. *ApJ*, 667:131–148, September 2007.

J. E. Greene, L. C. Ho, and A. J. Barth. Black Holes in Pseudobulges and Spheroidals: A Change in the Black Hole-Bulge Scaling Relations at Low Mass. *ApJ*, 688:159–179, November 2008.

L. J. Greenhill, C. R. Gwinn, R. Antonucci, and R. Barvainis. VLBI Imaging of Water Maser Emission from the Nuclear Torus of NGC 1068. *ApJ*, 472:L21+, November 1996.

L. J. Greenhill, J. M. Moran, and J. R. Herrnstein. The Distribution of H 2O Maser Emission in the Nucleus of NGC 4945. *ApJ*, 481:L23+, May 1997.

B. Groves, B. Nefs, and B. Brandl. The mid-infrared [SIV]/[NeII] versus [NeIII]/[NeII] correlation. *MNRAS*, 391:L113–L116, November 2008.

M. Guainazzi, G. Matt, W. N. Brandt, L. A. Antonelli, P. Barr, and L. Bassani. A broadband X-ray view of NGC 4945. *A&A*, 356:463–474, April 2000.

M. Guainazzi, P. Rodriguez-Pascual, A. C. Fabian, K. Iwasawa, and G. Matt. Unveiling the nature of the highly obscured active galactic nucleus in NGC 5643 with XMM-Newton. *MNRAS*, 355:297–306, November 2004.

L. Hao, Y. Wu, V. Charmandaris, H. W. W. Spoon, J. Bernard-Salas, D. Devost, V. Lebouteiller, and J. R. Houck. Probing the Excitation of Extreme Starbursts: High-Resolution Mid-Infrared Spectroscopy of Blue Compact Dwarfs. *ApJ*, 704:1159–1173, October 2009.

G. Hasinger, T. Miyaji, and M. Schmidt. Luminosity-dependent evolution of soft X-ray selected AGN. New Chandra and XMM-Newton surveys. *A&A*, 441:417–434, October 2005.

B. Häussler, D. H. McIntosh, M. Barden, E. F. Bell, H.-W. Rix, and et al. GEMS: Galaxy Fitting Catalogs and Testing Parametric Galaxy Fitting Codes: GALFIT and GIM2D. *ApJS*, 172:615–633, October 2007.

T. M. Heckman. An optical and radio survey of the nuclei of bright galaxies - Activity in normal galactic nuclei. *A&A*, 87:152–164, July 1980.

T. M. Heckman, G. Kauffmann, J. Brinchmann, S. Charlot, C. Tremonti, and S. D. M. White. Present-Day Growth of Black Holes and Bulges: The Sloan Digital Sky Survey Perspective. *ApJ*, 613:109–118, September 2004. [H04]

T. M. Heckman, A. Ptak, A. Hornschemeier, and G. Kauffmann. The Relationship of Hard X-Ray and Optical Line Emission in Low-Redshift Active Galactic Nuclei. *ApJ*, 634:161–168, November 2005.

P. C. Hewett, C. B. Foltz, and F. H. Chaffee. The evolution of bright, optically selected QSOs. *ApJ*, 406:L43–L46, April 1993.

R. C. Hickox and M. Markevitch. Absolute Measurement of the Unresolved Cosmic X-Ray Background in the 0.5-8 keV Band with Chandra. *ApJ*, 645:95–114, July 2006.

R. C. Hickox and M. Markevitch. Resolving the Unresolved Cosmic X-Ray Background in the Chandra Deep Fields. *ApJ*, 661:L117–L121, June 2007.

S. J. U. Higdon, D. Devost, J. L. Higdon, B. R. Brandl, J. R. Houck, P. Hall, D. Barry, V. Charmandaris, J. D. T. Smith, G. C. Sloan, and J. Green. The SMART Data Analysis Package for the Infrared Spectrograph on the Spitzer Space Telescope. *PASP*, 116:975–984, October 2004.

L. C. Ho, A. V. Filippenko, and W. L. Sargent. A search for 'dwarf' Seyfert nuclei. 2: an optical spectral atlas of the nuclei of nearby galaxies. *ApJS*, 98:477–593, June 1995.

L. C. Ho, A. V. Filippenko, and W. L. W. Sargent. A Search for "Dwarf" Seyfert Nuclei. III. Spectroscopic Parameters and Properties of the Host Galaxies. *ApJS*, 112:315–+, October 1997a. [Ho97]

L. C. Ho, A. V. Filippenko, and W. L. W. Sargent. A Search for "Dwarf" Seyfert Nuclei. V. Demographics of Nuclear Activity in Nearby Galaxies. *ApJ*, 487:568–+, October 1997b.

L. C. Ho, E. D. Feigelson, and et al. Detection of Nuclear X-Ray Sources in Nearby Galaxies with Chandra. *ApJ*, 549:L51–L54, March 2001.

L. C. Ho, J. E. Greene, A. V. Filippenko, and W. L. W. Sargent. A Search for "Dwarf" Seyfert Nuclei. VII. A Catalog of Central Stellar Velocity Dispersions of Nearby Galaxies. *ApJS*, 183:1–16, July 2009.

P. F. Hopkins, G. T. Richards, and L. Hernquist. An Observational Determination of the Bolometric Quasar Luminosity Function. *ApJ*, 654:731–753, January 2007.

P. F. Hopkins, L. Hernquist, T. J. Cox, and D. Kereš. A Cosmological Framework for the Co-Evolution of Quasars, Supermassive Black Holes, and Elliptical Galaxies. I. Galaxy Mergers and Quasar Activity. *ApJS*, 175:356–389, April 2008.

H. Horst, A. Smette, P. Gandhi, and W. J. Duschl. The small dispersion of the mid IR - hard X-ray correlation in active galactic nuclei. *A&A*, 457:L17–L20, October 2006.

H. Horst, P. Gandhi, A. Smette, and W. J. Duschl. The mid IR - hard X-ray correlation in AGN and its implications for dusty torus models. *A&A*, 479:389–396, February 2008.

J. R. Houck, T. L. Roellig, and et al. The Infrared Spectrograph (IRS) on the Spitzer Space Telescope. *ApJS*, 154:18–24, September 2004.

F. P. Israel. Centaurus A - NGC 5128. *A&AR*, 8:237–278, 1998.

T. Itoh, C. Done, K. Makishima, G. Madejski, and et al. Suzaku Wide-Band X-Ray Spectroscopy of the Seyfert2 AGN in NGC 4945. *PASJ*, 60:251–+, January 2008.

K. Iwasawa, K. Koyama, H. Awaki, H. Kunieda, K. Makishima, T. Tsuru, T. Ohashi, and N. Nakai. X-ray evidence for Seyfert activity buried in the infrared galaxy NGC 4945. *ApJ*, 409:155–161, May 1993.

N. Iyomoto, Y. Fukazawa, N. Nakai, and Y. Ishihara. BeppoSAX Observation of NGC 3079. *ApJ*, 561:L69–L72, November 2001.

T. H. Jarrett, T. Chester, R. Cutri, S. E. Schneider, and J. P. Huchra. The 2MASS Large Galaxy Atlas. *AJ*, 125:525–554, February 2003.

G. Kauffmann, T. M. Heckman, C. Tremonti, J. Brinchmann, S. Charlot, S. D. M. White, S. E. Ridgway, J. Brinkmann, M. Fukugita, P. B. Hall, Ž. Ivezić, G. T. Richards, and D. P. Schneider. The host galaxies of active galactic nuclei. *MNRAS*, 346:1055–1077, December 2003a.

G. Kauffmann, T. M. Heckman, S. D. M. White, S. Charlot, C. Tremonti et al. Stellar masses and star formation histories for 10^5 galaxies from the Sloan Digital Sky Survey. *MNRAS*, 341:33–53, May 2003b.

K. I. Kellermann, R. Sramek, M. Schmidt, D. B. Shaffer, and R. Green. VLA observations of objects in the Palomar Bright Quasar Survey. *AJ*, 98:1195–1207, October 1989.

L. J. Kewley, M. A. Dopita, R. S. Sutherland, C. A. Heisler, and J. Trevena. Theoretical Modeling of Starburst Galaxies. *ApJ*, 556:121–140, July 2001a.

L. J. Kewley, C. A. Heisler, M. A. Dopita, and S. Lumsden. Optical Classification of Southern Warm Infrared Galaxies. *ApJS*, 132:37–71, January 2001b.

E. Y. Khachikian and D. W. Weedman. An atlas of Seyfert galaxies. *ApJ*, 192:581–589, September 1974.

A. R. King, J. E. Pringle, and J. A. Hofmann. The evolution of black hole mass and spin in active galactic nuclei. *MNRAS*, 385:1621–1627, April 2008.

S. D. Kirhakos and J. E. Steiner. X-ray and infrared selected AGN. II - Optical spectroscopy. *AJ*, 99:1722–1739, June 1990.

G. R. Knapp, P. Guhathakurta, D.-W. Kim, and M. A. Jura. Interstellar matter in early-type galaxies. I - IRAS flux densities. *ApJS*, 70:329–387, June 1989.

J. A. Kollmeier, C. A. Onken, C. S. Kochanek, A. Gould, D. H. Weinberg, M. Dietrich, R. Cool, A. Dey, D. J. Eisenstein, B. T. Jannuzi, E. Le Floc'h, and D. Stern. Black Hole Masses and Eddington Ratios at $0.3 < z < 4$. *ApJ*, 648:128–139, September 2006.

J. Kormendy and R. C. Kennicutt, Jr. Secular Evolution and the Formation of Pseudobulges in Disk Galaxies. *ARA&A*, 42:603–683, September 2004.

J. Kormendy and D. Richstone. Inward Bound—The Search For Supermassive Black Holes In Galactic Nuclei. *ARA&A*, 33:581–+, 1995.

A. Krabbe, T. Böker, and R. Maiolino. N-Band Imaging of Seyfert Nuclei and the Mid-Infrared-X-Ray Correlation. *ApJ*, 557:626–636, August 2001.

S. M. LaMassa, T. M. Heckman, A. Ptak, A. Hornschemeier, L. Martins, P. Sonnentrucker, and C. Tremonti. XMM-Newton Observations of a Complete Sample of Optically Selected Type 2 Seyfert Galaxies. *ApJ*, 705:568–586, November 2009.

O. Laurent, I. F. Mirabel, V. Charmandaris, P. Gallais, S. C. Madden, M. Sauvage, L. Vigroux, and C. Cesarsky. Mid-infrared diagnostics to distinguish AGNs from starbursts. *A&A*, 359:887–899, July 2000.

A. Lawrence. The relative frequency of broad-lined and narrow-lined active galactic nuclei - Implications for unified schemes. *MNRAS*, 252:586–592, October 1991.

N. A. Levenson, K. A. Weaver, T. M. Heckman, H. Awaki, and Y. Terashima. Accretion and Outflow in the Active Galactic Nucleus and Starburst of NGC 5135. *ApJ*, 602: 135–147, February 2004.

A. Li and B. T. Draine. Infrared Emission from Interstellar Dust. II. The Diffuse Interstellar Medium. *ApJ*, 554:778–802, June 2001.

B. Luo, F. E. Bauer, W. N. Brandt, D. M. Alexander, B. D. Lehmer, D. P. Schneider, M. Brusa, A. Comastri, A. C. Fabian, A. Finoguenov, R. Gilli, G. Hasinger, A. E. Hornschemeier, A. Koekemoer, V. Mainieri, M. Paolillo, P. Rosati, O. Shemmer, J. D. Silverman, I. Smail, A. T. Steffen, and C. Vignali. The Chandra Deep Field-South Survey: 2 Ms Source Catalogs. *ApJS*, 179:19–36, November 2008.

D. Lutz, R. Maiolino, H. W. W. Spoon, and A. F. M. Moorwood. The relation between AGN hard X-ray emission and mid-infrared continuum from ISO spectra: Scatter and unification aspects. *A&A*, 418:465–473, May 2004.

D. Lynden-Bell. Galactic Nuclei as Collapsed Old Quasars. *Nature*, 223:690–694, August 1969.

P. Madau, H. C. Ferguson, M. E. Dickinson, M. Giavalisco, C. C. Steidel, and A. Fruchter. High-redshift galaxies in the Hubble Deep Field: colour selection and star formation history to $z\tilde{}4$. *MNRAS*, 283:1388–1404, December 1996.

G. Madejski, P. Życki, C. Done, A. Valinia, P. Blanco, R. Rothschild, and B. Turek. Structure of the Circumnuclear Region of Seyfert 2 Galaxies Revealed by Rossi X-Ray Timing Explorer Hard X-Ray Observations of NGC 4945. *ApJ*, 535:L87–L90, June 2000.

J. Magorrian, S. Tremaine, D. Richstone, R. Bender, G. Bower, A. Dressler, S. M. Faber, K. Gebhardt, R. Green, C. Grillmair, J. Kormendy, and T. Lauer. The Demography of Massive Dark Objects in Galaxy Centers. *AJ*, 115:2285–2305, June 1998.

R. Maiolino and G. H. Rieke. Low-Luminosity and Obscured Seyfert Nuclei in Nearby Galaxies. *ApJ*, 454:95–+, November 1995.

R. Maiolino, M. Salvati, L. Bassani, M. Dadina, R. della Ceca, G. Matt, G. Risaliti, and G. Zamorani. Heavy obscuration in X-ray weak AGNs. *A&A*, 338:781–794, October 1998.

R. Maiolino, O. Shemmer, M. Imanishi, H. Netzer, E. Oliva, D. Lutz, and E. Sturm. Dust covering factor, silicate emission, and star formation in luminous QSOs. *A&A*, 468: 979–992, June 2007.

M. A. Malkan, V. Gorjian, and R. Tam. A Hubble Space Telescope Imaging Survey of Nearby Active Galactic Nuclei. *ApJS*, 117:25–+, July 1998.

A. Marconi, A. Capetti, D. J. Axon, A. Koekemoer, D. Macchetto, and E. J. Schreier. Peering through the Dust: Evidence for a Supermassive Black Hole at the Nucleus of Centaurus A from VLT Infrared Spectroscopy. *ApJ*, 549:915–937, March 2001.

A. Marconi, G. Risaliti, R. Gilli, L. K. Hunt, R. Maiolino, and M. Salvati. Local supermassive black holes, relics of active galactic nuclei and the X-ray background. *MNRAS*, 351:169–185, June 2004.

N. L. Martín-Hernández, D. Schaerer, E. Peeters, A. G. G. M. Tielens, and M. Sauvage. High spatial resolution mid-infrared spectroscopy of the starburst galaxies NGC 3256, II Zw 40 and Henize 2-10. *A&A*, 455:853–870, September 2006.

C. Matsumoto, A. Nava, L. A. Maddox, K. M. Leighly, D. Grupe, H. Awaki, and S. Ueno. An XMM-Newton Observation of the Seyfert 2 Galaxy NGC 6300. I. The Nucleus. *ApJ*, 617:930–938, December 2004.

G. Matt, W. N. Brandt, and A. C. Fabian. The iron Kalpha line complex in Compton-thick Seyfert 2 galaxies. *MNRAS*, 280:823–834, June 1996.

G. Matt, et al., , and . Hard X-ray detection of NGC 1068 with BeppoSAX. *A&A*, 325: L13–L16, September 1997.

G. Matt, A. C. Fabian, M. Guainazzi, K. Iwasawa, L. Bassani, and G. Malaguti. The X-ray spectra of Compton-thick Seyfert 2 galaxies as seen by BeppoSAX. *MNRAS*, 318: 173–179, October 2000.

R. J. McLure and J. S. Dunlop. The cosmological evolution of quasar black hole masses. *MNRAS*, 352:1390–1404, August 2004.

M. Meléndez, S. B. Kraemer, B. K. Armentrout, R. P. Deo, D. M. Crenshaw, H. R. Schmitt, R. F. Mushotzky, J. Tueller, C. B. Markwardt, and L. Winter. New Indicators for AGN Power: The Correlation between [O IV] 25.89 μm and Hard X-Ray Luminosity for Nearby Seyfert Galaxies. *ApJ*, 682:94–103, July 2008a. [M08]

M. Meléndez, S. B. Kraemer, H. R. Schmitt, D. M. Crenshaw, R. P. Deo, R. F. Mushotzky, and F. C. Bruhweiler. Constraining the Active Galactic Nucleus Contribution in a Multiwavelength Study of Seyfert Galaxies. *ApJ*, 689:95–107, December 2008b.

J. S. Miller and R. W. Goodrich. Spectropolarimetry of high-polarization Seyfert 2 galaxies and unified Seyfert theories. *ApJ*, 355:456–467, June 1990.

A. F. M. Moorwood, P. P. van der Werf, J. K. Kotilainen, A. Marconi, and E. Oliva. Starburst superwind and LINER activity in NGC4945. *A&A*, 308:L1+, April 1996.

J. R. Mould, J. P. Huchra, and et al. The Hubble Space Telescope Key Project on the Extragalactic Distance Scale. XXVIII. Combining the Constraints on the Hubble Constant. *ApJ*, 529:786–794, February 2000.

J. Moustakas and R. C. Kennicutt, Jr. An Integrated Spectrophotometric Survey of Nearby Star-forming Galaxies. *ApJS*, 164:81–98, May 2006.

J. S. Mulchaey, A. Koratkar, M. J. Ward, A. S. Wilson, M. Whittle, R. R. J. Antonucci, A. L. Kinney, and T. Hurt. Multiwavelength tests of the dusty torus model for Seyfert galaxies. *ApJ*, 436:586–598, December 1994.

J. R. Mullaney, D. M. Alexander, M. Huynh, A. D. Goulding, and D. Frayer. Characterizing the far-infrared properties of distant X-ray detected AGNs: evidence for evolution in the infrared-X-ray luminosity ratio. *MNRAS*, 401:995–1012, January 2010.

R. Narayan and I. Yi. Advection-dominated accretion: A self-similar solution. *ApJ*, 428: L13–L16, June 1994.

C. H. Nelson, R. F. Green, G. Bower, K. Gebhardt, and D. Weistrop. The Relationship Between Black Hole Mass and Velocity Dispersion in Seyfert 1 Galaxies. *ApJ*, 615: 652–661, November 2004.

H. Netzer, V. Mainieri, P. Rosati, and B. Trakhtenbrot. The correlation of narrow line emission and X-ray luminosity in active galactic nuclei. *A&A*, 453:525–533, July 2006.

C. Norman, G. Hasinger, R. Giacconi, R. Gilli, L. Kewley, M. Nonino, P. Rosati, G. Szokoly, P. Tozzi, J. Wang, W. Zheng, A. Zirm, J. Bergeron, R. Gilmozzi, N. Grogin, A. Koekemoer, and E. Schreier. A Classic Type 2 QSO. *ApJ*, 571:218–225, May 2002.

C. A. Onken, B. M. Peterson, M. Dietrich, A. Robinson, and I. M. Salamanca. Black Hole Masses in Three Seyfert Galaxies. *ApJ*, 585:121–127, March 2003.

C. A. Onken, L. Ferrarese, D. Merritt, B. M. Peterson, R. W. Pogge, M. Vestergaard, and A. Wandel. Supermassive Black Holes in Active Galactic Nuclei. II. Calibration of the Black Hole Mass-Velocity Dispersion Relationship for Active Galactic Nuclei. *ApJ*, 615: 645–651, November 2004.

D. E. Osterbrock and G. J. Ferland. *Astrophysics of gaseous nebulae and active galactic nuclei*. Astrophysics of gaseous nebulae and active galactic nuclei, 2nd. ed. by D.E. Osterbrock and G.J. Ferland. Sausalito, CA: University Science Books, 2006, 2006.

M. J. Page. The fraction of galaxies that contain active nuclei and their accretion rates. *MNRAS*, 328:925–930, December 2001.

F. Panessa and L. Bassani. Unabsorbed Seyfert 2 galaxies. *A&A*, 394:435–442, November 2002.

F. Panessa, L. Bassani, M. Cappi, M. Dadina, X. Barcons, F. J. Carrera, L. C. Ho, and K. Iwasawa. On the X-ray, optical emission line and black hole mass properties of local Seyfert galaxies. *A&A*, 455:173–185, August 2006.

E. Peeters, H. W. W. Spoon, and A. G. G. M. Tielens. Polycyclic Aromatic Hydrocarbons as a Tracer of Star Formation? *ApJ*, 613:986–1003, October 2004.

C. Y. Peng, L. C. Ho, C. D. Impey, and H.-W. Rix. Detailed Structural Decomposition of Galaxy Images. *AJ*, 124:266–293, July 2002.

B. M. Peterson and A. Wandel. Keplerian Motion of Broad-Line Region Gas as Evidence for Supermassive Black Holes in Active Galactic Nuclei. *ApJ*, 521:L95–L98, August 1999.

A. Pope, R. S. Bussmann, A. Dey, N. Meger, D. M. Alexander, M. Brodwin, R.-R. Chary, M. E. Dickinson, D. T. Frayer, T. R. Greve, M. Huynh, L. Lin, G. Morrison, D. Scott, and C.-H. Yan. The Nature of Faint Spitzer-selected Dust-obscured Galaxies. *ApJ*, 689: 127–133, December 2008.

K. A. Pounds, J. N. Reeves, A. R. King, and K. L. Page. Exploring the complex X-ray spectrum of NGC 4051. *MNRAS*, 350:10–20, May 2004.

C. Ratnam and P. Salucci. The mass distribution in the innermost regions of spiral galaxies. *New Astronomy*, 5:427–439, December 2000.

M. J. Rees. Black Hole Models for Active Galactic Nuclei. *ARA&A*, 22:471–506, 1984.

G. T. Richards et al. The Sloan Digital Sky Survey Quasar Survey: Quasar Luminosity Function from Data Release 3. *AJ*, 131:2766–2787, June 2006.

J. R. Rigby, G. H. Rieke, J. L. Donley, A. Alonso-Herrero, and P. G. Pérez-González. Why X-Ray-selected Active Galactic Nuclei Appear Optically Dull. *ApJ*, 645:115–133, July 2006.

D. Rigopoulou, D. Kunze, D. Lutz, R. Genzel, and A. F. M. Moorwood. An ISO-SWS survey of molecular hydrogen in starburst and Seyfert galaxies. *A&A*, 389:374–386, July 2002.

G. Risaliti, R. Maiolino, and M. Salvati. The Distribution of Absorbing Column Densities among Seyfert 2 Galaxies. *ApJ*, 522:157–164, September 1999.

G. Risaliti, M. Salvati, M. Elvis, G. Fabbiano, A. Baldi, S. Bianchi, V. Braito, M. Guainazzi, G. Matt, G. Miniutti, J. Reeves, R. Soria, and A. Zezas. The XMM-Newton long look of NGC 1365: uncovering of the obscured X-ray source. *MNRAS*, 393:L1–L5, February 2009.

I. Robson. *Active galactic nuclei*. 1996.

E. E. Salpeter. Accretion of Interstellar Matter by Massive Objects. *ApJ*, 140:796–800, August 1964.

D. B. Sanders and I. F. Mirabel. Luminous Infrared Galaxies. *ARA&A*, 34:749–+, 1996.

D. B. Sanders, J. M. Mazzarella, D.-C. Kim, J. A. Surace, and B. T. Soifer. The IRAS Revised Bright Galaxy Sample. *AJ*, 126:1607–1664, October 2003.

M. Sarzi, J. C. Shields, K. Schawinski, H. Jeong, K. Shapiro, R. Bacon, M. Bureau, M. Cappellari, R. L. Davies, P. T. de Zeeuw, E. Emsellem, J. Falcón-Barroso, D. Krajnović, H. Kuntschner, R. M. McDermid, R. F. Peletier, R. C. E. van den Bosch, G. van de Ven, and S. K. Yi. The SAURON project - XVI. On the sources of ionization for the gas in elliptical and lenticular galaxies. *MNRAS*, 402:2187–2210, March 2010.

S. Satyapal, D. Vega, T. Heckman, B. O'Halloran, and R. Dudik. The Discovery of an Active Galactic Nucleus in the Late-Type Galaxy NGC 3621: Spitzer Spectroscopic Observations. *ApJ*, 663:L9–L12, July 2007.

S. Satyapal, D. Vega, R. P. Dudik, N. P. Abel, and T. Heckman. Spitzer Uncovers Active Galactic Nuclei Missed by Optical Surveys in Seven Late-Type Galaxies. *ApJ*, 677: 926–942, April 2008. [S08]

D. Schaerer and G. Stasińska. On the origin of [O iv] emission in Wolf-Rayet galaxies. *A&A*, 345:L17–L21, May 1999.

K. Schawinski et al. The Effect of Environment on the Ultraviolet Color-Magnitude Relation of Early-Type Galaxies. *ApJS*, 173:512–523, December 2007.

M. Schmidt. 3C 273 : A Star-Like Object with Large Red-Shift. *Nature*, 197:1040–+, March 1963.

M. Schmidt and R. F. Green. Quasar evolution derived from the Palomar bright quasar survey and other complete quasar surveys. *ApJ*, 269:352–374, June 1983.

H. R. Schmitt. The Difference between the Narrow-Line Regions of Seyfert 1 and Seyfert 2 Galaxies. *ApJ*, 506:647–657, October 1998.

S. Serjeant et al. Herschel ATLAS: The cosmic star formation history of quasar host galaxies. *A&A*, 518:L7+, July 2010.

C. K. Seyfert. Nuclear Emission in Spiral Nebulae. *ApJ*, 97:28–+, January 1943.

N. I. Shakura and R. A. Sunyaev. Black holes in binary systems. Observational appearance. *A&A*, 24:337–355, 1973.

G. A. Shields. Thermal continuum from acretion disks in quasars. *Nature*, 272:706–708, April 1978.

H. Shirai, Y. Fukazawa, M. Sasada, M. Ohno, D. Yonetoku, S. Yokota, R. Fujimoto, T. Murakami, Y. Terashima, H. Awaki, S. Ikeda, M. Ozawa, and T. G. Tsuru. Detailed Hard X-Ray Measurements of Nuclear Emission from the Seyfert2 Galaxy NGC4388 with Suzaku. *PASJ*, 60:263–+, January 2008.

R. Siebenmorgen and E. Krügel. Dust in starburst nuclei and ULIRGs. SED models for observers. *A&A*, 461:445–453, January 2007.

C. Simpson. The luminosity dependence of the type 1 active galactic nucleus fraction. *MNRAS*, 360:565–572, June 2005.

J. D. T. Smith, L. Armus, and et al. Spectral Mapping Reconstruction of Extended Sources. *PASP*, 119:1133–1144, October 2007.

A. Soltan. Masses of quasars. *MNRAS*, 200:115–122, July 1982.

T. Storchi-Bergmann, A. L. Kinney, and P. Challis. Ultraviolet to Near-Infrared Spectral Distributions of Star-forming and Seyfert 2 Galaxies. *ApJS*, 98:103–+, May 1995.

I. Strateva, Ž. Ivezić, G. R. Knapp, V. K. Narayanan, and et al. Color Separation of Galaxy Types in the Sloan Digital Sky Survey Imaging Data. *AJ*, 122:1861–1874, October 2001.

E. Sturm, D. Lutz, A. Verma, H. Netzer, A. Sternberg, A. F. M. Moorwood, E. Oliva, and R. Genzel. Mid-Infrared line diagnostics of active galaxies. A spectroscopic AGN survey with ISO-SWS. *A&A*, 393:821–841, October 2002.

Y. Tanaka, H. Inoue, and S. S. Holt. The X-ray astronomy satellite ASCA. *PASJ*, 46: L37–L41, June 1994.

H. I. Teplitz, V. Desai, L. Armus, R. Chary, J. A. Marshall, J. W. Colbert, D. T. Frayer, A. Pope, A. Blain, H. W. W. Spoon, V. Charmandaris, and D. Scott. Measuring PAH Emission in Ultradeep Spitzer IRS Spectroscopy of High-Redshift IR-Luminous Galaxies. *ApJ*, 659:941–949, April 2007.

Y. Terashima and A. S. Wilson. The Luminous X-Ray Source Population in M51 Observed with Chandra. *ApJ*, 601:735–758, February 2004.

S. Tommasin, L. Spinoglio, M. A. Malkan, and G. Fazio. Spitzer-IRS High-Resolution Spectroscopy of the 12 μm Seyfert Galaxies. II. Results for the Complete Data Set. *ApJ*, 709:1257–1283, February 2010.

P. Tozzi, R. Gilli, V. Mainieri, C. Norman, G. Risaliti, P. Rosati, J. Bergeron, S. Borgani, R. Giacconi, G. Hasinger, M. Nonino, A. Streblyanska, G. Szokoly, J. X. Wang, and W. Zheng. X-ray spectral properties of active galactic nuclei in the Chandra Deep Field South. *A&A*, 451:457–474, May 2006.

E. Treister and C. M. Urry. The Evolution of Obscuration in Active Galactic Nuclei. *ApJ*, 652:L79–L82, December 2006.

E. Treister, J. H. Krolik, and C. Dullemond. Measuring the Fraction of Obscured Quasars by the Infrared Luminosity of Unobscured Quasars. *ApJ*, 679:140–148, May 2008.

E. Treister, C. M. Urry, and S. Virani. The Space Density of Compton-Thick Active Galactic Nucleus and the X-Ray Background. *ApJ*, 696:110–120, May 2009.

S. Tremaine, K. Gebhardt, R. Bender, G. Bower, A. Dressler, S. M. Faber, A. V. Filippenko, R. Green, C. Grillmair, L. C. Ho, J. Kormendy, T. R. Lauer, J. Magorrian, J. Pinkney, and D. Richstone. The Slope of the Black Hole Mass versus Velocity Dispersion Correlation. *ApJ*, 574:740–753, August 2002.

J. Tueller, R. F. Mushotzky, S. Barthelmy, J. K. Cannizzo, N. Gehrels, C. B. Markwardt, G. K. Skinner, and L. M. Winter. Swift BAT Survey of AGNs. *ApJ*, 681:113–127, July 2008.

Y. Ueda, M. Akiyama, K. Ohta, and T. Miyaji. Cosmological Evolution of the Hard X-Ray Active Galactic Nucleus Luminosity Function and the Origin of the Hard X-Ray Background. *ApJ*, 598:886–908, December 2003.

C. M. Urry and P. Padovani. Unified Schemes for Radio-Loud Active Galactic Nuclei. *PASP*, 107:803–+, September 1995.

F. Valdes, R. Gupta, J. A. Rose, H. P. Singh, and D. J. Bell. The Indo-US Library of Coudé Feed Stellar Spectra. *ApJS*, 152:251–259, June 2004.

R. V. Vasudevan and A. C. Fabian. Piecing together the X-ray background: bolometric corrections for active galactic nuclei. *MNRAS*, 381:1235–1251, November 2007.

R. V. Vasudevan and A. C. Fabian. Simultaneous X-ray/optical/UV snapshots of active galactic nuclei from XMM-Newton: spectral energy distributions for the reverberation mapped sample. *MNRAS*, 392:1124–1140, January 2009.

R. V. Vasudevan, R. F. Mushotzky, L. M. Winter, and A. C. Fabian. Optical-to-X-ray emission in low-absorption AGN: results from the Swift-BAT 9-month catalogue. *MNRAS*, pages 1234–+, August 2009.

R. V. Vasudevan, A. C. Fabian, P. Gandhi, L. M. Winter, and R. F. Mushotzky. The power output of local obscured and unobscured AGN: crossing the absorption barrier with Swift/BAT and IRAS. *MNRAS*, 402:1081–1098, February 2010.

S. Veilleux and D. E. Osterbrock. Spectral classification of emission-line galaxies. *ApJS*, 63:295–310, February 1987.

S. Veilleux, D.-C. Kim, D. B. Sanders, J. M. Mazzarella, and B. T. Soifer. Optical Spectroscopy of Luminous Infrared Galaxies. II. Analysis of the Nuclear and Long-Slit Data. *ApJS*, 98:171–+, May 1995.

S. Veilleux, D.-C. Kim, and D. B. Sanders. Optical Spectroscopy of the IRAS 1 JY Sample of Ultraluminous Infrared Galaxies. *ApJ*, 522:113–138, September 1999.

C. Vignali, D. M. Alexander, R. Gilli, and F. Pozzi. Discovery of Compton-thick quasars in the Sloan Digital Sky Survey. *MNRAS*, 404:48–59, May 2010.

P. Vignati, S. Molendi, G. Matt, M. Guainazzi, L. A. Antonelli, L. Bassani, W. N. Brandt, A. C. Fabian et al. BeppoSAX unveils the nuclear component in NGC 6240. *A&A*, 349: L57–L60, September 1999.

A. Wandel. The Black Hole-to-Bulge Mass Relation in Active Galactic Nuclei. *ApJ*, 519: L39–L42, July 1999.

A. Wandel, B. M. Peterson, and M. A. Malkan. Central Masses and Broad-Line Region Sizes of Active Galactic Nuclei. I. Comparing the Photoionization and Reverberation Techniques. *ApJ*, 526:579–591, December 1999.

M. J. Ward, T. Geballe, M. Smith, R. Wade, and P. Williams. Near-infrared spectra of Seyfert nuclei. I - The reddening problem. *ApJ*, 316:138–144, May 1987.

M. G. Watson, , , and et al. The XMM-Newton serendipitous survey. V. The Second XMM-Newton serendipitous source catalogue. *A&A*, 493:339–373, January 2009.

K. A. Weaver, M. Meléndez, R. F. Mushotzky, S. Kraemer, K. Engle, E. Malumuth, J. Tueller, C. Markwardt, C. T. Berghea, R. P. Dudik, L. M. Winter, and L. Armus. Mid-

Infrared Properties of the Swift Burst Alert Telescope Active Galactic Nuclei Sample of the Local Universe. I. Emission-Line Diagnostics. *ArXiv e-prints*, April 2010.

D. W. Weedman. Seyfert galaxies, quasars and redshifts. QJRAS, 17:227–262, September 1976.

D. W. Weedman, L. Hao, S. J. U. Higdon, D. Devost, Y. Wu, V. Charmandaris, B. Brandl, E. Bass, and J. R. Houck. Mid-Infrared Spectra of Classical AGNs Observed with the Spitzer Space Telescope. *ApJ*, 633:706–716, November 2005.

M. W. Werner, T. L. Roellig, and et al. The Spitzer Space Telescope Mission. *ApJS*, 154: 1–9, September 2004.

M. Whittle. Virial and jet-induced velocities in Seyfert galaxies. I - A compilation of narrow line region and host galaxy properties. *ApJS*, 79:49–75, March 1992.

V. Wild, T. Heckman, P. Sonnentrucker, B. Groves, L. Armus, D. Schiminovich, B. Johnson, L. Martins, and S. LaMassa. A complete census of AGN and their hosts from optical surveys? *ArXiv e-prints*, January 2010.

L. M. Winter, R. F. Mushotzky, C. S. Reynolds, and J. Tueller. X-Ray Spectral Properties of the BAT AGN Sample. *ApJ*, 690:1322–1349, January 2009.

M. A. Worsley, A. C. Fabian, F. E. Bauer, D. M. Alexander, G. Hasinger, S. Mateos, H. Brunner, W. N. Brandt, and D. P. Schneider. The unresolved hard X-ray background: the missing source population implied by the Chandra and XMM-Newton deep fields. *MNRAS*, 357:1281–1287, March 2005.

Y. Yang, A. S. Wilson, G. Matt, Y. Terashima, and L. J. Greenhill. Suzaku Observations of the Circinus Galaxy. *ApJ*, 691:131–139, January 2009.

T. Yaqoob, K. D. Murphy, R. E. Griffiths, Y. Haba, H. Inoue, T. Itoh, R. Kelley et al. Precision Fe Kα and Fe Kβ Line Spectroscopy of the Seyfert 1.9 Galaxy NGC 2992 with Suzaku. *PASJ*, 59:283–299, January 2007.

X. Z. Zheng, E. F. Bell, R. S. Somerville, H.-W. Rix, K. Jahnke, F. Fontanot, G. H. Rieke, D. Schiminovich, and K. Meisenheimer. Observational Constraints on the Co-Evolution of Supermassive Black Holes and Galaxies. *ApJ*, 707:1566–1577, December 2009.